New methods for identifying dune system reactivation drivers and responses, Nebraska Sandhills

Catherine Elizabeth Buckland

Supervisors: Dr R.M. Bailey & Professor D.S.G. Thomas

Jesus College

Thesis submitted for the degree of
Doctor of Philosophy



University of Oxford
Trinity Term 2018

Abstract

Two billion people living in drylands are affected by land degradation and the destabilisation of surface sediments. However, a detailed understanding of the combined effects of natural and anthropogenic factors in contributing to sediment remobilisation is absent from the literature. A quantified awareness of vegetation cover sensitivities and resultant land degradation to forcing factors is needed if the vegetation and landscape response to future climatic changes and human pressure are to be better predicted.

Measuring past environmental response in a location with a known disturbance history allows us to identify thresholds and explore the relationship between disturbance forces and sedimentary response within a dryland environment. The Nebraska Sandhills, located in the Central Great Plains, is a semi-arid dune field with a reactivation history spanning the last 10,000 years and a well-documented history of forcing factors over recent decades. Whilst regional reactivations in the Central Great Plains have largely been attributed to palaeoclimatic change, the role of humans (e.g. The Dust Bowl of the 1930s), in particular over grazing, has also been cited as a potential cause of land degradation and sediment reactivation.

Using quartz luminescence dating, secondary datasets of forcing factors and statistical inference methods, this thesis identifies the record of sediment deposition in near-surface aeolian stratigraphies in the northern remits of the Nebraska Sandhills and explores the relationship between environmental sensitivity and external disturbance factors. High-resolution luminescence techniques allow us to construct a detailed chronological history of sedimentary deposition events over the last 900 years, producing a record of the environmental response across a range of aeolian features within the semi-arid setting. Combined with a detailed history of climatic, grazing and wildfire pressures, supervised machine learning techniques explore the relationship between forcing factor and environmental response, highlighting the importance of both regional and localised conditions in contributing to the heterogeneous sedimentary response found in the record.

Acknowledgements

Firstly, a very big thank you goes to my supervisors Dr Richard Bailey and Professor Dave Thomas for their endless time, guidance and support over the past four years. A wealth of experiences from the field, lab and hours spent coding, have given me great enjoyment over the past four years. I am also very grateful to Szilvia Bajkan for guiding me through luminescence preparation and providing me with unwavering support in the laboratory stages of the project.

Thank you also to Sallie, Julie, Mona, Aayush and Kaja for their advice and encouragement in the lab. I am very grateful also to David Wedin, Paul Hanson, and their colleagues at the University of Nebraska-Lincoln who were instrumental in developing the pilot field season in Nebraska and provided valuable feedback as the project progressed. I would also like to acknowledge the staff at the Gudmundsen Sandhills Laboratory and Niobrara Valley Preserve – especially Amanda Hefner, who kindly assisted with logistics at Niobrara and helped gather archived datasets once I had returned to Oxford. Thank you also to EJ and Charlene Hansen-Webber and Al and Lois Steuter and for their assistance in the field - their expertise and knowledge was imperative to collecting the best datasets available for this research project.

Thank you to NERC for providing the research funding and studentship to complete this research project, as well as Elsevier and Jesus College for graduate research grants which have allowed me to attend international conferences and present the key findings from this thesis.

Finally, to Darren, for being my sound board on all things sandy and Nebraskan. You have spent the last four years listening to me discuss decay curves, blowouts and Matlab error messages, all with the utmost patience and support.

Contents

Abstract i
Acknowledgements iii
Contents v
List of figures xi
List of tables xvi
List of equations xviii
Units xviii
Abbreviations xix

SECTION ONE: RESEARCH CONTEXT

Chapter 1: Introduction

1.1 Introduction 4
1.1.1 Motivation 4
1.2 Research Questions 7
1.3 Thesis Structure 8

Chapter 2: Context

2.1 Introduction 12
2.2 Drivers of surface reactivation 12
2.3 A focus on climatic factors 13
2.4 The role of humans 15
2.5 A gap in our understanding 17
2.6 Approach 18
2.7 Records of environmental response 20
2.7.1 Dune profiles 20
2.7.2 Blowouts 21
2.8 Application of OSL 22
2.8.1 OSL measures date since deposition 22
2.8.2 OSL techniques and young sediments 23
2.8.3 High-resolution and near-surface OSL applications 24
2.9 Nebraska Sandhills: Site selection and rationale 26
2.9.1 Known history of disturbances 27
2.9.2 Existing history of activation 28
2.9.3 Quartz-rich sediments 29

2.10 Statistical Inference tools 31
2.11 Summary 33

SECTION TWO: FIELD AND LABORATORY EXPERIMENTS

Chapter 3: Field sampling and laboratory experiments

3.1 Introduction 38
3.2 Sediment sampling 38
3.2.1 Sample extraction 41
3.2.2 Sampling strategy 41
3.3 Changepoint analysis 53
3.3.1 Particle size analysis 55
3.4 OSL dating 55
3.4.1 Principles of OSL dating 55
3.4.2 Transporting OSL samples 56
3.4.3 OSL sample preparation 57
3.4.4 Equipment set-up 58
3.4.5 SAR measurement protocol 59
3.4.6 Dose recovery test 59
3.4.7 Selecting integration intervals 61
3.4.8 Calculating the environmental dose rate 64
3.4.9 Age estimation 69

Chapter 4: Testing the suitability of p-IR IRSL for dating young samples (< 200 yrs) (PAPER 1)

Prelude 72
Abstract 73
4.1 Introduction 74
4.2 Methods and Instrumentation 77
4.2.1 Samples 77
4.2.2 Sample preparation and instrumentation 77
4.3 Selecting appropriate measurement parameters for Quartz and Feldspar 79
4.3.1 Quartz 79
4.3.2 K-feldspar 83
4.4 Comparing rates of anomalous fading 87
4.5 Comparing the bleaching rate of quartz and feldspar 89

4.6 Comparison of natural residual signals 90
4.7 Selection of appropriate rejection criteria for young samples 95
4.7.1 Recuperation 96
4.7.2 Identifying partial bleaching and dominant slow components using $D_e(t)$-plots 97
4.8 Conclusions 102

Chapter 5: Identifying chronostratigraphic breaks in aeolian sediment profiles using near-surface luminescence dating and changepoint analysis (PAPER 2)

Prelude 106
Abstract 107
5.1 Introduction 108
5.2 Methods 115
5.2.1 Study site 115
5.2.2 Field sampling 116
5.2.3 Particle size variability 119
5.2.4 L_x/T_x measurements on bulk samples 119
5.2.5 Changepoint analysis 120
5.2.6 SAR luminescence measurements 123
5.2.7 Dose rate calculation 124
5.2.8 Maximising signal potential 125
5.3 Results 128
5.3.1 L_x/T_x profiles using bulk sample sediment 128
5.3.2 Changepoint analysis on L_x/T_x profiles 130
5.3.3 Age-depth profile estimates 135
5.4 Discussion 138
5.4.1 Relative age profiles across a dune 138
5.4.2 Reproducing signals above noise 141
5.4.3 Predicting age-depth profiles from mid-point age estimates 144
5.4.4 Complicating factors on sample age 146
5.4.5 Application of this approach to longer time-series 147
5.5 Conclusions 149

SECTION THREE: DATA ANALYSIS

Chapter 6: Secondary datasets and analysis methods

6.1 Introduction 154
6.2 Datasets of environmental conditions 154
6.2.1 Growing season precipitation 155
6.2.2 Palmer Drought Severity Index (PDSI) 155
6.2.3 Local tree ring growth index 156
6.2.4 Wildfire 157
6.2.5 Grazing pressure history 158
6.2.6 Wind velocity 160
6.3 Analysing the datasets 161
6.3.1 Traditional descriptive analysis 161
6.3.2 Lagged-analysis 162
6.3.3 Artificial neural networks 163

Chapter 7: Complex disturbance-driven reactivation of the largest dunefield in the western hemisphere during the last 500 years (PAPER 3)

Prelude 168
Abstract 169
7.1 Introduction 170
7.1.1 Approach 172
7.2 Study site and methods 174
7.2.1 Study area 174
7.2.2 Dunefield disturbance record 175
7.2.3 Vegetation cover drivers 180
7.3 Results and Discussion 184
7.3.1 Dune reactivation histories 184
7.3.2 Integrating deposition and driver profiles 193
7.4 Evidence for the role of individual disturbance factors 200
7.4.1 The role of climate 201
7.4.2 The role of wildfires 203
7.4.3 The role of grazing pressure 204
7.5 Synergies between disturbance factors 206
7.6 Assessing the utility of the luminescence record 207
7.7 Older deposition events 209
7.8 Conclusions 211

Chapter 8: Using artificial neural networks to predict future dryland responses to human and climate disturbances (PAPER 4)

Prelude 214

Abstract 215

8.1 Landscape reactivation in dryland systems 216

8.2 Experimental design 219

8.3 Nebraska Sandhills: a test case 220

8.4 Results 222

8.4.1 Model training 222

8.4.2. Scenario testing 224

8.5 Discussion 229

8.5.1 Drivers of future deposition events 229

8.5.2 Limitations of the approach 231

8.5.3 Wider significance 234

8.6 Methods 235

8.6.1 ANN1 235

8.6.2 ANN2 238

8.6.3 Future scenario forecasting 240

SECTION FOUR: CONCLUSIONS

Chapter 9: Discussion

9.1 RQ 1: Can land surface responses to recent environmental change be identified chronologically in the sedimentary record? 249

9.1.1 High-resolution SAR OSL dating 250

9.1.2 Capturing a more complete record 251

9.1.3 Assessing the utility of the luminescence record 254

9.1.4 Summary 258

9.2 RQ 2: Can we associate environmental conditions with depositional episodes? 259

9.2.1 Can we associate specific depositional episodes to specific or combined driving conditions? 260

9.2.2 Can we identify the nature of events driving environmental change in the region? 266

9.2.3 Implications for wider dune studies 272

9.2.4 Summary 273

9.3 RQ 3: Can a suitable method be identified to predict future surface reactivations leading to deposition? 274

9.3.1 Model highlights 275
9.3.2 Future scenario predicting 276
9.3.3 ANN model limitations 277
9.3.4 Summary 279
9.4 Overall conclusions 280
9.5 Future research 282
9.5.1 Additional external parameters 282
9.5.2 Additional geomorphic features 283
9.5.3 Improving the neural network 284
9.5.4 Summary 287

References 289

Appendices

Appendix A: Author contribution 316
Appendix B: Aerial site imagery and site descriptions 318
Appendix C: Additional sediment cores 337
Appendix D: Integration interval analysis 340
Appendix E: Environmental dose rates 348
Appendix F: Supplementary Information – Paper 2 (Chapter 5) 351
Appendix G: Wildfire tree scar records 358
Appendix H: Homesteading Deeds 360
Appendix I: Genealogy website data 361
Appendix J: Conversations with grassland ecologists and local ranchers 364
Appendix K: Supplementary Information – Paper 3 (Chapter 7) 368
Appendix L: Supplementary Information – Paper 4 (Chapter 8) 372

List of Figures

Main Body

Figure 2.1 Schematic of 'filtering' process where information on palaeoenvironmental conditions is gradually removed from the sedimentary record 24

Figure 2.2 Location of Nebraska Sandhills within the state of Nebraska 27

Figure 3.1 50 cm vertical sediment tube being hammered into upper sediments 41

Figure 3.2 Location of sites sampled during the initial pilot fieldwork in 2015 42

Figure 3.3 Sedimentary profile of blowout backwall where horizontal sediment samples GSL15/3/2 and GSL15/3/3 were extracted 43

Figure 3.4 The linear ridge looking eastward from the blowout backwall at the location of the five sediment cores 45

Figure 3.5 Aerial photograph showing location of the five vertical sediment cores sampled as part of the grid variability analysis 46

Figure 3.6 Aerial photograph of the Grassland Destabilisation Experiment located on the Barta Brothers Ranch 47

Figure 3.7 Example of archived aerial photographs of the USDA FSA 50

Figure 3.8 Location of the six sampling sites selected across the NVP and surrounding area 51

Figure 3.9 Results from equivalent dose measurements of annealed quartz during transport 57

Figure 3.10 Example of luminescence decay curve and position of final integration limits used to calculate net luminescence signal 63

Figure 4.1 Dose recovery preheat plateau results for large aliquots of quartz fraction of sample GSL15/1/3 80

Figure 4.2 Dose recovery preheat plateau results for small aliquots of quartz fractions of sample GSL15/1/3 81

Figure 4.3 p-IR IRSL K-feldspar large aliquot dose recovery preheat plateau results 85

Figure 4.4 p-IR IRSL K-feldspar small aliquot dose recovery preheat plateau results 86

Figure 4.5 Distribution of signal intensity from single grains of four discs of sediment sample BBR15/1/1/10 94

Figure 4.6 Z-values vs D_e plot based on $D_e(t)$-plots of Bailey (2003) 99

Figure 4.7 Luminescence decay curve and component fit of regenerative dose point aliquot 'A' 101

Figure 5.1 A representation of the assumptions made about depositional structure when sedimentary sections are under-sampled 111

Figure 5.2 Location map of the Niobrara Valley Preserve and Gudmundsen Sandhills Laboratory within the Nebraska Sandhills 117

Figure 5.3 Changepoint model outputs for sediment core NVP16/4/3 based on different levels of model sensitivity 122

Figure 5.4 OSL depletion curve of NVP15/4/1/21 with and without a convex quartz lens placed in front of the photomultiplier tube 126

Figure 5.5 Calibration LED OSL counts / Background OSL counts vs Voltage 127

Figure 5.6 L_x/T_x vs. Depth profiles of un-prepared sediment samples from ten cores taken at the Niobrara Valley Preserve site 129

Figure 5.7 Transect NVP16/4 and the location of the four sediment cores extracted 131

Figure 5.8 Plot showing L_x/T_x vs. Depth for sediment core NVP16/4/4 133

Figure 5.9 Original and repeat runs of L_x/T_x vs. Depth profiles coupled with Changepoint analysis 134

Figure 5.10 L_x/T_x profiles coupled with changepoint model outputs and fully-prepared SAR age estimates 136

Figure 5.11 Changepoint model outputs for two sediment cores when different levels of model sensitivity are applied 144

Figure 6.1 Schematic diagram highlighting the complexities in the theoretical model that exists between the predictor variables and the target dataset 165

Figure 7.1 Location map of study area within the northern remits of the Nebraska Sandhills 176

Figure 7.2 Aerial photographs showing location of transects and sediment cores taken at each of the six sites 188

Figure 7.3 Individual forcing factors and OSL ages stacked for each of the six study sites from 1840 – 2020 AD 199

Figure 7.4 Figure shows the lag (in years) between disturbance event and the proceeding luminescence age identified at each of the sites 202

Figure 7.5 Summary plot of OSL ages from dune in the Nebraska Sandhills and surrounding dunefields 210

Figure 8.1 Results from both in-sample and out-of-sample testing across the six sites in ANN1 223

Figure 8.2 Results from training network ANN2 simulating the relationship between growing season precipitation and temperature conditions with tree ring growth over the periods 1908-1997 AD 225

Figure 8.3 Simulated tree ring growth indices based on two different climate scenarios 225

Figure 8.4 ANN1 and ANN2 simulated output results based on two future climate scenarios and three different grazing pressures 227

Figure 8.5 Output results when new scenarios of climatic conditions, grazing pressure and wildfire occurrence are combined over a 100-year period 229

Figure 8.6 Schematic figure demonstrating how the wide training window of activity as defined by the target dataset forces the model to train the equivalent period of input datasets to that target 233

Figure 8.7 Schematic diagram demonstrating the model architecture o the final models used in ANN1 239

Figure 8.8 Schematic diagram demonstrating the model architecture of the final models used in ANN2 239

Figure 8.9 Schematic demonstrating that MSE caused by variation in magnitude of peaks between training and predicted datasets is not useful because the event occurred at the same point in time 244

Figure 9.1 Example of common age units found between sediment cores at sits B, C and D. 253

Figure 9.2 Plot of land patent records for the original homesteading of the land sections in northern Brown County 262

Figure 9.3 Picture of the colonising vegetation species that are typically found in blowouts across the Sandhills 264

Figure 9.4 Erosion pins on the edge of a cleared deflation basin at the Barta Brothers Ranch 267

Appendices

Figure B.1 Archived aerial photographs of the USDA FSA 319

Figure B.2 Google Earth images taken of the six study sites from 1993-2015 321

Figure B.3 Site A (Blowout feature) – field photograph 325

Figure B.4 Site B (Windmill site) – field photograph 328

Figure B.5 Site C (Parabolic dune) – field photograph 330

Figure B.6 Site D (Homestead site) – field photograph 332

Figure B.7 Site E (1930s dune) – field photograph 334

Figure B.8 Site F (Old rolling dunes) – field photograph 336

Figure D.1 Example of the component fitting code output based on the OSL signal measured for a single regeneration point 341

Figure D.2 Example of the individual component levels and proportions of the signal for each 0.1 s of time 342

Figure D.3 Example of calculating the net OSL signal from the fast component 342

Figure D.4 Example of calculating RSE and fast component proportions based on a range of signal and background interval lengths 343

Figure D.5 Plot demonstrating how varying the signal window whilst keeping background integration interval constant changes the RSE 344

Figure D.6 Example data showing % net OSL signal from fast component and RSE with different signal / background combinations 345

Figure D.7 Plot of 'k-value' against percentage of net OSL signal from fast component and RSE % 345

Figure D.8 Comparison between sensitivity-corrected natural / regenerative signal and sensitivity-corrected test dose for different values of 'k' 347

Figure F.1 Preheat test results for sample NVP16/5/1/30 355

Figure G.1 Approximate GPS location of the trees that were used in the fire scar collection analysis 359

Figure K.1 Typical OSL decay curves and dose response curves for samples NVP16/4/2/26 and NVP16/6/2/7 368

Figure K.2 Bayesian modelled age-depth plot for sediment cores NVP15/1/1 and NVP15/3/1 369

Figure K.3 Bayesian modelled age-depth plot for sediment core NVP15/4/1 370

Figure K.4 Historical aerial images of western section of study area in Brown County, Nebraska 371

Figure L.1 Location map of NVP within the Nebraska Sandhills and US 372

Figure L.2 Tree ring growth index compiled using multiple ring widths from Ponderosa pines in the vicinity of the NVP 373

Figure L.3 PDF of stacked OSL ages taken from six sites across the NVP and surrounding ranches 375

Figure L.4 Historic growing season weather data 1908 – 1998 AD 378

Figure L.5 Example outputs from autoregressive model to identify the level of noise associated with the growing season precipitation dataset and simulate new 'noise' for future climates 379

Figure L.6 Growing season precipitation totals and average maximum and minimum growing season daily temperatures associated with the two simulated climate scenarios 380

Figure L.7 Example of change in mean and standard error output profile when different numbers of repeats and % of best peak performing models were used in the final calculation 382

Figure L.8 Plots demonstrating the weak anticorrelation associating tree ring growth with the likelihood for episodes of sediment deposition across the two climate profiles simulated 383

List of Tables

Main Body

Table 2.1 Examples of environmental dose rate range found at previously studied sites across the Nebraska Sandhills 30

Table 3.1 Table of initial OSL results from horizontal pilot samples taken from the Gudmundsen Sandhills Laboratory 44

Table 3.2 Table presents the unlogged-CAM calculated equivalent doses from six large aliquots per depth per sample 46

Table 3.3 Final seventeen vertical sediment cores used 52

Table 3.4 Small aliquots of fully-prepped quartz were used to complete dose recovery tests 60

Table 3.5 Examples of water content calculated for multiple depths of sediment cores 66

Table 3.6 Examples of overburden densities used in the previously published literature 66

Table 3.7 Sensitivity analysis to determine the impact on final age estimation using different combinations of moisture content and overburden density 68

Table 4.1 A modified p-IR IRSL protocol used for equivalent dose determination of p-IR IRSL 85

Table 4.2 Anomalous fading g-values calculated for the K-feldspar and quartz fractions of sample GSL15/1/3 89

Table 4.3 Residual doses (Gy) for large aliquots of quartz and K-feldspar grains following various time intervals outside 90

Table 4.4 Table comparing the natural residual results when tested on different minerals, protocols, aliquot size and age model 92

Table 4.5 $D_e \pm$ error calculated according to the application of the different recuperation threshold options 97

Table 4.6 Z-values associated with three aliquots for both the natural and luminescence signal and a regenerative dose point 100

Table 5.1 Sediment cores specifically referred to in Chapter 5 118

Table 5.2 OSL results for cores NVP15/1/1, NVP15/3/1 and NVP15/4/1 137

Table 6.1 Table of data sources used to produce grazing pressure index according to a scale of 1 (low), 2 (moderate) and 3 (high pressure) 159

Table 7.1 Sediment core latitude, longitude and elevation details 177

Table 7.2 Results for all sub-samples measured using full-preparation OSL dating 185

Table 7.3 Land use, settlement, and assumed grazing history based on archival records and oral histories of Brown County, Nebraska 197

Table 8.1 Description of two different climate scenarios used to generate forecasted tree ring growth indices 241

Table 8.2 Description of six combinations of future climatic, land use and wildfire conditions that have been used in this study to simulate alternate sediment movement likelihood predictions across the six sites 242

Appendices

Table C.1 Table of sediment cores not dated in the final reconstruction of historical sediment reactivation 338

Table E.1 Details of U, Th, K contents used for environmental dose rate calculations for sub-samples used in OSL dating 348

Table E.2 Table of individual dose rate contributions for each sample calculated using DRAC 349

Table F.1 Grain size distribution results for six sediment cores 352

Table F.2 Dose recovery results from six samples following the applied measurement conditions 354

Table F.3 Table of dose rate component measurements for multiple depths within sediment cores NVP15/1/1, NVP15/3/1 and NVP15/4/1 356

Table G.1 Wildfire occurrence alongside the number of tree scar records each fire was recorded in 358

Table H.1 Date that each of the sections containing the sample sites used in this project were first bought as part of the homestead act and the transition from ‘unorganised’ to ‘organised’ territory 360

Table L.1 Summary table of the grazing pressure exerted on each of the six sites over the last 400 years 374

Table L.4 Final OSL dates of deposition per changepoint section 376

List of Equations

Main Body

Equation 3.1 The age equation for luminescence dating 56

Equation 3.2 Calculation of the environmental dose rate 64

Equation 4.1 Calculation of the g-value associated with anomalous fading 87

Appendices

Equation D.1 Three equations used in the calculation of the RSE of the sensitivity-corrected net luminescence signal 346

Units

ka	Thousands of years before present	**AD**	Anno Domini
°C	Degrees Centigrade	**µm**	Microns
Gy	Gray (1 Gy = 1 J kg $^{-1}$)	**a.u.**	Arbitrary units
kPa	Kilopascal		

Abbreviations

AI	Artificial Intelligence	**MSE**	Mean squared error
ANN	Artificial Neural Network	**NCA**	National Climate Assessment
ARD	Arkansas River dunes	**NCDC**	National Climatic Data Center
BBR	Barta Brothers Ranch	**NOAA**	National Oceanic and Atmospheric Administration
CAM	Central Age Model	**NRCS**	Natural Resources Conservation Service
CROPS	Changepoints for a Range of Penalties	**NS**	Nebraska Sandhills
D_e	Equivalent Dose	**NVP**	Niobrara Valley Preserve
DRAC	Dose Rate and Age Calculator	**OSL**	Optically Stimulated Luminescence
DRC	Dose Response Curve	**p-IR IRSL**	Post-infrared Infrared Stimulated Luminescence
DRT	Dose Recovery Test	**PDF**	Probability Density Function
FSA	Farm Service Agency	**PDSI**	Palmer Drought Severity Index
GDEX	Grassland Destabilisation Experiment	**PELT**	Pruned Exact Linear Time
GSL	Gudmundsen Sandhills Laboratory	**PH**	Preheat
H_2O_2	Hydrogen peroxide	**PMT**	Photomultiplier Tube
HCl	Hydrochloric acid	**SAR**	Single Aliquot Regenerative
HD	Hutchinson dunes	**SG**	Single grain
HF	Hydrofluoric acid	**SGC**	Standardised Growth Curves
ICOMMOTR	International Committee on Soil Moisture and Temperature Regimes	**SML**	Supervised Machine Learning
ICP-MS	Inductively-coupled plasma mass spectrometry	**SPI**	Standard Precipitation Index
IR	Infrared	**TL**	Thermoluminescence
IRSL	Infrared Stimulated Luminescence	**TNC**	The Nature Conservancy
LED	Light-emitting diode	**T_x**	Test dose luminescence signal (associated with the natural OSL measurement)
LM	Levenberg-Marquadt	**UNL**	University of Nebraska-Lincoln
L_x	Natural luminescence signal	**USDA**	United States Department of Agriculture
L_x/T_x	Sensitivity-corrected OSL signal	**UV**	Ultraviolet
MAM	Minimum Age Model	**WD**	Wray dunes
MCA	Medieval Climatic Anomaly		

SECTION ONE

RESEARCH CONTEXT

Chapter 1

Introduction

1.1 Introduction

1.1.1 Motivation

Drylands represent c.40% of the terrestrial landscape and are home to a third of the world's population (Wang *et al.*, 2012). Dryland environments are sensitive to both human and natural disturbances, with external forces inducing greater levels of landscape dynamism, including aeolian erosion and land degradation. Land degradation and surface sediment mobilisation are key environmental issues in drylands, with their consequences estimated to directly affect 2 billion people (Middleton, 2011). Land degradation induces a variety of problems for local communities (Middleton and Sternberg, 2013; Reynolds *et al.*, 2007b; Wang *et al.*, 2012) including: the removal of fertile soils and nutrients (Wasson and Nanninga, 1986), the burial of small plants (Goossens, 2003) and damage to infrastructure, livestock and crops (Wiggs, 2011a). Such are the consequences, the Millennium Ecosystem Assessment (2005) considers land degradation as one of the major environmental issues of the 21st century. Understanding the causes of land degradation and subsequent aeolian erosion are therefore of paramount importance in the face of future environmental change.

Existing research has identified ecological thresholds and surface vegetation sensitivity to external forcing (Mangan *et al.*, 2004), including grazing pressure (Belsky, 1992; Biondini et al., 1998a; Milchunas et al., 1989), fire (Arterburn *et al.*, 2018; Ravi *et al.*, 2009; Whicker *et al.*, 1999), land use (Cook *et al.*, 2009) and climatic drivers (e.g. drought severity) (Geist and Lambin, 2004; Middleton, 2016; Swain *et al.*, 2011). Nevertheless, a translation of our understanding of controls on

vegetation cover into an awareness of the potential for sediment mobilisation is absent. With growth in human population pressure (Lark *et al.*, 2015) and climate models predicting increasing precipitation variability (Christensen *et al.*, 2007), there is a greater need to understand the sensitivities of dryland landscapes, with future pressures potentially activating currently stabilised dune sediments. Identifying a relationship between the driving forces and landscape response is central to predicting future landscape reactivation and environmental change in contemporary dryland systems.

Whilst studies on Quaternary scales have suggested that climatic factors are key in driving historic dunefield reactivations (e.g. Forman *et al.*, 2001; Halfen and Johnson, 2013; Stokes *et al.*, 1997), there are still many things unknown about the *contemporary* processes driving modern land degradation, erosion and the aeolian reactivation of dune sediments on shorter annual-to-decadal timescales. Existing sediment mobility indices focus on precipitation as a key factor influencing the level of protective vegetation cover and wind speed as a key determinant of the erosivity potential in the system. However, an empirical understanding of the role and importance of other disturbance events, such as fire, grazing and land use on this relationship, remains outstanding.

Studies that focus on climatic disturbance have excluded various human activities which influence the balance between erosivity and erodibility potential (e.g. Schubert *et al.*, 2004). Yet we can identify within historical memory that human activities can have a profound influence on the level of land degradation, an example being the amplified degradation of the Great Plains Dust Bowl, US during the 1930s. As summarised by Barchyn and Hugenholtz (2013:172):

"*Reactivation can be driven by changes in aridity, increased wind speed, fire, biogenic disturbance, human disturbance, or a combination of the previous. How these controls fit together and define the reactivation potential of dune fields is presently unknown*".

To advance our understanding of the role of external forces on landscape stability and the potential for sediment mobility, independent measurements of both environmental response and the individual disturbance forces are required. By studying landscape response over the recent historical period during which we have detailed climatic, land use and wildfire disturbance data, we can begin to identify the associations between the environmental conditions and the likelihood of surface sediment reactivation.

In the absence of a process-based mechanistic model, we can use a range of techniques to elucidate the relationship between drivers and response. In this project, a unique combination of empirical luminescence chronologies of deposition events for the recent decade-to-century scale past, and secondary datasets of disturbance history are used. This study assesses the capacity to recognise relationships using traditional correlative methods as well as novel applications of statistical inference techniques.

1.2 Research Questions

The overall aim of this research project is to ***explore the relationship between surface reactivation and external disturbance factors in a semi-arid environment***. This thesis tackles the core aim through a combination of field, laboratory and modelling techniques that address three primary research questions:

1) Can land surface responses to recent environmental change be identified chronologically in the sedimentary record?
2) Can we associate environmental conditions with depositional episodes?
3) Given our knowledge of the past, can we identify a suitable method to predict future surface reactivations leading to deposition?

The field and laboratory work undertaken during this project provides empirical luminescence datasets that are used to show geochronological evidence of recent land surface response to historical environmental changes and disturbance forces. Luminescence-dating techniques have long been used to produce chronologies of deposition on Quaternary timescales but are relatively under-used on decade-to-century timescales. Determining the capabilities of luminescence methods to identify chronological episodes of deposition in the recent sedimentary record is a valuable addition to our understanding of luminescence methods and the environmental response of surface sediments to disturbance forcing.

Empirical luminescence measurements taken from near-surface sediments across six study sites in northern Nebraska are used to produce chronologies of

accumulation across a range of geomorphological features. Chronologies of accumulation history are then used to identify the environmental response to a set of known historical climatic, fire and land use conditions in the local area.

To allow for the relationship between disturbance conditions and environmental response to be dynamically-modelled, artificial neural networks (ANNs) are used to identify the connection between the environmental response and a set of known historical conditions. Once trained on historical conditions, ANNs are used to simulate environmental response under a range of scenarios that model different levels of climatic, grazing and fire pressure.

1.3 Thesis Structure

This thesis is structured and prepared for the papers route adhering to the School of Geography and the Environment, University of Oxford guidelines. The main results are detailed and discussed in the four papers, presented here in their thesis-adapted form. The papers are presented in chapter format, but the content remains unaltered from that which has either been published by, or submitted to, the respective journals. Co-author contributions are noted in Appendix A.

Section One: Research Context

Section one provides an overview of the research motivation, a brief summary of the existing literature and the aims and structure of the thesis (**Chapter 1**). The second half of this section (**Chapter 2**) details an in-depth literature review of our understanding of the drivers of land degradation and surface destabilisation,

with a focus on the use of dunes as a measure of environmental response. The application of luminescence techniques to produce high-resolution chronologies of recent surface accumulation, and supervised machine learning (SML) tools to answer questions about deposition drivers, are introduced.

Section Two: Field and Laboratory Experiments

Section two focuses on the methods and results associated with addressing the first research question and identifying the appropriate means for extracting an environmental signal of surface response from the sedimentary record. **Chapter 3** comments on the field sites explored in pilot and final field sampling as well as the laboratory methods used in the experimental stages of luminescence dating (i.e. **Chapters 4** (**Paper 1**) and **5** (**Paper 2**)).

Chapters 4 (**Paper 1**) and **5** (**Paper 2**) focus on refining luminescence protocols to allow us to date young aeolian sediments accurately (**Paper 1**), permitting a reconstruction of historical deposition events in the sedimentary record. Having established a suitable method for dating the sediments, **Paper 2** highlights a new approach for sample selection which captures the structure of the geochronological record and produces high-resolution accumulation chronologies without requiring inefficient preparation and dating of entire dune sedimentary profiles.

Section Three: Data Analysis

With the methods for reconstructing the chronology of environmental response founded, section three focuses on comparing the luminescence-derived history of deposition events from six selected geomorphological features against climatic and anthropogenic records to identify a relationship with disturbance conditions. **Chapter 6** begins this section with an outline of the datasets used to reconstruct historical environmental conditions and the methods applied in **Chapters 7** (**Paper 3**) and **8** (**Paper 4**).

Paper 3 uses traditional descriptive methods, typically used in palaeoenvironmental studies, to compare the timings of known disturbances and climatic perturbations with our reconstructed history of deposition events and other regional dune field accounts. In an attempt to refine this analysis, **Paper 4** explores the potential to use SML techniques to identify (potentially non-linear) dynamics between disturbance and response in this environmental context, allowing us to extend our knowledge from past events into future scenario forecasting.

Section Four: Conclusions

Chapter 9 summarises the results across the four papers to directly assess how the original thesis aims and research questions have been addressed. This final chapter also discusses the wider implications of this research within the literature and potential future extensions of this research project.

Chapter 2

Context

2.1 Introduction

This chapter explores our current understanding of the drivers of dune sediment reactivation in semi-arid environments based on existing literature. Whilst the terms 'land degradation', 'surface reactivation', 'sediment mobilisation' and 'aeolian erosion' are all used within the literature, in the context of this research project, these terms refer to the removal of surface protective vegetation and the subsequent movement of dune sediments (i.e. sand and dust) around the environment. After exploring the existing literature, this chapter details the approach, field site rationale and methodological considerations undertaken in this project.

2.2 Drivers of surface reactivation

Land degradation and surface reactivation occur when the protective layer of surface vegetation is removed from a previously stabilised landscape and the underlying sediments are exposed to aeolian erosion. The likelihood of erosion occurring, and sediment being moved within the system, is a function of the balance between erosivity and erodibility (Wiggs, 2011b). Erodibility refers to the susceptibility of the underlying sediment to erosion, whilst erosivity refers to the potential for sediment to be eroded, and there are a variety of interdependent factors which contribute towards balancing this relationship. In semi-arid aeolian environments, the main effect of vegetation cover is to reduce the potential and likelihood of aeolian sediment transport (Barchyn and Hugenholtz, 2013a; Houser *et al.*, 2015; Hugenholtz and Wolfe, 2005a, 2005b), acting as a protective skin to

prevent the surface sediment from being directly eroded (Wolfe and Nickling, 1993). The factors contributing to the removal of vegetation and thus the potential for reactivation include: aridity, wind speed, turbulence, agriculture, grazing, human disturbance and fire. Yet, how these factors together contribute to define the likelihood for land degradation and the reactivation of dunes is currently unknown (Barchyn and Hugenholtz, 2013a).

2.3 A focus on climatic factors

Despite this myriad of contributory factors, existing research has largely focused on the role of climate, specifically precipitation and wind, in contributing to the likelihood for sediment reactivation on dune systems (e.g. Lancaster, 1988; Stokes and Swinehart, 1997). For example, the Lancaster (1988) dune mobility index is based upon the percentage of time wind speed exceeds a threshold as well as the ratio of precipitation to potential evapotranspiration. Equally, the Fryberger Drift Potential index calculates the potential for sediment transport in relation to wind speed and direction (Saqqa and Saqqa, 2007). Whilst the Fryberger Drift Potential index was initially derived as a tool to help understand the relationship between contemporary winds and modern dunes, numerous studies have since applied the Fryberger (1979) and Lancaster (1988) indices to Quaternary investigations with the aim of understanding palaeoclimatic histories and predicting future reactivations (e.g. Bogle *et al.*, 2015; Bullard *et al.*, 1997; Lancaster and Helm, 2000; Muhs *et al.*, 2003; Muhs and Holliday, 1995; Muhs and Maat, 1993; Rich, 2013). Thomas *et al.* (2005) extended this work with their potential activity index which predicted future dune remobilisation likelihoods based on emissions

scenarios, wind velocity, precipitation and the associated lagged effects on vegetation cover. However, an empirical understanding of the role and importance of other disturbance events and parameters on this relationship is absent.

On Quaternary timescales (i.e. thousands of year), a focus on purely climatic factors may be appropriate to explain changing regional dune dynamics. For example, Forman *et al.* (2001) suggest that a 25% decrease in precipitation during the growing season for a decade or longer, led to the regional-scale megadroughts and complete dune reactivations identified in sedimentary records across the Great Plains of America. Equally, Miao *et al.* (2007) comment that centuries to millennia-scale activity over hundreds of square kilometres in the Great Plains is likely driven by climatic mechanisms. On these timescales, climatic disturbances perhaps can be considered the primary driver of dune dynamics, but on shorter timescales, a range of processes operating at a series of spatial scales cause a complex pattern of heterogeneous reactivation, driving land degradation and the formation of erosional features (e.g. blowouts) across the landscape that cannot be explained by climatic processes alone. For example, a focus on purely climatic forcings fails to explain why we might find examples of both active and stabilised dunes under contemporary climatic conditions (Muhs and Maat, 1993; Tsoar, 2005; Yizhaq *et al.*, 2009, 2007) within the same area. Likewise, the occurrence of blowouts (deflation hollows) resulting from localised vegetation disturbance in otherwise stabilised dune settings prevents us from unambiguously connecting aeolian stratigraphy at individual study sites to changes in regional climate (Mason *et al.*, 2004).

2.4 The role of humans

Despite the role of climatic trends and perturbations in influencing precipitation regimes and thus vegetation cover, the role of anthropogenic activities at the local scale must also be considered. As noted above, land degradation in dryland regions results from various factors, including human-influenced activities as well as natural processes (Middleton and Sternberg, 2013). Whilst sometimes difficult to classify (e.g. grazing is technically a biogenic disturbance), human activities are found to be important in damaging the surface vegetation of stabilised dunes. Whether it be through agricultural practices and farming (Middleton, 2011; Viglizzo and Frank, 2006; Worster, 1979), grazing (Ash and Wasson, 1983; Biondini et al., 1998b; Milchunas et al., 1989; Thomas, 1988; Yan et al., 2013) or increasing the frequency of fires (Arterburn *et al.*, 2018; Esteves *et al.*, 2012; Levin *et al.*, 2012; Santín and Doerr, 2016; Wiggs *et al.*, 1994), human activities can lead to enhanced vegetation removal and erosion in dryland regions.

Whilst animal grazing in drylands can have positive effects for preserving grassland species diversity (Lu *et al.*, 2017), overgrazing (Liu and Diamond, 2005; Osborn, 1996), the concentration of livestock in particular areas of the environment (e.g. bison like to group in wallows) or around water sources, reduces aboveground biomass (Yan *et al.*, 2013) and can lead to localised erosion of the surface vegetation. For example, blowout formation in the Great Plains has previously been attributed to disturbance by cattle (Mason *et al.*, 2004).

Similarly, whilst wildfires help to maintain grassland ecosystems biodiversity (Helzer, 2010) and prevent the encroachment of woody shrubs, they can also have land degradational effects in locations where vegetation recovery is slow (Santín

and Doerr, 2016). In semi-arid grasslands, wildfires remove above-ground biomass, exposing the underlying sandy sediments to aeolian erosion (Burzlaff, 1962; Esteves *et al.*, 2012; Frolik and Sheperd, 1940; Wiggs *et al.*, 1994) and increasing the likelihood of surface disturbance (e.g. blowout formation). Wildfires need ignition, dry available fuel and suitable environmental conditions in order to grow and spread (Knorr *et al.*, 2014). Human activities and development in dryland regions have the capacity to influence these parameters both directly and indirectly (Bowman *et al.*, 2011), thus increasing wildfire frequency and disrupting the capacity for vegetation cover to suitably recover.

Integrating the role of disturbances, such as grazing and fire frequency, into our understanding of dune reactivation will help identify the drivers of past destabilisation events as well as assess the likelihood for future surface disturbances. For example, whilst the 1930s US drought was severe, Lee and Gill (2015) found that it was not climatologically unusual over centennial timescales and a synergy of both natural and anthropogenic "extreme events" (i.e. economic depression and poor land management techniques) was necessary to create the conditions of the 1930s Dust Bowl. Equally, recent localised reactivations and blowout occurrences across the Great Plains have been attributed to the combined effects of both natural and anthropogenic disturbance (Barchyn and Hugenholtz, 2013b; Lee and Gill, 2015; Stubbendieck, 2008; Wolfe *et al.*, 2002, 2007). As Wolfe *et al.* (2007) detail, anthropogenic disturbances such as fire (Boyd, 2002; Levin *et al.*, 2012; Miller *et al.*, 2012), overcultivation (Nickling and Wolfe, 1994), vehicle usage (Cordova, 2005), overgrazing (Stubbendieck, 2008) and

deforestation, all contribute towards dune surface reactivation as well as climatic drivers.

With known periods of human-influenced land degradation in history (e.g. the 1930s US Dust Bowl), a greater understanding of the respective role of all disturbance factors is needed to help predict future landscape changes. Identifying the factors responsible for inducing dune reactivation should not assume climatic variability is exclusive of other drivers in semi-vegetated aeolian environments (Wolfe *et al.*, 2007). Equally, we should consider that the importance of each individual driver varies over time, and that synergies between the forcing factors are key (Reynolds *et al.*, 2007a) in crossing thresholds which induce landscape reactivation. Several parameters may influence dune dynamics and reactivation in different ways according to their magnitude (Provoost *et al.*, 2011).

2.5 A gap in our understanding

In sum, existing research has explored the role of climate, and in particular, drought events in driving dune reactivation over long (millennial) timescales and wide (regional) spatial areas, but a thorough investigation of the combined role of both climatic and anthropogenic influences on partial and localised reactivations has not yet been completed. Recent studies suggest a new model is needed, integrating the role of anthropogenic disturbances into our understanding (Barchyn and Hugenholtz, 2013a; Houser *et al.*, 2015; Lee and Gill, 2015; Mangan *et al.*, 2004; Mayaud *et al.*, 2017a; Thomas and Bailey, 2017; Yizhaq *et al.*, 2009), yet these ideas remain largely theoretical. Using empirical datasets of historical events,

the association between natural and anthropogenic activities, and the likelihood for sediment reactivation, is yet to be completed.

2.6 Approach

This study seeks to explore the relationship between surface reactivation and environmental conditions in a semi-arid environment. In theory, if we can measure both the drivers and the response, we can identify the historical relationship and qualify the respective roles of forcing factors in the environment. Using a combination of environmental response (taken from the near-surface dune sedimentary records) and a history of known disturbance (taken from secondary datasets), this study uses a novel synthesis of traditional descriptive analysis as well as supervised machine learning (SML) methods to explore the potential for deciphering the complex non-linear relationships between aeolian dryland geomorphology and the climatic and anthropogenic perturbations in the Nebraska Sandhills.

A chronology of environmental reactivation is produced using a combination of: intense near-surface sediment sampling across dune and blowout features, changepoint analysis (Killick and Eckley, 2014) and high-resolution quartz optically stimulated luminescence (OSL) dating, to produce a chronology of sand accumulation events. In aeolian systems, reactivation occurs in pulses where erosion and deflation of sediment at one point is immediately followed by deposition at another (Bailey and Thomas, 2014). OSL ages allow disturbance and redeposition to be recognised for time periods that predate real-time and satellite photography, including at decadal-centennial timescales over recent centuries,

covering a period during which we can see different spatial scales of reactivation driven by a range of disturbance factors. Whilst advances in real-time measurements of sediment transport thresholds and dynamics have increased our understanding of instantaneous aeolian processes (Thomas and Wiggs, 2008), we need to measure landscape response over longer time periods to capture the lagged response to combinations of disturbance drivers and vegetation dynamics. Whilst in some research topics, ergodic characteristics allow us to substitute time for space, this is not the case in dryland aeolian environments where lags and interactions occur in only the temporal dimension (i.e. we cannot substitute deep time and the evolution of landscape response through increased spatial coverage). As noted in Houser *et al*. (2015), the relationship between disturbance, vegetation removal and subsequent sediment entrainment, is lagged. As such, whilst short-term (sub-annual-annual) real-time studies are important for informing us about surface entrainment thresholds (e.g. Bogle *et al.*, 2015), they lack the ability to detect the lagged response of vegetation cover to disturbance factors (Stubbendieck, 2008) and thus resultant sediment mobilisation. By comparison, OSL-dated chronologies of deposition which span decadal-centennial time periods are able to provide a history of landscape reactivation to a range of historical disturbance factors which have induced a lagged response in vegetation cover and subsequent sediment remobilisation.

To produce a history of known disturbances we need data of the drivers that have impacted vegetation cover across the Nebraska Sandhills. In the absence of a direct measure of long-term surface vegetation cover, secondary datasets of factors impacting vegetation dynamics are used. Existing research in the Central Great

Plains and prairie grasslands (e.g. Biondini *et al.*, 1998; Forman *et al.*, 2001; Grassini *et al.*, 2010; Mangan *et al.*, 2004; Milchunas *et al.*, 1989; Schmieder *et al.*, 2011, 2012; Stubbendieck, 2008) has identified levels of historical precipitation, grazing, wild fire and land use changes as key factors affecting vegetation cover. Records of these parameters are gathered from a range of existing instrumental and archival datasets providing information on precipitation, land use change, wild fire occurrence, and regional drought.

2.7 Records of environmental response

2.7.1 Dune profiles

Sedimentary sequences of dune profiles provide an environmental history of the geomorphological response to historic forcing conditions. Generally, research at the Quaternary timescale has considered dunes as a palaeoaridity feature (Shaw and Thomas, 2002; Stokes *et al.*, 1997a, 1997b), or a palaeowind indicator (Chase, 2009), and have been used to reconstruct palaeoclimatic histories (e.g. Burrough and Thomas, 2013; Halfen and Johnson, 2013; Hesse *et al.*, 2004; Thomas, 2005). As noted earlier, this may be suitable in a region devoid of vegetation, where wind erosivity was the primary factor influencing sediment movement, or on Quaternary timescales where regional drought was the dominant environmental factor. However, in modern semi-arid grasslands, the connection between dune stratigraphy and climate is more complex since localised disturbances also play a crucial role in eroding the protective vegetation cover. The myriad of disturbance factors that occur at a range of temporal and spatial scales suggests that dunes are

more complex – representing a filtered collection of both erosional and depositional events (Bailey and Thomas, 2014). Changes in dune dynamics and the resultant sedimentary archives, are due to a series of driving factors (Thomas and Bailey, 2017) including: wind energy (Livingstone *et al.*, 2007), rainfall (Thomas et al., 2005), and the conditions that affect vegetation (Yan and Baas, 2015). However, the extent to which each individual external factor influences dune dynamics remains an open question (Barchyn and Hugenholtz, 2013a; Thomas and Bailey, 2017). Using high-resolution OSL techniques, chronologies of past deposition events from near-surface dune sediments can provide a history of environmental response to the range of forcings, as recorded in the sedimentary record.

2.7.2 Blowouts

As well as near-surface dune sediments, stratigraphies found at disturbance-induced erosional features in the landscape are key to reconstructing a history of disturbance-driven sediment reactivations. Blowouts, for example, are deflation hollows produced by the wind erosion of pre-existing sand deposits (Hesp, 2002) and are typically found on the upper slopes of vegetated dunes (Farrar, 2008) where a disturbance has produced a breach in the protective vegetation cover (Wolfe and Nickling, 1997). It is the study of active blowouts that has been essential in highlighting the complex relationships between multiple forcing factors and feedbacks in inducing instability and sediment mobilisation. For example, Hugenholtz and Wolfe (2006) suggest that both climatic perturbations and feedback effects are important in the development of blowout formations, which can be used as a proxy of landscape destabilisation. This sensitivity to localised

disturbance suggests that blowout sediments will likely preserve a sedimentary record of historic events which have eroded sediment from the basin and redeposited on the blowout flanks / lip. Identifying suitable study sites, such as blowouts, from which to reconstruct a history of recent disturbance-driven environmental response is essential to answering the overall research aim.

2.8 Application of OSL

2.8.1 OSL measures date since deposition

OSL dating methods measure the time that has elapsed since the last exposure of accumulated sediments to sunlight or high temperatures. In aeolian systems, OSL techniques provide an excellent method of dating quartz-rich sedimentary records and reconstructing environmental history, providing time-series of deposition events in an environment relatively starved of alternative proxies (Thomas and Burrough, 2012). In the context of this study, when sediment is disturbed and entrained by the wind, the sediment is bleached, and the luminescence signal is reset. Once the sediment has been redeposited, a combination of radioactive decay in the surrounding sediment and cosmogenic rays cause a new luminescence signal to begin accumulating in the sediment crystals (Duller, 2008).

Henceforth, the age derived from OSL dating methods provides us with the time that has elapsed since the cessation of aeolian activity and subsequent burial of sediment. Aeolian reactivation and deposition of sand grains occurs on the temporal scale of seconds-minutes; thus, luminescence ages, that are typically

annual in scale (± 5% errors), provide the date of burial (which is synonymous with deposition) of the sediment. In this study therefore, a luminescence-derived chronology provides us with a history of the episodes when vegetation disturbance was extensive enough to result in sediment remobilisation, bleaching of sand, and subsequent deposition and burial.

2.8.2 OSL techniques and young sediments

Using OSL methods to identify environmental response in young, near-surface sediments, is a relatively under-explored application of the technique. OSL is typically best applied to older sediments spanning periods of hundreds to thousands of years (Rhodes, 2011), however, developments within the technique have had a profound effect upon the field, enabling younger materials to be dated (Duller, 1996). For example, studies by Bailey *et al.* (2001), Ballarini *et al.* (2003), Reimann *et al.* (2012) and Stokes *et al.* (2004) have all shown that within a variety of settings, and with a range of preparation techniques, we can apply luminescence techniques to young (< 100 years) samples with good results. Equally, the application of un-logged age models (Arnold *et al.*, 2009; Galbraith and Roberts, 2012) and Bayesian approaches (Cunningham *et al.*, 2015a, 2015b) have been explored to improve the accuracy achieved when using OSL methods on young sediment samples. These previous examples demonstrate the feasibility of dating recently deposited sediment samples using luminescence techniques. Building on this existing research, this project refines existing OSL techniques and devises a protocol suitable for dating young sediments from the Nebraska Sandhills.

2.8.3 High-resolution and near-surface OSL applications

Accumulation histories of sedimentary sequences are complex stacked records of periods of sand deposition. Cycles of heterogeneous erosion and subsequent re-deposition in the landscape result in a 'filtering' of the signal, with environmental information progressively lost with time and field sampling methods (Bailey and Thomas, 2014) (Figure 2.1).

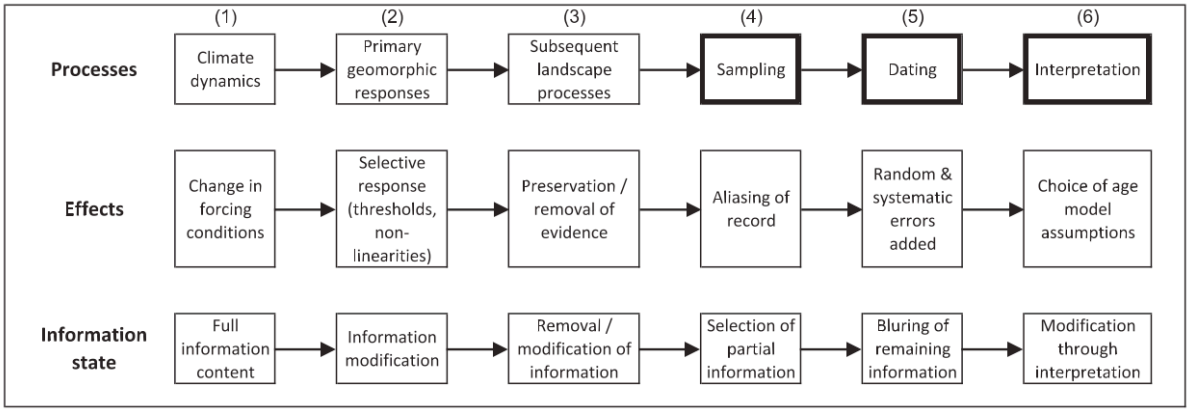


Figure 2.1 Schematic of 'filtering' process where information on palaeoenvironmental conditions is gradually removed from the sedimentary record with time and with subsequent sampling and dating methods. Figure extracted from (Bailey and Thomas, 2014).

A spatially and temporally heterogeneous sedimentary record complicates the reconstruction of environmental response. As Figure 2.1 elucidates, a single sedimentary sample from the stratigraphic record is unlikely to capture the entire depositional history of the feature or landform being studied due to progressive filtering which produces an incomplete history of deposition events. Spatial variability driven by environmental 'noise' and local dune-scale processes that induce accumulation and erosion (Leighton et al., 2014b; Munyikwa, 2005; Stone and Thomas, 2008; Telfer et al., 2017, 2010; Thomas and Burrough, 2013), all

further confound our ability to construct a chronology of dune activity phases. With this in mind, a high volume of sediment sampling and dating is needed to identify a signal amongst a noisy background of post-depositional factors. For example, Telfer (2011) successfully demonstrates the potential for using intensive sampling and OSL dating to answer questions about dune growth and evolution in the south-western Kalahari. Intensive sampling and OSL dating can be used as an effective tool to reconstruct significant periods of dune reactivation in drylands despite the high levels of environmental noise and spatially-inconsistent records characterising aeolian environments.

In this research project, not only is this application of OSL dating relatively novel since it requires dating a large number of young samples, but also because it focuses on near-surface samples (i.e. in order to capture the most recent section of the sedimentary record and therefore historical disturbances). Previous studies have avoided near-surface sampling for fear of bioturbation and recycled signals. Hesse (2014) highlights the obvious flaw in this theory, assuming that the present is dissimilar to the past. As Hesse (2014) noted, at some point, all buried sediments were near to the surface, and as these sediments are assumed suitable for dating, then near surface samples (i.e. upper 0.5 m) today ought to meet the criteria for dating suitability, so long as a sufficient dose has accumulated for dating. In relation to this research project therefore, OSL techniques provide a suitable chronological tool to reconstruct a history of sediment reactivation over a time period during which records of historical climate and disturbance factors are available (i.e. last 100-200 years).

2.9 Nebraska Sandhills: Site selection and rationale

The Nebraska Sandhills is the largest aeolian dunefield in the Western Hemisphere (Ahlbrandt and Fryberger, 1980; Loope and Swinehart, 2000), covering 57,000 km^2, and characterised by a range of barchanoid ridges, megabarchans, parabolic and linear dunes (Swinehart, 1998) (Figure 2.2). Currently stabilised by extensive perennial warm-season grasses (Bleed, 1998), the vegetation on the dunes is dominated by shallow-rooted grasses that sit far above the water table (Schmeisser McKean *et al.*, 2014). The climate ranges from sub-humid in the east to semi-arid in the west (Bleed, 1998), induced by a large precipitation gradient from c.400 mm/yr in the west to in excess of 600 mm/yr in the east (Wilhite and Hubbard, 1998). This key feature of the Sandhills affects vegetation distribution and evapotranspiration across the region (Schmieder *et al.*, 2012), producing a range of habitats suitable for a variety of vegetation species (Wilhite and Hubbard, 1998) which have adapted to the variation in climate, topography, and soil types across the Sandhills. Prevailing winds from the north-west blow during the winter months, with more southerly wind regimes dominating in the summer months. The Nebraska Sandhills were selected as a suitable location for this project for three reasons: a known record of historical disturbances; existing history of activation; and suitable sediments for applying OSL dating methods.

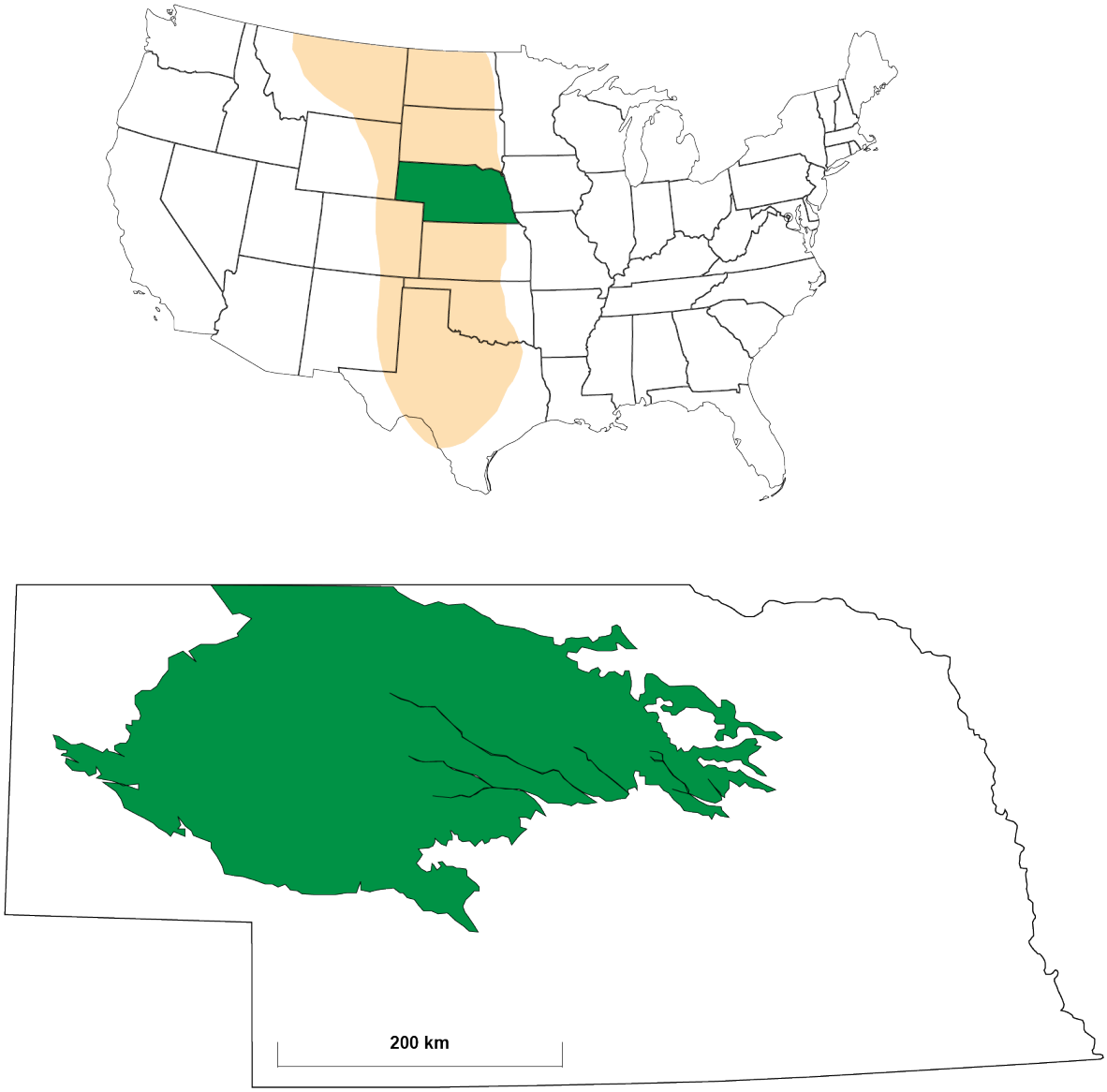


Figure 2.2 *Upper:* Location of Nebraska positioned within the Central Great Plains (orange) relative to the United States of America. *Lower:* Extent of the Nebraska Sandhills within the state of Nebraska.

2.9.1 Known history of disturbances

Measurements of natural and anthropogenic disturbances have been kept for over 100 years in the region and thus provide a history of known forcing factors that we can use when identifying the relationship between cause and effect regarding landscape reactivation. Without instrumental and direct measurements

of known forcing factors, the study would be forced to use alternative environmental proxies to infer climatic change (e.g. lake records), thus making any argument regarding the role of climate change and environmental response circular. An extensive history of land deeds, early 19th century European accounts, weather station records and oral accounts from descendants of original homestead settlers provides a rich collection of data sources which can be used to reconstruct the pressures on the environment and dune surfaces.

2.9.2 Existing history of activation

Secondly, an extensive body of existing literature in the Nebraska Sandhills, and more widely in the Central Great Plains, has produced a range of studies which have demonstrated that reactivation of the dune fields has occurred at a variety of spatial and temporal scales over the last 10,000 years (Ahlbrandt and Fryberger, 1980; Forman et al., 2008, 2005; Halfen et al., 2012; Holliday, 2001; Loope and Swinehart, 2000; Mason et al., 2011, 2004; Miao et al., 2007; Muhs and Wolfe, 1999; Schmeisser McKean et al., 2014; Schmeisser et al., 2010, 2009a; Schmieder et al., 2011; Sridhar et al., 2006; Stokes and Swinehart, 1997). Some of the regional reactivations have been attributed to palaeoclimatic changes (Forman et al., 2005, 2001; Mason et al., 2004; Miao et al., 2007; Muhs and Holliday, 1995; Sridhar et al., 2006; Stokes and Swinehart, 1997), with more recent localised reactivations theorised as driven by a combination of climate and anthropogenic activities (e.g. Mangan *et al.*, 2004) and the growth of blowouts in response to vegetation disturbance (Mason *et al.*, 2004). Specifically within the Sandhills, Forman *et al.* (2005) have identified aeolian activity in the western Sandhills at c.3700, 670, 470,

240, and more recently only 140 and 70 years ago. As well as geochronological evidence from the sedimentary record, explorer accounts from the late-18th and early-19th centuries demonstrate that whilst the region is largely vegetated now, this has been a dynamic environment on recent timescales (Muhs and Holliday, 1995).

Whilst the Sandhills are broadly presently stabilised, an improved understanding of these dunes during previous periods of drought and disturbance is needed to predict future dynamics and reactivations (Schmeisser McKean *et al.*, 2014). With recent modelling studies suggesting that temperatures will rise and precipitation will decrease across the Great Plains over the next century (Bathke *et al.*, 2014; Christensen *et al.*, 2007; Feng *et al.*, 2014), the likelihood of drought during the growing season will increase. Some studies have already documented a drying of the Great Plains since the 1980s (Damberg and AghaKouchak, 2014), and with future land use change difficult to predict (Lark *et al.*, 2015; Lee and Gill, 2015), identifying the sensitivities of the geomorphology to natural and anthropogenic activities is key to predicting future reactivations. This context of existing literature confirms the suitability of the site as a location that experiences both periods of stability and instability, allowing us to explore the idea of thresholds and sensitivities.

2.9.3 Quartz-rich sediments

Finally, existing luminescence studies from the region have detailed the quartz-rich nature of the dune sediments (Forman *et al.*, 2005; Muhs, 2004) and the naturally high occurring environmental dose rates (c.2 Gy/ka) (Table 2.1) (typically for quartz-rich sediments, environmental dose rates range 1-1.5 Gy/ka (Buylaert *et*

al., 2012)). These sedimentological conditions are favourable for luminescence dating, especially for young aeolian sediments that naturally produce dim signals with high levels of noise.

Table 2.1 Examples of environmental dose rates found at previously studied sites across the Nebraska Sandhills. Average environmental dose rates c.2 $Gy.ka^{-1}$ are found across the sites already studied using luminescence techniques across the Nebraska Sandhills.

Reference	Location	Environmental dose rate range ($Gy.ka^{-1}$)
(Miao *et al.*, 2007)	Crescent Lake	1.6 – 2.12
	Gudmundsen Ranch	2.02 – 2.81
	Kroeger Blowout	1.95 – 2.52
	Hwy 91 Linear Dune	2.0 – 2.57
	Briefcase Wayside	1.64 – 1.79
	Merritt Reservoir	2.26 – 2.38
	Hansen Ranch	2.02 – 2.28
	Diamond Bar Ranch	1.82 – 2.21
	Collier Ranch	1.67 – 1.87
	Johnson Ranch	1.73 – 2.08
	Barta Brothers Ranch	1.78 – 2.57
	Calamus	1.64 – 2.66
(Forman *et al.*, 2005)	Cottonwood Lake	1.69 – 2.78
	Home Valley Lake	1.57 – 2.52
	Round Lake	1.53 – 2.18
(Stokes and Swinehart, 1997)	Whitman	1.84 – 2.88
	Merritt Reservoir	1.57 – 2.13
(Goble *et al.*, 2004)	Kroeger Blowout	2.1 – 2.49
	Yao's Blowout	1.8 – 2.24
(Schmeisser McKean *et al.*, 2014)	Goeke Ranch	2.14 – 2.59
	Peterson Ranch	1.89 – 2.22
	Johnson Ranch	1.71 – 2.17
	Nebraska National Forest	1.52 – 2.07
	Diamond Bar Ranch	1.86 – 2.31
	Hansen Ranch	2.19 – 2.37
	Barta Brothers Ranch	1.81 – 2.65

With this context in mind, three sites (1 - The Gudmundsen Sandhills Laboratory, 2 - The Niobrara Valley Preserve and surrounding ranches, 3 - The Barta Brothers Ranch) in the Nebraska Sandhills were visited in an initial pilot field trip in 2015 to take a variety of test samples from a range of contexts and experiment with different sampling strategies. Following initial luminescence experiments in the laboratory, and based on access to secondary datasets, the Niobrara Valley Preserve and surrounding ranches was selected as the main site of focus for this research project and subsequent fieldwork in 2016.

2.10 Statistical Inference tools

To identify an environmental response, suitable chronometric tools and field locations have been identified; yet, these need to be paired with an appropriate tool for analysing relationships between the environmental response and disturbance forces. Machine learning encapsulates a set of tools that provide an automated method of building empirical models from data alone (Lary *et al.*, 2018). In the absence of a process-based mechanistic model which connects the individual drivers and environmental response, but in the presence of a significant number of observations, we can use data-based tools of analysis to elucidate the associations and calculate relationships in systems. In an ideal world, if we had a complete theoretical understanding of all processes, statistical inference techniques would not be necessary (Lary *et al.*, 2016).

A particular subdivision of SML is that of artificial neural networks (ANNs). ANNs are a subset of models, inspired by an abstraction of the central nervous system, and are applied in machine learning with pattern recognition and

classification (Salkind, 2007). ANN methods are a branch of artificial intelligence (AI) research, with the aim to simulate the intelligent behaviour of biological neural networks (Livingstone, 2009). ANN methods have been used for over 50 years to identify relationships in large observational datasets. However, it is in the last decade that the real benefits of ANN techniques have grown with the increase in computing power and capacity to work with Big Data.

ANNs are structured similar to biological neural networks, with a series of neurons interconnected through an architecture of hidden layers. In supervised learning examples, the ANN is trained through a learning process, with the identified outputs trained alongside a series of inputs (Zou *et al.*, 2009). Within the geosciences, ANNs have successfully been applied in a range of dendroclimatic (Fang *et al.*, 2000; Tiwari and Maiti, 2011; Woodhouse, 1999; Zhang *et al.*, 2000), geomorphological (Rahmati *et al.*, 2017), landslide spatial prediction (Pham *et al.*, 2018) and aeolian studies (Houser *et al.*, 2015; Jamali *et al.*, 2018; Shanmugam *et al.*, 2016; Vaz and Silvestro, 2014). Where traditional statistical techniques have in many cases assumed a linear relationship (e.g. between climate and tree growth), ANNs have provided a method that allows for the relationships to be both unknown and more complex both in terms of between the input variables and with the target dataset (Woodhouse, 1999).

Without access to a process-based mechanistic model connecting external climatic and anthropogenic drivers to near-surface deposition events, ANNs are an appropriate tool to use in this empirical data-focused research project where we can measure both the environmental response and the recorded external disturbances.

2.11 Summary

Previous attempts to identify the drivers of Quaternary scale sediment remobilisation in dryland regions have focused largely on climatic factors, suggesting that dune stratigraphies can be successfully used to reconstruct palaeoclimatic histories. However, over shorter more recent timescales, late Holocene dune stratigraphies represent an environmental response to a range of climatic and anthropogenic activities such as grazing and fire occurrence. Whilst the role of these individual disturbance factors in damaging vegetation cover and contributing to aeolian erosion has been widely cited, research to date has not integrated the relative contributions of both natural and human disturbances when identifying sediment reactivation sensitivities. Recent theoretical studies suggest a new model is needed that integrates the associations between natural and anthropogenic activities, but this is yet to be empirically tested.

SECTION TWO

FIELD AND LABORATORY EXPERIMENTS

Chapter 3

Field sampling and laboratory experiments

3.1 Introduction

Research methods have been split into two chapters to illustrate the techniques used at different stages of the research. This methods chapters details the approach used to reconstruct a chronological history of deposition events from aeolian dune records. A record of recent aeolian deposition events was extracted from near-surface sediments using a combination of field sampling and high-resolution OSL dating. As well as the details of the methods used, results from pilot field work sampling and initial laboratory experiments are detailed in this chapter to demonstrate how the final sampling strategies and luminescence protocol were derived. A second methods chapter will follow in Section 3 (Chapter 6).

3.2 Sediment sampling

Drylands present significant challenges for environmental investigations with respect to interpreting and understanding the contexts of sedimentary sequences (Munyikwa, 2005). The likelihood of sediment being eroded and removed or deposited and accumulating during an activation event changes both in space and time, meaning that no single location represents a sole source or accumulation feature. Coupled with periods of wider erosion and deposition, breaks in sedimentary sequences are expected across a range of temporal and spatial scales (Bailey and Thomas, 2014). The ability to correctly interpret dryland sedimentary deposits and luminescence chronologies therefore requires an improved understanding of geomorphological processes, but also a suitable sampling framework that incorporates the variety of geomorphological responses

to any given environmental forcing. To capture the environmental signal against a backdrop of high levels of environmental noise, sample numbers need to be increased to ensure a signal is detectable and a broad range of geomorphological features needs to be sampled.

As discussed in section 2.7, near-surface dune sediments and aeolian erosional features, such as blowouts, are suitable features to sample when seeking to identify the sedimentary response to disturbance events. Additional disturbance features, such as those associated with groundwater pumps and homestead sites provide alternative structures in the environment that can be directly tested for their related impact on the sedimentary record. Sampling from features that have responded to and record sediment mobility due to the forcing factors of interest (i.e. climate and human activities) is essential. In addition to features of notable disturbance in the field, samples from relatively stabilised aeolian features (i.e. vegetated parabolic dunes, low-lying rolling vegetated dunes), provide a comparison against which to test geomorphological sensitivity within a local landscape.

By comparison, focusing on sedimentary sequences from alluvial, fluvial or colluvial settings would not provide us with a depositional history that tackles our primary project aim. Firstly, aeolian erosion features in the Nebraska Sandhills are not considered to be limited by wind energy and therefore episodes of mobilisation are driven by disturbance forces that damage vegetation cover and induce sediment reactivation. Dunes and blowouts, which are widespread in the Nebraska Sandhills, provide us with a *local* response. Fluvial systems are connected to wider regional dynamics; thus the sedimentary response cannot be associated solely with localised

conditions when the feature may be dependent on circumstances from an alternate setting (e.g. sediment supply upstream). Similarly, the ephemeral and sometimes erosive nature of fluvial systems in drylands could result in subtle depositional events being removed from the system, or not recorded due to a lack of rainfall. In comparison, the extensive dune sediments, coupled with the high wind energy of the Nebraska Sandhills means that aeolian deposited sediments provide suitable records of local land degradation, as opposed to a signal complicated by limited sediment supply or erosive force. Whilst fluvial, alluvial and colluvial features could inform about alternative forms of disturbance-driven deposition (e.g. hydrological controls, sediment supply), when ranking all geomorphological forms that would be available for inclusion in this project, aeolian features likely provide the most comprehensive records of deposition events. Moreover, OSL techniques are better applied to wind-blown sediments as opposed to those transported via water. Water-lain sediments can be poorly bleached during transport (Wallinga, 2002), resulting in potentially large burial age overestimations – a significant problem when working with relatively young sediments.

With this in mind, for this investigation, multiple vertical cores were extracted across transects from a variety of aeolian geomorphological features including: fence line dunes, deflation blowouts, parabolic dunes and across different land use settings (e.g. windmill-powered groundwater pump, original homestead settlement). This section details the sample extraction method and sampling strategy used in the pilot and main field work seasons.

3.2.1 Sample extraction

Sampling at arbitrary points within a vertical section (particularly when there is no visible stratigraphy) runs the risk of missing events, therefore vertical cores were deemed a better option, allowing us to capture a more complete sequence in the field for later sub-sampling. 50 cm black opaque plastic tubes were hammered vertically into surface sediments, extracted in-situ, retrieved and capped (Figure 3.1).

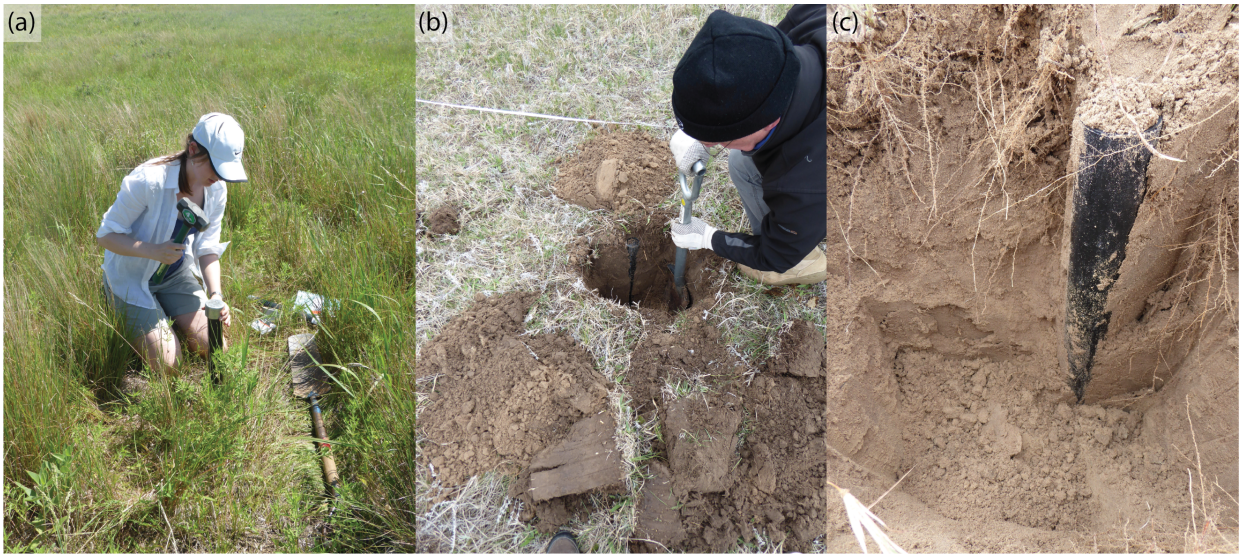


Figure 3.1 (a) 50 cm vertical sediment tube being hammered into upper dune sediments. (b & c) Example of vertical sample tube in-situ and being extracted from near-surface dune sediments.

3.2.2 Sampling strategy

Pilot fieldwork samples

The sampling strategy tested during pilot fieldwork was used to inform the final approach to be deployed for the main sampling trip in 2016. Initial pilot research in 2015 sampled sediments from three separate regions of the Nebraska Sandhills: Gudmundsen Sandhills Laboratory (GSL), Niobrara Valley Preserve

(NVP) and the Barta Brothers Ranch (BBR) (Figure 3.2). In addition to the 50 cm vertical cores described in 3.2.1, a selection of horizontal cores were extracted from deeper sections of exposed profiles where notable changes in lithology were found. 20 cm horizontal sample cores from an individual depth provide a greater volume of comparably aged sediment, allowing us to explore various methods on the same sample during initial OSL experiments.

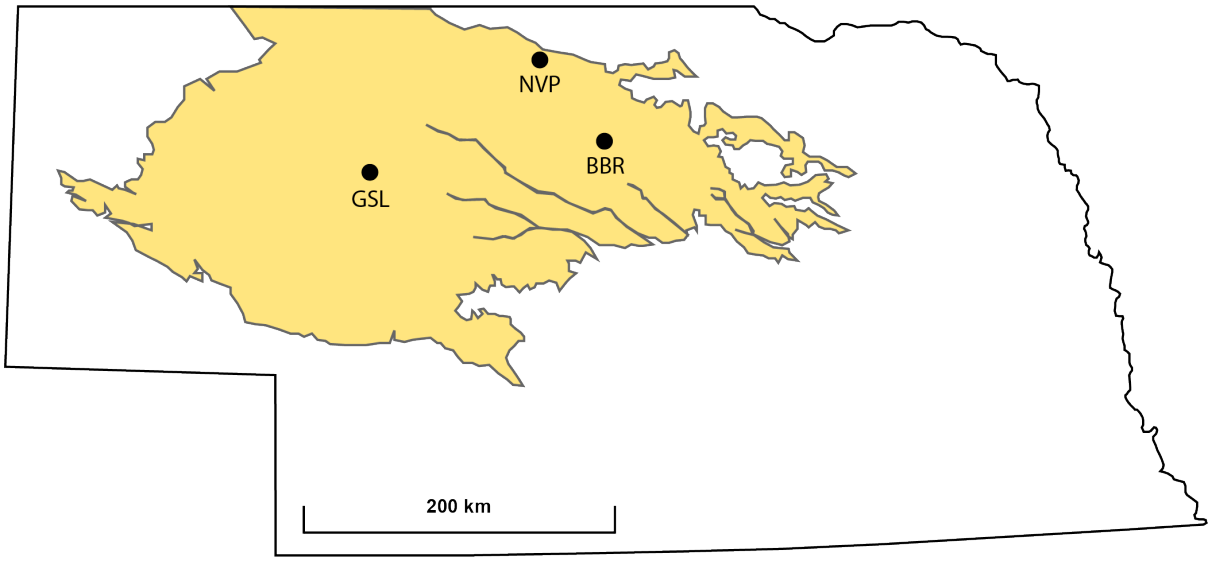


Figure 3.2 Location of sites sampled during the initial pilot fieldwork in 2015: the Gudmundsen Sandhills Laboratory (GSL), the Niobrara Valley Preserve (NVP) and the Barta Brothers Ranch (BBR).

Specifically at GSL, pilot samples were taken from a range of depths, including from two exposed blowout profiles (Figure 3.3) to identify the maximum depth needed to capture up to the last 200 years of sedimentary history (Table 3.1). Sediment samples GSL15/1/2 and GSL15/1/3 are taken from an exposed blowout referred to as Yao's Blowout in the existing literature (Forman *et al.*, 2005; Goble *et al.*, 2004; Mason *et al.*, 2004; Schmeisser McKean *et al.*, 2014). Pilot samples were dated using the luminescence methods and protocols described in full in

section 3.4.5; pilot sample ages have been presented here to demonstrate the rationale for sampling strategy. These initial ages confirmed that blowout sedimentary sequences contained evidence of recent depositional events, and that 50 cm was an appropriate length of profile to capture events from a period during which records of grazing pressure, land use change and climatic changes are available.

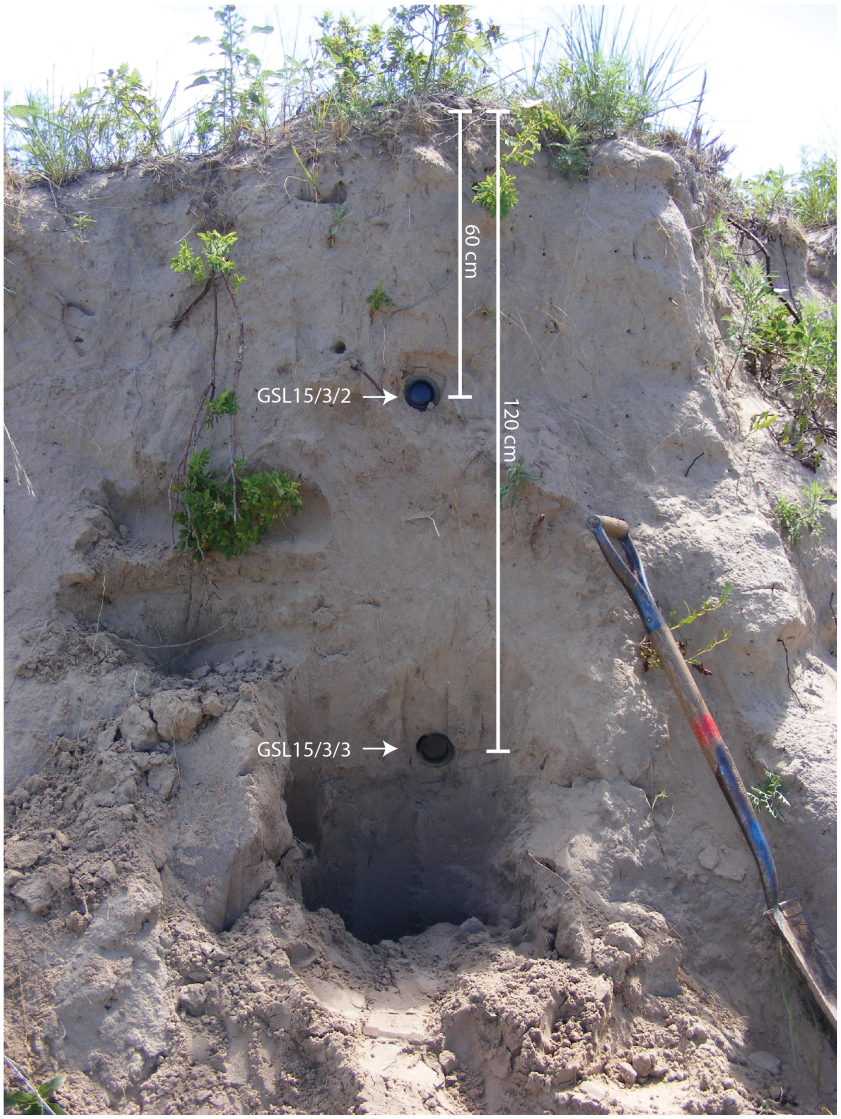


Figure 3.3 Sedimentary profile of one of the sampled blowouts at GSL. GSL15/3/2 and GSL15/3/3 were sampled at 60 and 120 cm below the surface respectively. Sediment sample GSL15/3/3 was extracted 10 cm above an identifiable soil horizon in the backwall exposure.

Table 3.1 Table of initial OSL results from horizontal pilot samples taken from two blowout exposures at GSL. Using the dose rate calculated for sediment sample GSL15/1/3 (2.232 $Gy.ka^{-1}$), estimated ages show that the sediments range up to 750 years in the upper metre of sediments. Estimated ages were calculated following the methods outlined in section 3.4 but are presented here to demonstrate how initial OSL ages were used to guide the sampling strategy for the main field sampling. Initial pilot measurements on sediment core NVP15/4/1 also identified the age bracket captured in the upper 50 cm at NVP. These results have not been included in this section as NVP15/4/1 was re-dated following the full-preparation protocol in Paper 1 and used in the final dataset analysis of Paper 3.

Site	Sample	Latitude (°)	Longitude (°)	Depth (cm below surface)	$D_e \pm 1\sigma$ (Gy)	Estimated age ± 1σ (ka)
GSL	GSL15/1/2	42.08627	-101.36721	54	0.28 ± 0.03	0.13 ± 0.01
	GSL15/1/3	42.08627	-101.36721	97	1.68 ± 0.10	0.75 ± 0.04
	GSL15/3/2	42.07586	-101.38704	60	0.12 ± 0.01	0.05 ± 0.00
	GSL15/3/3	42.07586	-101.38704	120	0.26 ± 0.02	0.17 ± 0.01

Additionally, five 50 cm vertical samples were extracted from the upper sediments of a vegetated linear dune ridge at GSL in a grid pattern to identify the variability in age between sediments of comparable depths within a localised area (Figures 3.4, 3.5 & Table 3.2). The sample site was adjacent to a large westerly-facing blowout (sample site of GSL15/3/2 and GSL15/3/3) but appeared stabilised and well-vegetated during sampling. With no obvious variability in the sediments from the surface, this site was selected as a suitable location to test the variability in chronostratigraphy between sediment cores in close proximity. The four corners of the grid formed a 9 m x 9 m square, with a final sediment core taken from the centre of the grid (GSL15/2/5).

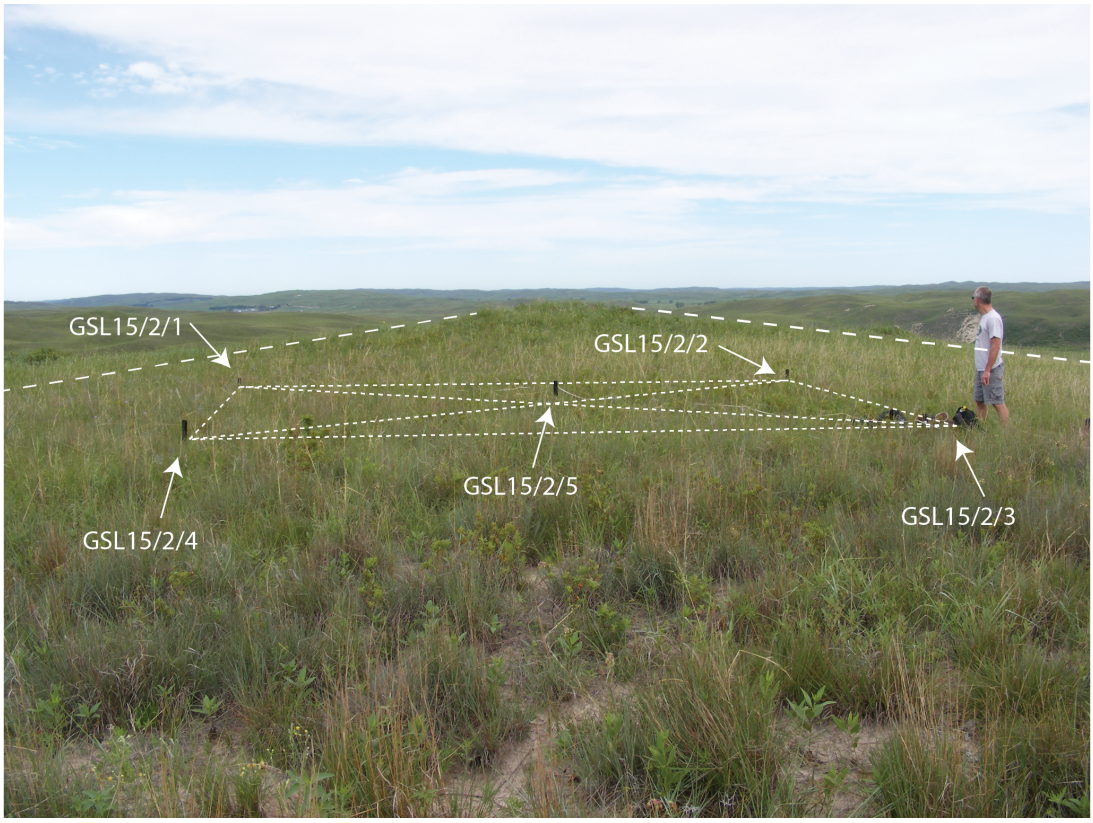


Figure 3.4 Sediment cores extracted from grid sampling strategy on an E-W trending linear dune ridge at GSL. Wide dashed lines demonstrate plateaued ride, dotted lines mark grid sampling site. Conditions during sampling showed the crest was well-vegetated with occasional patches of bare sand increasing towards the blowout.

Results from the grid sampling experiment demonstrated that variability between equivalent dose (D_e) (i.e. a proxy for age) at comparable depths between the sediment cores increased with depth (age) (Table 3.2), likely caused by greater cycles of deposition and erosion (Bailey and Thomas, 2014). These results highlighted that whilst very young sediments are comparable in age between cores, variability between cores within a short range (< 10 m) increased with depth and confirmed that multiple sediment cores across individual features would be required to reconstruct a more complete depositional history.

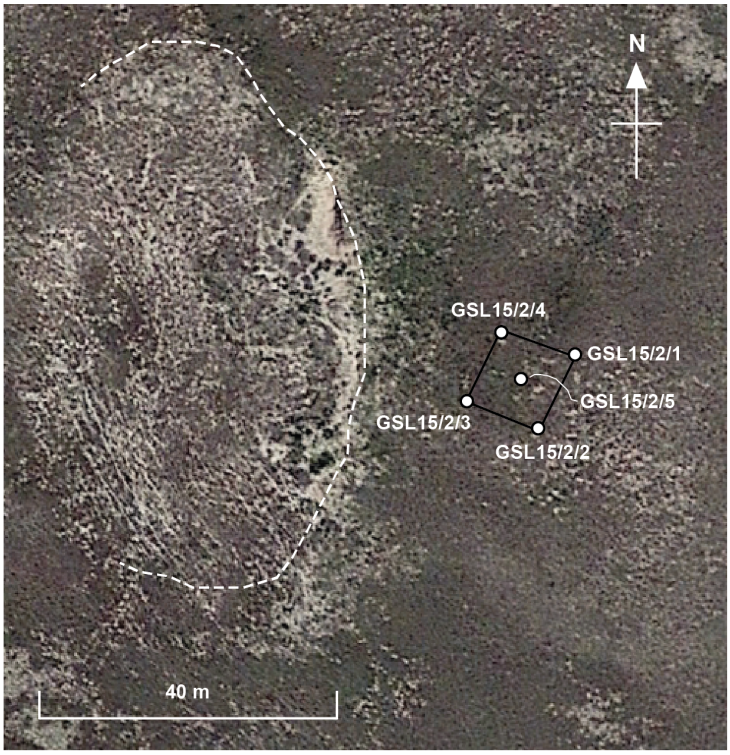


Figure 3.5 Aerial photograph showing location of the five vertical sediment cores sampled as part of the grid variability analysis. The grid sediment cores were extracted from a plateaued ridge on an E-W trending linear dune at GSL, adjacent to a westerly-facing blowout (white dashed line marks the blowout exposure). Satellite imagery courtesy of © 2017 Google Earth Pro, Landsat / Copernicus.

Table 3.2 Table presents the unlogged-CAM (Central Age Model) equivalent doses (D_e) from 6 large aliquots per depth per sample. Standard SAR (Murray and Wintle, 2000) cycle measurements were completed with preheats 200°C, measurement temperature 130°C, and quartz crystals 125-180 µm (see Section 3.4). Based on an environmental dose rate for sediment sample GSL15/2/5/45 of 2.2 $Gy.ka^{-1}$, approximate ages from the grid samples were in the range: 0 – 40 years.

Sediment Core	$D_e \pm 1\sigma$ (Gy) at 6 cm depth	$D_e \pm 1\sigma$ (Gy) at 26 cm depth	$D_e \pm 1\sigma$ (Gy) at 46 cm depth
GSL15/2/1	-0.009 ± 0.002	0.015 ± 0.004	0.06 ± 0.006
GSL15/2/2	0.00 ± 0.002	0.003 ± 0.002	0.082 ± 0.007
GSL15/2/3	0.004 ± 0.006	0.005 ± 0.001	0.009 ± 0.002
GSL15/2/4	-0.005 ± 0.001	0.004 ± 0.001	0.032 ± 0.003
GSL15/2/5	-0.006 ± 0.001	0.005 ± 0.001	0.037 ± 0.003

As well as pilot samples from GSL, a vertical core extracted from BBR was used to test luminescence protocols against a sediment sample of known age (Chapter 4: Paper 1). Sediment core BBR15/1/1 was sampled from a lunette dune that had formed on top of a fence line that had been erected around a Grassland Destabilisation Experiment plot in 2009 (Figure 3.6). With the date of the fencing known, the lunette dune that had accumulated on top of the fence should only contain a luminescence signal corresponding with a few years of burial, allowing us to test for residual doses[1].



Figure 3.6 Aerial photograph of the Grassland Destabilisation Experiment (GDEX) (co-ordinated by the University of Nebraska-Lincoln), located on the Barta Brothers Ranch. The GDEX is part of a long-running research project examining the effects of destabilisation on ground-water recharge. BBR15/1/1 was sampled from a lunette dune that had formed on the SE edge of a destabilised GDEX plot. Satellite imagery courtesy of © 2017 Google Earth Pro, Landsat / Copernicus.

[1] Residual dose refers to the remaining signal after theoretical bleaching. If a sediment has a residual luminescence dose after theoretical bleaching, it is said to have been partially-bleached.

Main sampling focus

During 2016 fieldwork, a series of 50 cm vertical sediment cores were extracted from sample sites at GSL and NVP. However, based on the number of secondary datasets available to reconstruct contextual history and the range of geomorphological features present, NVP was selected as the most appropriate site for full dating and analysis. Given the need to sample features that are sensitive to disturbance forces and capture the heterogeneity in response across the landscape, the final samples used for analysis were extracted from a range of dune, blowout, and fence line features in the NVP and surrounding commercial ranches. Using archived aerial imagery of the region (Figure 3.7 and Appendix B), individual features were selected from the landscape that were expected to capture a range of environments (i.e. Preserve versus commercial ranch) and deposition history over the past c.100 years. At each selected sampling site, up to four vertical sediment cores were extracted across transects traversing the dune-interdune or blowout feature.

In total, twenty-five sediment cores were extracted across eight different aeolian features / depositional settings within and around the NVP. However, within the time constraints of the study, sampling sites were prioritised in terms of those providing the greatest variation across the localised landscape and potential to yield a history of disturbance-driven deposition events. Following prioritisation, six out of eight sampling sites were selected for final analysis from the NVP suite of cores (Figure 3.8). Sediment cores from NVP16/1 and NVP16/3 were de-prioritised relative to the other six sampling sites at NVP. NVP16/1 was not included because it was extracted from a similar feature to Site A; therefore, a potential duplication.

Meanwhile, NVP16/3 was not prioritised due to the very high levels of erosion and disturbance found in the aerial imagery. A high volume of cattle tracks seen through the NVP16/3 blowout during field sampling suggested that the stratigraphy at this site would potentially be very mixed and produce a complicated signal of historical depositions. Instead, Site D (large blowout feature with associated homestead) nearby was prioritised as a comparable feature but with possibly better depositional preservation.

Based on aerial imagery and initial observations in the field, hypotheses of expected sediment activity were produced and are found in Appendix B alongside field images from the six sites studied. Of the total number of extracted cores, seventeen vertical sediment profiles across the six sampling sites were selected for the final dating and analysis at the Oxford Luminescence Dating Laboratory (Table 3.3). The additional cores extracted as part of the pilot and final field season, but not used in the reconstruction of historical reactivations are listed in Appendix C.



Figure 3.7 Example of archived United States Department of Agriculture (USDA) Farm Service Agency (FSA) historical aerial imagery taken from western section of study area in Brown County, Nebraska. Circled blowout shows location of sample site D in 1939 (left), 1954 (centre) and 1968 (right). Using these aerial images, zones of increased activity / stability relative to the surrounding dunes were located and blowout evolution identified. Please refer to Appendix B for complete collection of aerial imagery.

Figure 3.8 (*opposite*) Location of the six sampling sites selected across the NVP and surrounding area and the corresponding vertical sediment cores extracted at each site. Sites A (Blowout feature) & C (Parabolic dune) are located within the bounds of NVP. Site E (1930s dune) is located on the privately-owned commercial grazing Sandhill and Sun Ranch. Sites B (Windmill site), D (Homestead site) and F (Old rolling dune) are located on the privately-owned commercial grazing O'Kief ranch. White dashed line depicts outline of Site C parabolic dune and fence line dune found at Site E. Black shaded area represents nearby prairie dog town found at Site E. Satellite imagery courtesy of © 2017 Google Earth Pro, Landsat / Copernicus

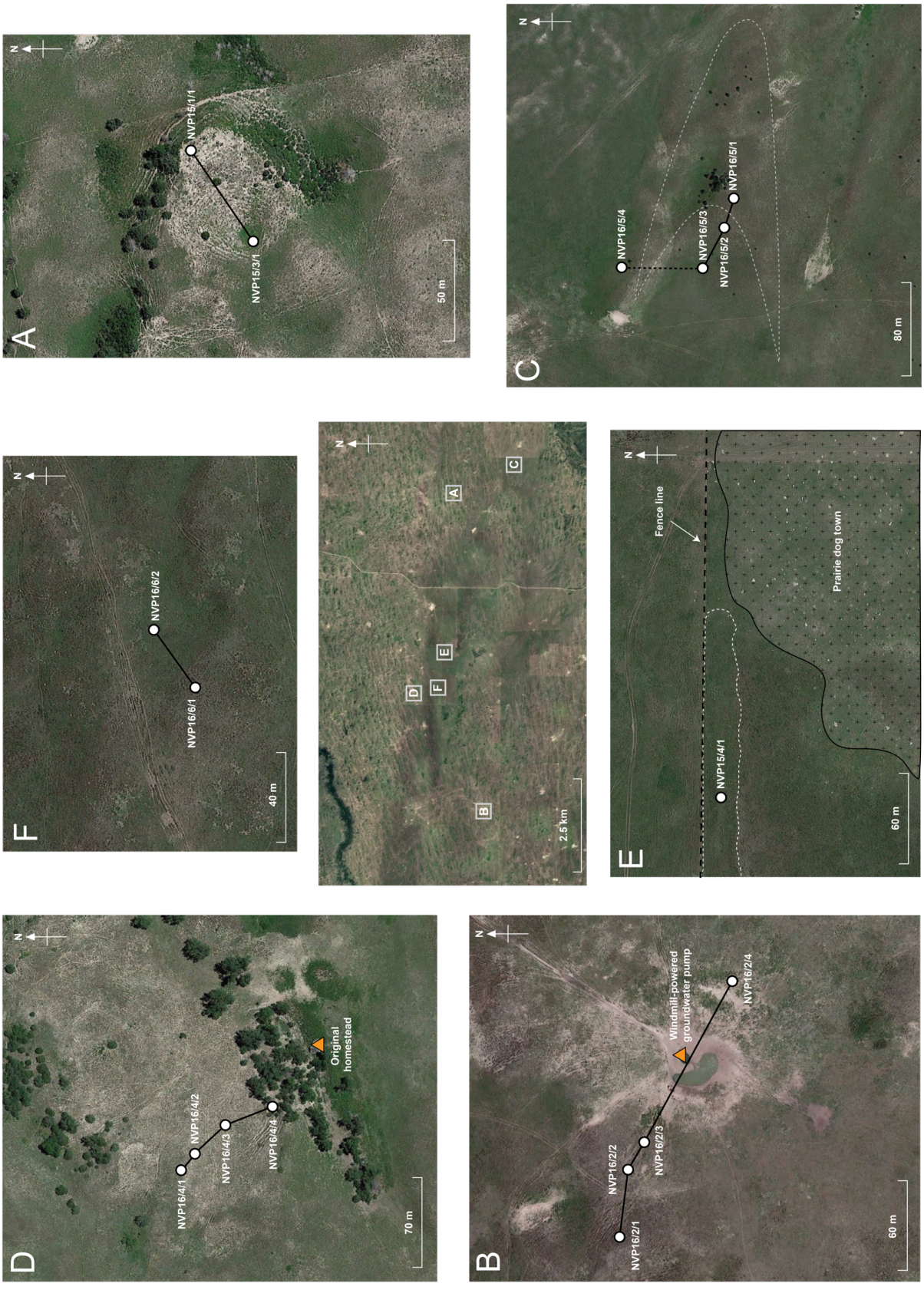

A
NVP15/1/1
NVP15/3/1
50 m
C
NVP16/5/4
NVP16/5/3
NVP16/5/2
NVP16/5/1
80 m
F
NVP16/6/2
NVP16/6/1
40 m
A
B
C
D
E
F
2.5 km
E
Fence line
Prairie dog town
NVP15/4/1
60 m
D
NVP16/4/1
NVP16/4/2
NVP16/4/3
NVP16/4/4
Original homestead
70 m
B
NVP16/2/1
NVP16/2/2
NVP16/2/3
Windmill-powered groundwater pump
NVP16/2/4
60 m

Table 3.3 Final seventeen vertical sediment cores used in analysis to address the main research question. Table extracted from Paper 3. Please refer to Appendix B for extended site descriptions and pictures of individual study sites.

Sediment core	Latitude (°)	Longitude (°)	Elevation (m a.s.l)	Site description
Site A – Blowout feature				
NVP15/1/1	42.73510	-100.03734	768	Is located on the eastern half of the NVP boundary and positioned on the upper slopes of one of the larger dune sections found in the vicinity, on the northern edge of the Hazel Creek palaeochannel. Aerial photography from 1954 and 1968 show site A was one of the most active blowouts in the Preserve. Present vegetation cover included patchy shrubs and grasses with patches of visibly bare sand. Sediment cores NVP15/1/1 and NVP15/3/1 were extracted from the top of the blowout backwall and base of the blowout respectively.
NVP15/3/1	42.73491	-100.03781	757	
Site B – Windmill site				
NVP16/2/1	42.72727	-100.14539	787	In the western limit of the study area, outside of the Niobrara Valley Preserve in the privately-owned O'Kief ranch. Four vertical sediment cores were extracted along a transect from the crest (NVP16/2/1) of a choppy dune, down the SE flank (NVP16/2 and 3), across a livestock disturbed interdune (no sample) and into a downwind deposition lobe (NVP16/2/4). The lobe appeared to be formed from sediment deflated from the disturbed area.
NVP16/2/2	42.72723	-100.14481	782	
NVP16/2/3	42.72713	-100.14458	781	
NVP16/2/4	42.72654	-100.14317	782	
Site C – The Parabolic dune				
NVP16/5/1	42.71943	-100.02847	763	A transect across a well-vegetated parabolic dune located SE of the Niobrara Valley Preserve limits. Cores from the easterly-facing parabolic dune (NVP16/5) include: parabolic dune nose (5/1), windward-dune slope (5/2), the deflation basin ahead of the dune (5/3), and from the northern arm of the parabolic dune (5/4). No active surface sands were present at the time of sampling.
NVP16/5/2	42.71953	-100.02880	762	
NVP16/5/3	42.71972	-100.02927	755	
NVP16/5/4	42.72039	-100.02929	758	
Site D – Homestead site				
NVP16/4/1	42.74444	-100.10461	768	Large blowout feature located north of the original homestead on the O'Kief's ranch. Choppy dune /

Sediment core	Latitude (°)	Longitude (°)	Elevation (m a.s.l)	Site description
NVP16/4/2	42.74437	-100.10448	764	basin feature appears to have accumulated against a fence line and copse of planted trees. Four cores taken along a transect trending NW-SE: crest of dune (NVP16/4/1), slope (NVP16/4/2), the deflation basin (NVP16/4/3), and up the opposite facing slope (NVP16/4/4). Transect was semi-vegetated with grasses and patches of bare sand found between grasses.
NVP16/4/3	42.74415	-100.10422	759	
NVP16/4/4	42.74380	-100.10403	761	
Site E –1930s dune				
NVP15/4/1	42.73719	-100.09194	761	Fence line dune located south-east of Site D on the Sandhill and Sun Ranch. Site E noted as having experienced deposition in the 1930s when sediment was eroded from the adjacent prairie dog town and deposited along the boundary fence of the ranch. One vertical core (NVP15/4/1) was extracted from this site to explore the variability in the landscape when placed near Sites D and F.
Site F – Old rolling dunes				
NVP16/6/1	42.73911	-100.10360	757	Selected as a comparison site to the other sampling sites as this location did not show any present evidence for recent reactivation, nor did the archived aerial photography or ranchers accounts. Two vertical sediment cores were extracted from this site: crest of vegetated rolling dune (NVP16/6/1) and from a relative low point (NVP16/6/2).
NVP16/6/2	42.73928	-100.10328	752	

3.3 Changepoint analysis

When dating periods of sediment accumulation within the vertical profiles, it was important to capture all depositional events. With seventeen cores of 50 cm profiles, dating at 1 cm intervals of sediment would require c.850 separate luminescence ages – significantly beyond the time constraints of this research project. Therefore, there was a need to sub-sample the profiles and identify where to focus dating given a lack of visible stratigraphy within the profiles. An improved

understanding of the depositional structure is also key to contextualising the overall luminescence ages, as well as justifying the selected locations of the final age estimates. If we assume discrete depositional events are separated by erosional unconformities, we can search for chronostratigraphic units within the profile. To identify the most appropriate sub-samples for luminescence measurement, a method was needed to locate the key break points in chronology with depth of the sedimentary profiles and focus luminescence dating efforts. An estimated continuous measure of age using L_x/T_x (sensitivity-corrected coarse luminescence signal) as a proxy was used to provide an effectively continuous estimate of age down-core. A statistical method referred to as 'Changepoint analysis' (Killick *et al.*, 2012) (also as 'broken stick' analysis (White *et al.*, 2010)) was applied to high-resolution L_x/T_x luminescence profiles as an algorithmic approach to locate distinct points of change in luminescence (i.e. age) along individual sediment cores and identify different units. The changepoint analysis identifies the location of multiple break points within the profile of each sediment core, should they exist, based on the variation in mean L_x/T_x with depth. All changepoint analysis was completed using the Changepoint package (Killick and Eckley, 2014) in R Studio. Changepoint model outputs were used to produce a depositional structure of chronological units within each vertically sampled core and inform which depths should be used for full-preparation OSL dating. Paper 2 discusses the preparation of sediments and the application of Changepoint analysis in more detail.

3.3.1 Particle size analysis

Particle size measurements were taken to look for correlation in grain size with the chronological units identified by changepoint analysis. Particle size measurements were calculated for a selection of vertical sediment profiles with sub-sample grain size data measured using a Malvern Mastersizer 3000 and analysed using GRADISTAT software version (8.0) (Blott and Pye, 2001). Sediment homogeneity in the particle size analysis ensured that the variability identified in the Changepoint analysis was a function of luminescence signal size. See Paper 2 for details of results.

3.4 OSL dating

3.4.1 Principles of OSL dating

OSL dating measures the time that has elapsed since the last exposure of mineral grains to sunlight. In aeolian systems, OSL techniques provide an excellent method of dating sedimentary records and reconstructing environmental history, providing time-series of deposition events in dryland aeolian settings. When a quartz (or feldspar) crystal has been deposited and shielded from all sunlight (and temperatures significantly above ambient levels), a charge accumulates in defects within the crystal lattice. This accumulated signal can be measured under controlled conditions, providing an 'equivalent dose' which can be used to estimate the time elapsed since the crystal was last 'bleached' (i.e. exposed to sunlight / deposited in an aeolian context) when the environmental dose rate is known (the background ionising radiation dose rate per year during sample burial). In the

absence of the true burial age, laboratory applied methods of luminescence dating allow us to measure the equivalent dose, the estimated environmental dose rate, and thus calculate an estimated age (Equation 3.1) (Duller, 2008; Preusser *et al.*, 2008).

Equation 3.1 The age equation for luminescence dating.

$$Estimated\ age\ (ka) = \frac{Equivalent\ dose\ (Gy)}{Estimated\ dose\ rate\ (Gy.ka^{-1})}$$

OSL was used to explore two key parts of this research project. First, an experimental stage identified the optimum luminescence preparation and measurement conditions for dating very young aeolian sediments (Paper 1). Second, having established the most appropriate luminescence protocol for dating young aeolian sands, OSL was applied to selected samples to reconstruct relatively high-resolution chronologies of surface sand reactivation across dune and blowout profiles (Paper 3).

3.4.2 Transporting OSL samples

Given the very low equivalent doses and young age of the sediment being measured in this study, it was essential to identify any potential sources of additional variability or change to the signal. Samples of annealed quartz were transported in glass vials alongside the sediment cores through airport security and transit to determine if the airport x-ray scanners or the cosmic dose absorbed during the flight between the US and UK, in any way impacted the luminescence signal of the sediment cores. Three samples were carried alongside different packages of the

sediment tubes and luminescence signals measured according to standard SAR protocols (Figure 3.9). Results show that no detectable luminescence signal resulted from the dose absorbed during transit (D_e = 0 ± 0.01 Gy), ensuring that these samples could thus be used for the main dating analysis of this project.

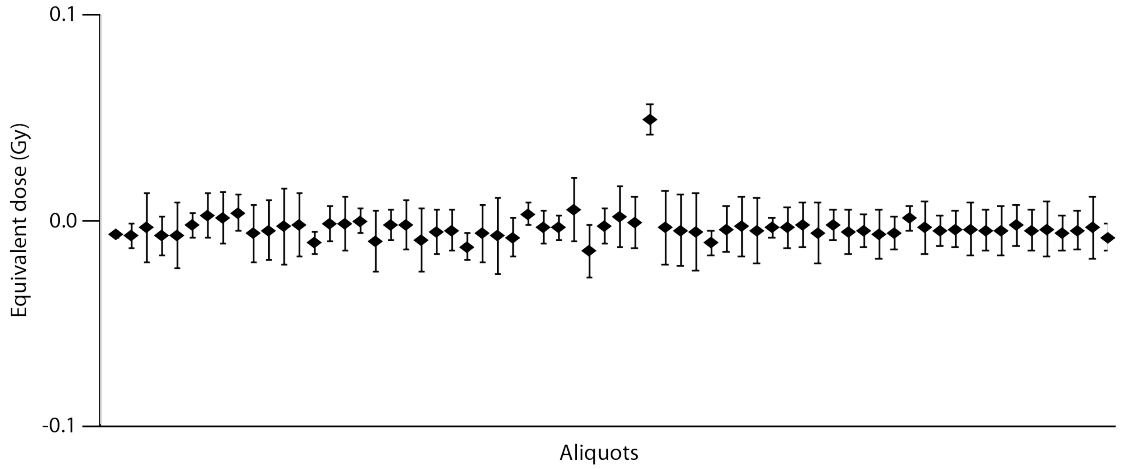


Figure 3.9 Results from equivalent dose measurements of annealed quartz that was stored alongside sediment tubes during transport from Nebraska to Oxford. A total of 66 large aliquots were prepped and measured following started SAR protocol with 200°C preheats to identify if any signal had been transferred to the quartz crystals during scanning at security. Graph shows that the results centre on 0 Gy and no signal has been transferred to the sediment samples during transportation.

3.4.3 OSL sample preparation

Samples were prepared and analysed under subdued orange light at the Oxford Luminescence Dating Laboratory. The 50 cm black opaque tubes (section 3.2.1) were split lengthwise and sediments sub-sampled at centimetre scale, dried and mounted onto single 8 mm diameter discs for initial changepoint analysis. Changepoint analysis (section 3.3) was applied to all sub-samples from the seventeen sediment cores prior to selection of sub-samples for full-preparation luminescence dating (see Paper 2). This method led to a range of mid-section and

end-point samples being identified from the cores as representative of dune activity phases and appropriate for full OSL dating.

Based on the results of the changepoint analysis, sub-samples that were selected for full OSL dating were treated in an excess of hydrochloric acid (HCl) and hydrogen peroxide (H_2O_2) to remove carbonates and organics prior to wet-sieving to the desired size fraction (125-180 μm). Density separation using sodium polytungstate was used to separate out the quartz grains, and a 60 minute etch in hydrofluoric acid (HF ~ 40%) followed by a final treatment in HCl were used to remove any remaining feldspar crystals. Samples that were prepared for infrared stimulated luminescence (IRSL) were separated using polytungstate to separate out the K-feldspar crystals and were not treated with a final HF etch.

3.4.4 Equipment set-up

All luminescence measurements were made using an automated Risø TL/DA 15 reader, equipped with infra-red (IR) (870 nm) and blue (470 nm) LEDs and $^{90}Sr/^{90}Y$ beta sources for irradiations (dose rate 0.068 – 0.065 Gy/s). A convex quartz lens placed in front of the photomultiplier tube was used to focus the signal and increase the number of counts recorded in the photomultiplier tube. For quartz measurement, luminescence was detected in the UV region using an EMI 9635Q alkali photomultiplier tube fitted with a 7.5 mm Hoya U-340 filter, whilst IRSL detection was achieved through a combination of Corning 7-59 and Schott BG39 filters.

3.4.5 SAR measurement protocol

Following chemical treatment, a minimum of sixteen small aliquots per selected sub-sample were measured following the single-aliquot regenerative-dose (SAR) protocol (Murray and Wintle, 2000; Wintle and Murray, 2006). To identify the most appropriate mineral, preparation methods and measurement conditions for dating young sediments, a series of experiments were completed and are explored in detail in Paper 1. Preheats (PH1 and PH2 - 200°C for 10 s) were determined following a series of preheat plateau and dose recovery tests and equivalent dose measurements were made following the measurement procedures (130°C blue LED stimulation) and rejection criteria outlined in Paper 1. Based on the young nature of the sediments, sub-sample equivalent doses were calculated using the un-logged Central Age Model (CAM) (Galbraith *et al.*, 1999).

3.4.6 Dose recovery test

To demonstrate the suitability of the preparation and measurement conditions used in Paper 1, a dose recovery test for a selection of sub-samples was completed. Dose recovery tests are used to ensure that the test dose used in the SAR protocol corrects for any sensitivity changes during the heating and measurement of the natural luminescence signal (Roberts *et al.*, 1999; Wallinga *et al.*, 2000; Wintle and Murray, 2006). Dose recovery tests involved removing the natural luminescence signal from the sample (i.e. bleach the sample using blue LEDs for two periods of 200 s at 20°C) and then exposing the sediment sample to a known dose of β-irradiation. The sediment sample was then measured using the SAR

protocol and the selected preheat temperatures (section 3.4.5). The appropriateness of the SAR protocol and preheats temperatures is determined if the measured signal matches the known dose (Duller, 2008). The size of the administered dose should be similar to the natural D_e of the sediments to mimic the natural conditions. In this study, given the young nature of the sediments dated, a low dose of irradiation was used (10 s ~ 0.65-0.68 Gy). Dose recovery experiments show that the ratio of administered to recovered dose to be within errors of unity for samples tested, and from this it is concluded the chosen sample measurement protocol is appropriate (Table 3.4).

Table 3.4 Small aliquots of fully-prepped quartz (125-180 μm) were used to complete dose recovery tests for a range of sediment samples. Normalised D_e's show that the measurement conditions selected in this study are appropriate for measuring the D_e of these young aeolian samples. The majority of normalised D_e's ± 1σ overlap with unity, at ± 2σ all samples overlap with unity.

Sample	Aliquots (n)	Normalised D_e ± 1σ	Overdispersion (OD) [2]
NVP15/1/1/25	15	1.01 ± 0.06	6 %
NVP15/3/1/25	18	1.02 ± 0.03	0 %
NVP15/4/1/25	20	1.01 ± 0.03	0 %
NVP16/2/1/25	11	0.99 ± 0.04	0 %
NVP16/2/3/34	6	0.96 ± 0.04	0 %
NVP16/2/4/45	20	1.07 ± 0.03	8 %
NVP16/4/1/25	15	1.03 ± 0.03	0 %
NVP16/4/2/26	9	1.01 ± 0.07	0 %
NVP16/4/3/43	5	1.0 ± 0.06	0 %

[2] Overdispersion (OD) is normally presented as a % and refers to the amount of variability in D_e of the sample that we would not expect to see. OD % is the amount of variability from the mean D_e that cannot be explained by grain-to-grain variability and beta dose rate heterogeneity. OD % increases exponentially as D_e approaches zero, and thus is not a viable measure of the dispersion of young samples. For this reason, OD is not described in length in this thesis.

Sample	Aliquots (n)	Normalised $D_e \pm 1\sigma$	Overdispersion (OD) ^{2}
NVP16/4/4/12	12	1.03 ± 0.03	6 %
NVP16/5/1/30	16	0.96 ± 0.03	9 %
NVP16/5/2/9	11	0.96 ± 0.03	17 %
NVP16/5/3/21	15	1.0 ± 0.03	7 %
NVP16/5/4/3	11	0.95 ± 0.03	0 %
NVP16/6/1/25	10	1.1 ± 0.04	6 %
NVP16/6/2/15	11	0.98 ± 0.07	7 %

3.4.7 Selecting integration intervals

To calculate the net luminescence signal, a background integral is subtracted from the initial integral of the OSL decay curve (Smith *et al.*, 1990). Selecting the integration intervals of the initial signal and background window determines the overall composition of the net luminescence signal. The quartz luminescence decay curve is not defined by a single decaying exponential (Huntley *et al.*, 1985), but by three components which are termed 'fast', 'medium' and 'slow' based on their rate of signal decay (Bailey *et al.*, 1997). Each individual component is characterised by separate optical and thermal properties (Bailey, 2010; Singarayer and Bailey, 2003) with the 'fast' component of the luminescence signal being identified as the most suitable component for dating as it is stable on geological timescales (Wintle and Murray, 2006) and is rapidly bleached by sunlight (Jain *et al.*, 2003; Singarayer and Bailey, 2003). When combined with the SAR protocol (Murray and Wintle, 2000), fast-dominated signals have been found to produce accurate age estimates.

Careful selection of integration interval width allows us to determine the proportion of each component in the overall net signal, and calculate the widths needed to produce the greatest levels of fast component (Bailey, 1998). As noted above, an equivalent dose dominated by the fast component is particularly important when dating young aeolian samples to remove any likelihood for an age overestimation caused by incomplete bleaching prior to deposition. Jain *et al.* (2003) and Tsukamoto *et al.* (2003) also found that the fast component of the luminescence signal displays less recuperation[3] than the medium and slow components; another critical reason why isolating the fast component of the signal is imperative for these young samples. Cunningham and Wallinga (2010) comment that the maximisation of the fast component, coupled with the minimisation of the medium component, is achieved when a short time interval is selected for both the initial and background signals. However, a short time for background signal also causes a reduction in the overall precision of the equivalent dose. This is particularly important in the present case as the signal associated with very young samples (<30 yrs) are relatively small and therefore prone to significant statistical uncertainty. Counting statistics gives an error proportional to the square root of the number of counts, which as a proportion of the signal, grows quickly as the count numbers are reduced. A criteria for selecting the optimal integration intervals which combines the largest percentage of the fast component with a low relative standard error of the net overall signal is needed. A series of steps were completed to identify the most suitable combination of signal and background integral widths and

[3] Recuperation refers to the thermally-induced transfer of charge from the medium and slow components traps into the fast traps (Aitken and Smith, 1988), resulting in a small measured signal when zero dose is applied.

locations for these signal profiles (Appendix D). Based on results from integration interval analysis, a relatively large signal window coupled with an early-background interval was selected. For all final equivalent doses produced in this study, the integration intervals 0.1-1.5 s for initial signal and 1.5-6 s for background signal were used (Figure 3.10).

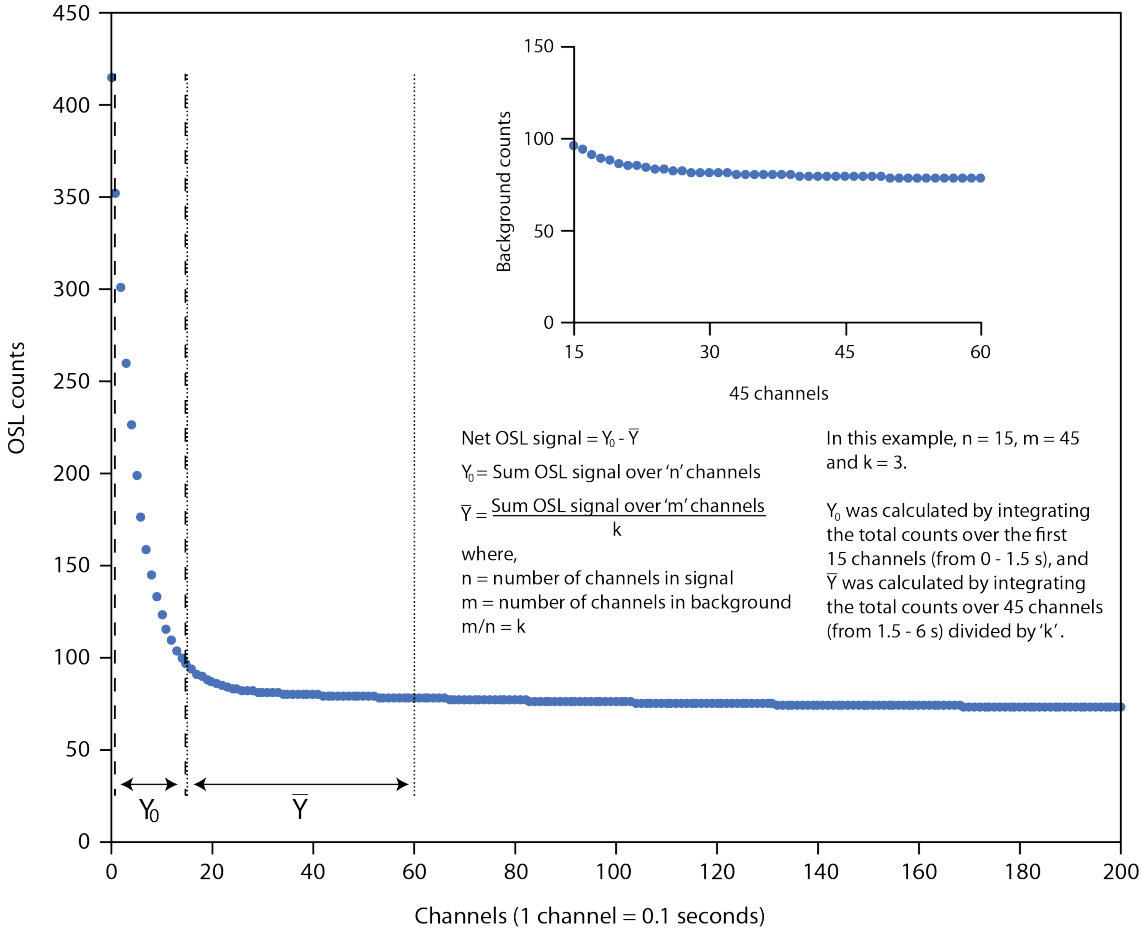


Figure 3.10 Example of luminescence decay curve and position of final integration limits used to calculate net luminescence signal. Figure demonstrates the calculation of the integrated signal and background components based on the number of channels used in the signal integration.

3.4.8 Calculating the environmental dose rate

Environmental dose rates refer to the amount of energy absorbed by a mineral from naturally occurring radiation in the sample and surrounding environment (Duller, 2008; Guérin, 2013) and are needed in order to convert equivalent dose measurements into an estimated age of deposition. The environmental dose rate is composed of contributions from alpha, beta and gamma radiation emitted by the radioactive decay of naturally occurring Thorium, Uranium and Potassium, and cosmic rays (Equation 3.2).

Equation 3.2 Calculation of the environmental dose rate. D_α = contribution of environmental dose from alpha radiation, D_β = contribution of environmental dose from beta radiation D_γ = contribution of environmental dose from gamma radiation, D_{cosmic} = contribution of environmental dose from cosmic radiation.

$$D_r = D_\alpha + D_\beta + D_\gamma + D_{cosmic}$$

Environmental dose rates were calculated using the Dose Rate and Age Calculator (DRAC) (and the calculations therein) (Durcan *et al.*, 2015) and details of the methods used to calculate radionuclide concentrations and water content levels are found below:

Radionuclide concentrations

Environmental dose measurements were calculated using radionuclide concentrations (^{232}Th, ^{238}U and ^{40}K) measured using ICP-MS. Where no stratigraphic change was noted, and radionuclide concentrations were normally distributed between sub-samples of the same sediment core, a weighted average of

radionuclide concentrations was used for multiple sub-samples within the respective sediment cores (Appendix E).

Water content estimation and overburden density sensitivity

One of the main sources of uncertainty in OSL dating is estimating the water content of the sediments since the time of burial. Estimating the water content of the sediments, is important to the overall age calculation as water attenuates the dose rate that the crystals receive whilst buried (Aitken, 1985; Guérin *et al.*, 2012; Nelson and Rittenour, 2015). The effect on age is approximately 1% difference in age per 1% water content (Aitken, 1998). Whilst many studies have historically used in situ moisture measurements from the time of sampling, in situ moisture content values are unlikely to be representative of average soil moisture conditions over the burial period of the sediment samples; therefore, an alternative modelling approach was applied in this study. This project used the method described in Nelson and Rittenour (2015) to calculate an improved approximation of the water content values over the burial period of the sediment. Soil moisture content values were calculated using grain size characteristics, the van Genutchen (1980) water retention equation and Rosetta Lite v.1.1 software within the Hydrus-1D modelling program (Simunek *et al.*, 2008). The gravimetric mean annual water state (kPa) for the sites used in this study was calculated according to the USDA-NRCS Soil Moisture Regimes and ICOMMOTR (1991) classification referred to in Nelson and Rittenour (2015). Examples of the water content calculated for different depths of sediment based on the grain size characteristics are shown in Table 3.5. Using previously published literature (Table 3.6), a range of overburden densities from

1.8-2.0 g/cm^3 ± 0.1 were selected for moisture content and overburden density sensitivity analysis.

Table 3.5 Examples of water content calculated for multiple depths of sediment cores GSL16/3/2 taken from GSL and NVP16/2/3 taken from NVP.

784 kPa used	**Gravitational water %**			**316 kPa used**	**Gravitational water %**		
Overburden density	**1.6 g/cm^3**	**1.9 g/cm^3**	**2.1 g/cm^3**	**Overburden density**	**1.6 g/cm^3**	**1.9 g/cm^3**	**2.1 g/cm^3**
GSL16/3/2/4	2.941	2.477	2.241	NVP16/2/3/3	2.631	2.215	2.004
GSL16/3/2/10	2.940	2.507	2.240	NVP16/2/3/5	2.686	2.262	2.046
GSL16/3/2/16	2.938	2.050	2.239	NVP16/2/3/17	2.606	2.194	1.985
GSL16/3/2/22	2.937	2.207	2.238	NVP16/2/3/19	2.520	2.122	1.920
GSL16/3/2/28	2.937	2.063	2.237	NVP16/2/3/25	2.580	2.173	1.966
GSL16/3/2/34	2.934	2.306	2.236	NVP16/2/3/33	2.564	2.159	1.953
GSL16/3/2/40	2.933	2.363	2.235	NVP16/2/3/47	2.509	2.113	1.912
GSL16/3/2/46	2.932	2.447	2.234	NVP16/2/3/49	2.462	2.073	1.876

Table 3.6 Examples of overburden densities used in the previously published literature.

Thomas *et al.* (2009)	Mean of 2.0 ± 0.1 g/cm^3
Nelson and Rittenour (2015)	1.9 g/cm^3
Durcan *et al.* (2015)	1.8 g/cm^3 (DRAC default setting)

Based on averages in the aeolian luminescence literature (typically up to 5 ± 2%), and the results in Table 3.5, a range of moisture content values from 2-5 ± 2% were tested for sensitivity analysis on the overall OSL age estimate (Table 3.7). The standard deviation across the range of results produced for the same sample with the varying combinations of moisture content and overburden density is relatively small, typically less than 2-3 years. This is corroborated with the difference between the highest and lowest age estimates being limited to less than

5% (c.0-8 years depending on age). However, within the uncertainty estimates there is no difference between the results produced for the same samples. Based on the specific grain size measurements from these sites, the moisture content calculated using Nelson and Rittenour (2015) method and the results of the sensitivity analysis (Table 3.7), a mid-range value of 3 ± 2 % moisture content, coupled with a 1.9 ± 0.1 g/cm^3 overburden density was selected for the age estimate calculations for all samples in this study.

Conversion and attenuation factors

Using standard conversion factors for grain size adjustments (Mejdahl, 1979), HF-etching (Bell, 1979), beta attenuation (Guérin *et al.*, 2011), water content (Aitken, 1985) and cosmic dose rates (Prescott and Hutton, 1994), annual dose rates were calculated and used for final age estimates. Environmental dose rates used for each individual sample are noted in Paper 3. Appendix E provides a detailed breakdown of the final environmental dose rate components for each sample.

Table 3.7 Sensitivity analysis to determine the impact on final age estimation using different combinations of moisture content and overburden density. Age and uncertainty are presented in (ka) for a series of samples from different depths in cores NVP15/4/1 and NVP15/1/1. The standard deviation of the multiple ages estimates for each sample is presented alongside the highest and lowest values calculated.

Sample	Age (ka) ± uncertainty (ka)												Statistical range			
	Moisture 2 ± 2 %			Moisture 3 ± 2%			Moisture 4 ± 2 %			Moisture 5 ± 2 %						
	OB 1.8 ± 0.1 g/cm³	OB 1.9 ± 0.1 g/cm³	OB 2.0 ± 0.1 g/cm³	OB 1.8 ± 0.1 g/cm³	OB 1.9 ± 0.1 g/cm³	OB 2.0 ± 0.1 g/cm³	OB 1.8 ± 0.1 g/cm³	OB 1.9 ± 0.1 g/cm³	OB 2.0 ± 0.1 g/cm³	OB 1.8 ± 0.1 g/cm³	OB 1.9 ± 0.1 g/cm³	OB 2.0 ± 0.1 g/cm³	St. Dev.	Lowest value	Highest value	Delta
NVP15/4/1/5	0.057	0.058	0.058	0.058	0.058	0.058	0.059	0.059	0.059	0.059	0.060	0.060	0.001	0.057	0.060	0.003
uncertainty	0.018	0.018	0.018	0.018	0.018	0.018	0.018	0.018	0.018	0.018	0.018	0.018	0.000	0.018	0.018	0.000
NVP15/4/1/10	0.062	0.062	0.062	0.062	0.062	0.063	0.063	0.063	0.063	0.064	0.064	0.064	0.001	0.062	0.064	0.002
uncertainty	0.006	0.006	0.006	0.006	0.006	0.006	0.006	0.006	0.006	0.007	0.007	0.007	0.000	0.006	0.007	0.001
NVP15/4/1/15	0.148	0.148	0.148	0.149	0.150	0.150	0.151	0.151	0.151	0.152	0.153	0.153	0.002	0.148	0.153	0.005
uncertainty	0.043	0.043	0.044	0.044	0.044	0.044	0.044	0.044	0.044	0.045	0.045	0.045	0.001	0.043	0.045	0.002
NVP15/4/1/20	0.107	0.107	0.107	0.108	0.108	0.108	0.109	0.109	0.109	0.110	0.110	0.110	0.001	0.107	0.110	0.003
uncertainty	0.022	0.022	0.022	0.022	0.022	0.030	0.023	0.023	0.023	0.023	0.023	0.023	0.002	0.022	0.030	0.008
NVP15/4/1/25	0.137	0.137	0.137	0.138	0.139	0.139	0.140	0.140	0.140	0.141	0.141	0.142	0.002	0.137	0.142	0.005
uncertainty	0.031	0.031	0.031	0.031	0.031	0.032	0.032	0.032	0.032	0.032	0.032	0.032	0.001	0.031	0.032	0.001
NVP15/4/1/30	0.170	0.170	0.170	0.171	0.172	0.172	0.173	0.174	0.174	0.175	0.175	0.176	0.002	0.170	0.176	0.006
uncertainty	0.031	0.031	0.031	0.031	0.031	0.031	0.031	0.032	0.032	0.032	0.032	0.032	0.001	0.031	0.032	0.001
NVP15/4/1/35	0.164	0.164	0.164	0.166	0.166	0.166	0.167	0.168	0.168	0.169	0.169	0.170	0.002	0.164	0.170	0.006
uncertainty	0.032	0.032	0.032	0.032	0.032	0.032	0.033	0.033	0.033	0.033	0.033	0.033	0.001	0.032	0.033	0.001
NVP15/4/1/40	0.209	0.209	0.210	0.211	0.212	0.212	0.213	0.214	0.214	0.216	0.216	0.216	0.003	0.209	0.216	0.007
uncertainty	0.038	0.038	0.038	0.038	0.039	0.039	0.039	0.039	0.039	0.039	0.039	0.039	0.000	0.038	0.039	0.001
NVP15/4/1/45	0.178	0.178	0.178	0.180	0.180	0.180	0.182	0.182	0.182	0.184	0.184	0.184	0.002	0.178	0.184	0.006
uncertainty	0.025	0.025	0.025	0.025	0.025	0.025	0.025	0.026	0.026	0.026	0.026	0.026	0.001	0.025	0.026	0.001
NVP15/1/1/1	0.001	0.001	0.001	0.001	0.001	0.001	0.001	0.001	0.001	0.001	0.001	0.001	0.000	0.001	0.001	0.000
uncertainty	0.012	0.012	0.012	0.012	0.012	0.012	0.012	0.012	0.012	0.012	0.012	0.012	0.000	0.012	0.012	0.000
NVP15/1/1/40	0.063	0.064	0.064	0.064	0.064	0.064	0.065	0.065	0.065	0.065	0.066	0.066	0.001	0.063	0.066	0.003
uncertainty	0.016	0.016	0.017	0.016	0.016	0.017	0.017	0.017	0.017	0.017	0.017	0.017	0.000	0.016	0.017	0.001
NVP15/1/1/50	0.055	0.055	0.055	0.055	0.055	0.055	0.056	0.056	0.056	0.056	0.056	0.057	0.001	0.055	0.057	0.002
uncertainty	0.014	0.014	0.014	0.014	0.014	0.014	0.014	0.014	0.014	0.014	0.014	0.014	0.000	0.014	0.014	0.000

3.4.9 Age estimation

The unlogged-Central Age Model (CAM) was selected as the most appropriate age model for processing these young aeolian sediments. Please see Paper 1 (Chapter 4) for a more detailed explanation of the age model selection that was applied in the luminescence dating of these sediments. Using DRAC (Durcan *et al.*, 2015), all sources of uncertainties associated with each component of the dose rate and the environmental dose measurement are propagated in quadrature to produce the overall age estimate uncertainty.

To improve the chronological resolution and reduce the uncertainty estimates, Bayesian age-depth models were produced for sediment cores that identified sub-samples with overlapping age estimates using the OxCal software package (version OxCal 4.3) (Bronk Ramsey, 2009). The model applies a sequential order upon the sub-sample OSL age estimates based on the depths and stratigraphical positions within the sediment core. Bayesian age-depth models were produced for sediment cores NVP15/1/1, NVP15/3/1 (site A) and NVP15/4/1 (site E) and modelled ages are presented alongside un-modelled ages in Paper 3 (Appendix K).

Chapter 4

PAPER 1

Paper 1 Prelude

The purpose of Paper 1 was to identify the most suitable measurement protocol for dating these young samples using luminescence techniques. Whilst OSL dating methods have been applied to sediments across a range of depositional ages, they are typically best applied to sediments with burial ages of 1-100 ka, when a large signal has accumulated in the crystal. Nevertheless, a series of studies have demonstrated the capacity to use OSL techniques to date modern and young sediment depositions. Paper 1 presents a series of experiments that were conducted to identify the optimal measurement and analysis conditions for dating young aeolian Nebraskan sedimentary deposits. Paper 1 compares the relative benefits of different minerals and their associated luminescence signals as well as a range of measurement conditions (e.g. preheat and stimulation temperatures). Finally, Paper 1 uses a sample of known modern age to verify the most suitable suite of measurement procedures and data-processing rejection criteria. Additional footnotes have been included in this thesis-adapted version to provide clarification on some OSL-specific terms.

Testing the suitability of p-IR IRSL for dating young samples (< 200 yrs)

Paper 1: Buckland, C. E., Bailey, R. M., Thomas, D. S. G.

Status: Revisions requested (by 26th October 2018) in *Radiation Measurements*

Abstract

Issues of partial bleaching and dim luminescence signals can lead to large uncertainties on young luminescence ages. Identifying the most appropriate luminescence protocol for dating young sediments is important for improving the accuracy of young aeolian sediment ages. This study compares the performance of quartz OSL and K-feldspar post-IR IRSL (p-IR IRSL) in a series of preheat plateau, bleachability, and natural residual tests. Sediments of known age are used to identify the most suitable aliquot size and age model choice for analysis. Results show that despite improved signal-to-noise ratios, and g-values within errors of zero, K-feldspar p-IR IRSL signals display a residual value that can lead to considerable age overestimations of very young sediments. Small aliquots of quartz with a moderate preheat temperature is considered the most appropriate conditions for measurement of these samples, coupled with the un-logged CAM which is able to account for negative and low D_e values.

4.1 Introduction

Methodological and technological advances in optically stimulated luminescence (OSL) dating (e.g. Bøtter-Jensen *et al.*, 2000; Murray and Wintle, 2000), and age model modifications (e.g. Arnold *et al.*, 2009), have meant that the accuracy of dating of young sediments has greatly improved over recent decades. Existing studies have successfully applied OSL techniques to young and known-age sedimentary samples (e.g. Bailey *et al.*, 2001; Ballarini *et al.*, 2003; Banerjee *et al.*, 2001; Cunningham and Wallinga, 2012, 2009; Madsen *et al.*, 2007; Olley *et al.*, 1999). However, the majority have focused on using the quartz mineralogical fraction to date the age of deposition. The rapid bleaching of the fast component of the quartz luminescence signal (Wintle and Murray, 2006) minimises the likelihood of partial bleaching, and coupled with a seemingly apparent absence of anomalous fading, quartz-focused studies have dominated young luminescence measurements.

Nevertheless, the application of feldspars to optical dating has many advantages. First, feldspars have generally been considered as an alternative mineral to date using infrared stimulated luminescence (IRSL) techniques when dating very old sediments (>100 ka) due to its higher saturation limit. Second, unlike quartz crystals, feldspars can be selectively measured under infrared excitation despite the presence of other minerals. Finally, a larger proportion of potassium-rich feldspar (hereafter referred to as 'K-feldspar') grains emit a detectable luminescence signal, which is generally brighter than the signal emitted from quartz grains (Duller *et al.*, 2003). A brighter luminescence signal will improve the signal-

to-noise ratio of luminescence measurements, boosting the capacity to measure young dim samples.

Yet, comparatively few studies use the K-feldspar fraction for dating sedimentological samples. K-feldspar IRSL techniques have generally been disregarded in favour of quartz OSL measurements for reasons such as anomalous fading of the K-feldspar luminescence signal. The instability of some of the signals in the feldspar grains results in a greater degree of anomalous fading [4] (Wintle, 1973) than found in quartz crystals, resulting in estimated age underestimations (Buylaert *et al.*, 2012). However, the introduction of the p-IR IRSL protocol proposed by Thomsen *et al.* (2008) to minimise levels of anomalous fading has led to a re-exploration of K-feldspar luminescence potential. A series of recent studies have sought to test the application of the p-IR IRSL protocol in a range of settings including dating modern and young sediments (Madsen *et al.*, 2011; Reimann and Tsukamoto, 2012), comparing the utility of the p-IR IRSL signal against quartz OSL in attempting to extend the luminescence age range (Colarossi *et al.*, 2015) and investigate the impact of varying measurement conditions of the protocol to minimise residual doses and fading of the luminescence signal (Buylaert *et al.*, 2009; Colarossi *et al.*, 2018; Jain *et al.*, 2015; Roberts, 2012).

Whilst the p-IR IRSL signal has been shown to be more stable over time than previously used $IRSL_{50}$ protocols, existing research has also suggested that the signal bleaches more slowly and thus results in greater residual signals than equivalent $IRSL_{50}$ and quartz OSL measurements. A summary of published p-IR IRSL residual

[4] Anomalous fading (Wintle, 1973) refers to the decay of an unstable luminescence signal. Anomalous fading leads to an underestimation of the true age of the sample if uncorrected for (Roberts, 2012).

results in Smedley *et al.* (2015) suggests that under specific measurement conditions, residual D_e values for multigrain aliquots have been recorded <1 Gy, with the youngest reported age of a known modern sample at 48 ± 6 years (Madsen *et al.*, 2011). These results hint at the potential routine application of p-IR IRSL protocols when measuring young sediment samples, particularly those that demonstrate a dim quartz component.

This study aims to identify a protocol for the routine dating of very young (< 200 a) aeolian dune sediments. In this study, the natural residual dose of known-age near-surface aeolian sediments from the Nebraska Sandhills are used to test the suitability of the p-IR IRSL protocol when calculating the D_e of young known-age aeolian sediments. Quartz and K-feldspar fractions have been extracted and measured against OSL blue and p-IR IRSL protocols to identify how the different minerals and protocols perform against a variety of preheat, dose recovery, anomalous fading and residual experiments.

Whilst previous studies have tested the optimum p-IR IRSL conditions for fluvial and coastal samples, this study tests the application of the p-IR IRSL method to young aeolian sediments extracted from a dryland location which typically experiences favourable bleaching conditions. With bleaching conditions considered non-limiting, it is anticipated that measuring the D_e of known age sediments should identify the lowest potential natural residual dose that we can expect to find within the K-feldspar grains. Further to this, this study explores the appropriate age model selection and rejection criteria application for measuring D_e's which straddle 0 Gy and exhibit noisy decay curves with large uncertainties.

4.2 Methods and instrumentation

4.2.1 Samples

Sediment samples GSL15/1/2, GSL15/1/3 and BBR15/1/1 extracted from the Nebraska Sandhills in July 2015 are used in this study. GSL15/1/2 and GSL15/1/3 are quartz-rich sediment samples extracted from the backwall of Yao's Blowout in the Gudmundsen Sandhills Laboratory (42.08627°N, 101.36721°W). BBR15/1/1 is a 50 cm vertical sediment core extracted from a lunette dune which has formed on the Barta Brothers Ranch since 2009 AD (42.24580°N, 99.65433°W). Sub-samples from BBR15/1/1 should therefore be of modern age (post-2009) and provide a suitable test case for determining natural residual doses between the different minerals and protocols. Sediments referred to in this paper form part of a wider research project investigating the recent environmental history and sensitivity of surficial sediments in the Nebraska Sandhills.

4.2.2 Sample preparation and instrumentation

All samples were treated in an excess of HCl and H_2O_2 to remove carbonates and organics prior to wet-sieving to the appropriate size fraction (multigrain aliquots: 125-180 µm, single-grain: 180-210 µm). Quartz fractions were isolated using sodium polytungstate density separation at 2.72 and 2.62 g/cm^3 followed by a 60 minute HF etch. K-feldspar fractions were isolated using sodium polytungstate density separation at 2.58 g/cm^3. 'K-feldspar' is used to refer to the fraction of feldspars that is dominated by potassium-rich feldspars as opposed to sodium-rich

feldspar crystals. All p-IR IRSL experiments referred to in this paper used the K-feldspar fraction of the sediment sample.

All luminescence measurements were made using an automated Risø TL/DA 15 reader, equipped with infra-red (IR) (870 nm) and blue (470 nm) LEDs and $^{90}Sr/^{90}Y$ beta sources for irradiations. A convex quartz lens placed in front of the photomultiplier tube was used to focus the signal and increase the number of counts recorded in the photomultiplier tube. For quartz measurement, luminescence was detected in the UV region using an EMI 9635Q alkali photomultiplier tube fitted with a 7.5 mm Hoya U-340 filter, whilst IRSL detection was achieved through a combination of Corning 7-59 and Schott BG39 filters.

Recycling ratio tests and an IR-depletion ratio point were included to monitor sensitivity and identify any feldspar contamination in the quartz OSL experiments (Duller, 2003). Recuperation levels were recorded and analysed alongside the range of protocol variations studied. Given the young nature of the sediments used in this study, dose response curves were fitted against a linear function and individual equivalent dose estimates were calculated using interpolation of the natural signal onto this line. Uncertainties were calculated following 1,000 Monte Carlo fits of the curve and propagated with a 2.5% measurement error. Sample equivalent doses were calculated using the un-logged Central Age Model (CAM) (Galbraith *et al.*, 1999) given the young nature of the samples measured (Arnold *et al.*, 2009).

4.3 Selecting appropriate measurement parameters for Quartz and Feldspar

Initial dose recovery preheat tests (Murray and Wintle, 2003) were performed for both combinations (OSL blue and p-IR IRSL) to determine optimum measurement conditions prior to testing for levels of anomalous fading and residual signal.

4.3.1 Quartz

OSL blue dose recovery preheat tests were completed using the quartz fraction of sediment sample GSL15/1/3 with preheats ranging from 160-250°C on small and large aliquots. All OSL blue measurements were made at 130°C for 100 s with a 6.5 Gy test dose.

Large aliquots of GSL15/1/3 normalised D_e versus preheat temperature produced expected D_e in line with unity within errors for all preheat temperatures used, with a greater spread in D_e found at higher temperatures (Figure 4.1). A slight increase in expected D_e was found with preheat temperature 250°C, suggesting some evidence of thermal transfer in the signal. Results from the recuperation cycles performed at both the beginning and end of the dose recovery SAR cycle show that recuperation increases with preheat temperature beyond 200°C. In sum, 200°C is shown to be the most appropriate preheat temperature to use when measuring young quartz samples to avoid thermal transfer and reduce levels of recuperation.

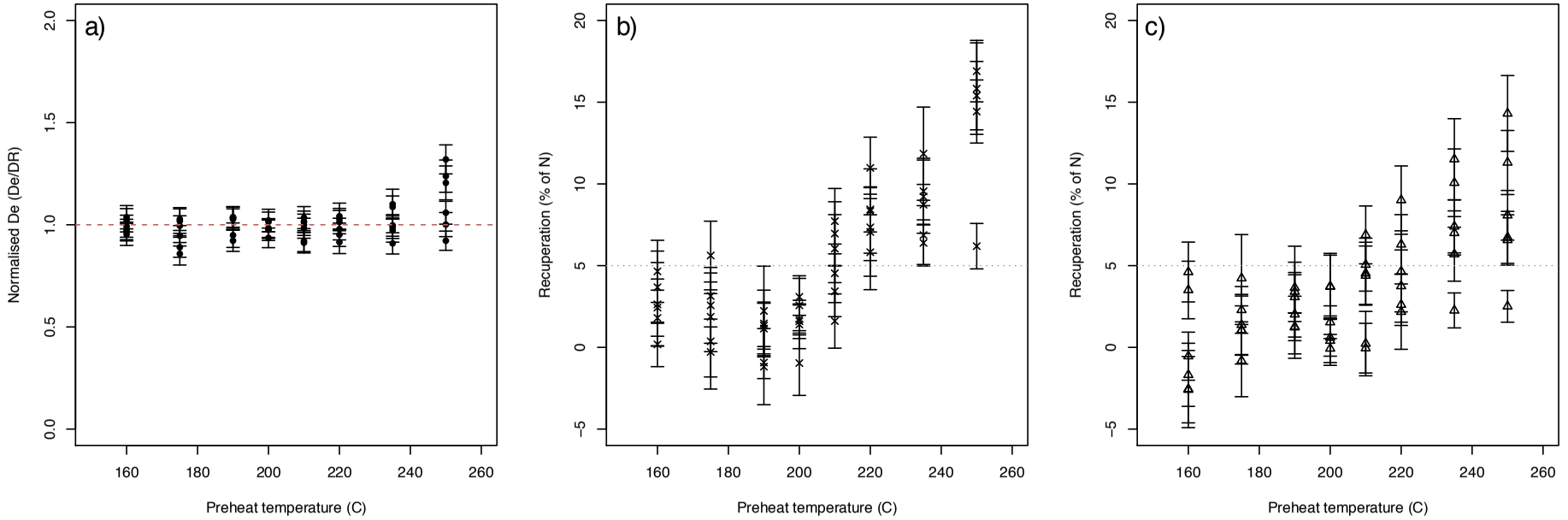


Figure 4.1 Dose Recovery preheat plateau results for large aliquots of quartz fraction of sample GSL15/1/3. (a) Normalised D_e versus preheat temperature – all temperatures used in the range 160-250°C produced expected D_e in line with unity within errors. Red dashed line through unity. (b) and (c) recuperation as % of the Natural signal versus preheat temperature at the beginning of the SAR cycle (b) and end of the SAR cycle (c). Grey-dashed line through 5% recuperation levels.

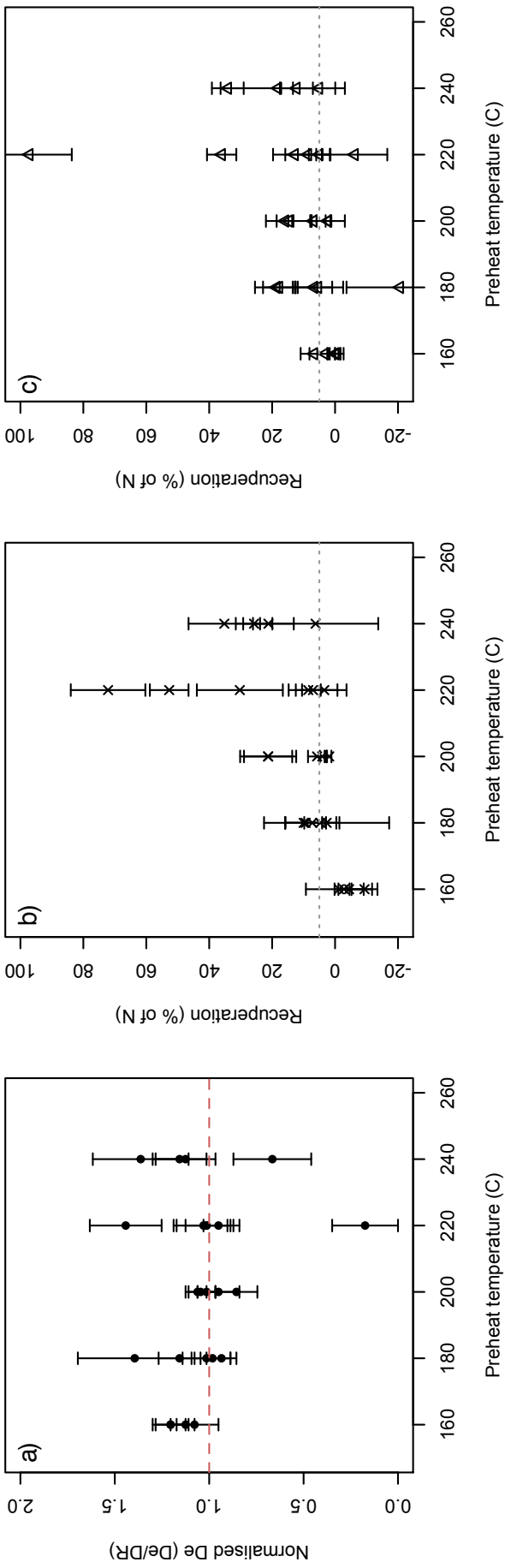


Figure 4.2 Dose Recovery preheat plateau results for small aliquots of quartz fractions of sample GSL15/1/3. (a) Normalised D_e versus preheat temperature. Red dashed line through unity. (b) and (c) recuperation as % of the Natural signal versus preheat temperature at the beginning of the SAR cycle (b) and the end of the SAR cycle (c). Grey-dashed line through 5% recuperation of the Natural dose.

As expected, small aliquots of normalised D_e versus preheat temperature demonstrated more variability than the large aliquots due to a greater averaging of bright and dim grains on the larger aliquots (Figure 4.2a). Results across all preheat temperatures demonstrate an ability to recover the expected dose within errors, yet a tighter clustering of results is identified at 200°C. Recuperation is found to be slightly lower across all preheat temperatures when measured at the end of the SAR cycle (Figure 4.2c) as opposed to the beginning of the SAR cycle (Figure 4.2b), likely due to increased sensitisation of the grains during the SAR cycle. A factor of the small signal measured, large variability and error margins are found on the recuperation levels across all preheat temperatures, but a general increase with preheat temperature like the trend identified in the large aliquot results can equally be seen.

High recuperation is anticipated given the low dose of the dose recovery test used (c. 0.63 Gy) and the recuperation level is proportionally dependent on the size of the signal (< 1 Gy). Whilst a low dosage means that identifying recuperation is difficult, a low dosage was used to replicate a similar signal size to the natural signal from these young samples. It also opens the question over the appropriateness of a recuperation threshold rejection criteria when dating young samples. High levels of recuperation as a % of the Natural dose are expected when dating young samples and a normal distribution of D_e's exist around the true dose. Rejecting D_e's which fail a recuperation threshold may result in an over estimation of the overall D_e and thus age of the sediment. Therefore, despite some aliquots suggesting higher levels of recuperation than the widely cited 5% threshold (Jacobs *et al.*, 2006; Murray and Olley, 2002), 200°C has been selected as the most appropriate preheat temperature

for dating the quartz fractions of these young sediments. See Section 4.7 for further discussion of appropriate rejection criteria for young sediment samples.

4.3.2 K-feldspar

Existing p-IR IRSL studies have used preheat temperatures ranging from 150°C – 290°C. Thomsen *et al.* 2008 recommended a p-IR IRSL protocol that coupled 250°C preheat temperatures with 225°C p-IR IRSL measurement temperatures to reduce fading rates. Yet a range of studies dating notably young sediments have suggested the use of a lower preheat temperature when applying the p-IR IRSL protocol (Madsen *et al.*, 2011; Reimann *et al.*, 2012, 2011; Reimann and Tsukamoto, 2012).

A series of dose recovery preheat plateau experiments were completed to identify the most appropriate measurement parameters for measuring the K-feldspar fraction of these samples using the p-IR IRSL protocol. Experiments were completed using sediment samples GSL15/1/2 and GSL15/1/3 with 10 s preheats ranging from 160-255°C on large and small aliquots. IRSL measurements were made at 50°C for 80 s followed by a p-IR IRSL measurement for 80 s with a 6.5 Gy test dose. Based on the method described in Roberts (2012), all p-IR IRSL measurement temperatures used in this study were 30°C cooler than the corresponding preheat temperatures. Roberts (2012) found that changes in equivalent dose when measured under the p-IR IRSL protocol were largely driven by changes in the elevated preheat temperature used as opposed to the p-IR IRSL stimulation temperature. Identifying the optimum preheat temperature conditions for these specific aeolian samples is crucial to producing reliable equivalent dose and age estimates.

Results show that at preheat temperatures 160-200°C normalised D_e is in agreement with the expected dose recovery D_e, yet beyond that temperature range, normalised D_e increases with preheat temperature, indicating thermal transfer of signal (Figure 4.3). Likewise, recuperation as a percentage of the natural appears to increase as a function of temperature beyond 220°C (increasing beyond 5%). Accordingly, 200°C was selected as the most appropriate p-IR IRSL preheat temperature to use for all further experiments of the protocol – coupled with an IRSL measurement at 50°C and the p-IR IRSL measurement at 170°C (Table 4.1). These results are in agreement with other studies (Madsen *et al.*, 2011; Reimann *et al.*, 2012, 2011; Reimann and Tsukamoto, 2012) which have demonstrated that a lower preheat temperature than that identified in the Thomsen *et al.* (2008) p-IR $IRSL_{225}$ protocol is appropriate for dating young samples.

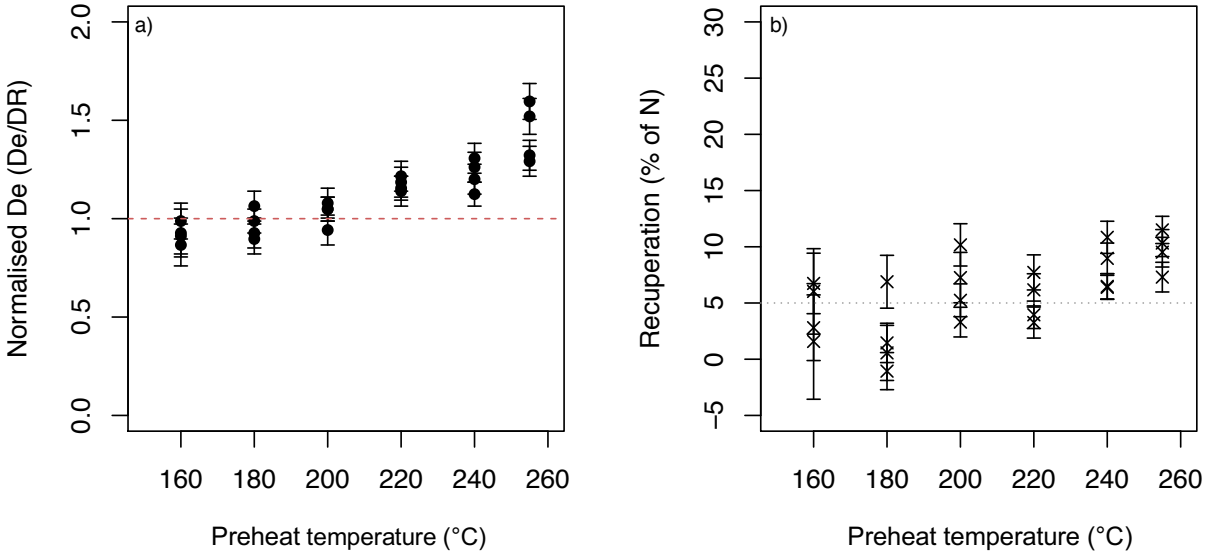


Figure 4.3 p-IR IRSL K-feldspar large aliquot dose recovery preheat plateau results. (a) Normalised D_e versus preheat temperature and (b) relationship between recuperation as % of natural signal versus preheat temperature. Red dashed line through expected D_e, grey dotted line through 5% recuperation of the Natural.

Table 4.1 A modified p-IR IRSL protocol used for equivalent dose determination of p-IR IRSL.

Step	***Treatment***	***Measured***
1	Dose (Natural, 0 Gy, 0.45 Gy, 0.85 Gy, 0.45 Gy)	-
2	Preheat (200°C for 10 s)	-
3	IRSL 100 s @ 50°C	-
4	IRSL 100 s @ 170°C	L_x
5	Test dose (6.5 Gy)	-
6	Preheat (200°C for 10 s)	-
7	IRSL 100 s @ 50°C	-
8	IRSL 100 s @ 170°C	T_x
9	IRSL 50 s @ 290°C	-

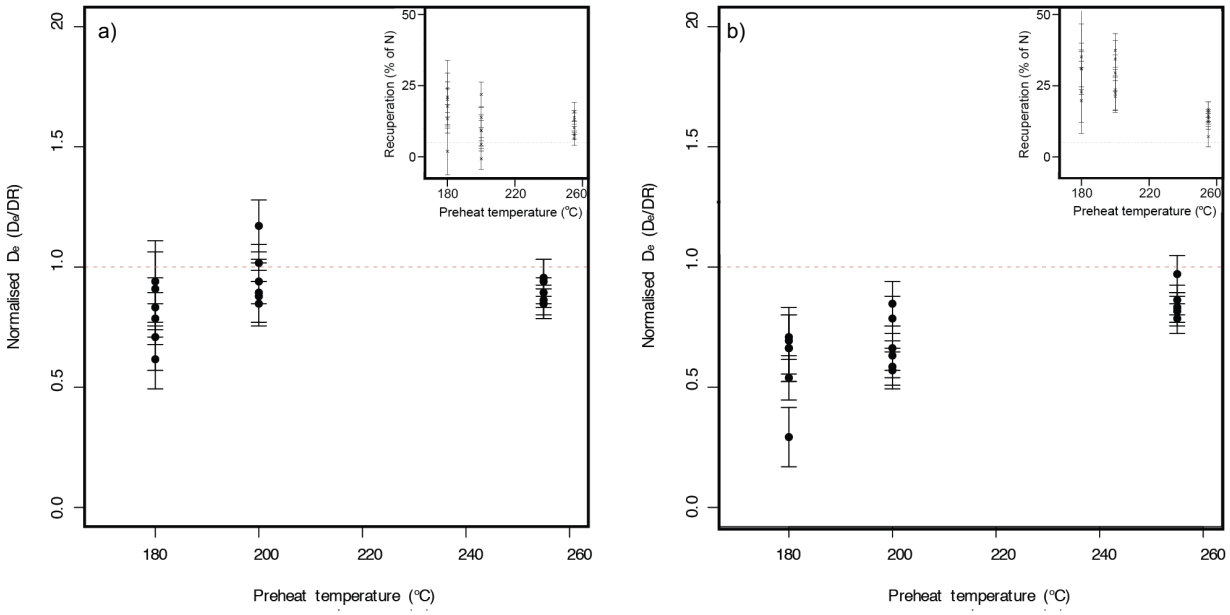


Figure 4.4 p-IR IRSL K-feldspar small aliquot dose recovery preheat plateau results. Normalised De versus preheat temperature with (a) and without (b) hot bleach (290°C) at the end of each SAR cycle. Red dashed line through expected D_e. (Inset) Respective recuperation plots as % of natural versus preheat temperature.

This result is further corroborated when D_e is measured on small aliquots (Figure 4.4). Furthermore, recuperation and dose recovery results demonstrate that a 290°C hot bleach [5] is required at the end of each SAR cycle. At all preheats tested, dose recovery results were under-estimated and higher recuperation levels identified when a hot bleach was not included following each SAR cycle (Figure 4.4b). In contrast, when the hot bleach is included, all preheat temperatures tested in the range 180-255°C agree with expected D_e within errors, with the weighted average D_e using 200°C closest to the expected D_e. Recuperation is consistently high across all preheat temperatures when a hot bleach is not included, and lowest at 200°C preheat temperature when a hot bleach is included in the measurement

[5] 'Hot bleach' treatments (stimulation at 290°C for 50 s) are included at the end of each SAR cycle to reduce the thermal transfer and thus levels of recuperation.

procedure. Results agree with large aliquot measurements, 200°C is the appropriate p-IR IRSL preheat temperature for these samples, coupled with a hot bleach at the end of each SAR cycle.

4.4 Comparing rates of anomalous fading

Anomalous fading is a key issue affecting the optical dating of some feldspar grains (Wintle, 1973), potentially resulting in an overall age underestimation of the sediment if not appropriately accounted for. To determine levels of anomalous fading, short-term fading experiments were completed for both combinations of sediments by bleaching large aliquots of sample GSL15/1/3 and subsequently providing a known irradiation. L_x/T_x measurements were taken immediately following irradiation and at various time intervals (up to 1000 hours) after irradiation.

Anomalous fading results were quantified by the g-value, which corresponds to the signal loss per decade of logarithmic normalised storage time (Aitken, 1985), as defined by Equation 4.1.

Equation 4.1

$$I = I_c \left[1 - \frac{g}{100} log_{10}\left(\frac{t}{t_c}\right)\right]$$

Where I is the intensity at time t, I_c is the intensity at time c, g is a constant (termed the g-value) and t_c is an arbitrary time.

Samples were preheated following irradiation, prior to storage following Auclair *et al.* (2003) who found that preheating prior to measurement led to an underestimation of the g-value, likely caused by thermal transfer.

Calculation of the g-value allows for luminescence ages for fading sediment samples to be corrected if the D_e lies within the linear dose response range (Auclair *et al.*, 2003; Huntley and Lamothe, 2001), which is typical of young sediments. Exploring the levels of anomalous fading present in the p-IR IRSL signal is therefore of great interest to this study since the young nature of the sediments in question would allow for any levels of anomalous fading to be potentially corrected, eliminating anomalous fading as a potentially unsolvable problem associated with IRSL dating. All g-values were calculated using the *analyse_FadingMeasurement* function (Kreutzer and Burow, 2017) in R Studio 1.0.153

Testing the stability of the luminescence record to ensure that there is minimal anomalous fading provides greater confidence in the natural luminescence signal measured. G-values for the K-feldspar p-IR $IRSL_{170}$ and quartz OSL_{130} fractions of sediment sample GSL15/1/3 are compared opposite (Table 4.2). Results show that using the preheat temperatures identified in 4.3, short-term fading does not appear to be a major problem across either protocol, with both values within uncertainties of zero. Values in the region 1.3 ± 0.3 %/decade have previously been considered as a laboratory artefact (Thiel *et al.*, 2011) and suggest minimal fading. The low values demonstrate that there is minimal short-term fading of the p-IR IRSL signal in these samples and therefore the K-feldspar fraction should not give an age underestimation if used to date these young samples.

Table 4.2 Anomalous fading g-values calculated for the K-feldspar and quartz fractions of sample GSL15/1/3.

Sample	*Mineral*	*Protocol*	*g-value (%/decade)*
GSL15/1/3	K-feldspar	p-IR $IRSL_{170}$	1.42 ± 1.97
GSL15/1/3	K-feldspar	$IRSL_{50}$	4.12 ± 2.0
GSL15/1/3	Quartz	OSL_{130}	1.54 ±2.04

4.5 Comparing the bleaching rate of quartz and feldspar

Residual bleaching tests were used to identify the residual dose in the quartz and K-feldspar grains following various periods of sunlight exposure. Identifying complicating factors such as residual doses, is imperative to determining the accuracy of the resultant natural equivalent doses, and thus in addressing the aim of identifying an appropriate measurement method for dating young samples.

Experiments were completed for both the quartz and K-feldspar fraction of sediment sample GSL15/1/3. Large aliquots were prepared of each mineral fraction and exposed to daylight conditions for various time intervals from 1 - 720 hours, before being measured for any residual luminescence signal. Small aliquot quartz OSL measurements suggest a natural D_e of 1.7 ± 0.06 Gy for sample GSL15/1/3.

Quartz results show that after all bleach times tested, all of the luminescence signal had been depleted and negative D_e's were measured (Table 4.3). In comparison, the p-IR IRSL signal of the K-feldspar fraction retained a residual dose after 1.5 and 9.5 hours, but was reduced to zero following an extended 30 days of bleaching time. Based on a dose rate of 2.852 ± 0.174 ($Gy^{ka\text{-}1}$) these results suggest that in each pulse of sediment activation and deposition, K-feldspar grains may be

retaining a residual dose upwards of c. 100 yrs; a significant over estimation when measuring young samples for age of deposition.

Table 4.3 Residual doses (Gy) for large aliquots of quartz and K-feldspar grains following various time intervals outside. Residual age is calculated based on GSL15/1/3 dose rate. [a] Time refers to total time outside (i.e. not total daylight hours) experiencing variable weather conditions during January 2016. Aliquots were placed in sample holders with a single layer of cling film used to protect aliquots from external contamination, outside on a flat windowsill facing into direct sunlight. [b] Dose rate based on natural environmental dose rate from original sample site location and mineral.

	Protocol	*Bleaching time (hours)* [a]	*Residual ± 1σ (Gy)*	*Dose rate during burial ± 1σ (Gy^{ka-1})* [b]	*Equivalent residual age ± 1σ (years)*
GSL15/1/3	OSL_{130}	1	-0.014 ± 0.018	2.232 ± 0.143	-6 ± 8
		24	-0.008 ± 0.018		-3 ± 8
		264	-0.012 ± 0.012		-5 ± 5
		720	-0.006 ± 0.015		-2 ± 6
GSL15/1/3	p-IR $IRSL_{170}$	1.5	0.276 ± 0.025	2.852 ± 0.174	97 ± 8
		9.5	0.152 ± 0.02		53 ± 7
		720	-0.000 ± 0.022		0 ± 8

4.6 Comparison of natural residual signals

To test the likelihood of sediments retaining a residual dose post-activation in the natural landscape, natural residual experiments were completed for both quartz and K-feldspar fractions of known age sediment sample BBR15/1/1. Samples were measured for their natural D_e following standard SAR OSL and p-IR IRSL protocols. Since these samples are of known modern (post-2009) age, any

luminescence signal (beyond 5-7 years) measured is indicative of a natural residual dose. A natural residual test which uses samples of a known modern age provides insight into how well individual minerals have been bleached in the natural environment, under more complex bleaching conditions, which is key to interpreting natural equivalent doses and luminescence ages.

This experiment was completed for a range of aliquot sizes: large, small and single grain analysis to identify whether any residual dose is restricted to a few isolated grains and can be excluded from the overall D_e calculation, or whether it is more commonly found amongst the crystals; identifying the optimum mode for measuring future natural luminescence signals. Comparing the natural residual found at a large aliquot, small aliquot, and a single grain scale is essential to identifying the degree of partial bleaching of sediment samples and should be used to inform the appropriate mode of measuring natural equivalent doses from other samples in the region.

Results from the natural residual test are shown for both protocols against a variety of aliquot sizes, with equivalent doses calculated following both the unlogged-Minimum Age Model (MAM-3) and unlogged-Central Age Model (CAM) age models following the recommendation of Arnold *et al.* (2009) (Table 4.4). The results are used to explore whether it is possible to identify an appropriate combination of measurement protocol, mineral and age model selection which reduces the natural residual to the expected level.

Table 4.4 Table comparing the natural residual results when tested on different minerals, protocols, aliquot size and age model. [1] Samples BBR15/1/1/5 and BBR15/1/1/10 were used for the natural residual test. Both sub-samples came from vertical sediment core BBR15/1/1 which was extracted from the near-surface sediments of a lunette dune which has formed since 2009 on the Barta Brothers Ranch. The lunette dune formed on the edge of a grassland destabilisation plot and buried a fence line that was erected in 2009 to surround the circular plot. All 50 cm of the BBR15/1/1 vertical core should theoretically be of modern age (~ 6 years old); BBR15/1/1/5 and BBR15/1/1/10 are sub-samples from 5 cm and 10 cm depth respectively. [2] Hot bleach (@ 290°C for 50 s) included at the end of each SAR cycle in the p-IR $IRSL_{170}$ protocol. [3] Ages ± 1σ (years). Moisture content 3 ± 2 % and overburden density 1.9 g/cm^3 used for all samples. [4] Single grain (180-210 μm). [5] Small aliquots at 2 mm (grain size 125-180 μm). [6] Large aliquots at 8 mm (grain size 125-180 μm).

Mineral	*Sample* [1]	*Protocol*	*Hot Bleach* [2]	*Age ± 1σ (years)* [3]					
				Single Grain [4]		*Small Aliquot* [5]		*Large Aliquot* [6]	
				MAM-3$_{UL}$	*CAM$_{UL}$*	*MAM-3$_{UL}$*	*CAM$_{UL}$*	*MAM-3$_{UL}$*	*CAM$_{UL}$*
K-Feldspar	BBR15/1/1/5 & /10	p-IR $IRSL_{170}$	Y	0 ± 33 *n = 46*	22 ± 18 *n = 46*	19 ± 12 *n = 11*	34 ± 6 *n = 11*	58 ± 5 *n = 6*	58 ± 6 *n = 6*
Quartz	BBR15/1/1/10	OSL_{130}	N	-51 *n = 7*	-51 *n = 7*	10.1 *n = 27*	**4 ± 7** *n = 27*	30 *n = 6*	29 ± 41 *n = 6*

K-feldspar results show that for both single grain and multi grain measurements, a residual dose is present and age estimates range from 0 ± 33 to 58 ± 6 years. In contrast with previously published data, the natural residual measured at a single grain and small aliquot scale in this study is smaller than previously dated modern analogue sediments. This demonstrates the potential application of p-IR IRSL optical dating of K-feldspar grains to aeolian sediments in semi-arid locations with the confidence that the residual dose will be minimal,

dropping below a 10% effect on age beyond 500 years. When measured at the single grain scale, coupled with the un-logged minimum age model, the smallest residual dose of 0 ± 34 years is achievable. However, the large uncertainty associated and the requirement for the minimum age model suggests that this is not the appropriate combination for dating these young aeolian samples. Theoretically, aeolian dune samples have been exposed to optimum conditions for bleaching, and following the criteria of Bailey and Arnold (2006) the central age model should be the most appropriate age model for samples of this description.

Quartz results show that large aliquots produced the greatest residual dose due to a bigger combined signal of grains with varying levels of bleaching and residual dose. In comparison, single grain results, coupled with the minimum or central age model both demonstrated the lowest residual dose with age estimates c. -51 years. It is likely that the very young (modern) age of the sediments means that individual luminescence decay curves are too dim to extract a sensible decay amongst the noise.

As discussed in Ballarini *et al.* (2007), the signal levels released by individual grains from young samples are much lower than in older samples, and coupled with a small percentage of grains giving rise to a D_e value (e.g. (Duller *et al.*, 2000; Duller and Murray, 2000; Jacobs *et al.*, 2013), single grain dating of young quartz sediments has many complications.

As Figure 4.5 highlights, if all grains provided the same luminescence signal, a linear line through the origin would be plotted. However, results from BBR15/1/1/10 single grain data show that over 90% of the OSL signal originates from less than 10% of the grains, suggesting the majority of grains do not contribute

to the overall luminescence signal. Likewise, the luminescence signal from aliquots of GSL15/1/3 is largely driven by less than 40% of the total number of grains.

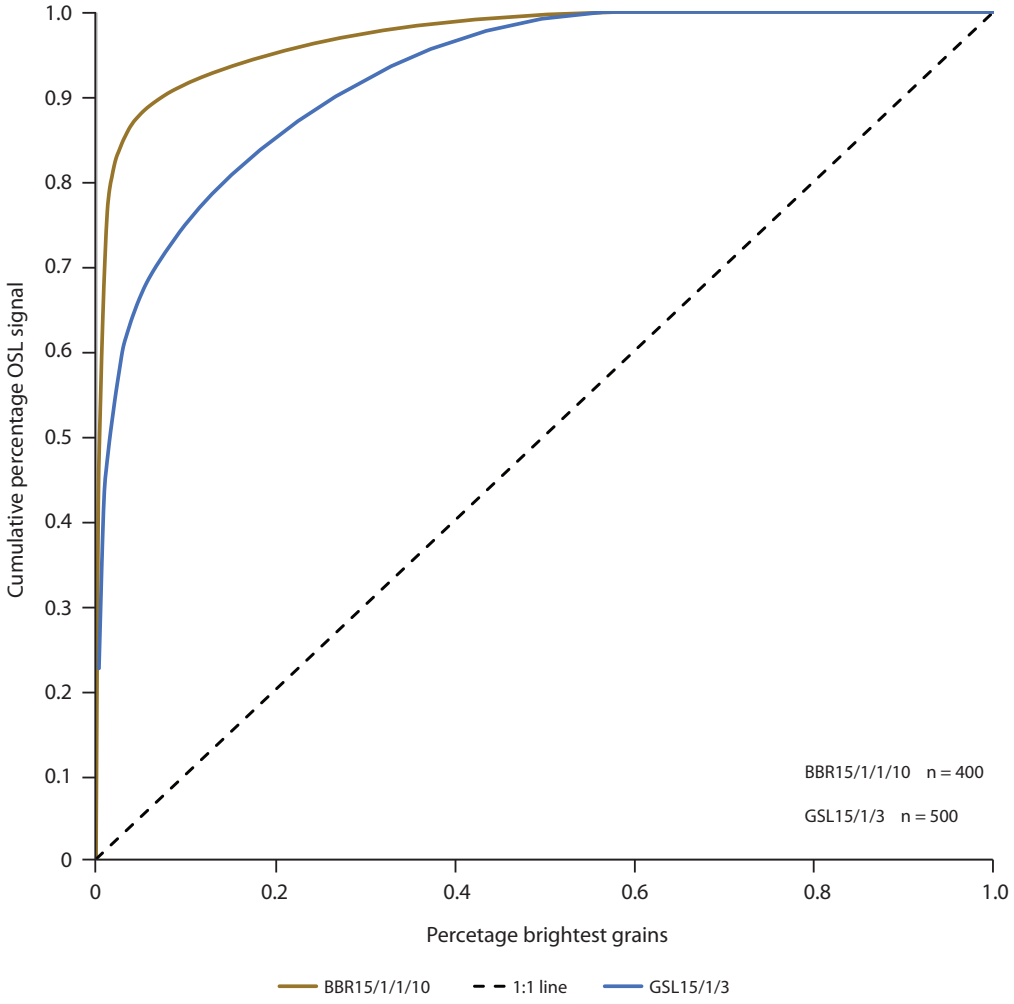


Figure 4.5 Distribution of signal intensity from single grains of four discs of sediment sample BBR15/1/1/10. The proportion of the total OSL light sum from the cumulative grains is plotted as a function of the proportion of the brightest grains. If all grains in a population had the same level of brightness, the results would plot along the 1:1 diagonal line that runs through the origin. 'n' denotes number of grains measured.

The most appropriate aliquot size and age model combination is identified as small aliquot coupled with the un-logged central age model which produced an

age estimate of 4 ± 7 years, which is in good agreement with the known age of 5-6 years of the sediments. Given the aeolian dune context of these sediments, we expect them to be well-bleached prior to deposition and thus the central age model presents the most appropriate age model for analysis.

Nevertheless, whilst the majority of sediments may be well-bleached, the near-surface nature of the samples may also experience problems associated with post-depositional mixing of the sediments (Bateman *et al.*, 2007) and partial-bleaching of aeolian deposits may occur for a couple of reasons. Firstly, aeolian deposition may occur at night when there is insufficient ambient light to reset the luminescence signal. Secondly, deposition may occur in a rapid process alongside numerous other sand grains (e.g. dust storm), preventing every grain from receiving the optimum light required to fully bleach the existing luminescence signal prior to rapid deposition and subsequent burial.

4.7 Selection of appropriate rejection criteria for young samples

Having established quartz as the optimum mineral for optically dating young sediments, the below section details the appropriate rejection criteria and analysis methods for studying young, dim quartz luminescence signals. Standard recycling ratio and IR-depletion ratio tests were applied to all luminescence datasets in this study. In addition, recuperation thresholds and $D_e(t)$-plot analysis were used to identify the most appropriate criteria for including individual aliquots in overall age model calculation.

4.7.1 Recuperation

As noted above, recuperation values associated with dating young aeolian sediments need to be treated carefully and a threshold should be applied with caution. Naturally high recuperation levels are expected when dating young sediments due to the noisy nature of the signals and the close proximity of the natural and zero dose points. Whilst an absolute recuperation value can be applied as a threshold for rejection as opposed to a relative value as % of the natural, this can only be applied if there is confidence that the natural D_e is not modern or close to the threshold set; prior knowledge of the expected age is required. Alternatively, a recuperation threshold can be applied as a % of the largest regeneration dose (King *et al.*, 2013).

A comparison of the different recuperation thresholds (Table 4.5) highlights that whilst the impact on the overall D_e of older sediments is minimal, it has a much greater influence on the overall D_e of a very young sediment age where the D_e is more than doubled when recuperation as % of natural or an absolute value is applied. As noted above these are not appropriate parameters to reject young luminescence signals and can lead to an estimated age overestimation. Whereas, the recuperation rejection when based on % of largest regeneration does not highlight any additional aliquots that needed to be rejected. Since minimal recuperation has been identified, it is not considered a key rejection criteria to apply when dating these particular samples.

Table 4.5 D_e ± error calculated according to the application of the different recuperation threshold options. Recycling ratio and IR-depletion ratio rejection criteria is applied to all four combinations, and subsequently combined with a different recuperation threshold based on % of Natural dose, absolute value (seconds), and % of largest Regeneration dose. D_e's have been calculated according to the un-logged Central Age Model with moisture content 3 ± 2 % and overburden density 1.9 g/cm^3 used for all samples. [1] Small aliquots of fully-prepared quartz grains measured. [2] Recycling ratio and IR-depletion ratio within ±10% of unity. [3] 1 s ~ c.14 years based on Gy^{ka-1} 2.32 ± 0.143, and beta source conversion 0.0647 Gy^{s-1}. [4] Largest regeneration dose ~ c.9 Gy. [5] One aliquot of GSL15/1/3 and three aliquots of BBR15/1/10 were rejected due to partial bleaching. See section 7.3 for rationale. [6] Denotes aliquots rejected in addition to those that failed the recycling ratio or IR-depletion ratio.

Sample	***Aliquots measured[1]***	***Failed recycling ratio or IR-depletion ratio[2]*** ***D_e ± error (Gy)***	***Failed recuperation as % of natural (5%)*** ***D_e ± error (Gy)***	***Failed recuperation as absolute value (1 s)[3]*** ***D_e ± error (Gy)***	***Failed recuperation as % of largest regen (5%)[4]*** ***D_e ± error (Gy)***
GSL15/1/3	48 [5]	10 aliquots 1.7 ± 0.06	6 aliquots[6] 1.65 ± 0.063	2 aliquots[6] 1.65 ± 0.059	0 aliquots[6] 1.7 ± 0.06
BBR15/1/1/10	30 [5]	0 aliquots 0.008 ± 0.01	14 aliquots 0.02 ± 0.018	7 aliquots 0.023 ± 0.013	0 aliquots 0.008 ± 0.01

4.7.2 Identifying partial bleaching and dominant slow components using $D_e(t)$ plots

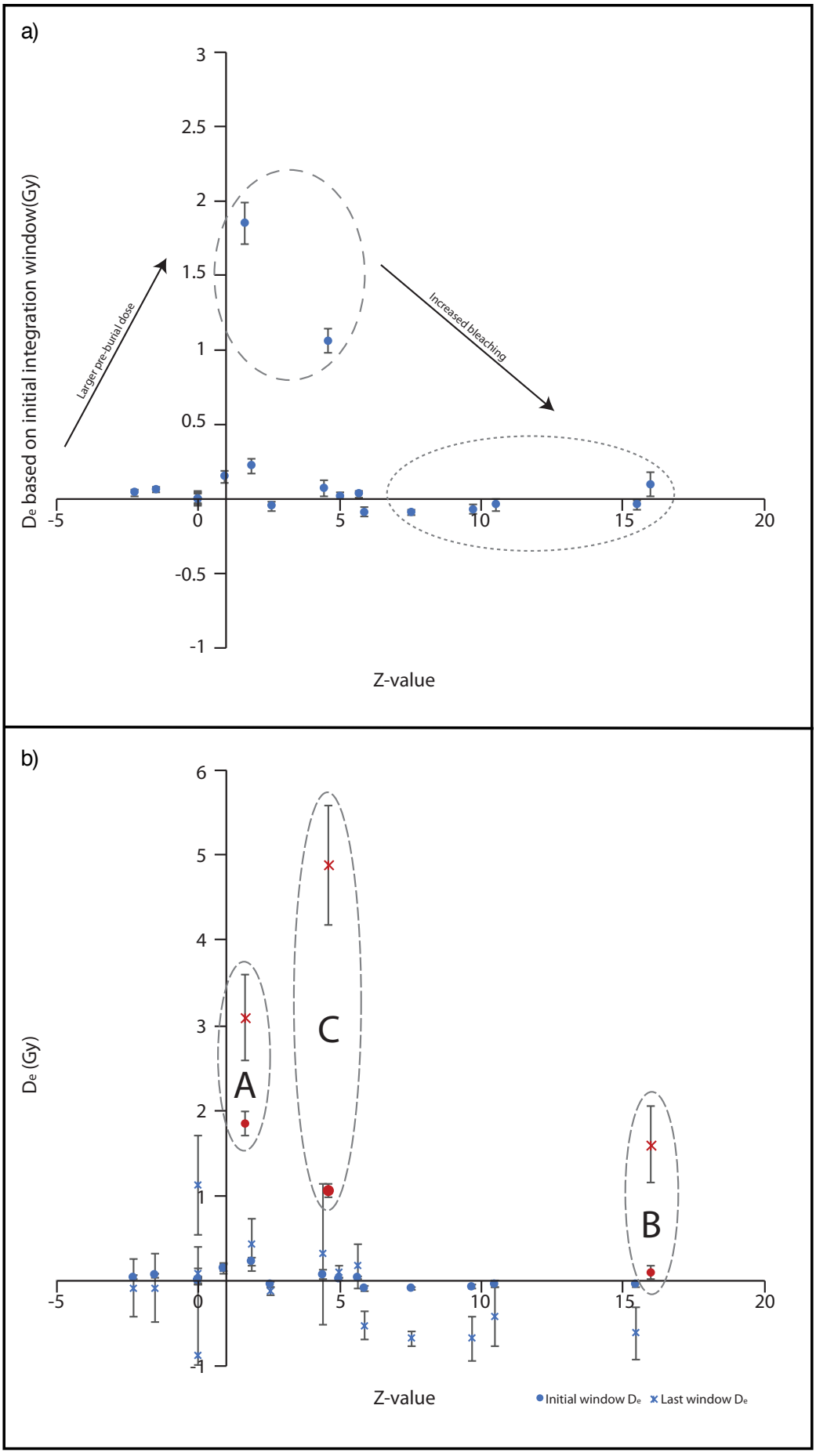
A series of $D_e(t)$-plots were used to identify aliquots which demonstrated partially-bleached signals and would contribute to an overall age overestimation. If all components of the luminescence signal were reset prior to deposition, movement of the signal interval along the decay curve would result in a flat $D_e(t)$-plot. In the case of partial bleaching, the slower bleached components retain a

larger residual signal and the $D_e(t)$-plot would appear to rise as the signal is integrated further along the decay curve (Bailey *et al.*, 2003).

Individual aliquot results from sediment sample BBR15/1/1/10 highlights that three aliquots (referred to as 'A', 'B','C') which demonstrate markedly larger D_e's than the remaining discs are also those which display a rising $D_e(t)$-plot and Z-values [6] > 1 (Figure 4.6). By replacing the natural dose with a regeneration dose point, is it possible to test whether or not this rising $D_e(t)$-plot is truly driven by partial bleaching, or a dominant slow component given the very young nature and low luminescence signal found within these sediments.

Figure 4.6 *(opposite)* (a) Z-value vs. D_e (based on initial integration window) plot based on $D_e(t)$-plots of Bailey (2003). Dashed line: aliquots inside dashed line circle represent partially-bleached signals that contain a greater proportion of the pre-burial dose. Dotted line: aliquots inside the dotted line circle represent those with large Z-values, but low D_e values. (b) Z-value vs. D_e (based on initial window) and D_e (based on final integration window). Aliquots with typically high Z-values are shown to have over-lapping initial and final D_e values. The large uncertainties associated with these aliquots is driven by the noisy dim signal and thus requires further analysis than > 1 Z-value to qualify as partially bleached. Likewise, some aliquots with high Z-values are artificially driven by negative final D_e values and equally are not partially bleached despite Z-value > 1. Three aliquots highlighted in red ('A', 'B', 'C') depict those which show Z-values which suggest partial bleaching – initial and final D_e values do not overlap, Z-values > 1, and all D_e's > 0. Whilst displaying high Z-values, the D_e's at various integration intervals are within errors and therefore the > 1 z-values have not been analysed further.

[6] Z-value refers to the ratio of the De from the final integral to that of the first channel. See Bailey (2003) for further explanation on the calculation of Z-values and $D_e(t)$ plots.

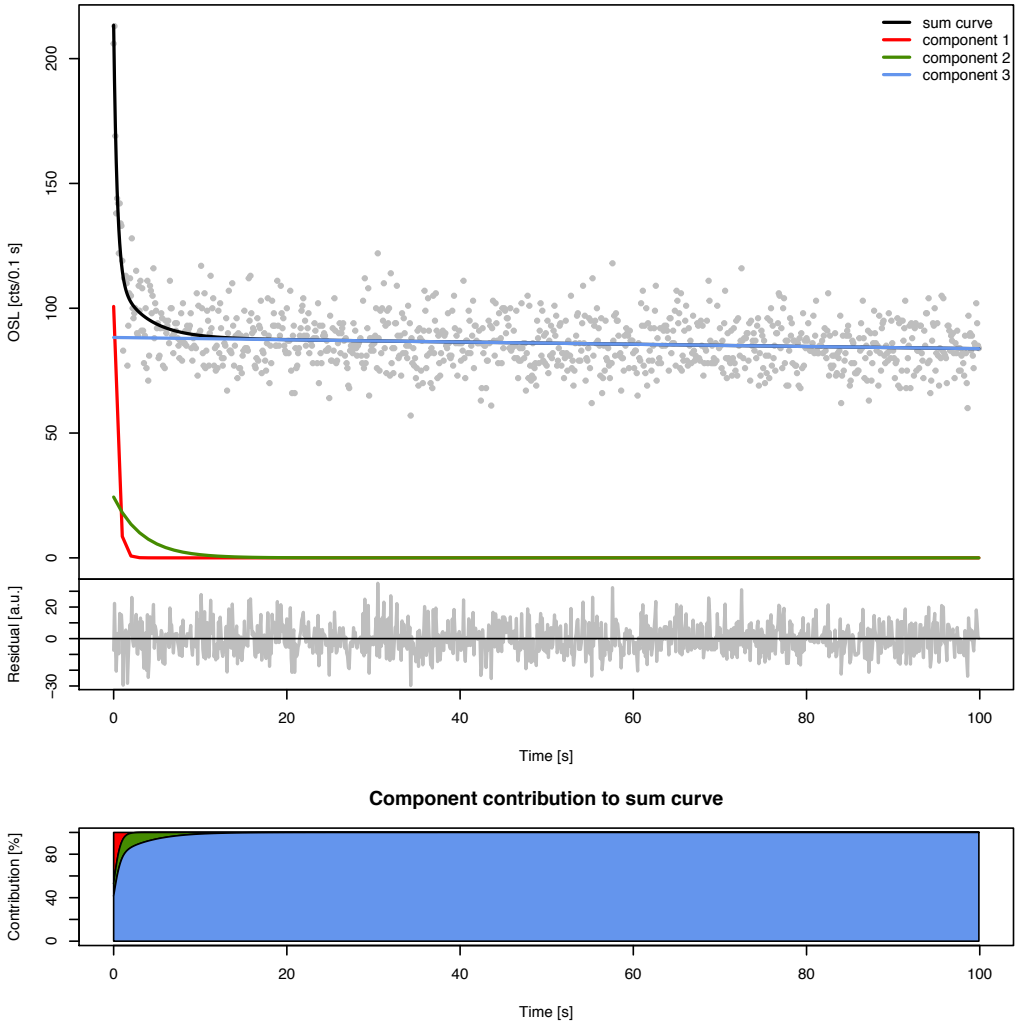

a)
De based on initial integration window(Gy)
Larger pre-burial dose
Increased bleaching
Z-value
b)
De (Gy)
A
C
B
Z-value
Initial window De
Last window De

Results show that replacing the natural with a regeneration dose point and calculating the corresponding Z-values highlights that aliquots 'B' and 'C' were partially bleached since their Z-values for a regeneration dose point (which we know to be fully bleached under controlled conditions) is < 1 (Table 4.6). It is likely that these aliquots contain a couple of quartz grains that were not well-bleached in the reactivation event (potential partial-bleaching explanations are explored in 4.6). However, aliquot 'A' continues to demonstrate a rising $D_e(t)$-plot despite being bleached within the SAR cycle prior to further irradiation and measurement.

Table 4.6 Z-values associated with three aliquots for both the natural luminescence signal and a regeneration dose point. Z-values for aliquots 'B' and 'C' are < 1 when replaced with the regeneration dose point, suggesting the natural luminescence signal was partially bleached.

Aliquot	***Z-value (Natural)***	***Z-value (Regen point)***
A	1.67	1.3
B	16	0.42
C	4.60	0.77

Through component fitting of the regenerative dose luminescence decay curve for aliquot 'A', the contribution of each of the individual components of the OSL decay curve can be calculated. Figure 4.7 highlights that the slow and medium components of the signal are contributing to almost 60% of the total luminescence signal in the first instance, and rapidly rise to 100% of the overall signal within 2 s of measurement time.



Time (seconds)	Individual component contribution (% of total OSL)		
	Fast	Medium	Slow
0	47	11	41
0.1	41	12	46
0.2	36	13	51
0.3	30	14	56
0.4	25	15	60
…			
1.8	1	14	85
1.9	1	13	86
2.0	1	13	86

Figure 4.7 Luminescence decay curve and component fit of regeneration dose point aliquot 'A'. Three components identified: fast, medium, slow with individual component contributions as % of the total OSL signal listed vs. Time (seconds). Component fitting completed using the fit_CWCurve function of the 'Luminescence' package in R Studio (Kreutzer, 2017).

The reason for the rise in $D_e(t)$ remain unclear, but may be associated with incorrect background subtraction (e.g. if there is significant decay of the slow component in the time prior to background measurement). As a conservative measure, we reject all aliquots that display this signal feature, to reduce the likelihood of 'false-positives'. Aliquots which display these characteristics should either be rejected since they will lead to a significant age overestimation of young samples, or individual fast components need to be extracted from the overall luminescence decay and D_e's calculated accordingly for that individual component. Previous curve fitting experiments (e.g. Jain *et al.*, 2003; Tsukamoto *et al.*, 2003) have demonstrated that the fast component shows less recuperation due to thermal transfer when preheating than the slow and medium components; another reason why luminescence signals with a strong fast component should be selected, especially for young samples with a comparatively small D_e. In this study, aliquots with dominant slow components were rejected since it was a problem isolated to only a few individual aliquots. Where these characteristics dominate, individual components would need to be analysed for all aliquots and D_e's should be calculated according to the fast component.

4.8 Conclusions

In this study, sediments extracted from a modern lunette dune of known age provided reliable test case for identifying the most suitable measurement and analysis combinations for dating young aeolian dune sediments. Given the young nature of the sediments, identifying the most rapidly bleached signal is imperative to ensure low residual doses and a more accurate chronology is produced. Whilst

K-feldspar rich samples produce brighter luminescence signals to their quartz equivalents, improving the signal to noise ratio, and reducing the uncertainties associated with D_e measurement, the natural residual doses appear from this study to be too large to date young samples.

Whilst p-IR IRSL protocols have increased the suitability of K-feldspar optical dating to a range of luminescence research projects, identifying and stimulating deeper electron traps which exhibit reduced levels of anomalous fading, the requirement for much longer bleaching periods to reduce residual doses complicates the accuracy when dating young sediments in a dynamic environment. Results are in agreement with those reported by Buylaert *et al.* (2012) which show that the p-IR IRSL signal bleaches more slowly than that from quartz when exposed to sunlight, increasing the likelihood and size of a residual dose; reducing the applicability of this protocol to young aeolian sediments.

Single-grain results when coupled with the un-logged minimum age model suggested that a modern age can be extracted from modern sediment samples, yet does not support the conclusion that dune sands are well-bleached, and therefore amenable to processing using the CAM. Nevertheless, at the higher age range where dating accuracy is less constrained by a residual dose, p-IR IRSL methods have the scope to produce accurate luminescence ages with reduced levels of fading than IRSL equivalents.

Quartz measurements produce D_e values in line with the expected age based on historical data. Within the age range of < 200a, quartz minerals coupled with a moderate preheat remain the optimum choice for optical dating, as far as we can

tell, due to fast bleaching rates and the importance of 0 residual doses at this age range.

Additionally, we find a revised set of rejection criteria is useful for accurately identifying aliquots / grains for reliable age estimation. Problems of incomplete bleaching or slow component dominance of the occasional grain have highlighted the importance of selecting the most appropriate aliquot size for measurement and rejection criteria, analysis and age-model selection post-measurement.

Investigations into aliquot sizes show that without a widespread issue with partial bleaching in these sediments, single-grain analysis is not needed for D_e calculation and small aliquots have an advantage of producing greater signal sizes. When markedly larger D_e's are identified within individual aliquots, $D_e(t)$-plots and component-fitting analysis can be used to identify the most well-bleached aliquots and those which have a dominant fast component.

Chapter 5

PAPER 2

Paper 2 Prelude

The results from Paper 1 show that it is possible to date young aeolian sediments using OSL techniques and provided us with the optimum measurement conditions that should be applied to these sediments to produce reliable chronologies of near-surface deposition in the Nebraskan sediment cores. The ideal combination included selecting only the quartz crystals from the 125-180 μm size fraction, coupled with a 200°C preheat and 130°C measurement temperature following standard SAR protocol and a specific set of rejection criteria that consider the young nature of the burial ages and isolate the most appropriate aliquots. Having established the OSL method for dating young sediments, it was then a question of how best to deploy the dating resource to reconstruct chronologies of deposition? More specifically, how should the vertical sediment cores be sub-sampled and dated to ensure they retained a high-temporal resolution whilst completing a wide spatial coverage within the time limits of this research project? Paper 2 demonstrates the application of wide field-sampling coupled with coarse luminescence measurements and Changepoint analysis to identify a new tool which provides us with chronological depositional structure in seemingly lithologically homogenous profiles, allowing us to focus our full-preparation luminescence dating efforts.

Identifying chronostratigraphic breaks in aeolian sediment profiles using near-surface luminescence dating and changepoint analysis

Paper 2: Buckland, C. E., Bailey, R. M., Thomas, D. S. G.
Status: Published in *Quaternary Geochronology* (46) p.45-58.

Abstract

Optical dating of depositional profiles provides information on environmental change and dune reactivation in aeolian systems. However, identifying the optimum locations and samples for luminescence dating is often confounded by a lack of visible internal structures and a highly discontinuous and heterogeneous record. We use a method that combines high-resolution coarse luminescence signals with statistical changepoint analysis to identify significant chronostratigraphic breaks. The changepoint algorithm demonstrates an ability to identify changes in a depositional profile with depth, allowing luminescence dating to be better-focused on specific points of chronological change. Likewise, this method ensures that chronostratigraphical breaks in the record are not missed due to coarse sampling strategies. This method is applied to a dataset from near-surface dune profiles from the Nebraska Sandhills, testing whether fully-prepped SAR luminescence ages from an identified chronostratigraphic section are representative of the wider unit identified in the changepoint analysis. Unlike previous methods, this therefore ensures that resultant chronologies are a factor of true chronological breaks as opposed to aliasing (i.e. misidentification of a signal) and capture the heterogeneous record across the dynamic environment.

5.1 Introduction

Depositional records in aeolian systems provide information on environmental change over Quaternary timescales. Robust high-resolution chronologies of depositional events are a fundamental part of reconstructing past aeolian systems dynamics and testing geomorphological hypotheses. Optically stimulated luminescence (OSL) dating techniques provide an excellent method of dating depositional records and reconstructing environmental history, providing time-series of deposition and activation events in an environment relatively starved of alternative proxies (Thomas and Burrough, 2012).

However, identifying appropriate locations for OSL sampling is difficult for two main reasons. First, selecting the most appropriate locations to extract sediment samples is often hampered by high levels of "environmental noise" in aeolian sedimentary systems. Aeolian systems can have spatially inconsistent records due to localised variability in the processes that induce accumulation and erosion (Leighton et al., 2014b; Munyikwa, 2005; Stone and Thomas, 2008; Telfer et al., 2017, 2010; Telfer and Thomas, 2007; Thomas and Burrough, 2013) including wind energy (Fryberger, 1979), sediment moisture content, vegetation cover (Wolfe and Nickling, 1993) and sediment availability (Kocurek and Lancaster, 1999). Thus, aeolian records are inherently discontinuous and this can be problematic when, for example, attempting to establish the history of dune accumulation and its relationship to climatic and environmental changes; a problem often compounded by a sampling strategy relying upon relatively few samples (Stone and Thomas, 2008; Telfer *et al.*, 2010). Individual chronological profiles from a feature reflect the localised response to a suite of disturbances (Leighton *et al.*, 2014b), and are

not necessarily representative of the wider landscape (or landform) response. Bailey and Thomas (2014) explore this with a quantitative model in which a series of 'filters' demonstrate how information on past forcing conditions is progressively lost from the stratigraphic record and a discontinuous sequence is produced. With a range of disturbance factors occurring at a series of spatial scales, sampling strategies which seek to understand aeolian geomorphological development need a method which averages out the environmental noise and identifies a true landscape response which captures the structure of the depositional profile whilst acknowledging the incomplete nature of the record (Thomas and Bailey, 2017). An accurate interpretation of aeolian geomorphological features (e.g. dune records) requires an improved understanding of how the luminescence ages relate to the sediments that have been preserved within the feature (Chase, 2009; Lomax et al., 2011; Munyikwa, 2005; Stone and Thomas, 2008; Thomas, 2013). Choosing the exact point at which to sample a chosen landscape or landform to build a profile of the landscape response, however, is a complex process.

Second, while lithostratigraphy and sedimentary structures can sometimes provide information in the field to guide sampling strategy (e.g. Atkinson *et al.*, 2011; Fitzsimmons and Telfer, 2008; Fitzsimmons *et al.*, 2007), visible structures are widely absent, and even if present, sampling strategies (e.g. vertical drilling) can make them invisible. In these contexts, it is not possible to visually identify optimal places to sample for dating. As Leighton *et al.* (2013) discuss, if the internal structure and bounding surfaces of dunes are not visible, the resultant chronology is at risk of being determined by sampling resolution as opposed to depositional structure within the feature. Hence, there is a need to ascertain a method which can identify

chronostratigraphical breaks in the record which were perhaps not long enough to allow the development of other boundaries (e.g. pedogenesis). A homogenous section may have accumulated gradually over time, or in an individual depositional event; yet it may also be the result of a series of short-lived sporadic and pulsed depositional events. Where distinctive lithological variations are not visible, the development of a high-resolution chronology is key to identifying the distinctive breaks in the record and assessing how the climatostratigraphy compares with the chronostratigraphy in the absence of lithostratigraphy (Leighton *et al.*, 2014b; Stevens *et al.*, 2006).

Sampling at only two points within a profile and extrapolating the age-depth relationship might be suitable in locations where a linear relationship exists between accumulation and depth and the site has experienced quasi-continuous deposition over time (Figure 5.1a). However, in aeolian systems we would not expect to find quasi-continuous accumulation; a pulsed depositional profile is far more likely for two reasons. Firstly, aeolian system sedimentary profiles are constructed because a series of accumulation and erosion events create discontinuous deposited profiles (Bailey and Thomas, 2014; Bateman *et al.*, 2017; Singhvi and Porat, 2008; Stone and Thomas, 2008; Telfer and Thomas, 2007). Secondly, the process of deposition is discontinuous in aeolian systems (i.e. at seconds, inter-seasonal, inter-annual, and timescales up to inter-millennial), and where there is a lack of visible stratigraphic or sedimentological variability, sampling will likely miss locations where chronostratigraphic breaks occur; losing an understanding of the overall depositional structure due to under-sampling. Understanding the depositional structure of the sedimentary profile is the key to

deciphering potential hiatuses in the accumulation record, but also in highlighting sections where post-depositional erosion may have impacted on the preserved record (Hughes, 2010).

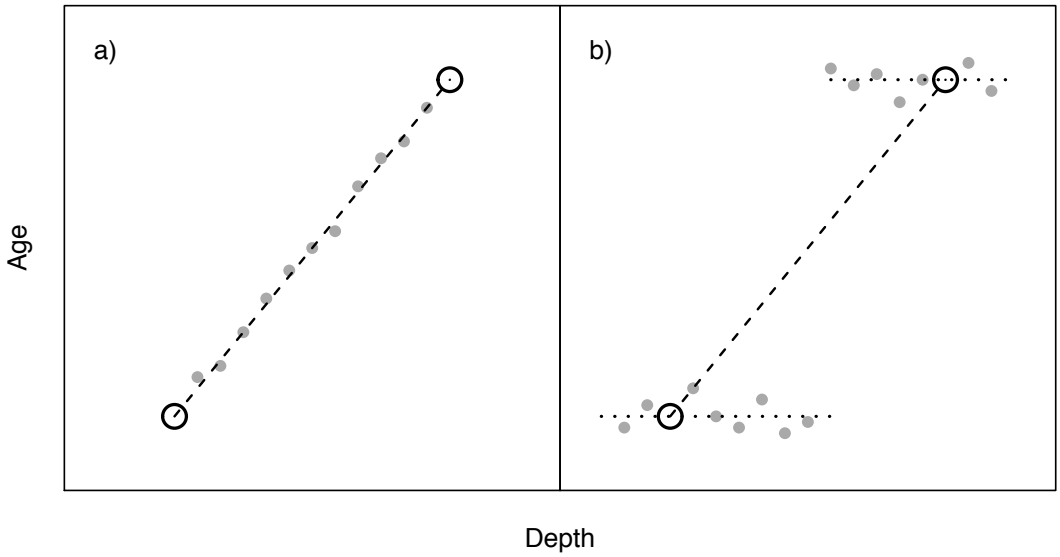


Figure 5.1 A representation of the assumptions made about depositional structure when sedimentary sections are under-sampled. (a) Sedimentary profile that has accumulated gradually over time in a quasi-continuous manner. (b) Sedimentary profile that has accumulated in pulsed events over time. Sampling at only two locations and inferring a linear relationship can mask the true structure and complexity of the underlying profile.

To capture the depositional variability of aeolian systems, several sediment samples (taken both vertically and horizontally) are needed for dating. In a system with significant levels of environmental noise, the only means to capture the complete signal is to increase sample numbers until a pattern can be identified amongst the noise. However, dating numerous sediments at a high-resolution is often not within the time and cost requirements of an individual project, and may prove futile if all the sediments in one feature are of the same age (i.e. within overlapping age errors). Equally, determining a threshold number of samples to

extract is hard to define and equally variable between sites depending on the sedimentary characteristics and the research question being investigated. Therefore, a means of rapidly scanning the sedimentary section to understand the depositional structure prior to focusing full-preparation dating efforts is needed.

In settings where stratigraphical information is absent, portable luminescence readers and partial-preparation techniques have the potential to provide a rapid guide to sampling strategy. Portable luminescence readers have made some progress in devising a method for rapid relative age testing (e.g. Bateman *et al.*, 2015; Stone *et al.*, 2015; Sanderson and Murphy, 2010). However, portable luminescence studies are limited in the scale of sub-sampling resolution that they can provide across a feature and it is still necessary to select the points at which to measure the signal. Considering this, whilst providing a rapid age estimate, the interpretation of sediment accumulation records may be prone to aliasing; a function of the sample selection as opposed to genuine chronostratigraphic breaks in the sequence. Furthermore, portable luminescence measurements are not sensitivity-corrected and are thus susceptible to changes in sensitivity. For example, the luminescence variability reported between samples measured using a portable luminescence reader could be dependent on the volume of sediment which is being measured or the sensitivity of sediment to OSL, potentially masking subtle changes in the chronology of the sediments across a sequence.

Alternatively, many existing studies have produced rapid assessments of equivalent dose (D_e) and estimated ages using a variety of partial-preparation techniques (e.g. Leighton and Bailey, 2015; Durcan *et al.*, 2010; Roberts *et al.*, 2009) to eliminate additional steps in age estimate production. Nevertheless,

applying partial-preparation techniques to a collection of samples still requires initial decision-making over which samples to measure. In addition, whilst not as lengthy as full-preparation procedures, completing partial-preparation and range-finder methods for numerous samples at a high-resolution is often outside the time capacity and resourcing of most research projects. Standardised Growth Curves (SGCs) have also been used to reduce the time required to produce age estimates (Munyikwa and Brown, 2014; Roberts and Duller, 2004; Telfer *et al.*, 2008; Yang *et al.*, 2011). However, whilst reducing the time spent producing age estimates, the method does not provide any additional insight into the depositional structure of the sediments or highlight the optimal locations to deploy focus full-preparation dating to extract maximum chronological information. In the absence of a method which allows us to produce rapid luminescence results at a high-resolution, a landscape response will be subject to high levels of environmental noise.

As part of a wider investigation into the recent aeolian dynamics of the Nebraska Sandhills, a high-resolution chronology of activity was required to allow deposition events to be determined. This paper presents a method for the rapid testing of relative age variability to inform sample selection for full luminescence dating; an approach that focuses on intensive sampling of the depositional environment in the field and then subsequent rapid analysis to establish which samples best capture break points in accumulation. The premise is that it is necessary to allocate luminescence dating efforts, expensive in both time and money, as effectively as possible. This research presents an attempt to identify the specific sampling locations where the environmental and chronological

information gained is of greatest value and best represents the history of accumulation and erosion.

This study uses L_x/T_x measurements (i.e. sensitivity-corrected natural luminescence signals) of un-prepared samples coupled with a statistical method (changepoint analysis) which identifies breaks in L_x/T_x-depth data to identify the depositional structure of near-surface sediments across a range of sand dunes and blowouts in the Nebraska Sandhills. L_x/T_x data is used to control for the effects of variation in aliquot mass and sample luminescence sensitivity (to dose) through the core. The noisy nature of a high-resolution bulk signal luminescence dataset requires a subsequent decision to be made about the structure of the depositional profile. This decision can be made qualitatively, identifying structures within the luminescence profile visually; however, this paper presents an algorithmic method through a statistical model. Using this approach, high-resolution age profiles are created which are used to identify step-changes in the record which can subsequently be used to focus full-preparation dating. Mid-point sub-samples from identified changepoint sections are dated using full-preparation methods and tested against fully-prepared ages from the corresponding sections to test the suitability of the method. In doing so, this paper aims to develop a method which can: improve stratigraphical understanding of aeolian features; identify optimum samples for luminescence dating; capture an environmental signal amongst noise; and determine if subtle variability in very young sediments can be identified at high-resolutions, guiding subsequent full-preparation and Single Aliquot Regenerative (SAR) (Murray and Wintle, 2000) dating methods on specific depths. Can subtle changes in chronostratigraphy be used to guide suitable sampling strategies in

locations devoid of lithostratigraphic and micromorphological variation? This study represents the first application of statistical changepoint analysis to luminescence datasets, and tests whether it is a viable tool to identify the depositional structure of visibly homogenous aeolian sediments using coarse L_x/T_x results. Near-surface aeolian dune sediments from the Nebraska Sandhills fulfilled the required criteria for this analysis. With the knowledge that these sediments have likely reactivated at a series of scales in the recent past, their visibly homogenous nature means that they are suitable sediments for the testing of this method.

5.2 Methods

5.2.1 Study site

The Nebraska Sandhills represent the largest dunefield in the Western Hemisphere (Ahlbrandt and Fryberger, 1980; Loope and Swinehart, 2000) and are currently stabilised by extensive prairie grassland. Existing research, as summarised in Halfen & Johnson (2013), has identified multiple Holocene reactivations using OSL dating throughout the Great Plains at 9.6-6.5ka, 3.8ka, 2.5ka (Miao *et al.*, 2007), with the most recent regional-scale period spanning the Medieval Climatic Anomaly (MCA) 1050-650 years BP (Forman *et al.*, 2005; Goble *et al.*, 2004; Loope and Swinehart, 2000; Mason *et al.*, 2004; Schmeisser McKean *et al.*, 2014; Schmeisser *et al.*, 2010; Stokes and Swinehart, 1997). Several less severe droughts have occurred after the MCA, such as during the 1930s Dust Bowl, that have caused increased areas of bare sand movement, but not complete reactivation as seen in the major droughts identified over the Holocene (Forman *et al.*, 2005). Evidence

from both the recent and more distant past has shown that aeolian activity has occurred repeatedly during the last 10,000 years at a variety of spatial scales.

5.2.2 Field sampling

A series of vertical sediment cores of approximately 50 cm depth were extracted from the upper surface sediments from dune and blowout features at two sites within the Nebraska Sandhills (Figure 5.2a): 1) The Gudmundsen Sandhills Laboratory (42.07575°N, 101.38680°W) and 2) – The Niobrara Valley Preserve and surrounding ranches (42.73719°N, 100.09194°W). Samples were extracted across transects which stretched across the topographic profile (i.e. from the crest / backwall of dunes, down the slopes and into the basin / interdune) of dune and blowout features with the aim of capturing sites of erosion and deposition within the local environment (Figure 5.2b & c). Vertical cores were extracted in situ by hammering 50 cm long light-tight tubes vertically into upper sedimentary sections, and transported to the Oxford Luminescence Dating laboratory for analysis (Table 5.1). The quartz-rich dune sediments (Muhs, 2004) comprised of visually homogeneous aeolian material with a lack of stratigraphical boundaries and relatively consistent dose rates.

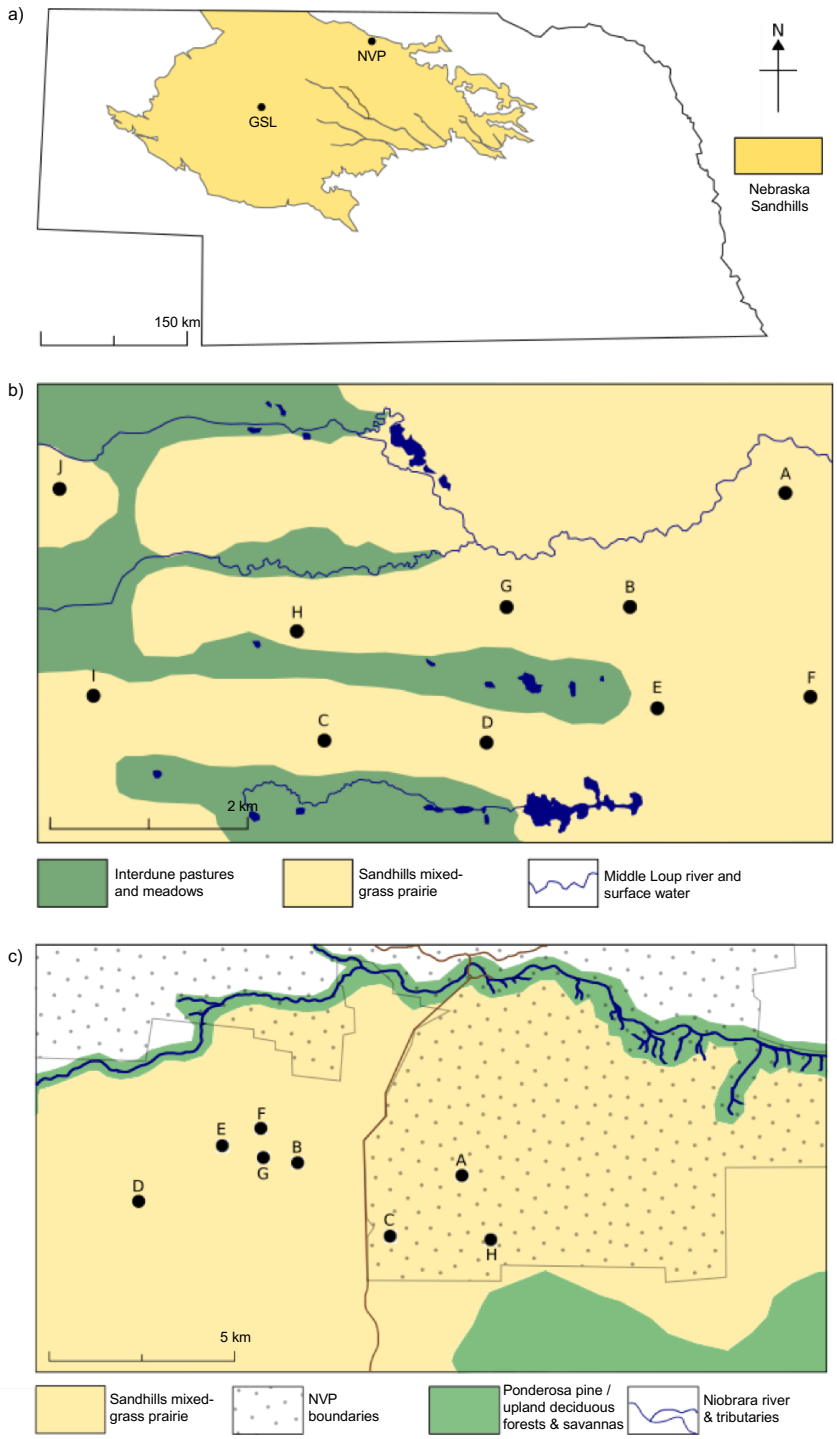


Figure 5.2 (a) Location map of the Niobrara Valley Preserve and Gudmundsen Sandhills Laboratory within the Nebraska Sandhills. (b) Map of the Gudmundsen Sandhills Laboratory showing sites where vertical sediment cores were extracted. 41 sediment cores extracted across the sites (A-J). A: GSL15/1/1, B: GSL15/2 (8 cores), C: GSL16/1 (4 cores), D: GSL16/2 (4 cores), E: GSL16/3 (4 cores), F: GSL16/4 (4 cores), G: GSL16/5 (4 cores), H: GSL16/6 (4 cores), I: GSL16/7 (4 cores), J: GSL16/8

(4 cores). (c) Map of Niobrara Valley Preserve and surrounding ranches showing sites where vertical sediment cores were extracted. 25 sediment cores were extracted across the sites (A-H). A: NVP15/1/1 & NVP15/3/1, B: NVP15/4/1, C: NVP16/1 (4 cores), D: NVP16/2 (4 cores), E: NVP16/3 (4 cores), F: NVP16/4 (4 cores), G: NVP16/5 (4 cores), H: NVP16/6 (2 cores). NB: NVP Site references (A-H) are not the same in this paper as they are in the wider thesis. Core references (i.e. NVP16/X/X are comparable). See Figure 5.7a for an example of sampling transects and 5.7b for image of visually homogenous sediment during core extraction.

Table 5.1 Sediment cores specifically referred to in this paper. Table details geomorphic setting, depth, latitude, longitude and elevation of the extracted cores. Site reference on Figure 5.2 is denoted in brackets for each vertical sediment core.

Core	Geom. setting	Depth (m)	Latitude	Longitude	Elevation (m a.s.l)
NVP15/1/1 (A)	Crest	0 - 0.5	42.73510˚	-100.03734˚	768
NVP15/3/1 (A)	Basin	0 - 0.5	42.73491˚	-100.03781˚	757
NVP15/4/1 (B)	Crest	0 - 0.5	42.73719˚	-100.09194˚	761
NVP16/2/2 (D)	Lower ridge	0 - 0.5	42.72723˚	-100.14481˚	782
NVP16/2/3 (D)	Slope	0 - 0.5	42.72713˚	-100.14458˚	781
NVP16/4/1 (F)	Crest	0 - 0.5	42.74444˚	-100.10461˚	768
NVP16/4/2 (F)	Slope	0 - 0.5	42.74437˚	-100.10448˚	764
NVP16/4/3 (F)	Basin	0 - 0.5	42.74415˚	-100.10422˚	759
NVP16/4/4 (F)	Slope	0 - 0.5	42.74380˚	-100.10403˚	751
NVP16/5/1 (G)	Crest	0 - 0.5	42.71943˚	-100.02847˚	763
NVP16/5/2 (G)	Slope	0 - 0.5	42.71943˚	-100.02880˚	762
GSL15/1/1 (A)	Blowout back wall	0 - 0.5	42.08627˚	-101.36721˚	1078
GSL16/1/3 (C)	Depression	0 - 0.5	42.06317˚	-101.42488˚	1113
GSL15/2/4 (B)	Crest	0 - 0.5	42.07575˚	-101.38680˚	1109
GSL16/2/4 (D)	Slope	0 - 0.5	42.06240˚	-101.40483˚	1079
GSL16/3/2 (E)	Depression	0 - 0.5	42.06588˚	-101.38376˚	1074
GSL16/4/3 (F)	Depression	0 - 0.5	42.06719˚	-101.36451˚	1066
GSL16/5/1 (G)	Crest	0 - 0.5	42.0755˚	-101.40309˚	1099
GSL16/5/3 (G)	Depression	0 - 0.5	42.07536˚	-101.40255˚	1093
GSL16/5/4 (G)	Gully	0 - 0.5	42.07515˚	-101.40218˚	1085
GSL16/7/1 (I)	Crest	0 - 0.5	42.06775˚	-101.45338˚	1140

Sediment cores were opened and prepared under subdued orange light at the Oxford Luminescence Dating laboratory. Tubes were split lengthwise to allow sub-sampling of sediments at the centimetre scale, producing up to fifty sub-samples per core. Sub-samples were left untreated and dried in the oven prior to luminescence measurement. One large aliquot (8 mm diameter) per sub-sample was prepared on aluminium discs. Subsequent methods and measurements were applied to each sub-sampled unit unless otherwise stated.

5.2.3 Particle size variability

Particle size measurements were determined for a selection of sediment profiles, with sub-sample grain size data measured using a Malvern Mastersizer 3000 and analysed using GRADISTAT software version 8.0 (Blott and Pye, 2001). Sediment cores which appeared homogenous both visibly and in terms of particle size analysis were selected as appropriate test materials for this study.

5.2.4 L_x/T_x measurements on bulk samples

Measurements of L_x/T_x were made on individual aliquots, from samples spaced every 1 cm along each 50 cm core to provide a relative guide of luminescence variability with depth. Bulk signal OSL measurements were made using Risø TL/DA 15 readers, detecting using a 7.5 mm Hoya U-340 filter. Single aliquot OSL blue luminescence measurements were conducted using 470 nm stimulation at 130˚C for 100 s with a convex quartz lens placed in front of the photomultiplier tube for both the natural luminescence measurement (L_x) and the test dose measurement (T_x). A test dose of 6.5 Gy was used to standardise the natural

bulk luminescence measurements along the depth of the individual sediment cores. Following a series of dose recovery and preheat plateau tests using fully-prepared samples (see Appendix F), a preheat of 200˚C for 10 s was used prior to both the natural luminescence (L_x) and test dose luminescence (T_x) measurements at 130˚C for 100 s.

5.2.5 Changepoint analysis

Whilst a qualitative visual assessment of structural breaks within the L_x/T_x depositional profile could be used to identify distinct points of change along a sediment core, an algorithmic approach is more suitable in this instance given the noisy nature of the dataset. All changepoint analysis was completed using the Changepoint package (Killick and Eckley, 2014) in R Studio. The Changepoint analysis package identifies the location of breakpoints within the profile of each sediment core based on the variation in mean L_x/T_x measurements with depth. The pruned exact linear time (PELT) algorithm (Killick *et al.*, 2012) was used, providing an exact segmentation unlike alternative methods (e.g. binary segmentation and segment neighbourhood algorithms) which represent a trade-off in speed and accuracy. Changepoint analysis requires the dataset to be in integer form; all L_x/T_x values were multiplied by 1,000 and rounded for this part of the analysis.

Within the changepoint analysis function, the user is required to enter a penalty value which determines the sensitivity of the model to changes within the dataset. Using a combination of the diagnostic plot and the argument that theoretically L_x/T_x should increase with depth, the model was repeated for each of the different penalty values identified in the CROPS (Changepoints for a Range of

Penalties) option of the model. The final model per profile was selected as the output with the highest sensitivity to variability that continues to make stratigraphical sense. i.e. the number of changepoints within the dataset will increase until the model produces an output that suggests there are age reversals within the sedimentary core.

Identifying the optimum penalty value in this way ensures that both type 1 and type 2 errors (a type 1 error is the incorrect rejection of a true null hypothesis, while a type 2 error is incorrectly accepting a false null hypothesis) have been considered within the final model selection. Individual occasionally high and low L_x/T_x values that lie beyond the general range of the surrounding data points may have been influenced by a single K-feldspar or very sensitive quartz grain. Given the intrinsic variability expected within a prepared sample, as well as the aggregation of all grain sizes in this study, variability which is beyond intrinsic scatter, but is not indicative of a change in the depositional age, is expected. Consequently, the model is adjusted to not be too sensitive to individual changes and avoid each data point being identified as a distinctive break within the sequence. Equally, a very large penalty value that reduces the sensitivity of the model and fails to detect any changepoints within the series is not appropriate. A method to objectively identify the depositional structure of the sedimentary profile to subsequently allow focus on dating samples from a range of different age groupings is needed. Therefore, selecting the penalty value which produces a changepoint model which accommodates noise and variability anticipated within

the dataset, whilst also making stratigraphical sense, is chosen to inform subsequent dating of the sediments (Figure 5.3).

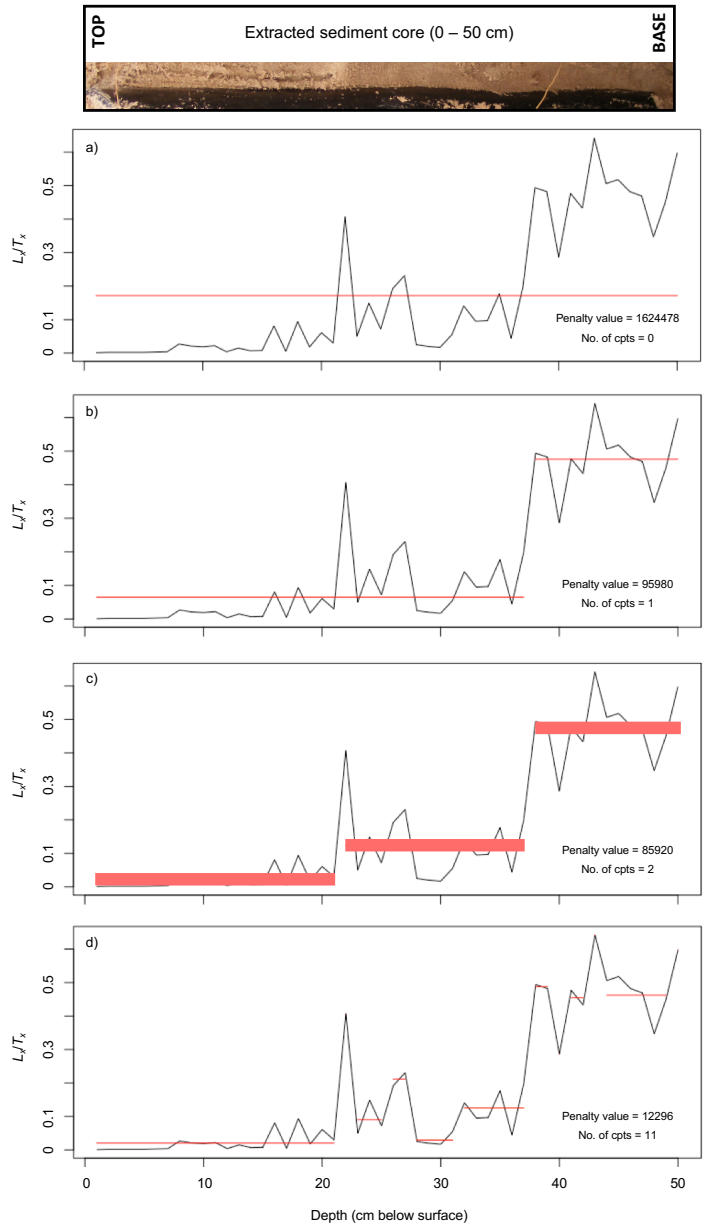


Figure 5.3 (a-d) Changepoint model outputs for sediment core NVP16/4/3 based on different levels of model sensitivity. (a) is an example where penalty value was set high and no changepoints were detected in the data sequence. Whereas in (d) the penalty value is very low and the model is overly sensitive to every change within the dataset. Based on the law of superposition, the sediments are expected to get older with depth and therefore reject the overly sensitive models which assume age reversals. Model output (c) has been selected as the most appropriate output for this example.

5.2.6 SAR luminescence measurements

Based on the results from the changepoint analysis, mid-point sub-samples from each of the identified changepoint sections were selected for full-preparation and SAR protocol (Wintle and Murray, 2006) luminescence measurement on prepared quartz. To test the validity of mid-point sub-samples in representing the general age of the wider changepoint sections, mid-point sub-sample ages were compared against a variety of fully-prepared SAR measurements from other sub-samples within corresponding changepoint sections. Whilst multiple age estimates from the same changepoint section may increase the chronological resolution of the profile, they may not be required if the mid-point sub-sample proves to be representative of the identified section.

Samples were treated in an excess of HCl and H_2O_2 to remove carbonates and organics prior to wet-sieving to the appropriate size fraction (125-180 μm) and a 60 minute etch in 40% HF. A minimum of 16 small aliquots per sub-sample were measured following the SAR protocol (Wintle and Murray, 2006) with preheats (PH1 & PH2 – 200°C for 10s) determined following a series of preheat plateau and dose recovery tests. Single aliquot OSL blue luminescence measurements were conducted using 470 nm stimulation at 130˚C for 100 s with a convex quartz lens placed in front of the photomultiplier tube. Recycling ratio tests and an IR-depletion ratio point were included to monitor sensitivity and identify any feldspar contamination (Duller, 2003). No significant recuperation was recorded along the length of the SAR cycle. Given the young nature of the sediments in this study, dose response curves were fitted against a linear function and individual equivalent dose estimates were calculated using interpolation of the natural signal onto this line.

Uncertainties were calculated following 1,000 Monte Carlo fits of the line and propagated with a 2.5% measurement error. Sample equivalent doses were calculated using the un-logged Central Age Model (CAM) (Galbraith *et al.*, 1999).

5.2.7 Dose rate calculation

Environmental dose rates were used to calculate age estimates for fully-prepared samples, and were determined by radionuclide (^{232}Th, ^{238}U and ^{40}K) concentrations measured using ICP-MS and calculated using the Dose Rate and Age Calculator (Durcan *et al.*, 2015). Annual dose rates were calculated using standard conversion factors (Adamiec and Aitken, 1998) and adjusted for grain size (Mejdahl, 1979), HF-etching (Bell, 1979), beta attenuation and water content (Aitken, 1985). Cosmic dose rate was calculated following Prescott and Hutton (1994). Beta attenuation was corrected for using Guérin *et al.* (2011). Following the method described in Nelson and Rittenour (2015), soil moisture content values were estimated using grain size characteristics, the van Genutchen (1980) water retention equation and Rosetta Lite v.1.1 software within the Hydrus-1D modelling program (Simunek *et al.*, 2008). In situ moisture content values in semi-arid environments are unlikely to be representative of mean soil moisture conditions over the burial period of the sediment; so, an alternative modelling approach is used here.

5.2.8 Maximising signal potential

Given the young nature of the sediments being analysed, the luminescence measurements are characteristically dim with low OSL counts (typically < 200 counts in the first second). To maximise the signal size of these sediments a convex quartz lens was used to improve signal collection efficiency, and the impact of increasing photomultiplier tube (PMT) voltage was explored to improve the signal to noise ratio.

Using the same aliquots, a known dose was administered to the sub-sample and measured with and without the convex quartz lens at 130˚C following a 10 s 200˚C preheat (Figure 5.4). A convex quartz lens acts to focus the signal and therefore can increase the number of counts recorded in the photomultiplier tube. Measurements on eight samples showed that the inclusion of the convex quartz lens doubled the signal size of the aliquot (mean net signal ratio of 2.04) and reduced the size of the relative standard error associated with the luminescence signal by c.30%. Based on these results, the convex quartz lens was used in all luminescence measurements in this paper to improve signal-to-noise ratio and thus reduce uncertainties.

OSL counts over a 10 s integrated time window were measured five times and averaged with and without the calibration LED on at voltages between 600-1500 volts. The signal to noise ratio based on the average values suggests 1200 V as the optimum voltage for measurement conditions (Figure 5.5). Beyond 1200 V the signal-to-noise ratio decreases due to increased background OSL counts. 1200 V was used for all luminescence measurements made during this study.

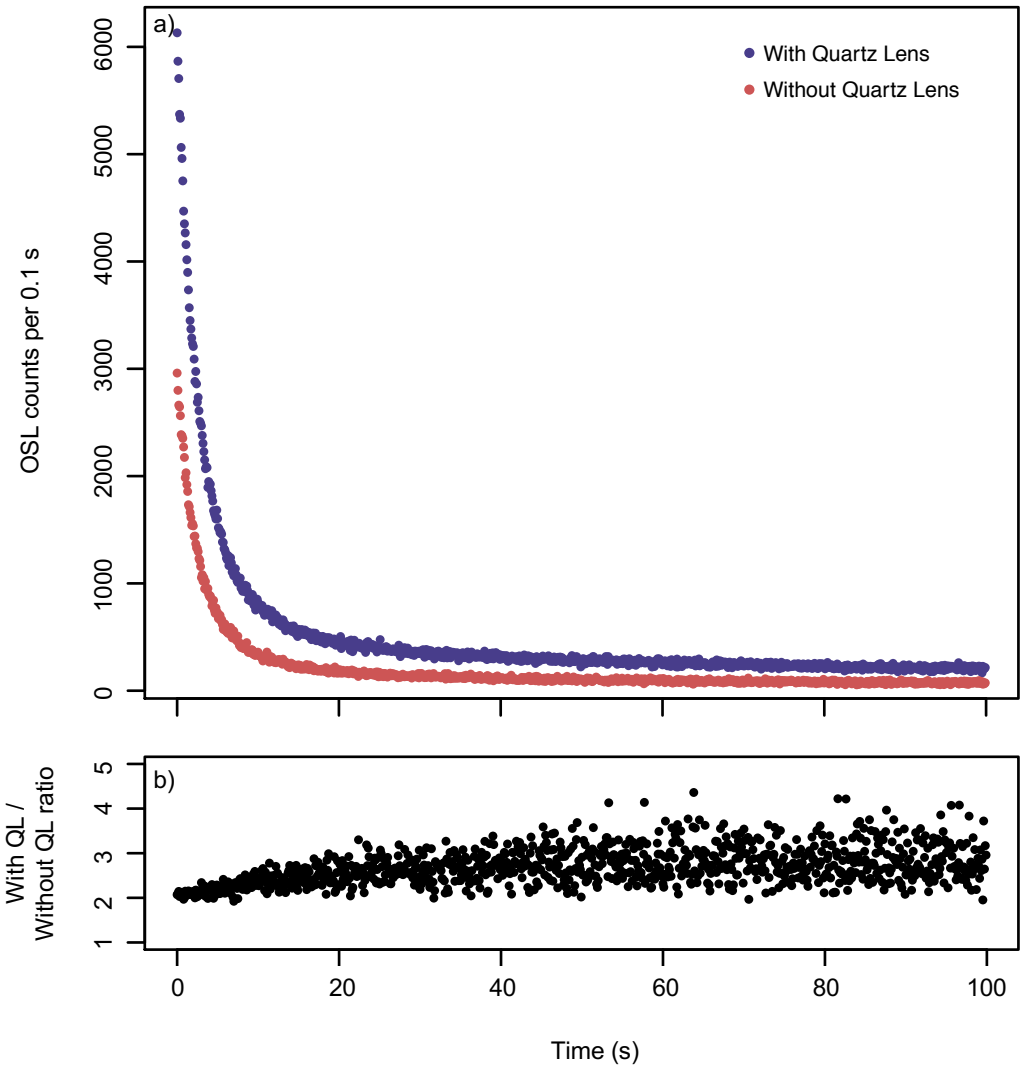


Figure 5.4 (a) OSL depletion curve of NVP15/4/1/21 with and without a convex quartz lens placed in front of the photomultiplier tube. (b) Ratio of 'with quartz convex quartz lens' to 'without convex quartz lens' signal size per channel of measurement.

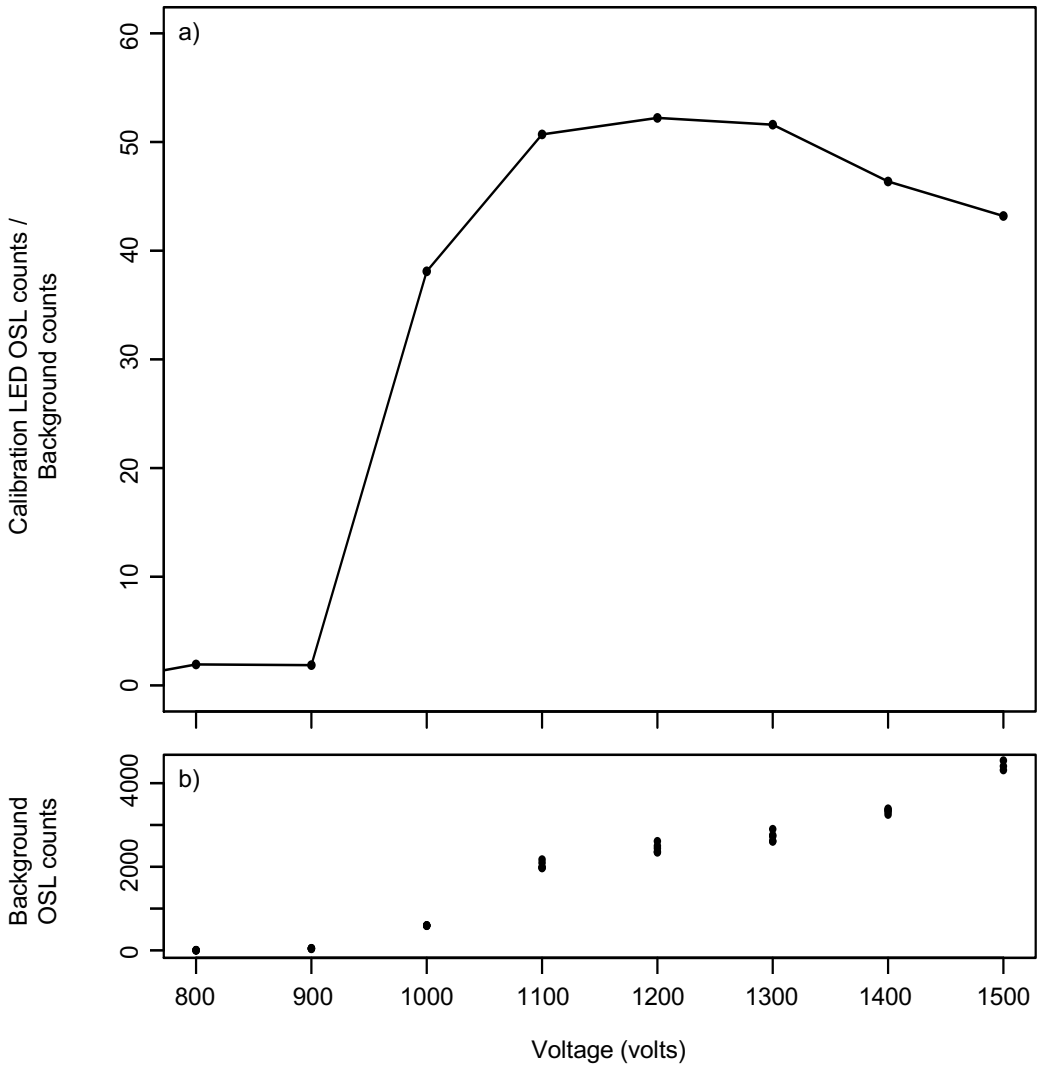


Figure 5.5 a) Calibration LED OSL counts / Background OSL counts vs. Voltage. Ratio plateaus from 1100-1200 V onwards. b) Background OSL counts vs. Voltage. Background OSL counts increase as a function of voltage.

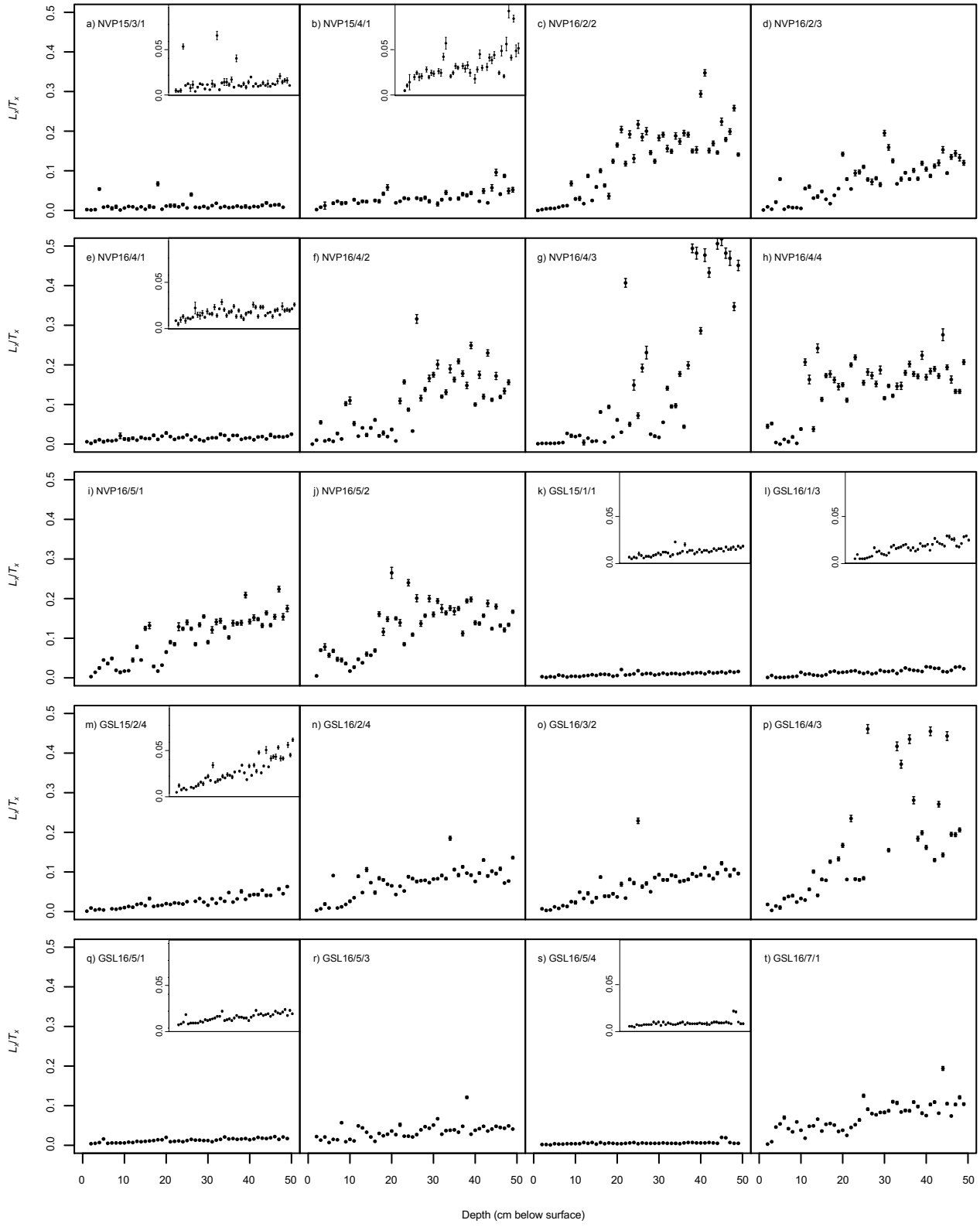
5.3 Results

5.3.1 L_x/T_x profiles using bulk sample sediment

L_x/T_x data shown in Figure 5.6 demonstrate that L_x/T_x tends to increase with depth across all sediment cores analysed in this study. Further to this, the L_x/T_x profiles demonstrate the noisy nature of the bulk luminescence measurement dataset, and hence a method is needed to objectively identify changepoints within the record. As discussed earlier, the depositional structure of aeolian system profiles varies depending on the history of localised erosion and deposition that has occurred at that specific site. The results from this research demonstrate the high variability in the depositional structures that can be found between sediment cores taken from similar features within an individual site. Whilst all profiles show a general increase in L_x/T_x with depth, they equally show large amounts of inter-sub-sample variability which appear to increase as a function of increasing L_x/T_x – suggesting multiplicative errors.

Figure 5.6 (*opposite*) (a-j) L_x/T_x vs. Depth (cm below surface) profiles of un-prepared sediment samples from ten cores taken at the Niobrara Valley Preserve site. (k-t) L_x/T_x vs. Depth (cm below surface) profiles of un-prepared sediment samples from ten cores taken at the Gudmundsen Sandhills Laboratory site. All sub-figures show noisy L_x/T_x datasets which consistently increase with depth. Fig 6 (e), (k), (l), (m) and (q) show examples of profiles with L_x/T_x values gradually increasing, suggesting these sediments have accumulated linearly over the period covered in the sediment core. Contrastingly, (n) & (t) appear to show more distinct populations of sediments which might suggest a depositional profile which has accumulated through pulsed depositional events, or which has been post-depositionally eroded over time. (c), (g) & (p) are good examples of the range of ages that have been found within the shallow 50 cm cores, showing distinct populations of sediment which

get older with depth. See Table 5.1 for GPS co-ordinates for individual cores.



5.3.2 Changepoint analysis on L_x/T_x profiles

L_x/T_x profiles from sediment cores taken across individual features have also been analysed to identify the utility of this method in detecting local relative variability in luminescence age across a feature (Figure 5.7). For example, there is clear variation in the L_x/T_x profiles across the sampling transect at site NVP16/4. Low and relatively homogenous values dominate the L_x/T_x profile at the crestal site (NVP16/4/1); little variability is detectable at this scale and across the 50 cm section. The slope sites (NVP16/4/2 and NVP16/4/4) both show similar L_x/T_x vs Depth profiles with L_x/T_x values < 0.2 dominating the shallower depths, whilst deeper sub-samples are characterised by higher L_x/T_x values and increased inter-aliquot variability. Finally, the basin of the dune profile (NVP16/4/3) shows the greatest range in L_x/T_x values across the length of the sediment core.

Figure 5.7 (*opposite*) (a) Transect NVP16/4 and the location of the four sediment cores extracted (Site F on Figure 5.2 Niobrara Valley Preserve map ~ Site D in main research project). Satellite imagery courtesy of © 2017 Google Earth Pro, Landsat / Copernicus. (b) Example of vertical sediment core in situ. (c) Side profile of transect NVP16/4 across blowout feature formed against the fence line of a historic homestead site near to the Niobrara Valley Preserve. (d-g) L_x/T_x vs. Depth profiles for sediment cores NVP16/4/1, NVP16/4/2, NVP16/4/3 and NVP16/4/4 (crest, slope, basin, slope) across transect with changepoint outputs. Changepoints identified as breaks in the horizontal red lines. (d) Changepoint output plot for sediment core NVP16/4/1 identified two distinct changes in the means of the samples at 8 and 44 cm. (e) Changepoint output plot for sediment core NVP16/4/2 one distinct change in the means of the samples at 25 cm. (f) Changepoint output plot for sediment core NVP16/4/3 identified two distinct changes in the means of the samples at 21 cm and 37 cm. (g) Changepoint output plot for sediment core NVP16/4/4 taken from the slope of the blowout feature identified one distinct change in the means of the samples at 10 cm. L_x/T_x values were multiplied by 1000 for changepoint analysis.

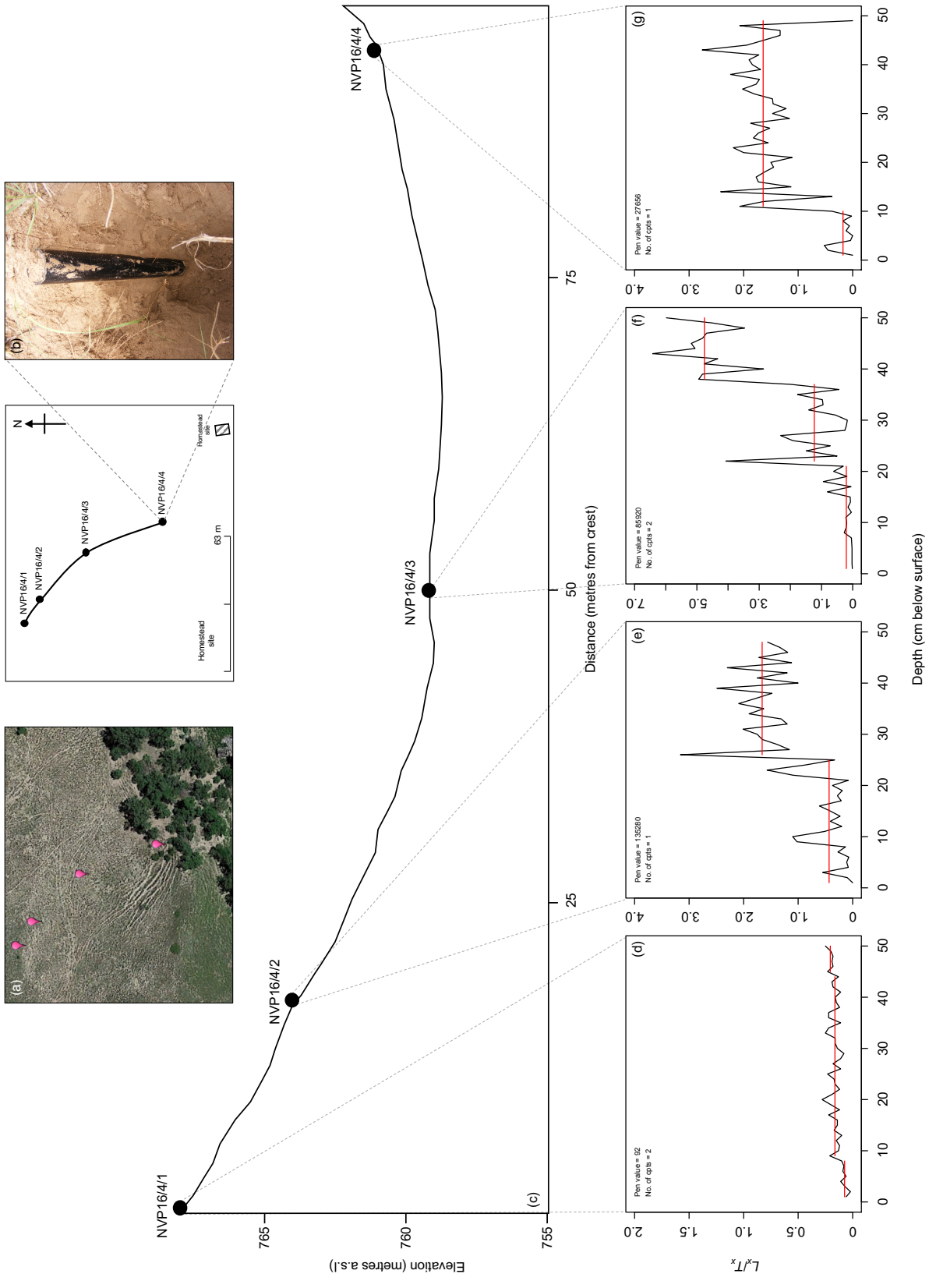

(a)
(b)
(c)
(d)
(e)
(f)
(g)
N
NVP16/4/1
NVP16/4/2
NVP16/4/3
NVP16/4/4
Homestead site
63 m
Elevation (metres a.s.l)
765
760
755
Distance (metres from crest)
25
50
75
L_x/T_x
0
0.5
1.0
1.5
2.0
Pen value = 92
No. of cpts = 2
Pen value = 135280
No. of cpts = 1
Pen value = 85920
No. of cpts = 2
Pen value = 27656
No. of cpts = 1
Depth (cm below surface)
0
10
20
30
40
50

Figure 5.7 displays the results of changepoint analysis when applied to the four sedimentary cores taken across the NVP16/4 transect near Niobrara Valley Preserve. Coupling L_x/T_x profiles with changepoint analysis allows us to identify statistically significant shifts in the mean of the L_x/T_x measurements with depth.

The variability found between aliquots within a single changepoint section (Population B) was not statistically different to the variability identified between multiple measurements from the same depth (48 aliquots of 14 cm depth were measured – Population A) (Figure 5.8). This demonstrates that where 10-50 cm has been identified by the changepoint model as one distinct section, this section has the same variability as found between 48 discs at 14 cm depth. The variability found between repeat measurements of the same depth is the same as that between depths down core that exhibit the same age.

Results of the original bulk measurements and changepoint output are compared against repeat L_x/T_x measurements across a selection of sediment cores in Figure 5.9. Whilst demonstrating an equally noisy response, the general trend and order of magnitude of the L_x/T_x measurements is the same between original and repeat measurements. Repeat measurements of the L_x/T_x vs Depth profiles show that similar results can be replicated despite the un-prepared nature of the sediments and the bulk signal measured. The output from the changepoint models show that there is some variability in the location of the break points identified between the original and repeat runs for the three cores tested, suggesting mid-point locations of the changepoint sections are more reproducible.

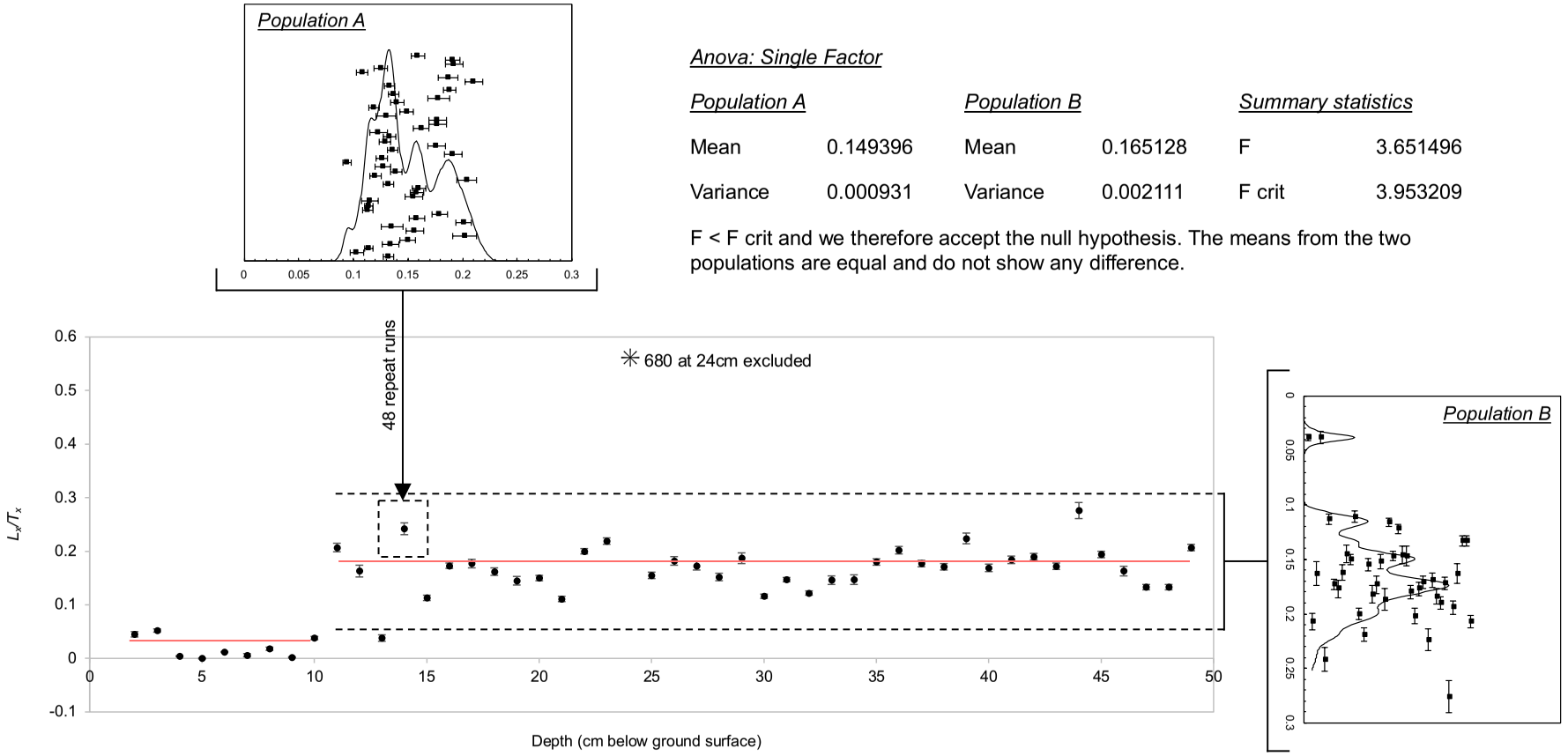


Figure 5.8 Plot showing L_x/T_x vs. Depth for sediment core NVP16/4/4. Changepoint analysis identified two distinct sections within the profile split at 10 cm depth. Population A shows the repeat L_x/T_x measurements for 48 aliquots of NVP16/4/4/14. Population B shows the distribution of L_x/T_x measurements for the aliquots measured from 13-49cm down core. ANOVA single factor analysis shows that there is no significant difference between Populations A and B.

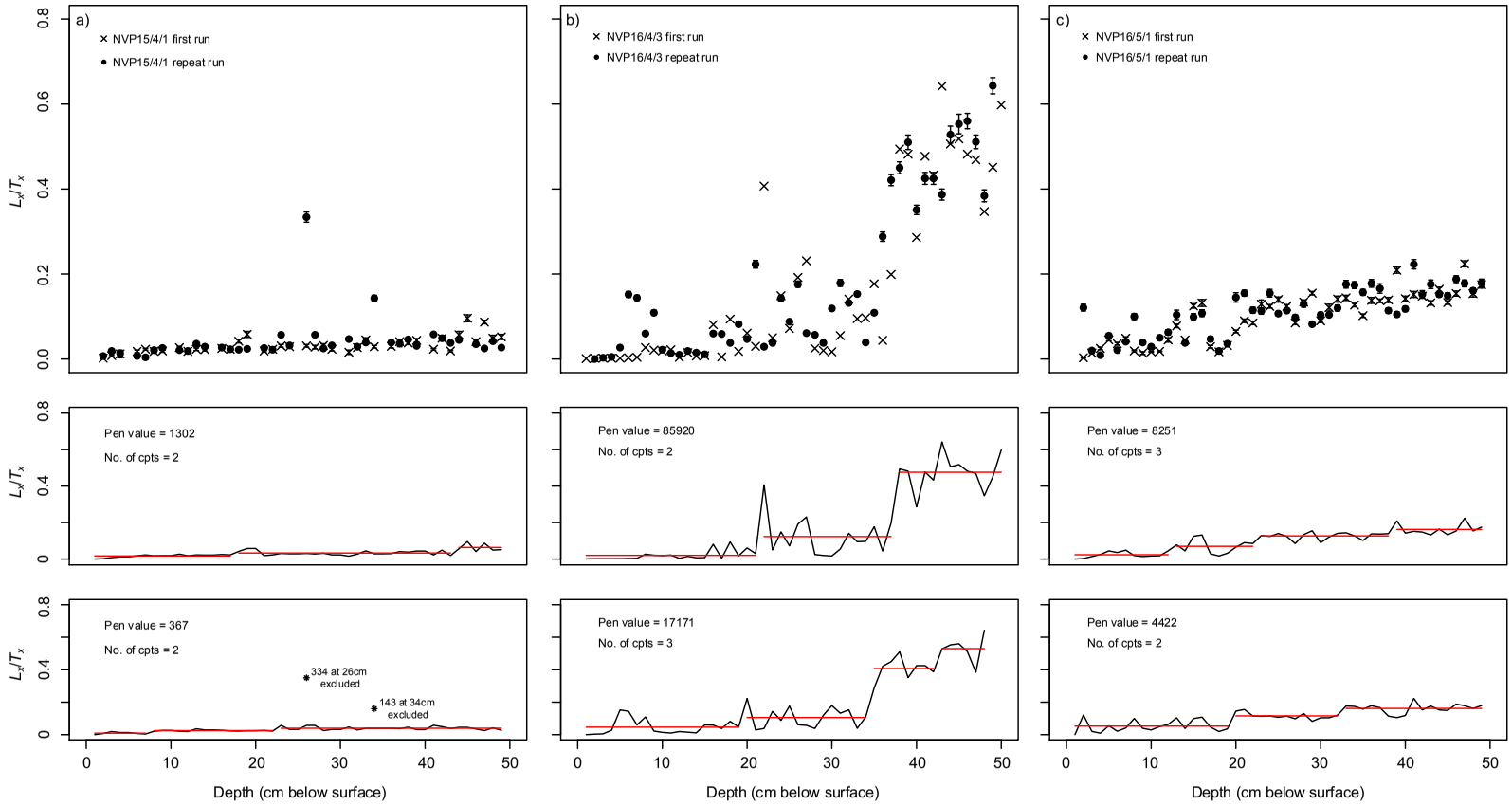


Figure 5.9 Original (crosses) and repeat runs (filled circles) of L_x/T_x vs. Depth profiles coupled with Changepoint analysis of each run. (a) Original and repeat analysis of sediment core NVP15/4/1 – changepoints identified at 17 and 43 cm in original analysis and 7 and 22 cm in repeat measurements. (b) Original and repeat analysis of sediment core NVP16/4/3 – changepoints identified at 21 and 37 cm in original analysis and 19, 34 and 42 cm in repeat measurements. (c) Original and repeat analysis of sediment core NVP16/5/1 – changepoints identified at 12, 23 and 38 cm in original analysis and 19 and 32 cm in repeat measurements. Breaks in the red lines represent changepoints in the sample means identified.

5.3.3 Age-depth profile estimates

Results testing whether mid-point age estimates using the SAR protocol are representative of the suggested changepoint sections are shown in Figure 5.10. Fully-prepared SAR ages for the mid-point sub-sample of each identified changepoint section were compared against age estimates produced for sub-samples at every 5-10 cm for three sediment cores (Table 5.2). Mid-point sub-samples were selected as the most appropriate sub-samples to select for full-preparation dating as the location of the mid-point is reproducible in repeat measurements. Contrastingly, as noted in Figure 5.9 the exact location of the individual changepoints within the profile often varies between repeat runs due to noise, highlighting the risk in opting for an end-point to represent the wider section. Results show that luminescence ages from the same changepoint section are congruent (within errors); mid-point ages are broadly representative of the wider section. Likewise, fully prepared SAR ages are found to be indistinguishable to the mid-point age calculated, and different from the adjacent changepoint sections in sediment cores with multiple changepoints (Figure 5.10c). Individual dose rates have been calculated using ICP-MS radionuclide measurements for each SAR age estimate.

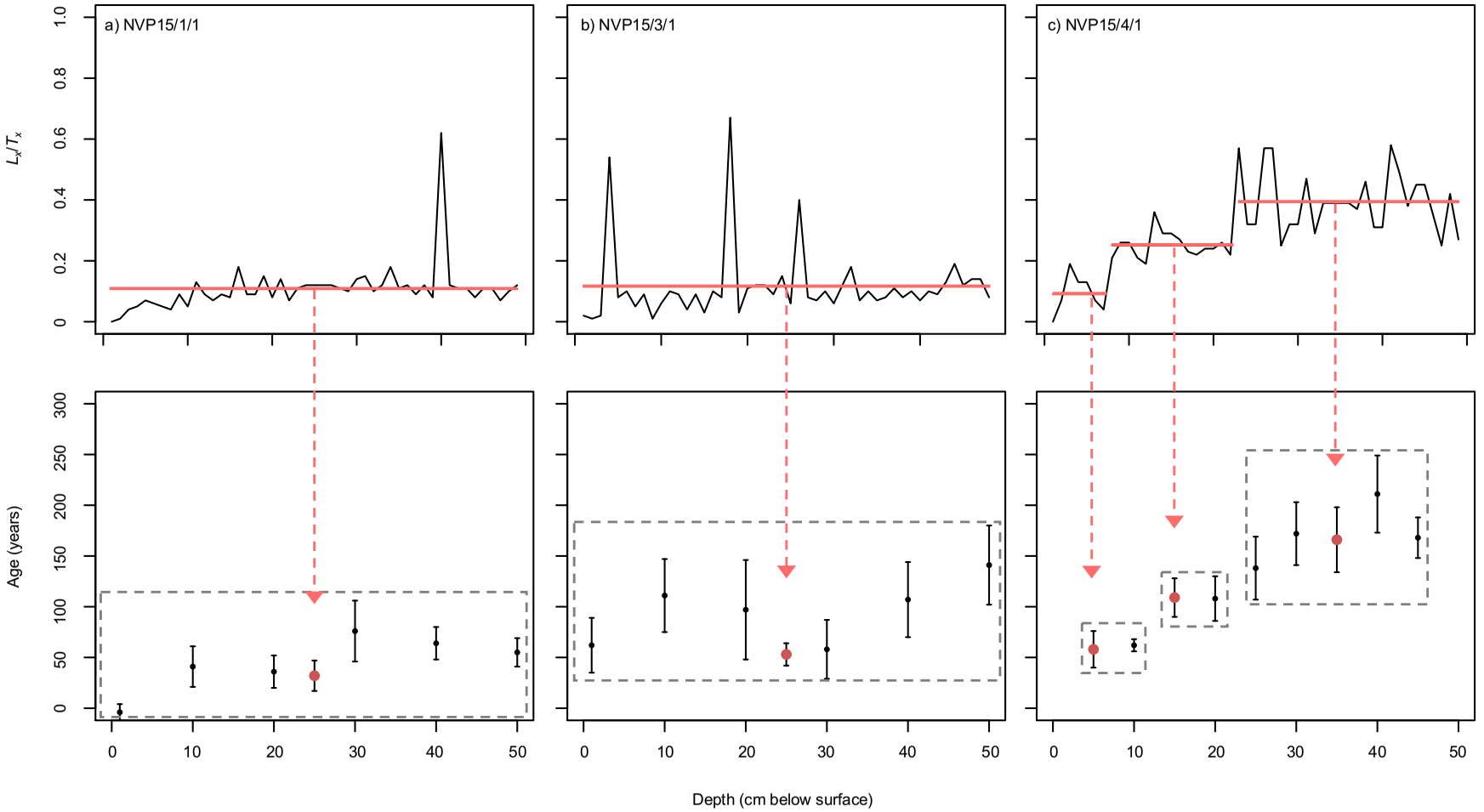


Figure 5.10 (*upper*) L_x/T_x profiles for sediment cores (a) NVP15/1/1, (b) NVP15/3/1, and (c) NVP15/4/1 coupled with changepoint model outputs. (*lower*) Fully-prepared SAR age estimates – sample in red denotes mid-point sub-sample from identified changepoint section. Grey dashed lines demarcate populations of ages that demonstrate similar results. Fully-prepared SAR OSL age estimates listed in Table 5.2.

Table 5.2 OSL results for cores NVP15/1/1, NVP15/3/1 and NVP15/4/1. All sub-sample ages were calculated using overburden density 1.9 ± 0.1 g/cm^3 and water content value of 3 ± 2 % following the method described in Nelson and Rittenour (2015). *n* is number of aliquots measured. [a] Depth of sub-sample below modern land surface, [b] Equivalent dose (Gy), [c] U (ppm), Th (ppm) and K (%) calculated based on individual radionuclide measurements, [d] Cosmic ray dose rate calculated based on sample elevation, latitude, longitude and depth of burial (Prescott and Hutton, 1994), [e] Total dose rate calculated using DRAC (Durcan *et al.*, 2015), [f] Years before 2015 AD.

Sample	Depth (cm)[a]	*n*	D_e (Gy)[b]	Grainsize (μm)	K (%)[c]	Th (ppm)[c]	U (ppm)[c]	D_{cosmic} (Gy ka^{-1})[d]	D_{total} (Gy ka^{-1})[e]	Age (years)[f]
NVP15/1/1/1	1	25	-0.0069 ± 0.02	125-180	1.54 ± 0.031	3.6 ± 0.072	0.8 ± 0.016	0.33 ± 0.03	1.97 ± 0.12	-4 ± 8
NVP15/1/1/10	10	19	0.087 ± 0.042	125-180	1.54 ± 0.031	3.6 ± 0.072	0.8 ± 0.016	0.30 ± 0.03	2.12 ± 0.13	41 ± 20
NVP15/1/1/20	20	16	0.08 ± 0.037	125-180	1.77 ± 0.002	2.52 ± 0.02	0.66 ± 0.01	0.28 ± 0.03	2.25 ± 0.05	36 ± 16
NVP15/1/1/25	25	18	0.071 ± 0.033	125-180	1.77 ± 0.002	2.52 ± 0.02	0.66 ± 0.01	0.27 ± 0.03	2.25 ± 0.05	32 ± 15
NVP15/1/1/30	30	22	0.17 ± 0.068	125-180	1.77 ± 0.002	2.52 ± 0.02	0.66 ± 0.01	0.26 ± 0.03	2.25 ± 0.05	76 ± 30
NVP15/1/1/40	40	19	0.14 ± 0.035	125-180	1.58 ± 0.032	3.7 ± 0.074	0.8 ± 0.016	0.25 ± 0.03	2.18 ± 0.13	64 ± 16
NVP15/1/1/50	50	19	0.12 ± 0.029	125-180	1.58 ± 0.032	3.7 ± 0.074	0.8 ± 0.016	0.24 ± 0.2	2.17 ± 0.13	55 ± 14
NVP15/3/1/1	1	20	0.1 ± 0.044	125-180	1.25 ± 0.025	2.2 ± 0.044	0.6 ± 0.012	0.33 ± 0.03	1.62 ± 0.10	62 ± 27
NVP15/3/1/10	10	21	0.19 ± 0.061	125-180	1.25 ± 0.025	2.2 ± 0.044	0.6 ± 0.012	0.30 ± 0.03	1.72 ± 0.10	111 ± 36
NVP15/3/1/20	20	21	0.20 ± 0.10	125-180	1.53 ± 0.009	3.08 ± 0.03	0.64 ± 0.01	0.28 ± 0.03	2.06 ± 0.05	097 ± 49
NVP15/3/1/25	25	26	0.11 ± 0.022	125-180	1.53 ± 0.009	3.08 ± 0.03	0.64 ± 0.01	0.27 ± 0.03	2.06 ± 0.05	53 ± 11
NVP15/3/1/30	30	19	0.12 ± 0.059	125-180	1.53 ± 0.009	3.08 ± 0.03	0.64 ± 0.01	0.26 ± 0.03	2.06 ± 0.05	58 ± 29
NVP15/3/1/40	40	21	0.19 ± 0.065	125-180	1.29 ± 0.026	2.6 ± 0.052	0.6 ± 0.012	0.25 ± 0.03	1.78 ± 0.11	107 ± 37
NVP15/3/1/50	50	23	0.25 ± 0.067	125-180	1.29 ± 0.026	2.6 ± 0.052	0.6 ± 0.012	0.24 ± 0.02	1.77 ± 0.11	141 ± 39
NVP15/4/1/5	5	20	0.14 ± 0.043	125-180	1.74 ± 0.035	4.9 ± 0.098	1.3 ± 0.026	0.32 ± 0.03	2.40 ± 0.05	58 ± 18

Sample	Depth (cm)[a]	*n*	D_e (Gy)[b]	Grainsize (μm)	K (%)[c]	Th (ppm)[c]	U (ppm)[c]	D_{cosmic} (Gy ka^{-1})[d]	D_{total} (Gy ka^{-1})[e]	Age (years)[f]
NVP15/4/1/10	10	20	0.18 ± 0.018	125-180	2.18 ± 0.01	5.42 ± 0.06	1.17 ± 0.02	0.31 ± 0.03	2.88 ± 0.06	62 ± 6
NVP15/4/1/15	15	17	0.3 ± 0.051	125-180	2.02 ± 0.01	4.96 ± 0.04	1.16 ± 0.01	0.29 ± 0.03	2.74 ± 0.06	149 ± 44
NVP15/4/1/20	20	19	0.28 ± 0.058	125-180	1.84 ± 0.02	4.97 ± 0.13	1.2 ± 0.03	0.28 ± 0.03	2.60 ± 0.06	108 ± 22
NVP15/4/1/25	25	19	0.38 ± 0.086	125-180	2.03 ± 0.01	4.77 ± 0.03	1.09 ± 0.01	0.27 ± 0.03	2.74 ± 0.06	138 ± 31
NVP15/4/1/30	30	19	0.46 ± 0.083	125-180	1.99 ± 0.01	4.58 ± 0.06	1.04 ± 0.02	0.26 ± 0.03	2.67 ± 0.06	172 ± 31
NVP15/4/1/35	35	19	0.44 ± 0.085	125-180	1.95 ± 0.02	4.82 ± 0.04	1.02 ± 0.01	0.26 ± 0.03	2.66 ± 0.06	166 ± 32
NVP15/4/1/40	40	19	0.52 ± 0.094	125-180	1.77 ± 0.02	4.43 ± 0.04	1.06 ± 0.01	0.25 ± 0.03	2.46 ± 0.05	211 ± 38
NVP15/4/1/45	45	27	0.41 ± 0.047	125-180	1.72 ± 0.034	4.5 ± 0.09	1.2 ± 0.024	0.25 ± 0.03	2.45 ± 0.05	168 ± 20

Overall, results showed that in these sediments, where no observable difference was found in sediment colour, sorting, or grain size (see Appendix F), L_x/T_x measurements and changepoint analysis were able to identify variation in sediment age. Sections that were visibly homogenous did not show any notable grain size variability. For example, results from the particle size analysis of sediment core NVP16/4/3 demonstrated a unimodal distribution of poorly-sorted medium-fine sands averaging 261 μm with a standard deviation 15 μm.

5.4 Discussion

5.4.1 Relative age profiles across a dune

Assuming L_x/T_x to be a proxy for age of deposition, the L_x/T_x profiles in Figure 5.7 allow us to identify relative changes in the ages of sediment across profiles of

individual aeolian landforms. L_x/T_x can arguably be considered a good proxy for age in these young Nebraskan sediments where the dose rates show little variability, varying up to a maximum of c.0.25 Gy ka^{-1} within each sediment core (Table 5.2), and the dose response is in the linear region (< 10 Gy) of the dose response curve; signal is proportional to age.

As expected, samples at the crestal site (Figure 5.7d) show low L_x/T_x readings throughout the 50 cm sedimentary core, suggesting modern age and a site of active sand movement. The two slope profiles (Figure 5.7e & g) demonstrate an increase in L_x/T_x with depth. No significant difference in particle size with depth, coupled with homogenous sands and no obvious horizon changes suggests that there is unlikely a large variation in the expected dose rate with depth and thus the L_x/T_x change can be assumed indicative of an increase in age. Given the untreated nature of the sediment, higher levels of variability between each aliquot than is normally identified in fully-prepared samples measuring isolated minerals and size fractions is expected. Finally, Figure 5.7 (f) shows a transition from young modern sand at the top of the core to much older sediments from c.36 cm onwards. If dose rates are homogenous, the oldest near-surface sediments across this profile are identified at the base of the dune, capped with modern sediments in the upper 17 cm. NVP16/4/3 is at present likely a source of sediment erosion, where a layer of bleached material overlies much older sediments which are gradually being deflated. In contrast, the slope profiles display an intermediary age sediment layer which does not appear to be represented within the basin (NVP16/4/3) profile. Uncertainty over depositional and erosional histories complicates the interpretation of the sediment cores. Deeper sediment cores taken from the slopes would confirm

whether the oldest material found in NVP16/4/3 is also preserved at deeper depths in the slope regions where less erosion and greater depositional activity has occurred.

The results demonstrate the utility of near-surface sediments as useful archives of environmental response to external disturbances. Near-surface sediments are under-represented in the published luminescence age record, due to concerns about the heterogeneity of the dose rate as well as bioturbation and reworking (Hesse, 2014). However, as Hesse (2014) notes, this theory relies on the assumption that the present is dissimilar to the past in that underlying sediments were not bioturbated when they once represented the surface layer. This study demonstrates that whilst variability is present, near-surface sediments can provide a useful insight into zones of reworking, erosion, and depositional structures across the profile of a landform. These core profiles are also useful in identifying the depth of surficial mixing and bleached material. In this example, the upper 50 cm at the crestal site appears to be modern, whilst this depth of "modern sand" changes across the dune transect. According to the slope profiles (Figure 5.7 e & g), the depth of modern sand ends at c.21 cm and 10 cm in cores NVP16/4/2 and NVP16/4/4 respectively.

Also of note is the change in level of centimetre-to-centimetre variability with increase in L_x/T_x (e.g. Figure 5.8 & 5.9). There are two potential reasons for this increased variability. Firstly, as sediments begin to accumulate a luminescence signal, inter-crystal and mineral variability will cause this signal to vary between sediments at a comparable level – this is expected and is encountered in all luminescence dating as the level of intrinsic variability. This level of variability is

not noted in the modern sediments identified in the upper core and crestal sections where no significant (if any) luminescence dose has been stored. Proportionally, any dose that had accumulated in the young sediments would be significantly lower than the older deeper segments, and thus variability would expectedly be proportionally lower. Secondly, heterogeneity in the microdosimetry of the surrounding sediment will also cause variability between individual quartz grains, with this variability increasing in absolute terms with L_x/T_x.

5.4.2 Reproducing signals above noise

Reproducibility of the signal within a noisy dataset has been assessed at both the individual aliquot scale, and across depositional profiles. Figure 5.8 demonstrates that the L_x/T_x variability for a particular 1 cm-thick sample (population A), is the same as the variability found between sub-samples within a deeper section (of tens of cm) defined as a single interval by changepoint analysis (population B). This suggests there is as much variability in L_x/T_x across a chronostratigraphic unit as there is within a single sample at a single 1cm-thick depth. It was important to test this variability to be sure that the different changepoint model outcomes generated for the different sites in Figure 5.9 are real and not an artefact of variability in L_x/T_x for any one sample. i.e. is the inter-changepoint variability small enough to not impact the location of the breakpoints in the model.

Despite the variability in L_x/T_x for individual sub-samples, the same broad sections are identified using the changepoint analysis algorithm (e.g. Figure 5.9b); highlighting that both type 1 and type 2 errors have adequately been accommodated for in the model selection criteria. Profiles which exhibited

generally lower L_x/T_x values produced more variability between the original and repeat changepoint outputs, whilst increased congruency between repeats is found in profiles which exhibit higher L_x/T_x values (i.e. Figure 5.9b). The sedimentary cores which demonstrate lower L_x/T_x measurements show reduced levels of changepoint similarity between repeat runs. This is due to increased sensitivity in the model, which identifies changepoints which structurally are less significant. Contrastingly, a lower sensitivity model is required (higher penalty value) for the sediment cores which demonstrate distinct and true structurally variability (i.e. NVP16/4/3 in Figure 5.9b). In this sense, the method is self-correcting whereby structural breakpoints which are significant and require a less sensitive model are more likely to be repeated in further repeat measurements of the same sediment profile. Meanwhile, breakpoints which are identified within a noisier setting with greater model sensitivity are structurally less significant.

The varying sensitivity requirement between models demonstrates the importance of identifying the appropriate penalty value to apply to the changepoint model for individual sedimentary sequences. In this study, the method is being used to identify changepoints within the profile where our dating efforts would be better focused, however subtle they might be, and subsequently inform further dating resources and interpretation. For example, the L_x/T_x profile in Figure 5.6 (m – GSL15/2/4) also shows a sedimentary sequence which has accumulated over time as a series of short and frequent pulsed depositional events as opposed to large and infrequent depositional events (e.g. Figure 5.6 (g – NVP16/4/3)). Yet the changepoint output for this profile identifies three sections within the profile, separated at 11 cm and 33 cm. It is important to recognise that all reactivation and

deposition events are pulsed. The accumulation of sand grains cannot be truly continuous since they are distinct events occurring when the wind velocity required for sediment entrainment is reached and the sediment is available for transport. In this sense, despite appearing to sit on a straight line, there are always breaks in the sedimentary accumulation profile that perhaps could be described as quasi-continuous. Given the low L_x/T_x values and quasi-continuous nature of the profile, a lower penalty value was selected in this model to increase the sensitivity of the model to changes in the mean of the L_x/T_x values with depth (i.e. GSL15/2/4 penalty value 6945, NVP16/4/3 penalty value 95979). The same penalty value (i.e. sensitivity) cannot be applied to all sedimentary profiles as the outputs would incorrectly identify age reversals in some of the sections, whilst missing subtle changes in the younger sections which have less distinct chronological breaks (Figure 5.11).

The likelihood that the changepoint model correctly identifies significant depositional breaks within the record is a function of its capacity to reproduce the same breakpoints with repeat measurements of the luminescence profile. Examples in this thesis (e.g. Figure 5.9b) have shown that the self-correcting mechanism of the model sensitivity ensures that the most distinct structural changes are preserved between repeat measurements, whilst subtle variability attributed to noise will shift the breakpoints in sedimentary samples which have accumulated through short, frequent and quasi-continuous deposition events.

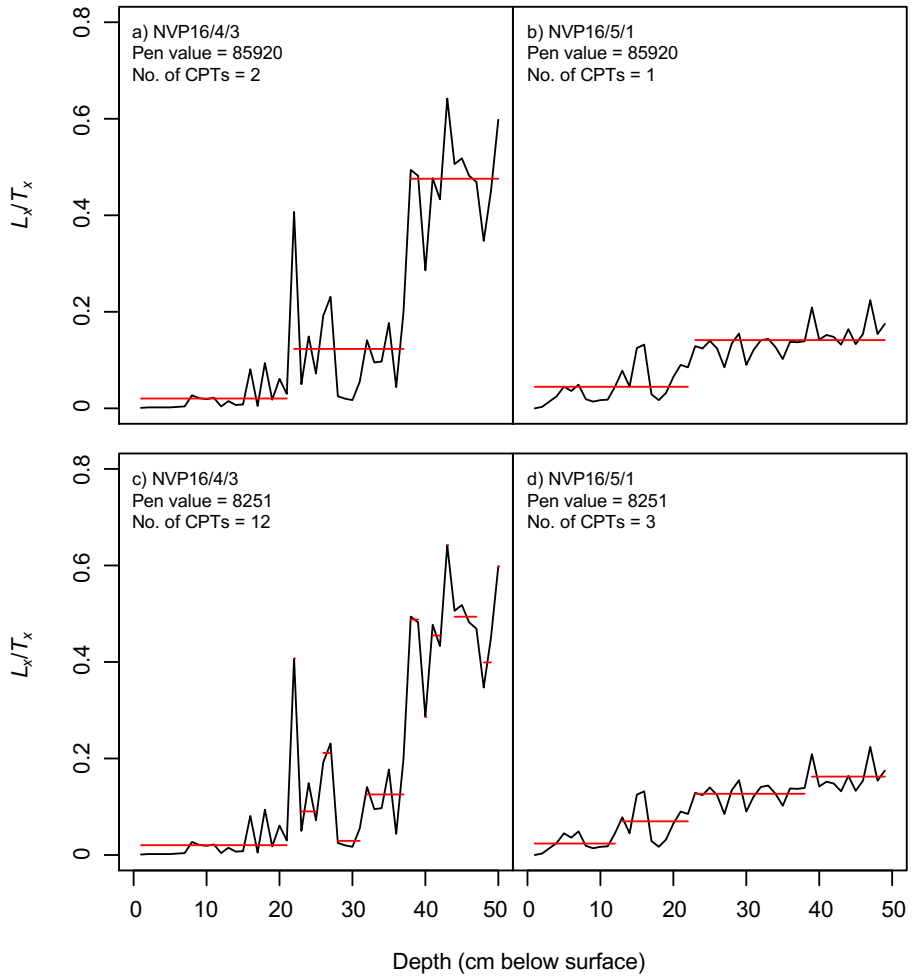


Figure 5.11 Changepoint model outputs for two sediment cores when different levels of model sensitivity are applied. Relatively low model sensitivity has been applied to outputs (a) and (b) for sediment cores NVP16/4/3 and NVP16/5/1 respectively. Relatively high model sensitivity has been applied to outputs (c) and (d) for NVP16/4/3 and NVP16/5/1 respectively. With reduced sensitivity, fewer changepoints are identified in NVP16/5/1, yet higher model sensitivity identifies additional changepoints within NVP16/4/3 which theoretically do not make sense as they suggest age-reversals.

5.4.3 Predicting age-depth profiles from mid-point age estimates

Mid-point age estimates from changepoint sections have been found to be generally representative of the age bracket of the wider identified changepoint

section. Nevertheless, the ability for the mid-point age to represent the whole section is ultimately determined by the sensitivity of the model and the age range covered within the sedimentary sequence. Age variation may occur within individually identified changepoint sections due to quasi-continuous accumulation of sediment within the same period of activation, and thus whilst the mid-point reflects the optimum location for measuring fully-prepared luminescence ages, additional ages will further improve the chronological resolution of the profile. For example, individual sections may demonstrate similar profiles to those found in Figure 5.6 (k) and (m), with gradually increasing L_x/T_x profiles punctuated by occasional step-changes in the depositional age – likely representing erosional boundaries or periods of pulsed deposition. Ultimately, the maximum information is achieved when the fully prepared luminescence ages are interpreted within the context of the depositional profile as identified in the L_x/T_x continuous measurements. These results demonstrate the utility of using changepoint analysis coupled with full-preparation dating techniques to produce a rapid age-depth profile of a sediment core, capturing the points of variability within the sedimentary profile whilst avoiding unnecessarily high volumes of sample dating. This positive result suggests that future sediment cores do not require a high-resolution chronology to reconstruct an age-depth profile that captures both accurate depositional ages and depositional structure within aeolian system sedimentary structures. The combination of L_x/T_x measurements, changepoint output and fully-prepared ages produces rapid and accurate results that not only aids interpretation of individual sediment profiles, but also permits a greater spatial coverage of

analysis which strengthens the overall reconstruction of environmental response within the landscape.

5.4.4 Complicating factors on sample age

One of the key assumptions of this study is that dose rate remains relatively homogeneous through each sediment core, suggesting the variability in L_x/T_x demonstrates changes in equivalent dose (i.e. age). This assumption is only valid in sediments which show homogenous sedimentary qualities and are not impacted by large volumes of heavy mineral contamination and are therefore subject to high levels of beta dose rate heterogeneity. Without any evidence for beta dose rate heterogeneity, dose rate changes over short spatial scales which generate high variability within the profile are not expected. However, in sedimentary environments which are quartz-dominated with very low levels of radionuclides, the soft component of the cosmic dose rate can be proportionally large and create a steep gradient of dose rate with depth in near-surface sediments. If dose rates are dominated by the cosmic dose rate component, caution should be taken when interpreting variability in L_x/T_x; additional dates may be required to construct a more informed age-depth profile.

In this study, dose rates calculated using ICP-MS measurements have shown very little variability from top to bottom of the sediment cores (Table 5.2). For example, the means and standard deviations of the dose rate data calculated for sediment cores NVP15/1/1, NVP15/3/1 and NVP15/4/1 are 2.17 ± 0.10 Gy ka^{-1}, 1.87 ± 0.19 Gy ka^{-1} and 2.62 ± 0.16 Gy ka^{-1} respectively. Coupled with relatively homogenous material, negligible grain size variability (e.g. mean and standard

deviation of sediment core NVP16/3/2 grain size: 248 ± 10 μm - see Appendix F), and a consistent sediment source over the time-period studied (and longer), there is little evidence to suggest that there would be strong variability in dose rates within the 50 cm core – except in locations where notably thick sod layers have been found overlying the dune sands. This conclusion is corroborated in the L_x/T_x profiles which consistently show an increase in L_x/T_x with depth. In addition, the high-resolution sampling in this study is comparable to making multiple measurements of the same sample under standard conditions, which would identify any significant levels of microscale dosimetry heterogeneity.

In sedimentary sections where variability in dose rate can be expected with depth (e.g. new field site, high volume of heavy minerals and zircons), each of the identified points for full-preparation dating should also be analysed for dose rate. The changepoint analysis allows us to crudely identify variability in the luminescence signal with depth which guides us for more thorough dating analysis. As part of this analysis, each fully-prepared SAR measurement should be coupled with new dosimetry measurements to corroborate whether the changes in L_x/T_x have been induced by equivalent dose or dosimetry.

5.4.5 Application of this approach to longer time-series

Whilst this study has applied the changepoint technique to short sedimentary cores which are young in age (often < 200 years), this approach can equally be applied to deeper and older sedimentary sections. For longer sedimentary sequences a bi-sectioning method might be applied, progressively increasing the sampling and measuring of L_x/T_x of un-prepared bulk material until it

shows no further stepped increases in values. For example, L_x/T_x measurements could be made at the top, middle and bottom of the core, and then additional measurements are made between the mid-points of the neighbouring points with the changepoint model re-run iteratively as each new L_x/T_x measurement is made. When the changepoint model no longer identifies any new changepoints (which conform to the model selection criteria), no further L_x/T_x measurements are required as the main breaks in the record have been identified. However, it should also be noted that for the same difference in age with older sediments, the difference in L_x/T_x values will be subtler when the ages of samples are above the linear section of the dose response curve. As age increases, the L_x/T_x values will appear closer until saturation of the dose response curve is reached and they will no longer produce any variation in L_x/T_x values. It is therefore expected that this method will become less sensitive as age increases, and this remains to be explored in future applications. A combination which incorporates portable luminescence reader measurements is likely more appropriate on significantly longer sedimentary sections to help guide sample strategy.

Each fully-prepared SAR age should be coupled with a new assessment of the dose rate at that corresponding depth to confirm if the notable changes in L_x/T_x occurred as a factor of age or dose rate. Increasing the number of L_x/T_x measurements in the changepoint model will improve the accuracy in identifying the breakpoints in the depositional profile. However, as noted this would rely on the assumption that the dose rate and sensitivity of the sediments has not changed significantly through the sedimentary core. Notable stratigraphic layers and

structures within the sample core should also be used to guide the sub-sampling and L_x/T_x measurements.

5.5 Conclusions

This study has presented a new method for identifying chronological change in visibly homogenous dune depositional profiles. Using an algorithmic approach, this study represents the first application of changepoint analysis to a luminescence dataset and has demonstrated the utility of such methods in focusing dating efforts when investigating aeolian system dynamics. High-volume sampling of visibly homogenous sediments can successfully capture chronostratigraphic variability when combined with statistical changepoint analysis to identify the breakpoints in the chronostratigraphy. Despite the un-prepared nature of the sediment samples, this research has demonstrated the possibility of measuring subtle changes in luminescence with depth, allowing us to identify step-changes in the depositional age of near-surface sediments. The significant reduction in preparation time is successful in allowing for rapid relative age assessment prior to in-depth accurate age generation using luminescence techniques**.** Whilst the sediments used in this example were young in depositional age (i.e. decades to century-scale) with expectedly weak luminescence signals, the large aliquots coupled with the convex quartz lens and the higher voltage used in the measuring of the signal allowed for optimisation of the signal size. Naturally occurring high dose rates (c.2.2 Gy/ka) in the region also provide suitable sediments for attempting to measure at the very young end of the age spectrum.

When considered together across an individual geomorphological feature within the aeolian system, multiple L_x/T_x profiles provide a relative age assessment that can help inform our understanding of the processes of erosion and deposition across individual features. Coupled with changepoint analysis and model selection criteria, the results have shown the potential to identify step-changes within L_x/T_x profiles which can focus dating efforts on points of change within the depositional setting. Further to this, in sedimentary sections devoid of significant lithological and mineralogical change, single fully-prepared SAR luminescence ages taken at the mid-point of identified changepoint sections can be used to produce age-depth profiles of near-surface sediments, reducing the need to date all sediment samples. Importantly, this study has confirmed the pulsed depositional nature of aeolian system sedimentary profiles and demonstrated a method which allows researchers to interpret luminescence ages within the context of a depositional structure. A method which combines depositional structure with chronology is particularly important in contributing to our overall understanding of what a luminescence date represents within the context of an individual sample or geomorphological feature. The findings presented demonstrate that L_x/T_x measurements coupled with changepoint analysis modelling of near-surface sediment cores provide a suitable method for reconstructing an environmental signal in an aeolian system characterised by high-volumes of environmental noise. What's more, this relatively quick approach, combining coarse L_x/T_x measurements with the use of the changepoint algorithm, facilities a better informed full-preparation dating approach where excess samples are not dated in order to produce accurate age-depth profiles.

SECTION THREE

DATA ANALYSIS

Chapter 6

Secondary datasets and analysis methods

6.1 Introduction

This section details the methods that were used to address the second and third research questions. Having established a method that allows us to successfully identify a chronological history of deposition in the sedimentary record in section 2, we then needed a series of historical environmental conditions to compare the reactivation record against. This chapter highlights the key datasets used in reconstructing a history of environmental conditions in the NVP region, before briefly explaining the methods used to identify associations between the drivers and environmental response.

6.2 Datasets of environmental conditions

To understand the reactivation of the surface we require knowledge of the changes in the most important factors that determine sediment mobility. Predominant amongst the factors that affect the ability of wind to move sediment, in relatively arid environments such as Nebraska, is vegetation cover (Wiggs *et al.*, 1994). Vegetation cover is both a protective 'skin' (Wolfe and Nickling, 1993) and a source of disturbance suppression that works to stabilise dune sediments and prevent surface reactivation (Barchyn and Hugenholtz, 2013). In the absence of levels of direct historical vegetation cover, secondary datasets taken from instrumental and archival records (including USDA, NOAA, NCDC, soil surveys, US Forest Service, and land ownership records from The Nature Conservancy archives) are used in this study to provide independent estimates of environment dynamics and known disturbances that affect vegetation cover levels. The factors

investigated in this study were: droughts, anthropogenically-induced change (e.g. land ownership histories, grazing pressures) and natural disturbances such as wildfires. Data for each of these factors was used to reconstruct a history of the disturbances that affected past vegetation cover levels, as described in the following sections.

6.2.1 Growing season precipitation

Precipitation levels directly affect drought occurrence, plant-available moisture, and thus levels of vegetation cover. Precipitation during the April-October growing season, (Stubbendieck, 2008) is the key determinant of vegetation cover in any year (Grassini *et al.*, 2010). Annual growing season totals were calculated using daily precipitation data taken from Ainsworth, Nebraska (42.58° N, -100.05° W, <10 miles from the study sites) and sourced from the National Centre of Environmental Information (https://www.ncdc.noaa.gov/ - accessed on 04/01/2018) for 1905-2015 AD. We compared growing season precipitation levels against the OSL chronologies of reactivation in Paper 3. Growing season precipitation was also used in Paper 4 as an input to calculate the relationship between climatic variables and reactivation (via a tree ring growth index).

6.2.2 Palmer Drought Severity Index (PDSI)

The Palmer Drought Severity Index (PDSI) is a metric of annual historical drought conditions (Palmer, 1965) based on tree ring records. In order to extend the PDSI coverage across multi-century timescales, we used data from the North American Drought Atlas (Cook and Krusic, 2004). The closest PDSI data point in

this study, grid point 161 (42.5° N, -100° W), is based on a cumulative regional signal taken from trees in a 2.5° x 2.5° grid, ranging from 8 – 33 tree ring records from 1500 – 2003 AD. Whilst the precipitation record using in this study provides daily measurements, PDSI values from Cook and Krusic, (2004) extend over the last 500 years, but at the expense of spatial detail in the coverage provided.

Unlike other indices, such as the Standard Precipitation Index (SPI) (McKee *et al.*, 1993), which is based solely on precipitation (Keyantash and Dracup, 2002), the PDSI as a measurement more closely matches vegetation response to drought than other drought indices (Woodhouse and Brown, 2001). We used the PDSI dataset to compare against the luminescence record directly in Paper 3, and to discuss the OSL results from this study in the context of other regional chronologies.

6.2.3 Local tree ring growth index

A local tree ring growth index (Brown *et al.*, n.d.) produced using trees felled on the Niobrara Valley Preserve (see Figure 3.2 for reminder of NVP location) was used as a proxy to extend the period of known historical climatic conditions. Unlike the PDSI, this tree ring growth index presents a localised as compared to regional signal. There is not an extensive population of trees across Nebraska, meaning that many of the PDSI grid points are often a cumulative signal of trees that cover very wide spatial areas. By contrast, the banks of the Niobrara river are forested, and provide suitable conditions for this tree ring index to be compiled and represent a local signal of changing climatic conditions. Samples of *Pinus ponderosa* were selected for the production of the NVP tree ring index (Brown *et al.*, n.d.); a species that is common, sensitive to drought, attains ages of up to 400 years, and has fewer

false tree rings than other species (Woodhouse and Brown, 2001). The number of tree samples used in the composite index ranges from 1, during the very early sections of the record (i.e. late 16th century AD), to 30 tree samples from the late 19th century AD onwards. The tree ring growth index was used as a proxy of climatic conditions and used as an input for modelling described in Paper 4. Please refer to Paper 4 for specific details about the use of this dataset.

6.2.4 Wildfire

Grassland wildfires remove above-ground biomass, potentially exposing the underlying sandy sediments to aeolian erosion. Wildfires in the Sandhills are recorded as being common in the area in pre-European settlement times (Bragg, 1995), with wildfires removing protective vegetation cover on the Nebraskan prairies (Burzlaff, 1962; Frolik and Sheperd, 1940) and increasing the likelihood for surface disturbance and blowout formation (Pool, 1914). Since these early reports, studies across the Sandhills (Arterburn *et al.*, 2018) and semi-arid grasslands more widely (Esteves *et al.*, 2012; Santín and Doerr, 2016; Twidwell *et al.*, 2013), have commented on the connection between wildfire occurrence and damage to surface protective vegetation cover.

A history of the local wildfires (up to 1980s) that have occurred in the study area was extracted from a tree scar record compiled by Professor T. Bragg (University of Nebraska-Omaha) using *Pinus ponderosa* samples (Appendix G) from the southern sections of the NVP and referred to in Guyette *et al.* (2011). The fire scar history of 38 tree samples spans the last 300 years and records 30 separate wildfires. To include fires relevant to the study area, only those identified in the

records of at least two individual trees were considered as likely to have had an impact extending widely over the landscape. A large wildfire that occurred in 2012, burning 66,000 acres across NVP and surrounding ranches, has also been included in the analysis. Wildfire history of the area has been used in Papers 3 and 4 to determine if any relationship can be identified between periods of sediment reactivation and wildfire frequency.

6.2.5 Grazing pressure history

Identifying grazing pressures across the study region over recent centuries is not possible due to data scarcity and difficulties in assessing past livestock movements in response to changing environmental conditions. In the absence of a single data source providing a history of individual stocking rates between each of the sampling sites, a collection of datasets (some qualitative) were gathered to produce an index of relative grazing / land use intensity (see Paper 3).

Local land ownership history and land use changes were obtained from a variety of sources including: original land alienation reports, historical reports, and interviews with local ranchers and preserve managers (Table 6.1). Key dates associated with the development of the railroad as well as land acts are included in this study. Notable periods of grazing and land use pressure change were identified with periods classified as either: 1 - low pressure, 2 - moderate grazing pressure or 3 - high grazing pressure, based on: the level of population in the surrounding area, knowledge of ranching / agriculture strategies, land ownership chronologies and wild versus open / closed ranching levels. Together, these are used to suggest relative periods of increased and decreased pressure which can be analysed

alongside the other disturbance factors. Similar extrapolations of a quantitative classification index from qualitative datasets have successfully been completed in other areas of environmental science (e.g. Adamson and Nash, 2014; Grab and Nash, 2010; Nash *et al.*, 2016; Nicholson, 2001a, 2001b, Nicholson *et al.*, 2012a, 2012b) to identify variability in historical climates. Refer to Paper 3 for the final grazing intensity index.

Table 6.1 Table of data sources used to produce grazing / land use pressure index according to a scale of 1 (low pressure), 2 (moderate pressure) and 3 (high pressure). Information was predominantly sourced from a range of historical accounts documented in books, genealogy websites and oral histories shared by ranchers and preserver managers. The final time brackets and intensity scores were discussed and verified with local grassland ecologist Dr Al Steuter (commercial ranch owner and previous Ranch Manager at the Niobrara Valley Preserve).

Data source	Data type	Information provided
Stubbendieck (1998)	Book chapter: *Range Management*, in: An Atlas of the Sand Hills	- History of establishment of ranching in the region
Miller (1998)	Book chapter. *Land Development and Use*, in: An Atlas of the Sand Hills	- History of ranching strategies in the region
US Department of the Interior: Bureau of Land Management https://glorecords.blm.gov	Land ownership records (Appendix H)	- Dates that each study site plot was first bought from the US Government
The Nature Conservancy (contact: Amanda Hefner)	Land alienation reports	- Provided details of farm inventory in early 20th century
Nebraska Historic Buildings Survey of Brown County, Nebraska (1989)	Historical building survey	- Details of any previous homesteads / buildings on any of the study sites alongside dates
Memorial Library http://www.memoriallibrary.com	Website with Brown County history (Appendix I)	- History of the growth of towns / settlements in Brown County
Access Genealogy www.accessgenealogy.com	Website with Brown County history (Appendix I)	- Land acts and impact on region - History of the first EuroAmerican settlers and the transition from cattle

Data source	Data type	Information provided
		men, to ranches, merchants - History of the growth of towns / settlements in Brown County
Nebraska Geneaology www.usgennet.org	Website with Brown County history (Appendix I)	- Land acts and impact on region - Railroad history - History of droughts during the late 19th century with the early EuroAmerican settlers
Dr Al Steuter (rancher, grassland ecologist, former NVP TNC manager)	Conversations in the field (Appendix J)	- Local history of NVP and surrounding ranches
Doug Kuhre (NVP TNC cattle manager)	Conversations in the field (Appendix J)	- Local history of NVP and surrounding ranches
Larry O'Kief (local rancher)	Telephone interview (Appendix J)	- Local history of NVP and surrounding ranches

6.2.6 Wind velocity

Whilst wind erosivity potential is key in determining whether sediment will or will not be mobilised when surfaces are bare, wind speed data from Valentine, Nebraska (42.88° N, -100.55° W) from 1987 – 2017 AD has shown that average daily wind speeds have exceeded the entrainment thresholds 4.5 m/s (Lancaster, 1988) and 5.97 m/s (Bullard *et al.*, 1996) for 97% and 88% of the period respectively. Given this, wind speed was not considered a limiting factor on sediment transport in our study location when surfaces are bare and has not been included as a controlling variable on sediment movement. We can assume that wind is not a limiting factor over the timescale of interest (years-decades). The lack of dependency on wind velocity is another reason why this location was suitable for this study. Wind speeds have only been continuously recorded since the 1980s, providing a short period against which to compare the sedimentary response.

6.3 Analysing the datasets

Three different methods have been used to combine and analyse these datasets. To address the project aims and research questions, tools were needed that allowed the pulling together of a range of different datasets coming from a collection of visual, empirical and qualitative sources. This study has not relied solely upon empirical data from the field to answer questions about environmental change, but local histories, archived imagery and land alienation reports have also been important in informing our understanding of the pressures and changes in the Nebraskan grassland environment.

6.3.1 Traditional descriptive analysis

Having produced detailed chronologies of surface reactivation across a variety of features within the NVP, reactivation histories are discussed in the context of known disturbances and climatic change (Paper 3). A common form of time-series data analysis in palaeoenvironmental reconstructions involves vertically stacking the reconstructed chronologies from a range of environmental and climatic proxies to identify common patterns, perturbations, leads and lags in the system between parameters (e.g. Burrough and Thomas, 2013; Miao *et al.*, 2007). In the absence of independent chronologies, these methods of data analysis have been widely criticised for "wiggle matching" (Blockley *et al.*, 2012), where common patterns in the proxies are aligned against one another, removing the capacity to suggest causation and lags in the system. To guard against this criticism in the present work, each of the individual secondary datasets are associated with

independent chronologies, and the absolute dating of the sediment samples equally provides an independent history of surface reactivation.

Based on the ages identified in the OSL-dated reactivation record, this thesis explores whether known periods of drought (e.g. 1890s, 1930s, 1950s) can be identified within the environmental record. Likewise, Paper 3 comments on the availability of evidence to support whether reactivation in association with known periods of extensive wildfire or the introduction of homesteading to the region can be identified within the chronological record. The natural and anthropogenic disturbance records are assessed against the OSL chronologies from each of the six sites individually as well as against a stacked probability density function (PDF) from all OSL ages combined. While there are limitations with the use of PDF plots for age presentation (Thomas and Burrough, 2012), the continuous sampling in 50 cm cores and the use of changepoint analysis means that all recoded events have an equal probability of being sampled and key points of change in the sediment age have been identified. Equally, sediment cores extracted across the transects at each of the sampling sites has been stacked to ensure that a greater proportion of events are captured in the site representation. In this context therefore, PDFs are a useful aid to data interpretation (see Paper 3 for further details).

6.3.2 Lagged-analysis

Paper 3 also uses a form of lagged-analysis to determine if any significant relationships can be found between drought, land ownership changes, and wildfire with the OSL record. For many forcing factors, a lag period exists between the time of natural or anthropogenic disturbance, the period when vegetation responds, and

the threshold at which this leads to sediment reactivation. For example vegetation-die-off is not instantaneous in a drought event (Barchyn and Hugenholtz, 2013a; Mangan *et al.*, 2004; Peters *et al.*, 2006). Using PDSI data to establish droughts of different intensities, notable ranch establishment dates, and known wildfires in the local area, a lag time was calculated between these three different 'events' and the next accumulation of sediment recorded by an OSL age at each site. Lags were calculated using both the central OSL age value and the earliest possible age based on one sigma error. Further details can be found in Paper 3.

6.3.3 Artificial neural networks

The final method of data analysis uses statistical inference tools. As stated in section 2.9, statistical inference tools provide us with a method to identify associations and build empirical models from datasets (Lary *et al.*, 2018) in the absence of a process-based mechanistic model which connects the individual drivers and environmental response. Supervised machine learning (SML) techniques, and in particular, artificial neural networks (ANNs) have successfully been applied to many studies in the geosciences and have been summarised in section 2.9.

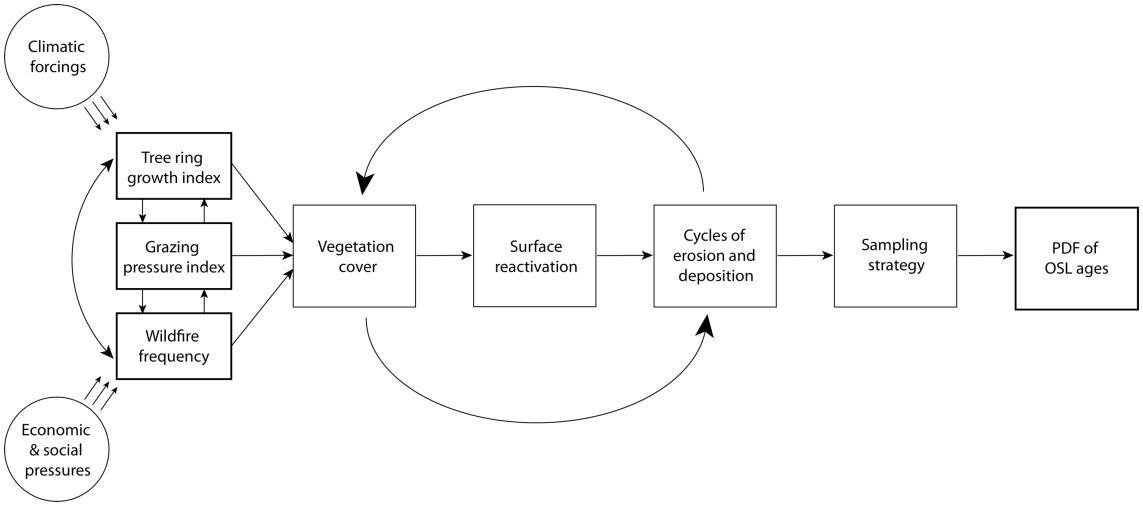
In particular, ANNs have the capacity to analyse non-linear relationships between datasets which is particularly important to this study where we are attempting to identify the associations between inputs and outputs with numerous layers of mechanisms and filters excluded from the model (Figure 6.1), for which a full process-based model does not exist. Without access to such an underlying mechanistic model, connecting external climatic and anthropogenic drivers to

near-surface reactivation events, ANNs are an appropriate tool to use in an empirical data-focused research project such as this, where we can confidently estimate both the drivers and the environmental response of the system. ANNs are 'self-learning' and are able to model complex datasets without the need to impose an understanding of the underlying processes.

In this study, the potential for ANNs was explored in the latter stages of the project following production of datasets of environmental response and external forcing factors. Paper 4 uses ANNs to model the non-linear relationships between the predictor variables (i.e. the parameters that drive vegetation cover) and the output terms (i.e. a measure of sediment reactivation likelihood). In order to complete this analysis, we needed two different ANN models: i) to qualify the relationship between vegetation cover drivers and the likelihood for identifying a luminescence age (i.e. sediment deposition) (ANN1), and ii) to construct new indirect climatic inputs (tree ring growth index) for predicting future sediment reactivation likelihoods (ANN2).

For ANN1, a stacked PDF of OSL ages from each of the six sampling sites was used as the target in the training dataset and three inputs were used as the predictor variables: i) historical tree ring growth index (Brown *et al.*, n.d.), ii) grazing pressure index (see section 6.2.5 and Paper 3), and iii) a reconstructed wildfire history from the NVP (Guyette *et al.*, 2011). See Paper 4 for further details on the pre-processing of the additional datasets, model architecture and methods of model validation.

Figure 6.1 Schematic diagram highlighting the complexities in the theoretical model that exists between the predictor variables (tree ring growth index, grazing pressure index, wildfire frequency) and the target dataset (PDF of OSL ages). This schematic diagram captures some of the additional layers of complexity and mechanistic relationships that we are unable to measure. Instead, ANNs allow us to insert datasets from two parts of the system, and the model can 'learn' the relationship, therefore avoiding the need to estimate mechanistic models and add further error and uncertainty to the process. A high degree of complexity is needed in the overall architecture to allow for the network to accommodate for these multiple hidden layers of complexity and filtering associated with our system. Please refer to Bailey and Thomas (2014) for further discussion of the filtering and complexities of sedimentary sequences.



Chapter 7

PAPER 3

Paper 3 Prelude

Having established a suitable luminescence protocol (Paper 1) and a more rigorous method for deploying limited dating resource (Paper 2), aeolian samples from NVP could be dated to produce a chronology of depositional events in the recent historical sedimentary record. Paper 3 presents a summary of the main OSL dates produced in this research project and assesses this chronological record of deposition alongside the available historical environmental data for climate, fire and human activity in the region. Paper 3 uses traditional descriptive analysis, aligning all primary and secondary data to determine if any causal relationships can be visually identified, or if any common environmental conditions can be associated with periods of reactivation in the near-surface record.

Complex disturbance-driven reactivation of the largest dunefield in the western hemisphere during the last 500 years

Paper 3: Buckland, C. E., Thomas, D. S. G., Bailey, R. M.
Status: Submitted to *Earth Surface Processes and Landforms* (16th August 2018)

Abstract

Understanding the historical activity of desert dune systems is important for identifying both the palaeoenvironmental drivers of change and the likelihood of future reactivation. Dating dune sediments in the Nebraska Sandhills has identified regional-scale dune activity over centennial and millennial timescales during the Holocene, occurring at 9.6-6.5 ka, 3.8 ka, 2.5 ka and most recently spanning the Medieval Climatic Anomaly 1050-650 years BP. These periods have been interpreted as palaeoclimatic evidence of intense aridity lasting decadal and centennial timescales. A detailed record of dune activity in the historical period, since European arrival, is however lacking, yet important for interpreting the role of human agency amongst the factors influencing disturbance. Without a high-resolution record of short term, historical, dune system activity, it is not possible to identify or quantify the drivers of localised aeolian reactivation and landscape susceptibility to different driving forces. In this paper, the individual drivers of vegetation disturbance are reviewed and presented alongside a luminescence-dated reconstruction of dune sediment deposition ages. This allows an integrated assessment of the relationship between drivers and environmental response over a recorded period. We investigated aeolian surface reactivations of dune and

blowout features in the Niobrara Valley Preserve and surrounding ranches in the northern limits of the Nebraska Sandhills. Results show peaks in dune surface deposition during the 1890s AD and 1940s AD, with spatial heterogeneity in the luminescence ages indicating that both regional (i.e. climatic) and local (i.e. land use) forcings contribute to surface disturbance.

7.1 Introduction

The Nebraska Sandhills, currently stabilised by extensive perennial warm-season grasses (Bleed, 1998), is the largest aeolian dunefield in the Western Hemisphere (Ahlbrandt and Fryberger, 1980; Loope and Swinehart, 2000) covering 57,000 km^2. Previous research, using optically stimulated luminescence (OSL) dating has identified multiple Holocene dune reactivations in the Great Plains, including at 9.6-6.5ka, 4.4-3.4ka, 2.3ka, with the most recent regional-scale period spanning the Medieval Climatic Anomaly (MCA) 1050-650 years BP (see overview in Halfen & Johnson 2013). Over millennial and centennial timescales, the dunefield reactivations have been interpreted as a proxy palaeoclimatic signal of decade or longer megadroughts, when growing season precipitation was at least 25% below average conditions (Forman *et al.*, 2001).

Over more recent timescales, localised and shorter duration aridity events have been identified in a range of proxies including lake sediments (Schmieder *et al.*, 2011), tree-ring records (Cook *et al.*, 2004) and the OSL-dated reactivation profiles of aeolian sediments (Forman *et al.*, 2005). These shorter events induced partial reactivation of the dunes, including during the 1930s Dust Bowl, that were not as spatially extensive as the MCA activation (Schmeisser McKean *et al.*, 2014).

Recent modelling studies suggest that over shorter timescales, local dune disturbance and activation is triggered by a more complex array of factors beyond simple precipitation reductions. Using the CENTURY ecosystem model, Mangan *et al*. (2004) suggested that the additive effects of fire or grazing in combination with *mild* drought conditions can create conditions that reduce biomass and favour aeolian disturbance. Stubbendieck (2008) also highlighted that a combination of factors can have a greater impact on vegetation than drought alone, highlighting the need for a more holistic approach to assessments of landscape disturbance drivers, which includes anthropogenic factors (Wolfe *et al.*, 2007). Barchyn & Hugenholtz (2013a) summarise causal disturbance forces in a conceptual model that integrates both natural and anthropogenic drivers of devegetation and thus aeolian erosion. The model hypothesises that a stabilised surface is reactivated following a disturbance event, where the term 'disturbance' refers to the rate of removal or destruction of vegetation by fire, grazing, and human manipulation of the environment as well as precipitation and drought. Whilst highlighting the need for a multifaceted assessment of disturbance, this model remains conceptual and requires empirical testing to quantify the reactivation potential of semi-arid landscapes. To date, a high-resolution study with empirical disturbance datasets has not been used to test the role of multiple factors in inducing landscape destabilisation.

In principle, if we have data for both forcing factors and landscape reactivation, it should be possible to connect disturbance drivers with an environmental response. However, the capacity to identify a coherent relationship between empirical measurements of environmental response and drivers has not

yet been assessed. By studying landscape response over the recent historical period, during which detailed climatic, land use and wildfire disturbance data have been recorded, we can identify the drivers of environmental change and how the site responded. As we expect drivers of environmental disturbance to change under future climates (e.g. Mangan *et al.*, 2004), it is important to identify a method that allows us to link drivers of environmental destabilisation with responses, facilitating the prediction of future reactivation potentials. The primary aim of this study is to provide an integrated review of the potential for empirical data to provide a link between disturbance response and drivers of surface activation in the northern Nebraska Sandhills region. Second, the study aims to assess the changing relative importance through time of natural and anthropogenic drivers of disturbance, including whether specific disturbance events can be linked clearly to distinct forcing factors.

7.1.1 Approach

Whilst anthropogenic activity is acknowledged as a contributory driver of disturbance in dryland aeolian systems, the relative significance and quantification of human versus natural factors is unknown. Barchyn and Hugenholtz (2013) identify the need for a multifaceted model of sediment reactivation, acknowledging the role of multiple drivers in disturbing the protective vegetation layer on the dune surface. We take this conceptual model further, using empirical data from the sedimentary record to test relationships between drivers and landscape reactivation in the Niobrara Valley Preserve and surrounding ranches in the northern Nebraska Sandhills (Figure 7.1). To address our aim, key datasets are needed that provide 1)

a measure of environmental reactivation, and 2) a record of potential disturbance drivers in the region.

For 1), a chronology of environmental reactivation is produced using a combination of: intense near-surface sediment sampling across dune and blowout features; changepoint analysis (Killick and Eckley, 2014, Buckland *et al.*, 2018 - Paper 2) and high-resolution quartz OSL dating, to produce a chronology of sand accumulation events. In aeolian systems, reactivation occurs in pulses where erosion and deflation of sediment at one point is immediately followed by deposition at another (Bailey and Thomas, 2014). OSL ages allow disturbance and redeposition to be recognised for time periods that predate real-time satellite and real-time measurements, encompassing a period during which we can see different scales of reactivation driven by a range of disturbance factors.

For 2), we need data for factors that have impacted vegetation cover across the Sandhills. Without a direct measure of long-term vegetation cover, existing research in the Central Great Plains and prairie grasslands (e.g. Biondini *et al.*, 1998; Forman *et al.*, 2001; Grassini *et al.*, 2010; Mangan *et al.*, 2004; Milchunas *et al.*, 1989; Schmieder *et al.*, 2011, 2012; Stubbendieck, 2008) has identified levels of historical precipitation, grazing, wild fire and land use changes as key factors that impact levels of vegetation. Records of these parameters are gathered from a range of existing instrumental and archival datasets providing information on precipitation, land use change, wild fire occurrence, and regional drought.

7.2 Study site and methods

7.2.1 Study area

Located on the south side of the Niobrara river in the northern limits of the Nebraska Sandhills, the southern section of the Niobrara Valley Preserve (NVP) and surrounding ranches used in this study cover an area c.30 km^2 (Figure 7.1). The area receives c.550 mm annual precipitation (1905 AD – present), with most of the rainfall occurring from April through to the end of August, and c.960 mm annual snowfall occurring falling from October – May. Prevailing winds from the south occur during the summer months (May – September), with stronger winds from the northwest dominating in the winter. The local area has been occupied with EuroAmerican settlers since the late-19th century and the introduction of the railroad through Brown County. Cattle ranching has remained the dominant land use in the local area since EuroAmerican occupation. A good record of recent historical events coupled with access to existing instrumental datasets and high environmental dose rates (e.g. Muhs, 2004) to aid in the OSL dating of young sediments, meant that this specific location was suitable for this research study.

Along with Google Earth imagery from 1993 onwards, archived aerial photography for 1939, 1954 and 1968 was used as a source of time-series data on vegetation cover change and observed locations of surface sediment exposure and activity. Whilst not a direct measure of sediment movement, these images provided excellent spatial coverage of all the areas included in the field sampling programme.

7.2.2 Dunefield disturbance record

Based on historical photography and geomorphological interpretations in the field, sampling aimed to capture: aeolian landscape features representative of the wider system, locations with variability in land use histories, and locations identified in aerial imagery as having been previously disturbed. In total, six sites were selected for sampling (Figure 7.1: A-F). As sedimentary profiles in aeolian environments are inherently discontinuous (Bailey and Thomas, 2014), multiple sediment cores were extracted at each site for OSL dating to ensure that zones of erosion and deposition within the system were captured (Buckland *et al.*, 2018 - Paper 2) (Figure 7.1). At each sample point, 50 cm black opaque plastic tubing was hammered vertically into surface sediments, retrieved and capped. A total of seventeen cores were returned to the Oxford Luminescence Dating Laboratory (Table 7.1).

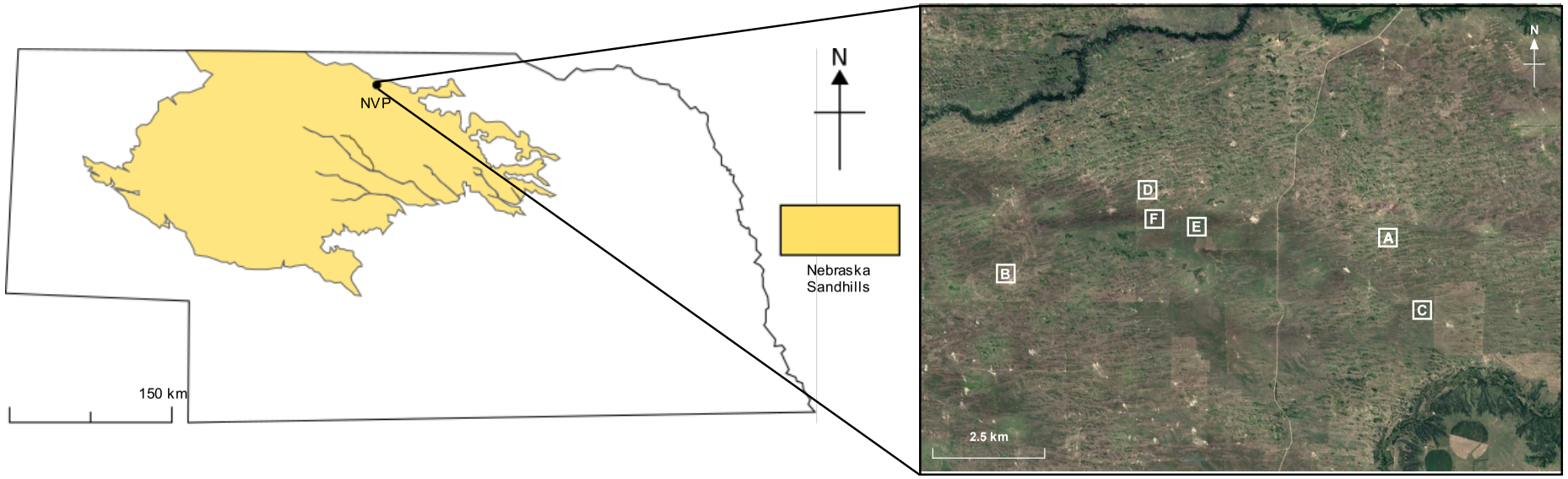


Figure 7.1 Location map of study area within the northern remits of the Nebraska Sandhills. Aerial image shows distribution of the six sample sites (Sites A-F) used in this study. Satellite imagery courtesy of © 2017 Google Earth Pro, Landsat / Copernicus.

Table 7.1 Sediment core latitude, longitude (decimal degrees) and elevation details. Site description for study sites A-F are detailed in Table 7.1.

Sediment core	Latitude	Longitude	Elevation (m a.s.l)	Site description
Site A – Blowout feature				
NVP15/1/1	42.7351	-100.0373	768	Is located on the eastern half of the NVP boundary and positioned on the upper slopes of one of the larger dune sections found in the vicinity, on the northern edge of the Hazel Creek palaeochannel. Aerial photography from 1954 and 1968 show site A was one of the most active blowouts in the Preserve. Present vegetation cover included patchy shrubs and grasses with patches of visibly bare sand. Sediment cores NVP15/1/1 and NVP15/3/1 were extracted from the top of the blowout backwall and base of the blowout respectively.
NVP15/3/1	42.7349	-100.0378	757	
Site B –Windmill site				
NVP16/2/1	42.7273	-100.1454	787	In the western limit of the study area, outside of the Niobrara Valley Preserve in the privately-owned O'Kief ranch. Four vertical sediment cores were extracted along a transect from the crest (NVP16/2/1) of a choppy dune, down the SE flank (NVP16/2 and 3) across a livestock disturbed interdune (no sample) and into a downwind deposition lobe (NVP16/2/4). The lobe appeared to be formed from sediment deflated from the disturbed area.
NVP16/2/2	42.7272	-100.1448	782	
NVP16/2/3	42.7271	-100.1446	781	
NVP16/2/4	42.7265	-100.1432	782	
Site C – The Parabolic dune				
NVP16/5/1	42.7194	-100.0285	763	A transect across a well-vegetated parabolic dune located SE of the Niobrara Valley Preserve limits. Cores from the easterly-facing parabolic dune (NVP16/5) include: parabolic dune nose (5/1), windward-dune slope (5/2), the deflation basin ahead of the dune (5/3), and from the northern arm of the parabolic dune (5/4). No active surface sands were present at the time of sampling.
NVP16/5/2	42.7195	-100.0288	762	
NVP16/5/3	42.7197	-100.0293	755	
NVP16/5/4	42.7204	-100.0293	758	
Site D –Homestead site				
NVP16/4/1	42.7444	-100.1046	768	Large blowout feature located north of the original homestead on the O'Kief's ranch.

Sediment core	Latitude	Longitude	Elevation (m a.s.l)	Site description
NVP16/4/2	42.7444	-100.1045	764	Choppy dune / basin feature appears to have accumulated against a fence line and copse of planted trees. Four cores taken along a transect trending NW-SE: crest of dune (NVP16/4/1), slope (NVP16/4/2), the deflation basin (NVP16/4/3), and up the opposite facing slope (NVP16/4/4). Transect was semi-vegetated with grasses and patches of bare sand found between grasses.
NVP16/4/3	42.7442	-100.1042	759	
NVP16/4/4	42.7438	-100.1040	761	
Site E –1930s dune				
NVP15/4/1	42.7372	-100.0919	761	Fence line dune located south of Site D on the Sandhill and Sun Ranch. Site E noted as having experienced deposition in the 1930s when sediment was eroded from the adjacent prairie dog town and deposited along the boundary fence of the ranch. One vertical core (NVP15/4/1) was extracted from this site to explore the variability in the landscape when placed near Sites D and F.
Site F – Old rolling dunes				
NVP16/6/1	42.7391	-100.1036	757	Selected as a comparison site to the other sampling sites as this location did not show any present evidence for recent reactivation, nor did the archived aerial photography or the ranchers accounts. Two vertical sediment cores were extracted from this site: crest of vegetated rolling dune (NVP16/6/1) and from a relative low point (NVP16/6/2).
NVP16/6/2	42.7393	-100.1033	752	

Samples were prepared and analysed under subdued orange light. The plastic tubing was split lengthwise and sediments sub-sampled at centimetre scale, dried and mounted onto single 8 mm diameter discs for initial changepoint analysis. Changepoint analysis, which allows significant breaks in sedimentation to be identified statistically, was applied to all sub-samples from the seventeen sediment cores prior to selection of sub-samples for full-preparation luminescence dating (Buckland *et al.*, 2018 - Chapter 5). This method led to a range of mid-section and

end-point samples being identified from the cores as representative of dune activity phases and appropriate for full OSL dating. Sensitivity-corrected OSL L_x/T_x profiles, and the locations of breakpoints were coupled with the age data from fully-dated samples to provide depositional structure context to the OSL ages.

Based on the results of the changepoint analysis, sub-samples that were selected for full OSL dating were treated in an excess of hydrochloric acid (HCl) and hydrogen peroxide (H_2O_2) to remove carbonates and organics prior to wet-sieving to the desired size fraction (125-180 μm). Density separation using sodium polytungstate was used to separate out the quartz grains, and a 60 minute etch in hydrofluoric acid (HF ~ 40%) followed by a final treatment in HCl were used to remove any remaining feldspar crystals.

Following chemical treatment, a minimum of sixteen small aliquots per selected sub-sample were measured following the single-aliquot regenerative-dose (SAR) protocol (Murray and Wintle, 2000; Wintle and Murray, 2006), with preheats (PH1 and PH2 - 200°C for 10 s) determined following a series of preheat plateau and dose recovery tests (Buckland *et al.*, 2018 - Chapters 4 & 5). Equivalent dose measurements were made following the measurement procedures outlined in (Buckland *et al.*, 2018 - Chapters 4 & 5). Partially-bleached aliquots were identified using a series of $D_e(t)$-plots (Bailey *et al.*, 2003) and rejected to avoid an overall age estimation. Based on the young nature of the sediments, sub-sample equivalent doses were calculated using the un-logged Central Age Model (CAM) (Arnold *et al.*, 2009; Galbraith *et al.*, 1999). See Appendix K (Part 1) for typical decay curve examples.

Environmental dose measurements were calculated using radionuclide concentrations (^{232}Th, ^{238}U and ^{40}K) measured using ICP-MS, and the Dose Rate and Age Calculator (Durcan *et al.*, 2015). Where no stratigraphic change was noted, and radionuclide concentrations were normally distributed between sub-samples of the same sediment core, a weighted average of radionuclide concentrations was used for multiple sub-samples within the respective sediment cores. Moisture content was estimated according to the method detailed in Nelson and Rittenour (2015) and calculated in the Hydrus-1D modelling program (Simunek *et al.*, 2008). Using standard conversion factors for grain size adjustments (Mejdahl, 1979), HF-etching (Bell, 1979), beta attenuation (Guérin *et al.*, 2011), water content (Aitken, 1985) and cosmic dose rates (Prescott and Hutton, 1994), annual dose rates were calculated and used for final age estimates.

To improve the chronological resolution and reduce the uncertainty estimates, Bayesian age-depth models were created for sediment cores that identified sub-samples with overlapping age estimates using the freeware OxCal software package (version OxCal 4.3) (Bronk Ramsey, 2009). The model applies a sequential order upon the sub-sample OSL age estimates based on the depths and stratigraphical positions within the sediment core. Bayesian age-depth models were produced for sediment cores NVP15/1/1, NVP15/3/1 (site A) and NVP15/4/1 (site E) and modelled ages are presented alongside un-modelled ages in Table 7.2.

7.2.3 Vegetation cover drivers

Vegetation cover is both a protective 'skin' (Wolfe and Nickling, 1993) and a source of disturbance suppression that works to stabilise dune sediments and

prevent surface reactivation (Barchyn and Hugenholtz, 2013). The key determinants of cover levels include precipitation, grazing pressure, wildfire occurrence and land use changes. Data for each of these factors was used to reconstruct past vegetation cover levels, as follows.

Precipitation directly affects drought occurrence, plant-available moisture, and thus levels of vegetation cover. Precipitation during the April-October growing season, (Stubbendieck, 2008) is the key determinant of vegetation cover in any year (Grassini *et al.*, 2010). Daily precipitation data from Ainsworth, Nebraska (42.58° N, -100.05° W, <10 miles from the study sites) was sourced from the National Centres of Environmental Information (https://www.ncdc.noaa.gov/ - accessed on 04/01/2018) for 1905-2015. Annual growing season totals were calculated, and years with >5% missing data were omitted from the analysis to avoid incorrect identification of drought conditions.

The Palmer Drought Severity Index (PDSI) is a metric of annual historical drought conditions (Palmer, 1965). In order to extend the range of PDSI coverage to capture multi-century timescales, we used data from the North American Drought Atlas (Cook and Krusic, 2004). The closest PDSI data point in this study, grid point 161 (42.5° N, -100° W), is based on a cumulative regional signal taken from trees in a 2.5° x 2.5° grid, ranging from 8 – 33 tree-ring records from 1500 – 2003 AD. Whilst the precipitation record using in this study provides daily measurements, PDSI values from Cook and Krusic, (2004) extend over the last 500 years, but at the expense of spatial detail in the coverage provided.

Wildfires can remove above-ground biomass, exposing the underlying sediments to aeolian processes. Precipitation levels are also linked to the likelihood

of wildfire occurrence, impacting both the availability of fuel for fire, and determining aridity levels and the subsequent likelihood for a fire to start (Guyette *et al.*, 2015). A wildfire history for the study site was compiled using data from the tree scar record for NVP in Guyette *et al.* (2011). The fire scar history of 39 tree samples spans the last 300 years and records 30 separate wildfires. To include fires relevant to the study area, only those identified in the records of at least two individual trees were considered as likely to have had an impact extending widely over the landscape. A large wildfire that occurred in 2012, burning 66,000 acres across NVP and surrounding ranches, has also been included in the analysis.

Identifying grazing pressures on the different sampling sites over the last 200 years is not possible due to data scarcity, and difficulties in assessing past livestock movements in response to changing environmental conditions. For example, land management strategies, stocking rates, and grazing levels will change on a variety of temporal scales in response to weather conditions such as winter blizzards and droughts. The impact of any concentration of livestock on vegetation (i.e. 'overgrazing') will also be affected by antecedent climate (e.g. Forman *et al.*, 2001). Given these complexities, a coarse-scale assessment of general grazing and land use intensity was developed with a temporal resolution appropriate for the data scale of other variables.

Based on local land use and grazing pressure data, a table of 'potential grazing pressure intensity' was produced (Table 7.3). Local land ownership history and land use changes have been sourced from original land alienation reports, historical reports, and interviews with local ranchers and Preserve managers. Key dates associated with the regional development of the railroad as well as land

ownership acts are included in this study. Notable periods of grazing and land use pressure change were identified, with periods classified as either: 1 (low pressure), 2 (moderate grazing pressure) or 3 (high grazing pressure) based on combining data on: the level of population in the surrounding area, knowledge of ranching / agriculture strategies, land ownership chronologies and wild versus open / closed ranching levels. Together, these are used to suggest relative periods of increased and decreased pressure which can be analysed alongside the other disturbance factors. Intensity classifications and time intervals have been verified by colleagues and local ranchers who have studied and managed pastures in the local region for many decades. Similar extrapolations of a quantitative classification index from qualitative datasets have successfully been completed in other areas of environmental science (e.g. Adamson and Nash, 2014; Grab and Nash, 2010; Nash *et al.*, 2016; Nicholson, 2001a, 2001b, Nicholson *et al.*, 2012a, 2012b) to identify variability in historical climates.

Wind erosivity potential is key in determining whether sediment will be mobilised when surfaces are bare. Wind speed data from Valentine, Nebraska (42.88° N, -100.55° W) from 1987 – 2017 AD has shown that average daily wind speeds have exceeded the wind speed entrainment thresholds 4.5 m/s (Lancaster, 1988) and 5.97 m/s (Bullard *et al.*, 1996) for 97% and 88% of the time respectively. Given this, wind speed has not been considered a limiting factor on sediment transport when surfaces are bare and has not been included as a key controlling variable on sediment movement in this location.

7.3 Results and Discussion

The reactivation ages for sub-samples dated across the six sites are presented in Table 7.2 and Figure 7.2. OSL ages are notably younger than those usually published in the luminescence literature. A combination of technique-focusing methods (Buckland *et al.*, 2018 - Paper 2) and optical mineralogical properties (Muhs, 2004) ensured that OSL methods could successfully be applied to these sediments to produce reliable age estimates < 200 years with errors as low as 5%. Reactivation ages from individual sub-samples are reported as calendar dates AD to allow comparison with the historical, instrumental and land use datasets.

7.3.1 Dune reactivation histories

The aim of the multiple-core sampling strategy was to ensure OSL-dated chronologies would capture the heterogeneity of the aeolian record within individual features, allowing both zones of erosion and accumulation to be represented in the final timeline of reactivation events. Capturing the variability in the record both within and between sampling sites is important in providing a fuller deposition history of the dunes, but also in developing an understanding of the variability in environmental response to a range of disturbances that act at different spatial scales. Vertical sediment profiles were typically characterised by homogenous light sands with a lack of any visible stratigraphy or organic matter; exceptions were noted at sites C and F where thin soil layers were found overlying aeolian sand units.

Table 7.2 Results for all sub-samples measured using full-preparation OSL dating. Sub-sample ages were calculated based on an overburden density 1.9 ± 0.1 g/cm^3 and water content 3 ± 2% following the method described in Nelson and Rittenour (2015). [A] Equivalent dose calculated using un-logged Central Age Model (Galbraith *et al.*, 1999). [B] Total dose rates calculated using DRAC (Durcan *et al.*, 2015), with weighted averages of radionuclide concentrations used in homogenous sediment cores. [C] Date presented in years (AD) based on sediment sampling in 2015 & 2016. [D] Bayesian modelled dates for sediment cores that showed overlapping ages between sub-samples (Bronk Ramsey, 2009) (Appendix K: Part 2)

Core	Sub-sample	Depth (cm below surface)	Aliquots (n)	$D_e \pm 1\sigma$ (Gy) [A]	Dose rate (Gy ka^{-1}) [B]	Age ± 1σ (ka)	Date ± 1σ (AD) [C]	Date ± 1σ (AD) [D]
Site A – Blowout feature								
NVP15/1/1/1	NVP15/1/1/1	1	25	-0.007 ± 0.016	1.98 ± 0.05	-0.003 ± 0.008	2018 ± 8	2014 ± 9
	NVP15/1/1/10	10	19	0.087 ± 0.042	2.13 ± 0.05	0.041 ± 0.02	1974 ± 20	1998 ± 10
	NVP15/1/1/20	20	16	0.08 ± 0.037	2.15 ± 0.05	0.037 ± 0.017	1978 ± 17	1984 ± 8
	NVP15/1/1/25	25	18	0.071 ± 0.033	2.15 ± 0.05	0.033 ± 0.015	1982 ± 15	1978 ± 9
	NVP15/1/1/30	30	22	0.17 ± 0.068	2.15 ± 0.05	0.079 ± 0.032	1936 ± 32	1971 ± 9
	NVP15/1/1/40	40	19	0.14 ± 0.035	2.15 ± 0.05	0.065 ± 0.016	1950 ± 16	1959 ± 10
	NVP15/1/1/50	50	19	0.12 ± 0.029	2.15 ± 0.05	0.056 ± 0.014	1959 ± 14	1948 ± 12
NVP15/3/1	NVP15/3/1/1	1	20	0.10 ± 0.044	1.65 ± 0.05	0.061 ± 0.027	1954 ± 27	1959 ± 18
	NVP15/3/1/10	10	21	0.19 ± 0.061	1.75 ± 0.04	0.109 ± 0.035	1906 ± 35	1951 ± 14
	NVP15/3/1/20	20	21	0.20 ± 0.10	1.76 ± 0.04	0.113 ± 0.057	1902 ± 57	1943 ± 12
	NVP15/3/1/25	25	26	0.11 ± 0.022	1.76 ± 0.04	0.062 ± 0.013	1953 ± 13	1939 ± 11
	NVP15/3/1/30	30	19	0.12 ± 0.059	1.76 ± 0.04	0.068 ± 0.034	1947 ± 34	1934 ± 12
	NVP15/3/1/40	40	21	0.19 ± 0.065	1.75 ± 0.04	0.108 ± 0.037	1907 ± 37	1923 ± 17
	NVP15/3/1/50	50	23	0.25 ± 0.067	1.74 ± 0.04	0.143 ± 0.039	1872 ± 39	1914 ± 25
Site B – Windmill site								
NVP16/2/1	NVP16/2/1/6	6	23	0.20 ± 0.045	2.29 ± 0.05	0.087 ± 0.02	1929 ± 20	
	NVP16/2/1/25	25	18	0.71 ± 0.071	2.36 ± 0.05	0.30 ± 0.031	1716 ± 31	
	NVP16/2/1/38	38	22	0.91 ± 0.11	2.36 ± 0.05	0.386 ± 0.047	1630 ± 47	
	NVP16/2/1/44	44	18	1.37 ± 0.071	2.35 ± 0.05	0.582 ± 0.032	1434 ± 32	

Core	Sub-sample	Depth (cm below surface)	Aliquots (n)	$D_e \pm 1\sigma$ (Gy) [A]	Dose rate (Gy ka^{-1}) [B]	Age ± 1σ (ka)	Date ± 1σ (AD) [C]	Date ± 1σ (AD) [D]
NVP16/2/2	NVP16/2/2/9	9	17	0.39 ± 0.091	2.32 ± 0.05	0.168 ± 0.039	1848 ± 39	
	NVP16/2/2/33	33	20	1.66 ± 0.082	2.36 ± 0.05	0.703 ± 0.038	1313 ± 38	
NVP16/2/3	NVP16/2/3/10	10	16	0.47 ± 0.13	2.33 ± 0.05	0.202 ± 0.056	1814 ± 56	
	NVP16/2/3/34	34	16	1.03 ± 0.095	2.36 ± 0.05	0.437 ± 0.041	1579 ± 41	
NVP16/2/4	NVP16/2/4/5	5	42	0.13 ± 0.047	2.28 ± 0.05	0.057 ± 0.021	1959 ± 21	
	NVP16/2/4/25	25	21	0.21 ± 0.042	2.36 ± 0.05	0.089 ± 0.018	1927 ± 18	
	NVP16/2/4/45	45	55	0.27 ± 0.052	2.35 ± 0.05	0.115 ± 0.022	1901 ± 22	
Site C – The Parabolic dune								
NVP16/5/1	NVP16/5/1/7	7	18	0.26 ± 0.10	2.46 ± 0.05	0.106 ± 0.041	1910 ± 41	
	NVP16/5/1/17	17	17	0.45 ± 0.057	2.52 ± 0.05	0.179 ± 0.023	1837 ± 23	
	NVP16/5/1/30	30	17	1.15 ± 0.065	2.53 ± 0.05	0.455 ± 0.027	1561 ± 27	
	NVP16/5/1/43	43	16	1.67 ± 0.093	2.52 ± 0.05	0.663 ± 0.039	1353 ± 39	
NVP16/5/2	NVP16/5/2/9	9	23	0.27 ± 0.059	2.33 ± 0.05	0.116 ± 0.025	1900 ± 25	
	NVP16/5/2/32	32	23	1.76 ± 0.079	2.18 ± 0.05	0.807 ± 0.04	1209 ± 40	
NVP16/5/3	NVP16/5/3/7	7	19	0.31 ± 0.040	2.48 ± 0.06	0.125 ± 0.016	1891 ± 16	
	NVP16/5/3/21	21	20	1.89 ± 0.11	2.92 ± 0.06	0.647 ± 0.04	1369 ± 40	
	NVP16/5/3/39	39	16	1.92 ± 0.11	2.59 ± 0.05	0.74 ± 0.045	1276 ± 45	
NVP16/5/4	NVP16/5/4/3	3	21	0.30 ± 0.088	2.40 ± 0.06	0.125 ± 0.037	1891 ± 37	
	NVP16/5/4/27	27	18	1.91 ± 0.099	2.56 ± 0.05	0.747 ± 0.042	1269 ± 42	
Site D – Homestead site								
NVP16/4/1	NVP16/4/1/5	5	17	0.072 ± 0.037	2.26 ± 0.05	0.032 ± 0.016	1984 ± 16	
	NVP16/4/1/25	25	27	0.13 ± 0.029	2.35 ± 0.05	0.055 ± 0.012	1961 ± 12	
	NVP16/4/1/45	45	20	0.17 ± 0.019	2.34 ± 0.05	0.073 ± 0.008	1943 ± 8	
NVP16/4/2	NVP16/4/2/5	5	28	0.19 ± 0.071	2.26 ± 0.05	0.084 ± 0.031	1932 ± 31	
	NVP16/4/2/20	20	17	0.30 ± 0.071	2.34 ± 0.05	0.128 ± 0.03	1888 ± 30	
	NVP16/4/2/23	23	64	1.34 ± 0.043	2.35 ± 0.05	0.571 ± 0.022	1445 ± 22	
	NVP16/4/2/26	26	30	1.16 ± 0.094	2.35 ± 0.05	0.494 ± 0.041	1522 ± 41	
	NVP16/4/2/36	36	38	1.48 ± 0.12	2.34 ± 0.05	0.632 ± 0.053	1384 ± 53	
	NVP16/4/2/46	46	39	1.59 ± 0.084	2.34 ± 0.05	0.681 ± 0.039	1335 ± 39	

Core	Sub-sample	Depth (cm below surface)	Aliquots (n)	$D_e \pm 1\sigma$ (Gy) [A]	Dose rate (Gy ka^{-1}) [B]	Age ± 1σ (ka)	Date ± 1σ (AD) [C]	Date ± 1σ (AD) [D]
NVP16/4/3	NVP16/4/3/11	11	22	0.33 ± 0.058	2.32 ± 0.05	0.142 ± 0.025	1874 ± 25	
	NVP16/4/3/29	29	17	0.73 ± 0.072	2.35 ± 0.05	0.311 ± 0.031	1705 ± 31	
	NVP16/4/3/43	43	18	4.69 ± 0.23	2.34 ± 0.05	2.005 ± 0.107	11 ± 107	
NVP16/4/4	NVP16/4/4/3	3	24	0.63 ± 0.12	2.21 ± 0.05	0.285± 0.055	1731 ± 55	
	NVP16/4/4/10	10	34	0.76 ± 0.081	2.31 ± 0.05	0.329 ± 0.036	1687 ± 36	
	NVP16/4/4/12	12	23	1.17 ± 0.11	2.32 ± 0.05	0.504 ± 0.049	1512 ± 49	
	NVP16/4/4/29	29	20	1.95 ± 0.10	2.35 ± 0.05	0.831 ± 0.046	1185 ± 46	
	NVP16/4/4/47	47	44	1.84 ± 0.074	2.34 ± 0.05	0.788 ± 0.036	1228 ± 36	
Site F – 1930s dune								
NVP15/4/1	NVP15/4/1/5	5	20	0.14 ± 0.043	2.51 ± 0.06	0.056 ± 0.017	1959 ± 17	1955 ± 11
	NVP15/4/1/10	10	20	0.18 ± 0.018	2.57 ± 0.06	0.07 ± 0.007	1945 ± 7	1942 ± 8
	NVP15/4/1/15	15	17	0.30 ± 0.051	2.60 ± 0.05	0.116 ± 0.02	1899 ± 20	1920 ± 11
	NVP15/4/1/20	20	19	0.28 ± 0.058	2.61 ± 0.05	0.107 ± 0.022	1908 ± 22	1905 ± 12
	NVP15/4/1/25	25	19	0.38 ± 0.086	2.61 ± 0.05	0.146 ± 0.033	1869 ± 33	1888 ± 13
	NVP15/4/1/30	30	19	0.46 ± 0.083	2.61 ± 0.05	0.176 ± 0.032	1839 ± 32	1873 ± 14
	NVP15/4/1/35	35	19	0.44 ± 0.085	2.61 ± 0.05	0.169 ± 0.2	1846 ± 33	1860 ± 14
	NVP15/4/1/40	40	19	0.52 ± 0.094	2.61 ± 0.05	0.2 ± 0.036	1815 ± 36	1848 ± 15
	NVP15/4/1/45	45	27	0.41 ± 0.047	2.6 ± 0.05	0.158 ± 0.018	1857 ± 18	1838 ± 16
Site F – Old rolling dunes								
NVP16/6/1	NVP16/6/1/4	4	17	0.21 ± 0.041	2.37 ± 0.05	0.089 ± 0.017	1927 ± 17	
	NVP16/6/1/12	12	17	0.75 ± 0.085	2.61 ± 0.06	0.287 ± 0.033	1729 ± 33	
	NVP16/6/1/25	25	17	1.49 ± 0.14	2.63 ± 0.06	0.567 ± 0.055	1449 ± 55	
	NVP16/6/1/41	41	16	1.87 ± 0.098	2.59 ± 0.05	0.722 ± 0.041	1294 ± 41	
NVP16/6/2	NVP16/6/2/7	7	16	0.43 ± 0.037	2.57 ± 0.06	0.168 ± 0.015	1848 ± 15	
	NVP16/6/2/15	15	18	1.14 ± 0.077	2.65 ± 0.06	0.43 ± 0.03	1586 ± 30	
	NVP16/6/2/34	34	19	1.82 ± 0.088	2.62 ± 0.06	0.695 ± 0.037	1321 ± 37	


D
N
NVP16/4/1
NVP16/4/2
NVP16/4/3
NVP16/4/4
Original homestead
70 m
Homogeneous light sands
Elevation (m a.s.l.)
768
763
758
17 m
33 m
43 m
Distance (m)
NVP16/4/1
NVP16/4/2
NVP16/4/3
NVP16/4/4
Depth below surface (cm)
1984 ± 16
1961 ± 12
1943 ± 8
1932 ± 31
1888 ± 30
1445 ± 22
1522 ± 41
1384 ± 53
1335 ± 39
1874 ± 25
1705 ± 31
11 ± 107
1731 ± 55
1687 ± 36
1512 ± 49
1185 ± 46
1228 ± 36
F
N
NVP16/6/2
NVP16/6/1
40 m
Elevation (m a.s.l.)
757
754
751
30 m
Distance (m)
NVP16/6/1
NVP16/6/2
Depth below surface (cm)
1927 ± 17
1729 ± 33
1449 ± 55
1294 ± 41
1848 ± 15
1586 ± 30
1321 ± 37
Homogeneous light sands
Dark sandy organics
Organics
N
D
F
E
B
2.5 km
B
N
NVP16/2/2
NVP16/2/1
NVP16/2/3
NVP16/2/4
60 m
Homogeneous light sands
Elevation (m a.s.l.)
788
784
780
49 m
24 m
130 m
Distance (m)
NVP16/2/1
NVP16/2/2
NVP16/2/3
NVP16/2/4
Depth below surface (cm)
1929 ± 20
1716 ± 31
1630 ± 47
1434 ± 32
1848 ± 39
1313 ± 38
1814 ± 56
1579 ± 41
1959 ± 21
1927 ± 18
1901 ± 22

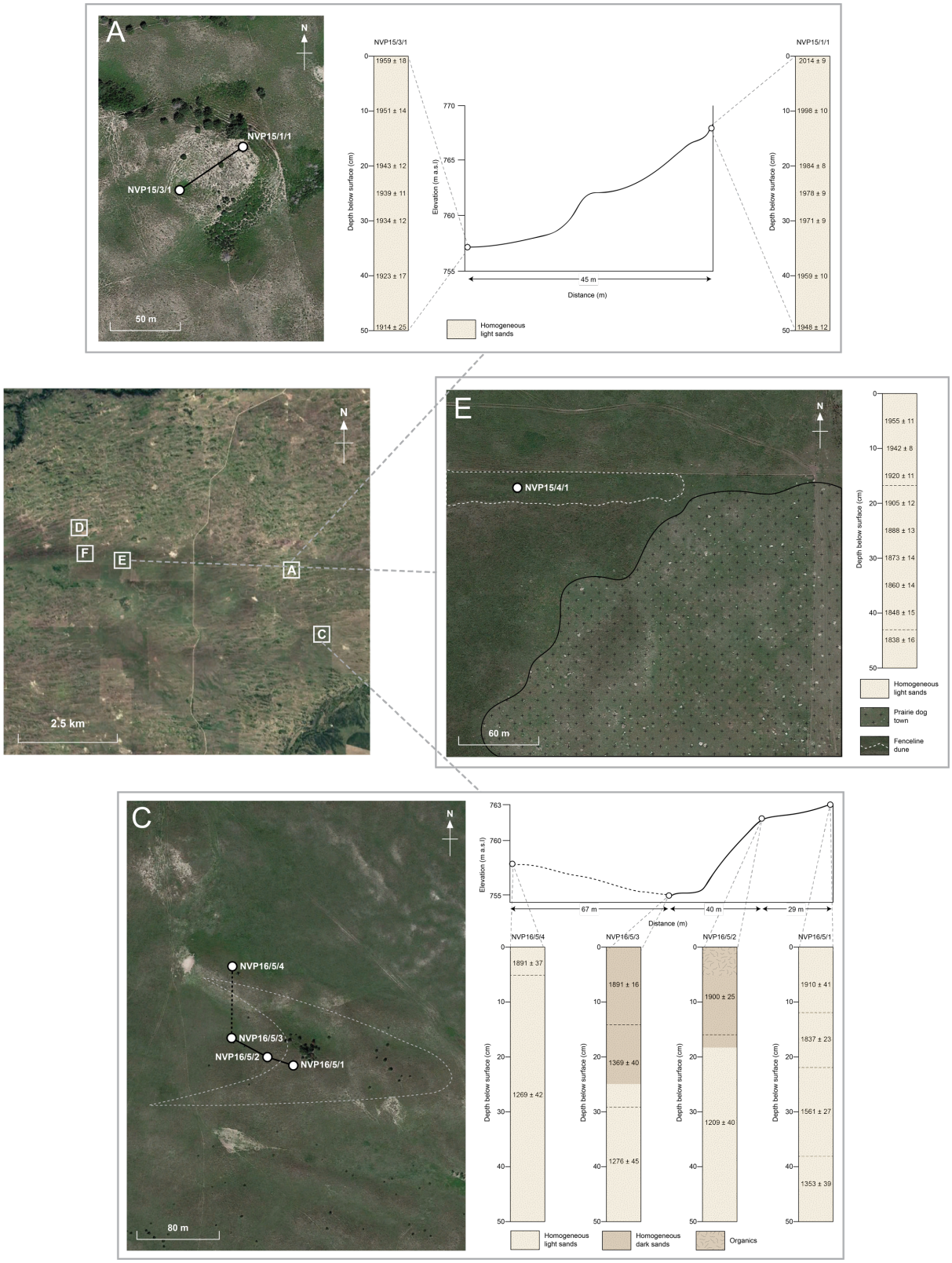


Figure 7.2 Aerial photographs showing location of transects and sediment cores taken at each of the six sites. Site transects, elevation profile, sedimentary logs and OSL results are presented for each sediment core. Dashed lines represent breakpoints in L_x/T_x measurements according to changepoint analysis. (A) Two cores were extracted at Site A – Blowout feature: NVP15/1/1 (42.7351° N, -

100.0373° W) and NVP15/3/1 (42.7349° N, 100.0378° W). Homogeneous light sands dominated both cores with no lithostratigraphic structure or significant changes in chronostratigraphy identified either visually or algorithmically. (B) Four cores were extracted at Site B – Windmill site: NVP16/2/1 (42.7273° N, -100.1454° W), NVP16/2/2 (42.7273° N, -100.1448° W), NVP16/2/3 (42.7271° N, -100.1446° W) and NVP16/2/4 (42.7265° N, -100.1432° W). Like site A, homogenous light sands dominated all four sediment cores at site B. (C) Four cores were sampled at Site C – Parabolic dune: NVP16/5/1 (42.7194° N, -100.0285° W), NVP16/5/2 (42.7195° N, -100.0288° W), NVP16/5/3 (42.7197° N, -100.0293° W) and NVP16/5/4 (42.7304° N, -100.0293° W) with a combination of organic units and aeolian sands found amongst the cores. (D) Four cores were extracted at Site D – Homestead site: NVP16/4/1 (42.7444° N, -100.1046° W), NVP16/4/2 (42.7444° N, -100.1045° W), NVP16/4/3 (42.7442° N, -100.1042° W) and NVP16/4/4 (42.7438° N, -100.1040° W). All four sediment cores taken at Site D comprise homogeneous light aeolian sands with active sands noted at the surface of NVP16/4/3 during field sampling. (E) One core was sampled at Site E – 1930s dune: NVP15/4/1 (42.7372° N, -100.0919° W) from a fenceline dune that anecdotally was active during the 1930s. (F) Two cores were extracted at Site F – Old rolling dunes: NVP16/6/1 (42.7391° N, -100.1036° W) and NVP16/6/2 (42.7393° N, -100.1033° W). Like profiles found at site C, both NVP16/6/1 and NVP16/6/2 showed upper organic-rich layers, overlying homogenous light sands. Changepoint analysis and noted lithological variability guided sub-sample selection for OSL dating. Satellite imagery courtesy of © 2017 Google Earth Pro, Landsat / Copernicus.

Initial field assessments at site A suggested sediment has been scoured from the base of a blowout by prevailing westerly winds, creating a deflation basin, and deposited on the eastern crest of the blowout. OSL results support initial field interpretations, with older ages found at the surface of the blowout basin (NVP15/3/1) and modern sediments located at the crest of the blowout backwall (NVP15/1/1). The presence of sediments dated from 1959 ± 18 AD, 1 cm below the surface of NVP15/3/1, suggests this is an active erosional site where a thin layer of bleached material overlies a profile that is gradually being eroded and redeposited at NVP15/1/1. Contrastingly, the 50 cm section from the crest of the backwall, shows a gradual accumulation of sediments from 1948 ± 12 AD until the

present day. The oldest near-surface sediments found at this site are dated to the end of the 19th century and agree with dune ages found at the other sampling sites.

OSL ages at site B reconstruct the history of reactivation across a transect running from a dune crest, across a disturbed inter-dune area where a windmill water pump focusses livestock concentration, to a lobe of redeposited sediment. Based on this understanding we would expect the first three sediment cores to represent zones of erosion whilst NVP16/2/4, shown in 1968 aerial imagery as an extending depositional lobe, is in a position of currently accumulating sand. Eleven OSL samples show the youngest ages are at site NVP16/2/4. Ages show a general increase in age down from the surface, extending back to 1901 ± 22 AD at 50 cm depth. NVP16/2/1, 2/2 and 2/3 have older surface sediments, potentially representing current sites of erosion where overlying sediments are progressively being removed and redeposited downwind. Whilst older ages could suggest zones of stability, the near-surface location of these ages, coupled with a distinct lack of organic matter suggests this is likely a zone of erosion as opposed to stability.

Greater sedimentological variability at site C, coupled with the presence of an overlying organic unit (NVP16/5/2 & NVP16/5/3), suggests less activity at this site than that found at the visibly active homogeneous sand sites. This theory is supported by OSL results that show older depositional events in the near surface sediments than those found in the visibly active sites of A and B. A large age range is covered across the sub-samples taken from the four cores, with 1910 ± 41 AD identified in the uppermost unit at NVP16/5/1 to 1209 ± 40 AD in the deepest part of NVP16/5/2. Coupled with the changepoint analysis, we can identify common chronological units between the sediment cores: 1) mid-13th century, 2) mid-14th

century, 3) late-19th / early-20th century, yet the lithological variation in this third unit suggests they may not be the same unit. The unit encompassing 1890-1900 AD is commonly found across other sampling sites.

Site D is located at an old homestead site and has evidence of significant landscape disturbance in the form of a large blowout feature. Sediment appears to have been scoured from the basin by the dominant northwesterly winds and deposited on adjacent dune slopes. Near-surface OSL ages span the late-20th century to 1st century AD, with common units appearing in multiple cores: i) the deepest units in both slopes (NVP16/4/2 and NVP16/4/4) extend back from the early-16th century; and ii) the middle unit in NVP16/4/3 and uppermost unit in NVP16/4/4 capture reactivation in the early-18th century. As expected, the upper crestal region (NVP16/4/1) is dominated by recent sediments.

OSL ages from NVP15/4/1 (site E) show periods of dune activity from the mid-19th century until the late-20th century, with ages in the 1890s and 1950s in agreement with those at other sites (Figure 7.2E). The changepoint model for this core required a high level of model sensitivity since a relatively short time period was covered in the sediment core; identified breaks are structurally less significant and may be influenced by noise within the coarse OSL profile.

Site F ages capture a series of reactivation events from 1927 ± 17 to 1291 ± 41 AD in the sediment profiles (Figure 7.2F). Break points in the chronology determined by changepoint analysis, coupled with the OSL ages, show distinct activity phases where one sigma age errors do not overlap. The ages of the deepest units in each core are within errors of each other, suggesting a spatially extensive period of activity in the late-13th / early-14th century with subsequent periods of

activity preserved in the overlying soil horizons. There is a distinct lack of post-1927 AD reactivation events recorded at this site, although successive reactivations may have been eroded from the landscape. However, the well-developed soil horizon, paired with a lack of archival or geomorphological evidence, suggests this site has likely been stable for the last 90 years.

7.3.2 Integrating deposition and driver profiles

Deposition profiles for each site are shown in Figure 7.3 alongside site-specific and regional scale disturbance datasets from 1840 AD to the present. The one sigma age uncertainties associated with the stacked OSL records restricts the capacity to identify individual episodes of surface deposition, with the results potentially interpretable as indicating quasi-continuous sediment movement through the period of analysis. While there are limitations with the use of probability density function (PDF) plots for age presentation (Thomas and Burrough, 2012), the continuous sampling in 50 cm cores and the use of changepoint analysis means that all recoded events have an equal probability of being sampled. In this context therefore, PDFs are a useful aid to data interpretation. Figure 7.3j shows peaks in the frequency of ages in the early-1900s and mid-1940s. A peak in ages in the mid-1940s occurs following the longest drought period identified in the record over the past 100 years. Likewise, the droughts of the late-1950s and mid-1970s coincide with clusters of OSL ages.

The PDSI record identifies multiple periods of drought in the mid and late-19th century, a short dry phase in the early-20th century, followed by episodic drought conditions during the 1930s, 1950s, and more recently in the late-20th

century (Figure 7.3a). The PDSI record agrees with the shorter observational precipitation record which shows drier growing seasons during the 1930s, 50s, 70s and infrequently during the last thirty years (Figure 7.3b). Wildfire occurrences (Figure 7.3c) have decreased in the 20th century following a peak from the mid-1870s to early 20th century. This peak coincides with the advent of EuroAmerican settlement and railroad construction through the Sandhills. Only study site A was located inside the boundary of the extensive wildfire in 2012, with sites D and C within 0.5-1 km of the fire boundary.

Notable socioeconomic events, land use changes, and a history of grazing pressure and strategy are presented in Figure 7.3 and explained in detail in Table 7.3. A shift from unorganised territory and open-range ranching occurred in the late-19th century, followed by a boom in immigration as settlers arrived in Brown County with the development of the railroad (post-1883). Whilst pressure on the land was high with initial settlers degrading the surface on the small plots they farmed, a gradual improvement in grazing strategy and land management practices has taken place over the last 70 years. All six sites sampled in this study are currently used for cattle grazing (site A has been used for bison grazing since 1985) and have been occupied since the late 19th – early 20th centuries.

Combined forcing factors coupled with a 5-year lag period are shown in Figure 3h to highlight periods when conditions were more favourable to surface reactivation. Following the conclusions of Mangan *et al.* (2004) and Stubbendieck (2008), these periods show a range of scenarios where different levels of drought intensity have been combined with known periods of intense grazing or wildfires to deduce a timeline of 'expected sediment movement'. Results suggest that pre-

1890, surface reactivation events were likely caused by a combination of drought conditions and wildfires in the local area. Subsequently, episodes of 'expected sediment movement' from 1890-1930 are more likely attributed to land degradation driven by a combination of overgrazing and increased aridity. Post-1930 is characterised by a marked reduction in the frequency of wildfires.

Aerial photographs from 1939, 1954 and 1968 as well as recent Google Earth imagery (1993 – present) provide a high spatial resolution of vegetation cover change across the samples sites and wider region (Appendix K: Part 3). Orange and red bars in Figure 7.3i demonstrate periods of 'almost bare' and 'completely bare' vegetation cover respectively for individual sample sites. Images show that site D has had almost no vegetation cover in all the photographs that have been assessed, with periods of completely bare surface coverage in the mid-20th century, and more recently when the wider environment has equally shown reduced vegetation cover.

Stacked OSL ages for each sample site allow for reactivation timings to be compared against forcing factor data (Figure 7.3i). A multicore strategy with stacked ages for each site ensures that both the zones of erosion and deposition are represented in the reactivation chronology of a localised feature. Exploring the results by sample site makes it possible to identify variability between the response of the geomorphological features (i.e. sites) where some forcings affect all sites (e.g. climate) but others are site-specific (e.g. grazing pressure).

Reactivation events at site A coincide with the date of original homesteading in the early-20th century, increased ranching pressures and the severe blizzard of 1948-49. These events also overlap with droughts identified in the historical record, while a lack of disturbances from the 1980s corresponds with the decommissioning

of commercial ranches and the establishment of the NVP. A peak in reactivation at site B from 1900 - 1930 AD occurs at the same time as the installation of the groundwater pump found at this site, which would have led to livestock concentrations in this area and increased environmental pressures. The reactivation history at site C shows a slightly earlier peak in activity with ages in the late-19th / early-20th century, coinciding with identifiable droughts in the PDSI record as well as notable blizzards. Site D OSL ages and uncertainties span the length of the period investigated, however, unlike other sites, there does not appear to be a peak in ages associated with the increase in settlement and ranching in the region. Given the persistently limited vegetation cover at this sample site, it is likely that a series of erosional events have left a complex and potentially incomplete record at site D. Site E also shows a near-continuous accumulation record from mid-19th to mid-20th century, but here peaks in accumulation can be identified in the 1900s and 1940s, which follow notable droughts recorded in the historical and PDSI records. Site F produces the fewest recent near-surface OSL ages, with no evidence for reactivation since the early-20th century.

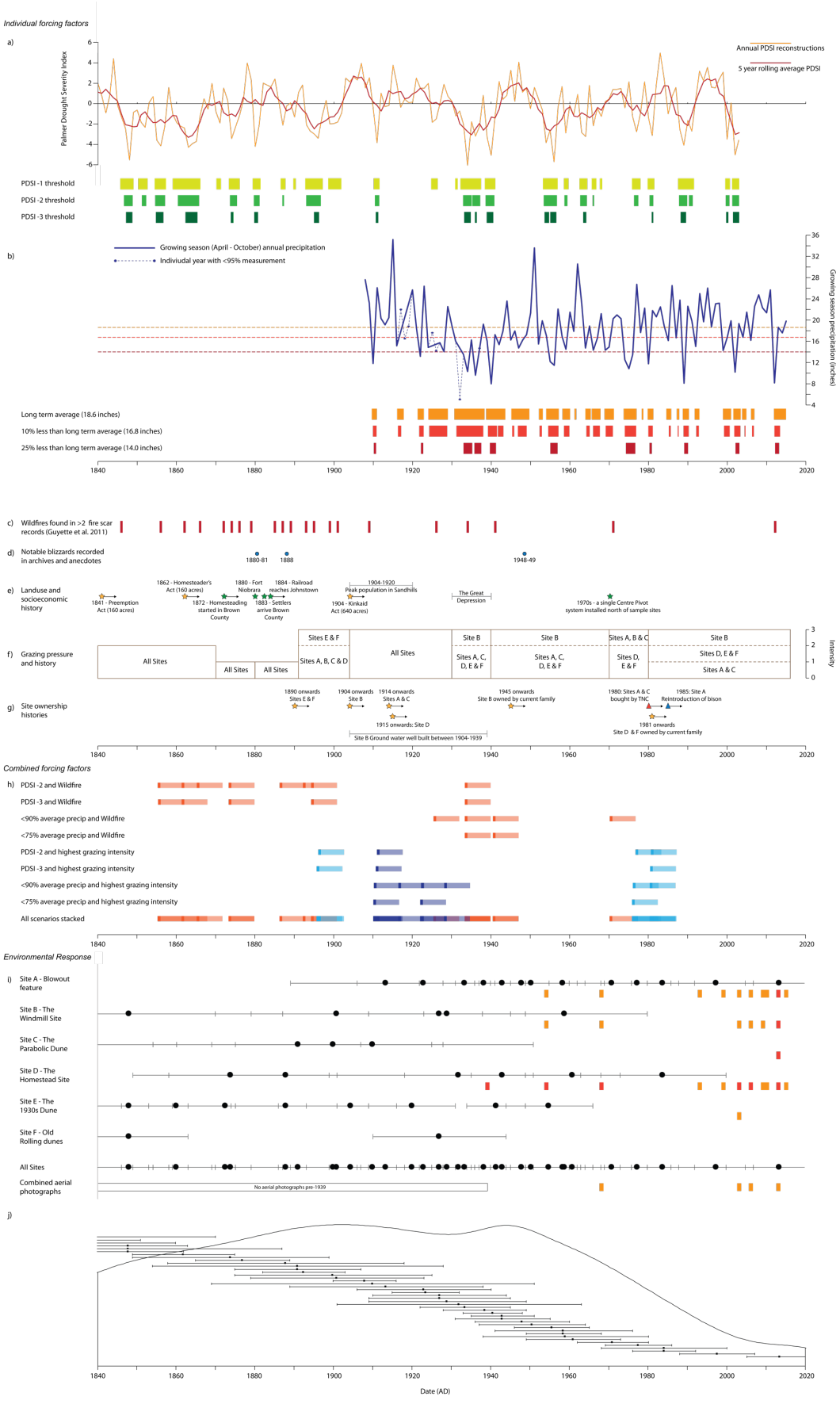
Table 7.3 Land use, settlement, and assumed grazing history based on archival records and oral histories of Brown County, Nebraska. In addition to those cited in the text, data sources include: Kay *et al*. (1989), Stubbendieck (1998), Nebraska Geneaology website (accessed December 2017), and conversations with Doug Kuhre (Ranch Manager at the Niobrara Valley Preserve). Time brackets (Date AD), commentary and intensity scores have been discussed with local grassland ecologist Dr Al Steuter (commercial ranch owner and previous Ranch Manager at the Niobrara Valley Preserve). Classification scores reflect: 1 – low grazing pressure, 2 – moderate grazing pressure, 3 – high grazing pressure. Variation in intensity scores between sampling sites is demonstrated in Figure 7.3.

	Comments / Supporting evidence	Score
Pre-1870s	- Prior to 1870, bison grazing intensities on all sites was probably in the range 2-3 due to the value of the Niobrara River and its tributaries as a reliable source of water throughout the year. - Year-long bison herds roaming and grazing in the nearby Niobrara River area would have made use of the available forage in this part of the Sandhills.	**2**
1870 – 80	- During the 1870s, cattlemen came to Brown County ahead of the railroad, attracted by the abundant prairie grasslands. Early ranching operations used a system of 'open range' – cattle roamed free. - By late 1870s, the bison had been cleared from the region, settlements and military forts were established (Baltensperger, 1985).	**1**
1880 – 90	- Winter of 1880-81 is recorded as one of the most severe ever known – ranchers suffered heavy losses and left the area, leaving the prairies open to settlement by farmers who arrived in the mid-1880s with the development of the railroad through Brown County. - Years 1884-85 were marked by a rush of new settlers to the Brown County region, however, few cattle ranches located in the Sandhills as grass covering was sparse; ranchers focused on grazing in the valleys. - Original EuroAmerican settlers only given 160 acres and were unsuccessful in attempts to farm the plots. Plots in the nearby area were heavily over-farmed and led to high levels of land degradation and damage to the surface vegetation. - Low level of grazing pressure on the immediate study location, but a higher score would be used for the surrounding areas which were heavily farmed and degraded during this period. - Many cattle died during severe winter of 1885-86, dry summer following year, and severe winter of 1888 (Perry and Stubbendieck, 1976).	**1**
1890 – 1904	- Crops failed following the previous dry years, farms were deserted, and the population of Brown County halved from 1890 – 1895. - 1890: Sample sites E & F were bought and homesteaded. - 1900 onwards: a new system of ranching operations was adopted – a transition from open range to controlled ranching (Miller, 1998). - Sites A, B, C & D: Intensity score 2. Sites E & F: Intensity score 3.	**2-3**
1904 – 30	- Following the Kinkaid Act (1904) which gave families 640 acres of land, population increased in the Sandhills. - Numerous small ranches sprung up in the Brown County area containing not only grazing cattle, but also wheat and dairy cattle. Percentage of regional Sandhills Cattle Ranching Area used for ranching pastures doubled from 42.4% in 1909 to 80.3% in 1928 (Hedges and Elliott, 1930). - 1904: Site B bought and homesteaded. Groundwater pump found at site B likely installed soon after purchasing. Site B groundwater pump is a site of persistent heavy trampling by cattle and thus has been graded 3 from this point forward. - 1914: Sites A & C were bought and homesteaded. - 1915: Site D bought and homesteaded. Original homestead is located c.50 m south east of site D transect. Non-naturally occurring tree species found at site D likely planted by the early homesteaders to create a wind break across the prairies. - Peak population in the Sandhills is noted from 1904-1920.	**3**
1930 – 40	- Population fell in the wider area during The Great Depression as Kinkaiders left the region, however, reductions in cattle herds in the Sandhills were less severe than in the rest of the state. Reports suggest that cattle were moved into the Sandhills from surrounding states (Miller, 1998). - Sites A, C, D, E & F: Intensity score 2. Site B: Intensity score 3.	**2-3**

	Comments / Supporting evidence	Score
1940 – 70	- As Kinkaiders left, ranchers acquired more land and grazing would have increased in the local area. - Less conservative (than present) grazing strategies used. - 1945: Change in ownership of site B – pasture purchased by current family. - Sites A, C, D, E & F: Intensity score 2. Site B: Intensity score 3.	**2-3**
1970 – 80	- Anecdotally specific sites are noted to have been overgrazed during this period, prior to the establishment of the Niobrara Valley Preserve. - Sites A, B & C: Intensity score 3. Sites D, E & F: Intensity score 2.	**2-3**
1980 onwards	- Conservative grazing strategies used post-1980 (e.g. rotation of pastures). - 1980: Change in ownership of sample sites A & C – pastures purchased by The Nature Conservancy, and establishment of the Niobrara Valley Preserve. - 1981: Change in ownership of site D – pasture purchased by current family. - 1985: Bison re-introduced to sample site A. - Sites B, D, E & F used as moderately grazed commercial grazing operations. - Sites A & C: Intensity score 1. Sites D, E & F: Intensity score 2. Site B: Intensity score 3.	**1-3**

Figure 7.3 *(opposite)* Individual forcing factors and OSL ages stacked for each of the six study sites from 1840 – 2020 AD. (a) Annual PDSI and 5-year running average PDSI values taken from Cook and Krusic (2004). Episodes corresponding with PDSI thresholds -1, -2, and -3 shown in green shaded bars. (b) Annual growing season precipitation (mm) from 1905 – 2015, dotted lines represent years with >5% missing data. Orange, red and dark red bars correspond with years with precipitation levels less than the long-term average, <90% of the long-term average, and <75% of the long-term average growing season rainfall respectively. Precipitation data sourced from the National Centers for Environmental Information (NOAA). (c) Wildfires found in two or more fire scar records taken from the data presented in Guyette *et al.* (2011). (d) Notable blizzards mentioned in historical records or referred to in oral histories. (e) Regional land use and socioeconomic history referring to notable changes in land acts, infrastructure and population in the wider Brown County region. (f) Grazing pressure 'intensity' and history based on the qualitative information detailed in Table 7.3. (g) Site ownership history based on known dates of land alienation and subsequent purchases. (h) Combined forcing factor scenarios based on combining periods of known PDSI and growing season precipitation thresholds with known wildfire events and periods of more intensive grazing as determined in Table 7.3. A 5-year lag has been included to identify a potential period during which sediment reactivation associated with the combined forcing factors might have occurred. Orange bars used for combinations including wildfire, blue bars used for combinations including grazing pressure. Dark blue used for periods when all sites experienced highest grazing pressure, light blue used for periods when two or more sites had highest grazing pressures. (i) OSL ages with uncertainties stacked by sample site and combined. Red and orange bars refer to evidence from aerial photographs for 'bare' and 'very bare' dune vegetation cover respectively. Combined aerial photography bars refer to the state of the wider region as opposed to individual sample sites – orange

bars do not refer to 'bare' dunes but are used when dune crests are bare and blowouts have visibly increased in size. *Refer to last page of thesis for A3 version of Figure 7.3.*



For many forcing factors, there is likely to be a lag time between the disturbing event and surface reactivation, for example because vegetation-die-off is not instantaneous in a drought event (Barchyn and Hugenholtz, 2013a; Mangan *et al.*, 2004; Peters *et al.*, 2006). Using PDSI data to establish droughts of different intensities, notable ranch establishment dates, and known wildfires in the local area, a lag time was calculated between these three different 'events' and the next accumulation of sediment recorded by an OSL age at each site. Lags were calculated using both the central OSL age value and the earliest possible age based on the one sigma error (Figure 7.4 a-b). Figures 7.4a and 7.4b show that all six sites have OSL evidence for sediment movement occurring within a 5-year lag of droughts represented by the smoothed PDSI record. A 5-year lagged response to notable land pressure changes is particularly visible for sites A, D and E (Figure 7.4c). The lagged response of sediment movement to wildfire (Figure 7.4d) suggests that site A has been affected more significantly by the wildfires in the latter half of the 20th century than other sites. Sites E and F showed evidence of sediment movement overlapping within a 5-year lag period of known wildfire events in the earlier part of the record.

7.4 Evidence for the role of individual disturbance factors

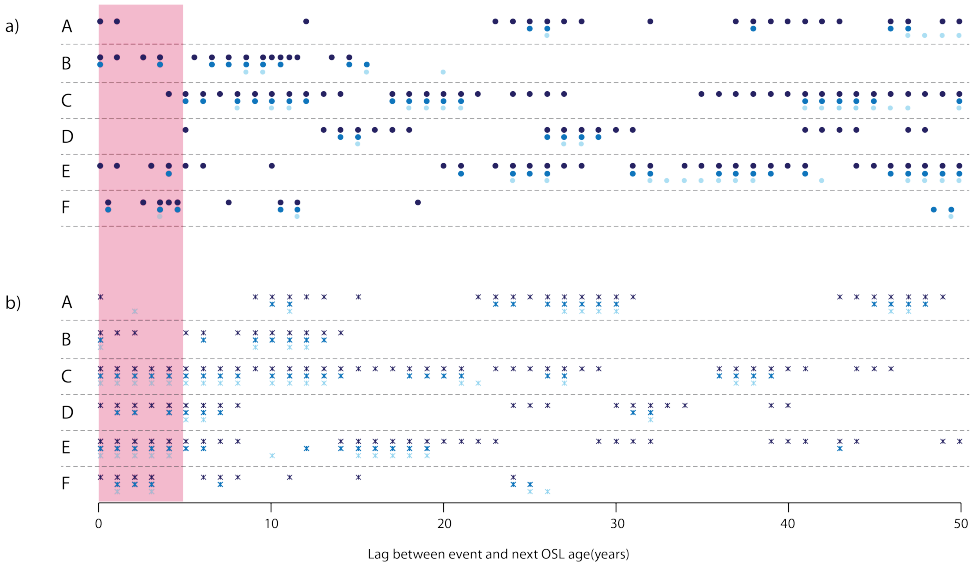
The relationship between individual drivers and resultant surface reactivation can be assessed by comparing the timing of identified periods of deposition in the OSL chronologies with notable periods of extreme drought, increased wildfire frequency and heightened land use pressure. However, the errors

on the OSL ages also do not allow individual disturbance events to always be linked to specific forcing factors.

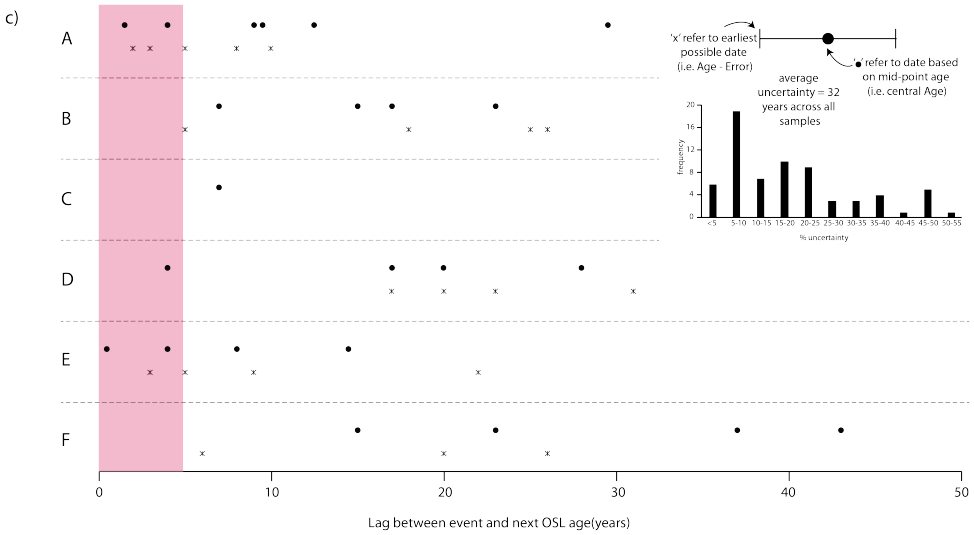
7.4.1 The role of climate

Based on PDSI reconstructions and precipitation measurements, periods of activation from all sites do and do not overlap with notable drought periods, suggesting a complex role of drought in impacting the surface vegetation and facilitating sediment transport by the wind. Whilst we might not expect the OSL ages and drought records to overlap perfectly, accounting for a lagged response of the vegetation and root networks prior to sediment remobilisation, Figure 7.4a also suggests that whilst drought might be accountable for a portion of the reactivation events, many episodes occur decades after a drought event. Not all disturbances occur following droughts, indicating the importance of other agencies of disturbance, considered below.

PDSI vs OSL



Land ownership vs OSL



Wildfire vs OSL

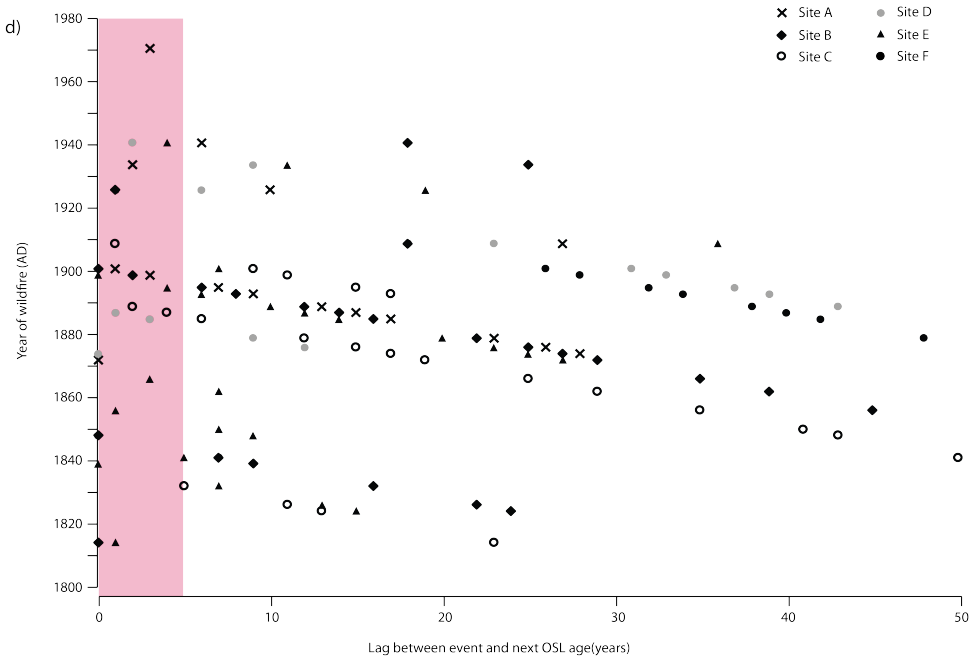


Figure 7.4 *(opposite)* Figure shows the lag (in years) between disturbance event and the proceeding luminescence age identified at each of the sites A-F. a) Lag time between next luminescence date and year of PDSI threshold (-2 = dark blue, -2.5 = mid-blue, -3 = light blue) based on 5-year rolling averages of PDSI. Lag time calculated between end of identified PDSI period and the central point of the luminescence age for each site. b) Lag time between next luminescence date and year of PDSI threshold (-2 = dark blue, -2.5 = mid-blue, -3 = light blue) based on 5-year rolling averages of PDSI. Lag time calculated between end of identified PDSI period and the earliest point of the luminescence age for each site. c) Lag time between next luminescence date and year of land ownership / land act change. Lag time calculated between identified event period and the central point (black circles) and earliest point (black crosses) of the luminescence age for each site. Land ownership / land act changes included: Individual site homestead dates, Kinkaid Act (1904), introduction of rail road to Johnstown (1884), and any other notable changes in land ownership. d) Lag time between next OSL date and identified wildfire from tree scar records. Lag calculated between identified wildfire and the central point of the OSL age for each site. Individual sites defined as per the figure key. Pink shaded bar highlights 5-year lag period. For clarity purposes, OSL age uncertainties have not been included in the individual sub-figures. A description of the OSL uncertainty profile is shown inset Figure 7.4c.

7.4.2 The role of wildfires

Given wildfires are relatively short-lived events, coupled with the age range of the OSL dates, periods of deposition across the study sites are overlapping within errors of wildfire events. However, a reduction in wildfire occurrence in the 20th century is countered with a peak in reactivation event evidence in the 1940s, suggesting wildfire alone is unlikely to initiate sediment remobilisation. Recent work by Arterburn *et al.* (2018) also suggests that wildfires do not necessarily lead to surface reactivation due to the rapid recovery of herbaceous biomass in grassland

ecosystems. Future analysis should seek to identify the recovery time required following a wildfire and the resilience of belowground root networks.

Another difficulty with ascribing evidence to wildfire-driven dune reactivation is the limited spatial extent of the disturbance. Wildfires can be extremely localised and based on Bragg's (1985) original account of the fire scar tree records used, we know that whilst many of the trees are located within the study region, we do not know the size of the individual fires. Acceptance of a null hypothesis and dismissal of the importance of wildfire disturbances, may therefore be driven by falsely assuming each fire would have caused a true disturbance to each site.

7.4.3 The role of grazing pressure

Identifying the role of grazing pressure on destabilising surface sediments is complicated for three reasons. Firstly, calculating levels of grazing pressure over long periods is very difficult to estimate due to technological and strategical advances in grazing management, land ownership changes and variability in scale (i.e. 'pressure' on the underlying surface from grazing can vary on a sub-ranch scale due to cattle grouping around features in the landscape). Secondly, grazing pressure is technically a biotic factor, but influenced and managed by humans (Barchyn and Hugenholtz, 2013a). Land management strategies will change in response to climatic factors (Helzer, 2010), and the non-linear response of humans to other changes cannot be captured in this basic representation of grazing pressure. For example, at what level of drought would ranchers choose to reduce the size of the herd, or alternate rotations between pastures. There is no single management

system that will be appropriate for all needs of ranching on the grasslands; management strategies are adapted as conditions change (Helzer, 2010). Finally, the response of individual animals to environmental conditions cannot be predicted. For example, herds typically shelter from the strong winds across the open prairie by grouping behind dune crests (Cunfer and Waiser, 2016), protecting themselves from the wind and eroding the surface vegetation; resulting in the formation of blowouts from the heavy localised trampling. Likewise, heavy trampling occurs around groundwater pumps, as found at site B. These examples suggest that intense grazing strategies are not necessarily required to exert localised grazing pressure on the landscape. Thus, whilst the summary in Table 7.3 goes some way to demonstrate broad-scale changes in land use and grazing pressure across the sites during the last 150 years, it is not able to completely capture the nuances in grazing pressure over this period.

Evidence to show the role of land use and grazing pressure on the vegetative cover is found across all sites except for site F. Reactivation ages found at sites A-E are all overlapping within a 5-year lag of ranch establishment dates, suggesting that a shift from open grazing to closed range ranching and settlement initiated more intensive land use. At site B, the downwind depositional lobe accumulated between 1904-1930, following construction of the water pump and drinking trough for livestock. Aerial photograph evidence and cattle tracks in the field suggest there is an inability for the surface vegetation to recover, likely driven by heavy trampling of cattle around this water hole. A lack of identifiable reactivations since the 1980s shows that despite periods of recent drought, and extensive wildfires (e.g. 2012), the sediment has not been reactivated. Meanwhile, the reintroduction of native

bison coupled with more conservative grazing strategies has arguably reduced the likelihood for reactivation; demonstrating a lack of commercial grazing pressure resulting in surface stability. However, the reintroduction of bison will have a complex overall outcome on the future surface stability since the disturbance effects of bison may be key in developing active sand dune habitats and restoring threatened vegetation species associated with active sites (Fox *et al.*, 2012).

7.5 Synergies between disturbance factors

While the assessment of individual disturbance factors may be effective for identifying relationships between forcing and environmental responses, it is likely that a combination of disturbance factors is important in inducing the conditions suitable for landscape reactivation (Mangan *et al.*, 2004; Stubbendieck, 2008). The suggestion that synergies are a key part of the forcing – response relationship is supported by the deposition age profiles demonstrating that geomorphological features in the landscape have responded to different disturbance drivers, evidenced by between-site age profile differences. Features that demonstrate recent geomorphic activity in the field, or had sparse vegetation cover, coincide with sites with recent reactivation ages (e.g. A, B, D & E). Meanwhile, sites with only older reactivation ages correspond to more rolling topography, upper soil horizon development, and denser vegetation cover. The heterogeneity in response records demonstrates that drought-alone is not the only cause of surface activity, while the analysis of the range of potential disturbance drivers and their geographic distribution shows good accord with the age profiles derived from the OSL analyses.

When multiple drivers act upon the landscape simultaneously, there is a greater likelihood of environmental susceptibility to reactivation. When grazing pressure is coupled with drought, their synergies reduce the threshold for each individual factor. For example, wildfire likelihood and extent (fuel availability) are both connected to precipitation (Guyette *et al.*, 2015), and cattle feeding behaviour adjusts in conditions of drought. Wildfire and grazing pressure are also inextricably connected. Analysis of historical bison behaviour suggests that herds congregated on recently burned grasslands (Biondini *et al.*, 1999; Helzer, 2010; Pfeiffer and Steuter, 1994). A reduction in above-ground biomass, due to intense grazing, can also reduce the level of fuel available for wildfires not only to start, but also spread. The management of wildfires has increased in recent decades, meaning that the impact of these naturally occurring disturbances in the landscape has reduced (Forman *et al.*, 2001). We can suggest potential periods of combined forcing factor pressure (e.g. Figure 7.3h) but are unable to identify the synergies between drivers in this multivariate dataset. Computational-based algorithms and models are needed to quantify the relationships between the drivers and the environmental response within this dataset.

7.6 Assessing the utility of the luminescence record

Given this study makes an unusual application of OSL data – to recent landscape disturbances - it is appropriate to evaluate this approach, since it is possible to test the results against other known records of disturbance. For example, the knowledge that the early settlers in the late-19th century heavily degraded the land, in addition to the widely-cited 1930s Dust Bowl, provide two specific phases

when surface reactivation was known and documented. Stacked OSL chronologies across the six study sites have successfully identified clusters of sediment reactivation signals during these periods, suggesting the reactivation response was recorded in the geomorphology and sufficiently sampled in the method used.

The results from the stacked chronologies highlight the benefits of a multi-core sampling strategy in the field. This approach shows how localised disturbance and sediment movement can be (e.g. the depositional lobe NVP16/2/4 that forms downwind of the groundwater pump at site B), and how a single sampling location would not alone capture the spatial complexity of sediment movement, nor its association with specific landscape features. When stacked these chronologies ensure that more of the reactivation signal is captured, and zones of erosion and accumulation in the current geomorphological state can be identified.

Large gaps in age profiles, however, may not indicate that deposition of surface sands is infrequent in this feature and thus large periods elapse between new deposits. High levels of reactivation may erode underlying sedimentary units, repeatedly reworking sediment and removing a signal form the OSL record. As discussed in Bailey and Thomas (2014), the likelihood of an incomplete record is almost inevitable in these dynamic environments and therefore it would be erroneous to assume there had not been any aeolian activity in the periods between the OSL ages. However, we can be confident that our intensive sampling strategy has captured a greater proportion of the reactivation history.

7.7 Older deposition events

Deposition events identified prior to 1840 AD have not been discussed in detail as they fall outside the period well-documented in the climatic and disturbance datasets. However, when compared alongside the OSL record from other regional dune locations, there is broad agreement in comparison to other records in the Central Great Plains (Figure 7.5). When compared against other Nebraska Sandhill studies (Figure 7.5), results highlight periods of aeolian activity centred on ~ 100 yrs ago, ~300 yrs ago, ~500 and ~700 yrs ago. This synchronicity in regional reactivation, coupled with a minimal human occupation impact on the landscape, suggests that long-term climatic factors are likely a key driver behind earlier reactivations. 5-year rolling average PDSI values equally show periods of notable drought occurring within errors of luminescence dates produced in this study. Nevertheless, this study has focused solely on the upper 50 cm of dune sediments, creating a reactivation record biased towards younger ages. Deeper sediment cores (especially at sites A & E) capturing older episodes of reactivation would improve the longer-term remobilisation record at the NVP, and the comparison with other records from within the region.

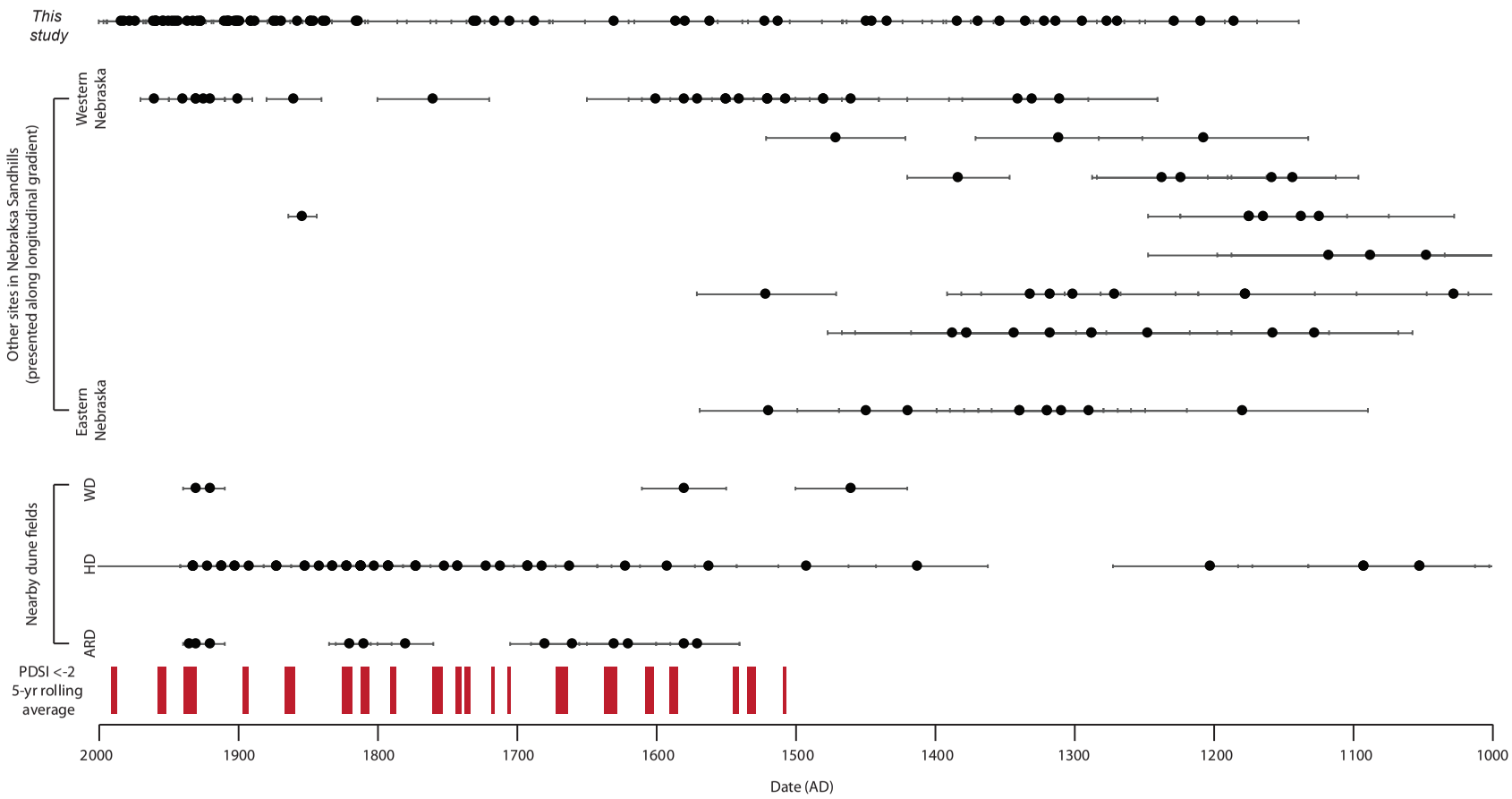


Figure 7.5 Summary plot of OSL ages from dunes in the Nebraska Sandhills and surrounding dunefields. OSL results from this study are presented alongside (i) existing OSL dates from the Nebraska Sandhills, and (ii) other nearby dunefields including Arkansas River Dunes (ARD), Hutchinson Dunes (HD) and the Wray Dunes (WD). OSL dates have been collected from a selection of existing Central Great Plains studies (Forman *et al.*, 2005, 2008; Goble *et al.*, 2004; Halfen *et al.*, 2012; Hanson *et al.*, 2009; Mason *et al.*, 2011; Miao *et al.*, 2007; Schmieder *et al.*, 2011).

7.8 Conclusions

OSL ages from near-surface dune sediments have produced a high-resolution history of sediment deposition events in the recent past in the northern limits of the Nebraska Sandhills. The use of a multi-core sampling strategy has successfully captured a more complete history of sediment mobilisation across individual features and the wider landscape than that which would be produced from individual core methods.

Peak episodes in sediment deposition occur in the late-19th century and 1940s. Reactivation in the late-19th century links to peaks in the wildfire record, the period of intense EuroAmerican expansion into the region and homesteading, and historically noted extreme weather conditions. Meanwhile, the peak in the 1940s follows the widely-cited US Dust Bowl, with extreme drought of the 1930s coupled with peak Sandhills population levels.

The variability found in the deposition profiles between the individual sampling sites suggests that no single factor is solely responsible for the reactivation history of the near-surface sediments. This is in agreement with existing studies (Barchyn and Hugenholtz, 2013a; Lee and Gill, 2015; Mangan *et al.*, 2004; Stubbendieck, 2008), which equally suggest vegetation degradation, and thus sediment remobilisation, is caused by a combination of factors, with no single individual forcing responsible for driving reactivation. Future research could seek to identify the leads, lags, and synergies between the driving forces and environmental response within this multivariate dataset by using alternative computer-based analysis and modelling techniques.

Chapter 8

PAPER 4

Paper 4 Prelude

The results from Paper 3 suggest that whilst the chronologies of deposition events inform us about the spatial heterogeneity of accumulation in the landscape, and the likely importance of multiple environmental forcing factors, the relatively short time period of analysis coupled with the OSL age uncertainties prevents us from identifying specific relationships between environmental conditions and the identified periods of deposition. Visual alignment and analysis of records, as is commonly used in environmental studies, is unable to rigorously identify feedbacks between drivers or identify complex non-linear dynamics within the system. Supervised machine learning (SML) tools, including artificial neural networks (ANNs), can bridge this gap, providing a new mode of analysis in the absence of a process-based mechanistic model. A supervised learning algorithm takes a known set of paired input-response data to train a model, which can subsequently be used to generate reasonable predictions for the response to new unseen datasets. Paper 4 uses a novel application of statistical inference techniques to examine the relationship between the known forcing factors (i.e. climate, wildfire and grazing pressure) and environmental response, as inferred through the OSL-derived chronology of depositional episodes. Due to the short nature of *Scientific Report* articles, the 'Methods' are found at the end of the paper and a substantial body of additional figures and explanation are found in the Supplementary Information (Appendix L).

Using artificial neural networks to predict future dryland responses to human and climate disturbances

Paper 4: Buckland, C. E., Bailey, R. M., Thomas, D. S. G.
Status: Submitted to *Nature Scientific Reports* (12th September 2018)

Abstract

Land degradation and sediment remobilisation in dryland environments is considered to be a significant global environmental problem. Given the potential for currently stabilised dune systems to reactivate under climate change and increased anthropogenic pressures, identifying the role of external disturbances in driving geomorphic response is vitally important. We developed a novel approach, using artificial neural networks (ANNs) applied to time series of historical reactivation-deposition events, to determine the relationship between historic periods of sand deposition in semi-arid grasslands and external climatic conditions, land use pressures and wildfire occurrence. We show that both vegetation growth and sediment re-deposition episodes can be accurately estimated. Sensitivity testing of individual factors shows that localised forcings (overgrazing and wildfire) have a statistically significant impact when the climate is held at present-day conditions. However, the dominant effect is climate-induced drought. Our approach has great potential for estimating future landscape sensitivity to climate and land use scenarios across a wide range of potentially fragile dryland environments.

8.1 Landscape reactivation in dryland systems

Land degradation and surface sediment remobilisation are major issues in drylands (United Nations, 2008), which cover 40% of the earth's land surface (Wang *et al.*, 2012), with their consequences estimated to directly affect up to 2 billion people (Middleton *et al.*, 2011). Surface destabilisation induces a variety of problems for local communities (Middleton and Sternberg, 2013; Reynolds et al., 2007b; Wang et al., 2012) including the removal of fertile soils and nutrients (Wasson and Nanninga, 1986), the burial of small plants, and damage to infrastructure, livestock and crops (Wiggs, 2011a). The interactions between climatic stress (i.e. drought) (Swain *et al.*, 2011), land use (Middleton, 2011; Viglizzo and Frank, 2006; Worster, 1979), grazing pressure (Ash and Wasson, 1983; Biondini et al., 1998a; Milchunas et al., 1989; Thomas, 1988; Yan et al., 2013) and wildfire (Arterburn *et al.*, 2018; Esteves *et al.*, 2012; Levin *et al.*, 2012; Santín and Doerr, 2016; Wiggs *et al.*, 1994) bring about damage to surface protective vegetation cover (Barchyn and Hugenholtz, 2013a; Wolfe and Nickling, 1993, 1997) and expose the underlying sediment to erosion by aeolian processes and land degradation (Reynolds et al., 2007b). Disturbance-driven degradation can lead to the reactivation of dryland geomorphological features, such as sand dunes, resulting in the formation of localised blowouts (Barchyn and Hugenholtz, 2013b; Hesp, 2002; Hugenholtz *et al.*, 2010; Hugenholtz and Wolfe, 2006; Provoost *et al.*, 2011; Wolfe and Nickling, 1997) or even large-scale dune remobilisation in some of the world's most vulnerable regions (Thomas et al., 2005; Wang et al., 2009). In turn, the creation of blowouts acts as an initial source of sediment that can lead to further reactivation and new dune formation (Barchyn and Hugenholtz, 2013b).

With increases in population pressure and land use, and climate models predicting increasing precipitation variability (Christensen *et al.*, 2007), there is a greater need to understand the sensitivity of dryland landscapes to future disturbances. In particular, there is a specific concern about how *individual* forcing factors interact with the environment to induce instability and land degradation (Barchyn and Hugenholtz, 2013a). Current methods of analysis often rely on simple visual comparisons between historic records and the correlation of individual forcing parameters against periods of reactivation in the record (Burrough and Thomas, 2013; Provoost *et al.*, 2011), or short-lived individual event analyses in the study of aeolian system surface change (Bogle *et al.*, 2015). Univariate analyses focus on individual drivers (see review (Provoost *et al.*, 2011)) but fail to identify the feedbacks between the range of climatic and anthropogenic forcing factors. At the Quaternary timescale sand dune reactivation studies, for example, have long been used as a proxy for palaeoaridity (Shaw and Thomas, 2002; Stokes *et al.*, 1997b, 1997a), with luminescence-derived chronologies used to infer periods of historic drought (Burrough and Thomas, 2013; Halfen and Johnson, 2013; Hesse et al., 2004; Thomas and Leason, 2005). Whilst a focus on climatic factors may be suitable on millennial timescales, more recent localised reactivations are driven by a combination of natural and anthropogenic disturbances. Aside from a climatic focus, many studies have commented on the role of wildfire (Arterburn *et al.*, 2018; Esteves *et al.*, 2012; Levin *et al.*, 2012; Santín and Doerr, 2016; Wiggs *et al.*, 1994) or grazing pressures (Ash and Wasson, 1983; Biondini et al., 1998a; Milchunas et al., 1989; Thomas, 1988; Yan et al., 2013), which in themselves demonstrate key biogenic relationships, but might mask the synergies within the wider system.

Whilst some studies have suggested the combined role of multiple forcing factors in contributing towards vegetation removal and landscape destabilisation (Barchyn and Hugenholtz, 2013a; Biondini et al., 1998a; Cook et al., 2009; Evans and Geerken, 2004; Herrmann et al., 2005; Lee and Gill, 2015; Mangan et al., 2004; Paudel and Andersen, 2010; Propastin and Kappas, 2008; Stubbendieck, 2008; Wessels et al., 2007; Wolfe et al., 2007), few have quantified the relationship between forcing factor and environmental response using traditional analytical methods.

Quantifying the role of individual parameters and identifying the complex relationship between the forces and geomorphological response is therefore essential to predicting the likelihood of future disturbance-driven reactivations. Ideally, a process-based model would be used to simulate hypothetical geomorphic responses to future climatic and anthropogenic forces. However, these mechanistic models do not yet exist in the form necessary for dryland aeolian environments.

Here, we apply a 'data-led' empirical approach, rather than trying to construct a mechanistic model (that comes with the problems of structural and parameter uncertainty). We explore the potential for novel applications of artificial intelligence (AI) techniques to improve our understanding of the relationship between climatic and anthropogenic disturbances and resultant geomorphic response in dryland environments. Artificial neural networks (ANNs) provide a hitherto underutilized method to simultaneously examine multiple forcing factors and uncover their complex relationships (Zhang *et al.*, 2018). A supervised learning algorithm takes a known set of paired input-target data and trains a model which can be used to generate reasonable predictions for the response to new unseen

data. As such, ANNs have been applied to a range of research problems from predicting stock markets (Ahangar *et al.*, 2010) to biomedical sciences (Zhang *et al.*, 2018) and monitoring water quality (Zhang *et al.*, 2015) to name a few. Specifically in environmental research, ANNs have successfully been applied in a range of dendroclimatic (Fang *et al.*, 2000; Tiwari and Maiti, 2011; Woodhouse, 1999; Zhang *et al.*, 2000), geomorphological (Pham *et al.*, 2018; Rahmati *et al.*, 2017) and aeolian studies (Houser *et al.*, 2015; Jamali *et al.*, 2018; Shanmugam *et al.*, 2016; Vaz and Silvestro, 2014).

8.2 Experimental design

The main drivers of vegetation disturbance and subsequent sediment reactivation are: climate-induced drought, grazing / land use pressure and wildfire disturbance; both currently and expected in the future. The goal of this study is to identify how changes in these drivers induce changes in sediment mobilisation. In this study, two ANNs were established to predict the likelihood for identifying episodes of sediment deposition in near-surface sand dune profiles given a set of forcing factors (i.e. climate, grazing pressure and wildfire occurrence). Luminescence-dated sediments from near-surface dune sands provide a historical chronology of deposition events which are used to represent episodes of sediment mobility within the system over the past 400 years (see Methods). Ideally, continuous time series of relevant climate data would be used as an input to train the first ANN (ANN1), and this is indeed possible over more recent time periods. However, such records are not long enough to cover the time period represented by the sediment deposition dates (c. the last 400 yrs). After searching for longer-

term records of relevant data, and proxies for climate conditions, we found tree-ring growth indices to provide the best available data. Rather than train the ANNs against climate data directly, we therefore trained them against tree-ring data as a proxy for climate (Brown *et al.*, n.d.; Cook *et al.*, 2004; Woodhouse, 1999; Woodhouse and Brown, 2001). In addition, we used historical records of grazing pressure and wildfire occurrence (see Methods and Appendix L: Note 2).

Using empirical data, we first identify the relationship between driving forces and sediment deposition events from the historical record before varying the disturbance factors under a set of future scenarios (alternate climatic, grazing and fire frequency futures) to deduce the environmental response and sensitivity to individual parameters. As the ANN was trained using historical tree-ring data, future climate scenarios must then also be expressed in this way. A second ANN predicted hypothetical tree-ring growth under two different future climatic regimes (ANN2; see Methods). We used two hypothetical climate futures combined with varying wildfire regimes and grazing pressures to sensitivity test the likelihood of deposition events when forcing factors were modelled under a range of conditions. All details are provided in Methods and the supplementary material (Appendix L).

8.3 Nebraska Sandhills: a test case

Empirical data from a detailed analysis of historical (10^1-10^3 years) land degradation in the Nebraska Sandhills (Buckland *et al.* Paper 3), a region synonymous with the 20th century US Dust Bowl and with the potential to experience serious disturbance in future decades (Schmeisser McKean *et al.*, 2014), provides input to this analysis. For our modelling experiments, we chose

chronologies of depositional events from six different geomorphological features in the northern Nebraska Sandhills to provide a measure of environmental response to disturbance events over the last 400 years (see Appendix L: Note 1). Six separate profiles, from a range of geomorphological features within the local area, are used for inter-site comparison (see Methods and Appendix L: Note 3). Input datasets taken from a tree-ring growth index (a proxy for climate), a simplified measure of historical grazing / land use pressure, and tree scar records (a proxy for wildfire history) provide the inputs for the model, representing natural and human disturbance forces (see Appendix L: Note 2).

ANN1 defines the relationship between climatic and human disturbance forces and the resultant episodes of near-surface sediment deposition. Luminescence-dated periods of deposition are presented as a continuous estimate of probability based on multiple discrete dates spanning the period of interest. ANN2 identifies the historical relationship between climatic inputs (annual growing season precipitation, average max and min temperatures) and tree ring growth (Brown *et al.*, n.d.) which is used for the second stage of sensitivity testing.

Model validation and testing were achieved through two methods: i) partitioning of the original dataset, ii) cross-validation between the dune sites. Datasets were randomly partitioned for training, validating and testing purposes during the training of the network. ANN1 consists of an input layer, four hidden layers (comprising 3:30:30:3 fully connected neurons) and an output layer, whilst ANN2 has an input layer, one hidden layer (9 neurons) and an output layer. ANN1 is a time-delay network, incorporating a delay line of up to 8 years between datasets for input (forcings) and output (sediment age probability) (see Methods).

8.4 Results

8.4.1 Model training

For each of the six study sites, when all sites were included in the training dataset (Figure 8.1: *upper, 'in-sample' prediction*), the timings of predicted deposition events (red) align well with the known dataset reconstructed from historical sediments (blue). Additional simulated peaks in the record (centred on 1730 and 1870 AD) suggest episodes of sediment deposition that we would expect to find if deeper sediment samples were extracted at sites A, C and E.

Cross-validation results ('*out-of-sample*' prediction) demonstrate the capacity to accurately predict the six known depositional profiles when the respective site has been excluded from the network training stage (Figure 8.1: *lower*). All sites, except B, show good correlation between the peak positions of the known target dataset and predicted model output.

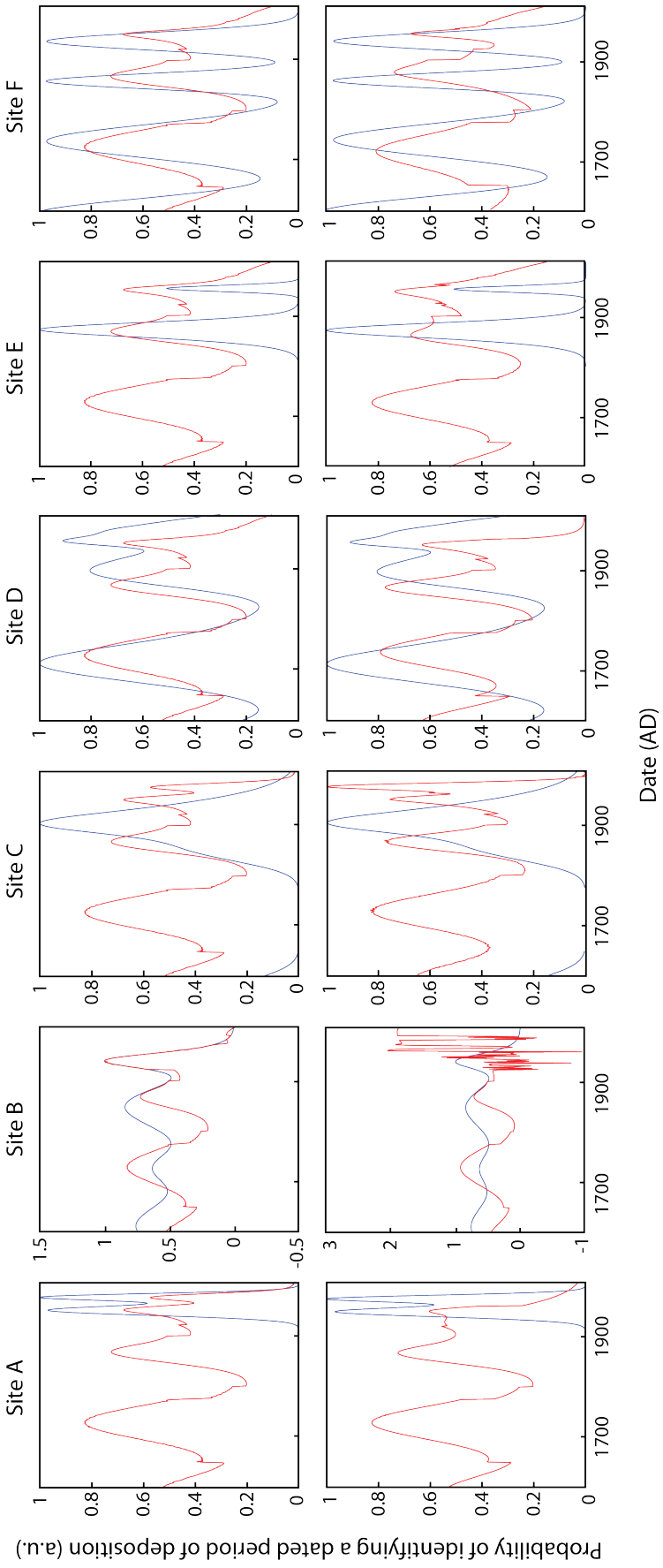


Figure 8.1 Results from both in-sample (*upper*) and out-of-sample (*lower*) testing across the six sites in ANN1. Blue lines refer to the known target datasets taken from empirical measurements of periods of deposition, and red lines are the predicted model outputs for each respective site. Due to the incomplete nature of sedimentary profiles (Bailey and Thomas, 2014), periods with no evidence of depositional events have been removed from the training dataset to prevent the model identifying these conditions as conducive to stability (i.e. sites A, C and E).

8.4.2 Scenario testing

In this section we assess how example combinations of the key drivers (climate, grazing pressure and wildfire) are expected to induce changes in sediment mobility, given the relationships learnt from historical data. First, using ANN2, after successfully predicting historical tree-ring growth from historical growing season precipitation totals and average max and min daily temperatures (Figure 8.2) (see Appendix L: Note 4), two new tree-ring growth futures were simulated based on two hypothetical climates (climate 1 & 2) (see Methods and Appendix L: Note 4) (Figure 8.3). Climate 1 growing season precipitation totals and max / min temperatures follow the trend set by long-term averages (1908 – 2015 AD). For comparison, climate 2 growing season temperatures increase by 2.5°C by the end of the century based on future regional projections across a suite of climate models under a low emission scenario (Bathke *et al.*, 2014).

Tree ring growth outputs across both climatic profiles produced results in line with theoretical expectations. After 8,000 model repeats, datasets which produced multiple extreme values outside of the bounds of the training set were excluded (see Methods); the mean and standard error were calculated with the remaining repeat datasets (Figure 8.3). Climate 1 shows a noisy signal with low-level sensitivity to precipitation and temperature changes (Figure 8.3a) while the greater climatic stresses of climate 2 force a reduction in tree-ring growth with time (Figure 8.3b).

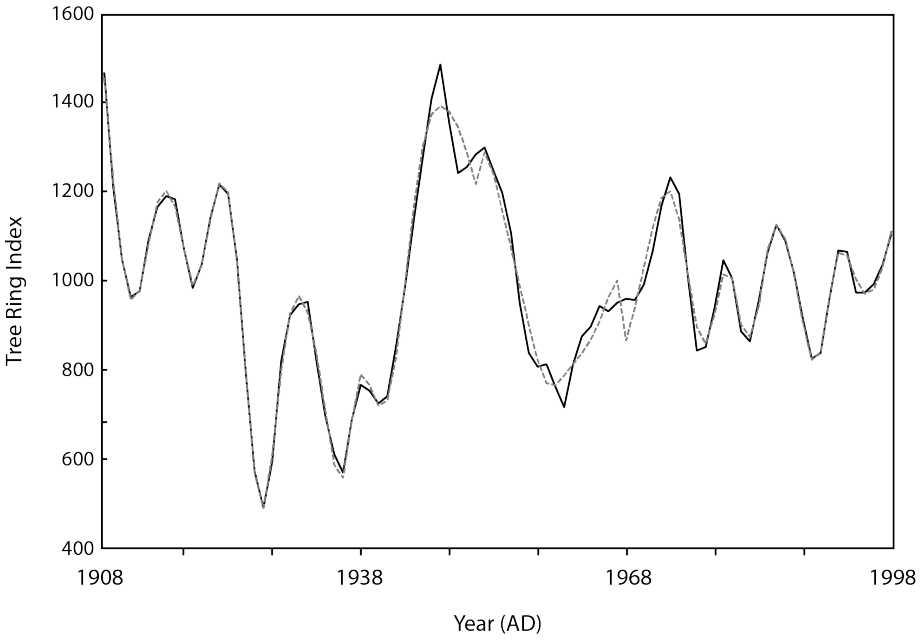


Figure 8.2 Results from training network ANN2 simulating the relationship between growing season precipitation and temperature conditions with tree ring growth over the period 1908 – 1997 AD. Black line represents known historical tree ring growth index (Brown *et al.*, n.d.) (smoothed 0.1 RLOESS), grey line is simulated tree ring growth based on the trained network.

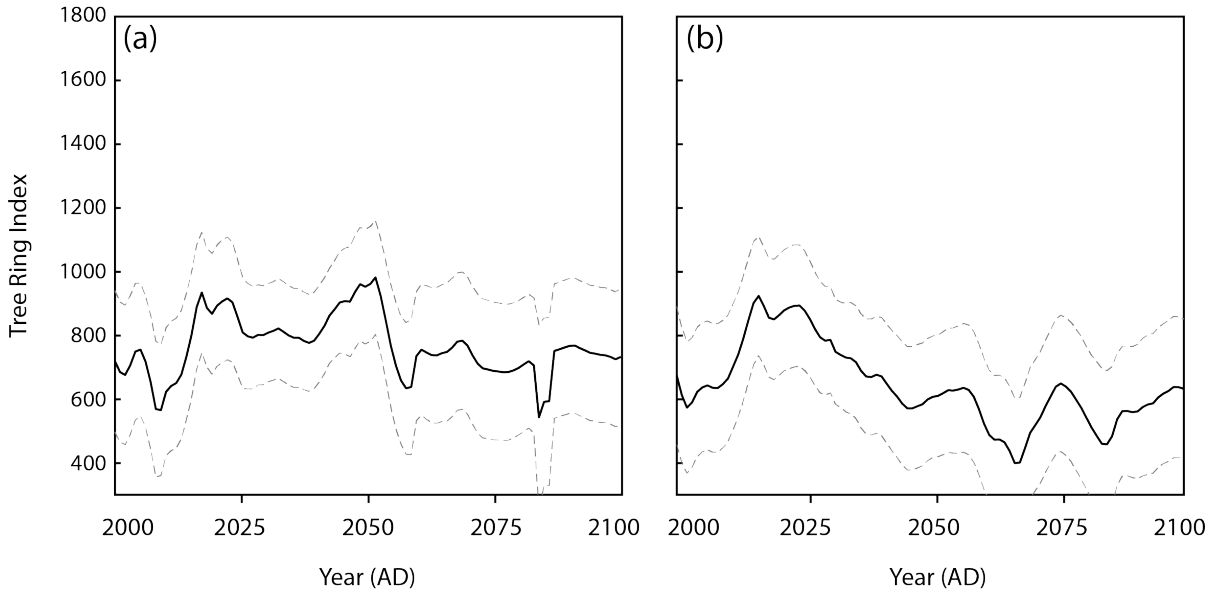


Figure 8.3 Simulated tree ring growth indices based on two different climate scenarios: (a) – Climate 1 (long-term averages), (b) – Climate 2 (low emission conditions with gradually increasing temperatures (see Methods). Mean (black) and standard errors (grey dashed) were calculated using 102 repeats. Multiple repeats ensured that the simulated dataset was not driven by random extreme values.

Second, using the trained ANN1 and three levels of grazing pressure, simulated tree ring growth indices produced six future likelihoods for identifying deposition events in the near-surface sediments. Across both climate futures, an antiphase relationship between tree ring growth and the likelihood for sediment deposition (deposition event score) suggests sediment movement is largely driven by climatic conditions (Figure 8.4, see Appendix L: Note 6). Under historical average climatic conditions (climate 1) a noisy signal is seen across all three combinations of grazing conditions with the output profile in general mirroring the signal found in the tree ring growth index (Figure 8.4a, c & e). Increased aridity (in climate 2), reduced the tree ring growth index with time, and similarly increased the likelihood of identifying a period of deposition in the sediment (i.e. higher deposition event score) (Figure 8.4b, d & f). This relationship is particularly visible under low grazing conditions but is less well-defined with noisy shallow peaks under higher levels of grazing pressure.

Third, to explore the added impact of increased grazing pressure (above background levels) and wildfire frequency, additional grazing pressure was added to low and moderate grazing regimes for a 10-year period (Figure 8.5 brown bars) and wildfires were added when average max temperatures >26.7°C (Figure 8.5 red bars). Temperature is considered a strong determinant of fire frequency in the Great Plains (Stambaugh *et al.*, 2008). Under low grazing conditions, an increase in pressure results in a lagged-system response with a notable increase in the likelihood to identify episodes of sediment deposition (Figure 8.5a). By contrast, when background grazing conditions are already at moderate levels, or when climates are tending towards more arid conditions, an increase in grazing pressure

does not alter the model projections (Figure 8.5c, e & g); the signal is driven by climatic disturbances as demonstrated in the tree-ring growth index. Additional grazing pressure was not added to the already heavily grazed scenarios (Figure 8.5 i-l).

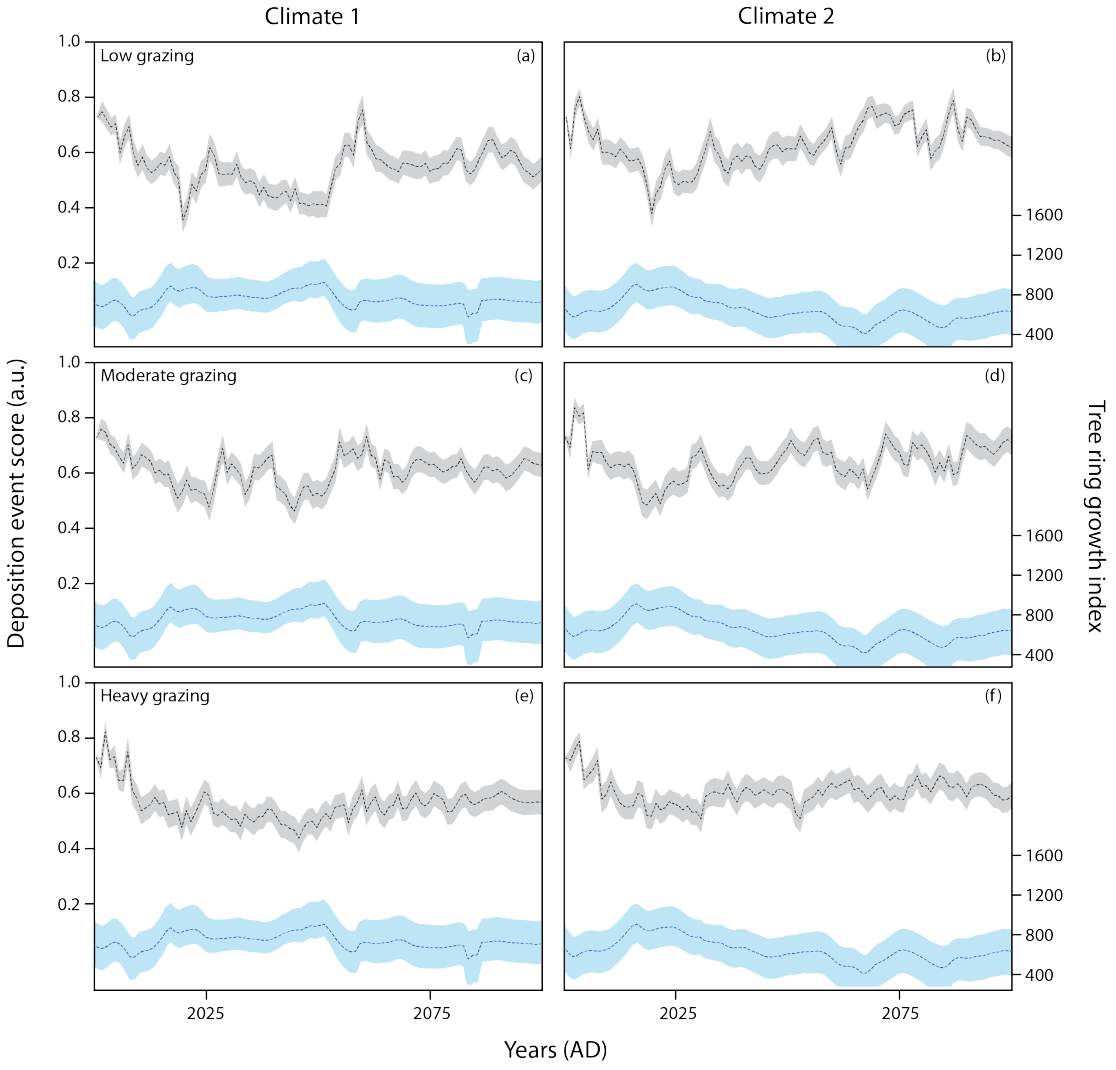
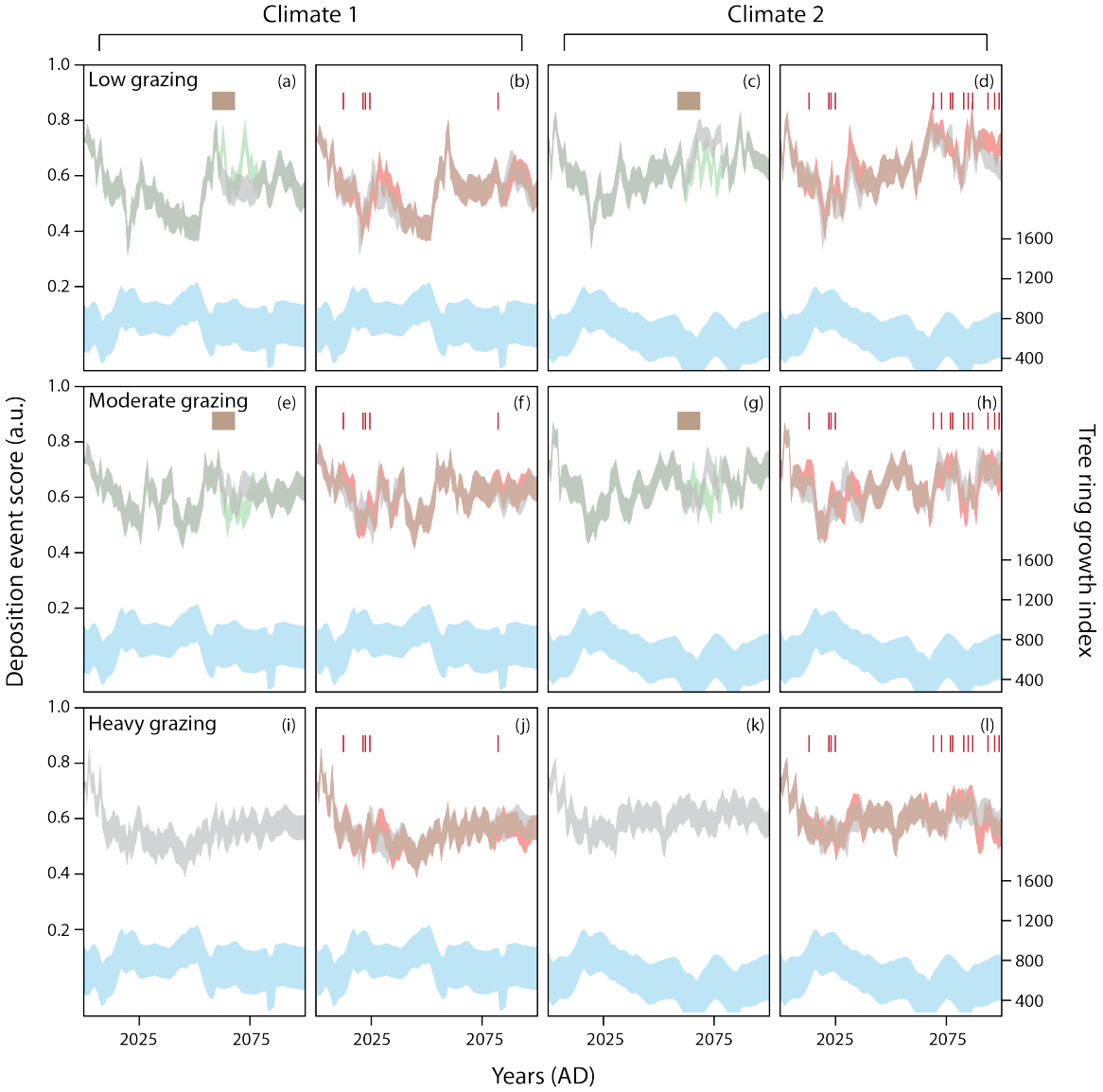


Figure 8.4 ANN1 and ANN2 simulated output results based on two future climate scenarios and three different grazing pressures. Blue output refers to simulated tree ring growth index based on climate 1 and 2 hypothetical scenarios. Grey output demonstrates ANN1 likelihood of identifying a depositional event. Dotted lines depict mean values calculated after repeat runs were screened for optimum model performance, shaded area corresponds with standard error. Repeat runs were screened according to ability to predict the correct location of deposition events in the training dataset (see Methods).

A complex relationship with wildfire occurrence shows a marginal increase in the deposition event scores following a wildfire event. Typically, wildfire occurrence results in an amplified likelihood of sediment deposition 1-2 years after the event and tends to follow the general trend of the output profile defined by the climatic conditions. An increased amplification of the sediment deposition likelihood associated with wildfire is particularly apparent under low grazing conditions with consecutive wildfires (Figure 8.5b & d). Under heavily grazed conditions, wildfire events do not cause a statistical increase in the likelihood of identifying sediment mobility in the record, except for following a series of three wildfire events (Figure 8.5j: 2021 – 2024 AD) under average climatic conditions (climate 1).

Figure 8.5 *(opposite)* Output results when new scenarios of climatic conditions, grazing pressure and wildfire occurrence are combined over a 100-year period. ANN1 outputs (deposition event scores) are presented as mean ± standard error following 5,000 repeats. Repeat runs were screened according to ability to predict the correct location of deposition events in the training dataset (see Methods). Six different disturbance scenarios (see Methods) are plotted across the 4 columns for each of the 3 different grazing pressure levels (Low grazing: a-d, Moderate grazing: e-h, Heavy grazing: i-l). Column 1: compares scenarios 1 and 2. Column 2: compares scenarios 1 and 3. Column 3: compares scenarios 4 and 5. Column 4: compares scenarios 4 and 6. Blue output: simulated tree ring growth index based on either climate 1 or 2. Grey output: ANN1 OSL output based on climate-only scenarios. Green output: includes added grazing pressure scenarios. Brown bar depicts period of increased grazing pressure. Red output: includes wildfire. Red bars represent years with wildfire occurrence.



8.5 Discussion

8.5.1 Drivers of future deposition events

Results highlight the dominance of climatic disturbance in driving vegetation growth (as shown in the tree ring growth index) which in turn explains the majority of the variability found in the deposition event score (ANN1 output). When additional grazing (or land use pressure) is added to a previously low pressure grazed environment, a significant increase in identifying periods of sediment

deposition is found. Yet, in environments under already stressed conditions (i.e. moderate / heavy grazing or drier climates), an increase in pressure bares no additional impact on the likelihood of identifying sediment movement in the geomorphic system. These results agree with previous studies (Gillson and Hoffman, 2007; Lohmann *et al.*, 2012) that have commented on the non-linear nature of dryland geomorphic systems, whereby a threshold of disturbance is required to initiate sediment reactivation. Our results show that the force exerted by external disturbances is not linearly related to the likelihood for periods of sediment deposition to be identified in the record; the geomorphic response is binary not continuous. Additional grazing pressure does not increase the likelihood for reactivation in a system that is already experiencing sediment mobilisation, but it might contribute to pockets of localised heterogeneity in the record and, in particular, the formation of blowouts (Hugenholtz and Wolfe, 2006; Mason *et al.*, 2004).

Whilst some studies have suggested that fire may not contribute to the likelihood of sediment reactivation in semi-arid grassland environments (Arterburn *et al.*, 2018), our findings support existing research (Esteves *et al.*, 2012; Santín and Doerr, 2016; Wiggs *et al.*, 1994) that has suggested that wildfires may damage surface vegetation and increase the likelihood for sediment remobilisation (e.g. Figure 8.5d : 2083-88 AD period) during periods of low climatic stress (Figure 8.5b). Under low and moderate grazing regimes, model outputs predict a marginal increase in the deposition event score following the 2012 wildfire. In 2012, a large wildfire (76,000 acres) stripped the study region of trees, shrubs and grass species. Yet, despite the extensive nature of the fire, anecdotally ranchers and preserve

managers commented on the lack of evidence for sediment remobilisation following this event – likely caused by extensive root networks (Arterburn *et al.*, 2018), sediment crusting (Viles, 2008), and wildfire management practices (Forman *et al.*, 2001). Changes in grazing strategy and landscape management following wildfires have been instrumental in determining the subsequent likelihood for sediment remobilisation. The model used in this example has been trained on the land management practices during the 20th-century and is unable to predict how future human decision-making will change. As such, whilst the model predicted a sediment response post-2012 fire, the lack of physical evidence to support this simulation is likely caused by non-analogous behaviour to the training dataset.

8.5.2 Limitations of the approach

Out-of-sample predicting is the main limitation for the approach outlined here; this is the likely inability to provide accurate forecasts when models are trained on a limited or non-analogous dataset. The unique set of input conditions found at site B is not replicated at any of the other 5 sites, and without another set of comparable data to train from, the predicted output is beyond the limited conditions represented in the training dataset (e.g. Figure 8.1 site B). In this study, we have attempted to reduce such errors in expanding the dataset by training across multiple study sites. As in all inferential methods, a larger dataset that encompasses more drought cycles would improve the training (and therefore the predictable capabilities) further. An inherent weakness of data-informed models in this context is that under future climate change, if forcing conditions (or combinations of conditions) stray significantly far from past experience (significantly 'non-

analogous'), supervised models may no longer be able to accurately predict future landscape responses.

Another difficulty using this method is associated with identifying what the relative peaks and troughs in the simulated outputs represent. As mentioned earlier, the network has been trained on a luminescence-dated target dataset which provides a continuous estimate of the probability of identifying a luminescence age (i.e. episode of deposition) in the sedimentary record. However, ascertaining what peaks in the simulation output correspond with a deposition 'event' in the profile is dependent on where the relative baseline associated with stability is positioned (i.e. are all periods with scores > 0 indicative of sediment mobilisation episodes?). In this study, the network has been trained on definitively identified episodes of sediment deposition, not periods of known stability (see Methods). A series of erosional filters gradually remove evidence of historic reactivation events from the sedimentary system (Bailey and Thomas, 2014). As such, our target dataset does not provide evidence for all deposition events, but more importantly, it does not provide definitive evidence of periods of stability. There is a distinct difference between an absence of evidence and an evidence of absence, but this is not resolved in the depositional record. A baseline at zero therefore, to represent no likelihood of identifying a deposition event in the forecasted plots, is incorrect and thus events are inferred as the most prominent relative peaks in the deposition event profile as opposed to those that are identified above a set threshold, or those that are representative of extreme model runs (see Appendix L: Note 5).

The relatively large error margins associated with dated episodes of deposition (see Appendix L: Note 3) further compound the difficulty in identifying

specific deposition events and associated conditions. This is problematic for the network training as input conditions over large windows are considered to be inducing a short-lived sediment reactivation event that is characterised by large uncertainties (Figure 8.6). Conditions that are therefore reflective of landscape stability may falsely be associated with identified periods of deposition. Since the model has trained against a dataset that has already undergone a series of natural filters (Bailey and Thomas, 2014), the simulated outcome does not necessarily depict every deposition event. Additional known point-in-time observations taken from historical aerial imagery, oral records, agricultural reports would improve the resolution of the training

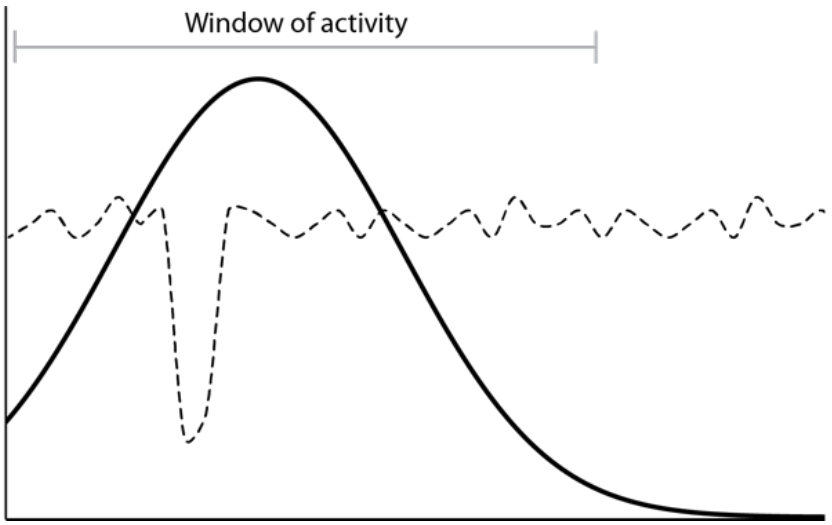


Figure 8.6 Schematic figure demonstrating how the wide training window of activity as defined by the target dataset (solid line) forces the model to train the equivalent period of input datasets (dashed line) to that target – even if the true 'disturbance' was only a short-lived event.

8.5.3 Wider significance

We have shown the capacity to use ANN models coupled with empirical datasets to improve our understanding of aeolian geomorphological systems and future sensitivity to climatic and human disturbance. Our results demonstrate how ANNs can identify relationships between paired historical input-target datasets, as well as the potential for trained models to make predictions about the likelihood of future reactivations. When known forcings are included in the simulations, we can identify peaks in reactivation driven largely by perturbations in climatic conditions, but also grazing pressure and fire frequency when aridity stresses are low. Results from this study suggest that fire can increase the capacity for near-surface reactivation and could be used to explain heterogeneity in local sediment profiles under low-stress climatic conditions. Likewise, the resilience of grasslands to grazing pressures is largely related to the ambient climate (Lohmann *et al.*, 2012). As expected, the dynamic nature of dryland environments means that the likelihood for sediment reactivation is not linearly related to individual forcings. Through ANN simulations, we demonstrate the dynamic relationships between disturbances and response, exploring the idea of thresholds and a lagged-response to external perturbations.

The black box nature of ANNs prevent a defined weighting of each disturbance parameter being produced, but sensitivity testing has demonstrated the non-linear response of the system to different combinations of disturbance conditions. These findings corroborate with existing research that synergies between forcing parameters are the key to near-surface reactivations in semi-arid grasslands (Mangan *et al.*, 2004; Stubbendieck, 2008).

Using cross-validation tests, we have demonstrated the bounds within which these models most optimally perform. Without all potential outcomes represented in the original training dataset, the ability to predict accurate outcomes is limited. If future models are to accurately predict future sediment reactivation events, non-linear multivariate tools are needed to fully-integrate the variety of parameters influencing near-surface activation. ANNs represent an opportunity within drylands, and wider landscape dynamics, to define environmental relationships and thresholds in systems where process-based mechanistic models are absent. The potential for future models, however, to accurately simulate hypothetical futures is constrained by the capacity to identify suitable training datasets that capture analogues for forthcoming conditions.

8.6 Methods

All neural networks have been developed in Matlab R2017b using the Neural Network toolbox and code written by the authors (CEB & RMB).

8.6.1 ANN1

ANN1 is an artificial neural network used to identify the relationship between climatic and anthropogenic disturbances and the likelihood of a luminescence age, indicating sediment deposition, to be found in the sedimentary record. ANN1 was trained with input-target data from 1590 - 1997 AD and used to stimulate the likelihood of identifying future deposition events in the sediment in the following 100 years under a series of alternative climatic and grazing pressure scenarios (see Future scenario forecasting).

Pre-processing input datasets

Three primary contributors to vegetation cover, and thus surface stability, were selected for inclusion in the model: grazing pressure, wildfire occurrence, and climatic conditions. Instrumental measurements (capturing the last 100 years of climatic data) were not used due to the relatively short time series measured. A longer dendrochronological record of tree ring growth from the Niobrara Valley Preserve (NVP) (Brown *et al.*, n.d.) provided an integrated record of precipitation and temperature change over the past 400 years. Annual tree ring growth data was extracted and smoothed by a factor of 0.2 RLOESS function, to allow a signal to be identified by the model amongst the environmental noise. Grazing pressure for the six dune sites was based on the levels identified in the index defined in Buckland *et al.* (submitted – 16/08/2018) and smoothed by a moving average factor of 0.1 to represent progressive changes in management strategy. Wildfire occurrence was included as a binary input (i.e. '1' – fire, '0' – no fire) based on the fire scar records from NVP (Guyette *et al.*, 2011).

Pre-processing target dataset

The target dataset for each of the six dune sites was represented by a probability density function (PDF) of stacked luminescence (optically stimulated luminescence – OSL) ages that depict episodes of sediment deposition in the dune profile. The target dataset represents a likelihood of identifying an OSL age, it does not necessarily capture every sediment reactivation event that has occurred for two reasons. First, historical events may have been eroded from the sedimentary record, and whilst a multicore strategy has been used to increase the overall representation

of reactivation events, due to the fragmented nature of aeolian sedimentary profiles some events may be eroded from the record. Second, the event may not have been captured in the OSL dating due to sampling strategy. Considering these caveats, whilst a peak in the PDF dataset represents a depositional event, a trough does not equally represent a period of stability. A positive peak is a true result, but a negative absence only suggests that we did not find evidence of an event. As such, it is essential to pre-process the target dataset to avoid falsely training the ANN to interpret certain conditions as conducive to stability. Where long gaps between peaks (regions of contiguous values at zero) were found in the luminescence record, target values were removed, preventing the model from associating periods which might be due to erosional loss of sediment to specific environmental conditions, thereby learning a false relationship (for the present purposes).

Model structure and architecture

Final model structure used 'timedelaynet' function to allow for an adjustable lag to be incorporated into the network architecture. A lag of up to 8 years for the input variables was selected following a series of trials of different time lags. Given the complex nature of the relationship between the input variables and the resultant likelihood of sediment movement, four hidden layers were used with a structure of [3 30 30 3] neurons in the layers (Figure 8.7). The Levenberg-Marquadt algorithm was used to train the network (minimizing distance between model outputs and target data) and the mean square error (MSE) of each model run was used as the performance indicator for each iteration. Training datasets were randomly partitioned for training (90%), validation (5%) and testing (5%) purposes during

cross-validation experiments, but to reduce over-fitting in the future scenario simulations this split was altered to increase the test portion of the datasets (50% training, 5% validation, 45% testing) and improve the robustness of the model outputs.

8.6.2 ANN2

ANN2 is an artificial neural network used to identify the relationship between individual climatic parameters (growing season precipitation, average max and min daily temperatures) and tree ring growth index (Brown *et al.*, n.d.) from 1908-1997 AD. ANN2 was used to produce simulated tree ring growth indices under a range of hypothetical new climatic scenarios.

Pre-processing datasets

Precipitation and temperatures measurements (sourced from Ainsworth Met Station (42.58° N, -100.05° W)) were used as input datasets and smoothed by a factor of 0.2. A tree-ring growth index produced using ponderosa pine tree rings within the NVP was used as the target dataset (Brown *et al.*, n.d.).

Model structure and architecture

Final model structure used 'fitnet' function, a single hidden layer with 9 neurons (Figure 8.8) and the Levenberg-Marquadt algorithm. Known time series data was randomly partitioned for training (70%), validation (10%) and testing (20%) purposes.

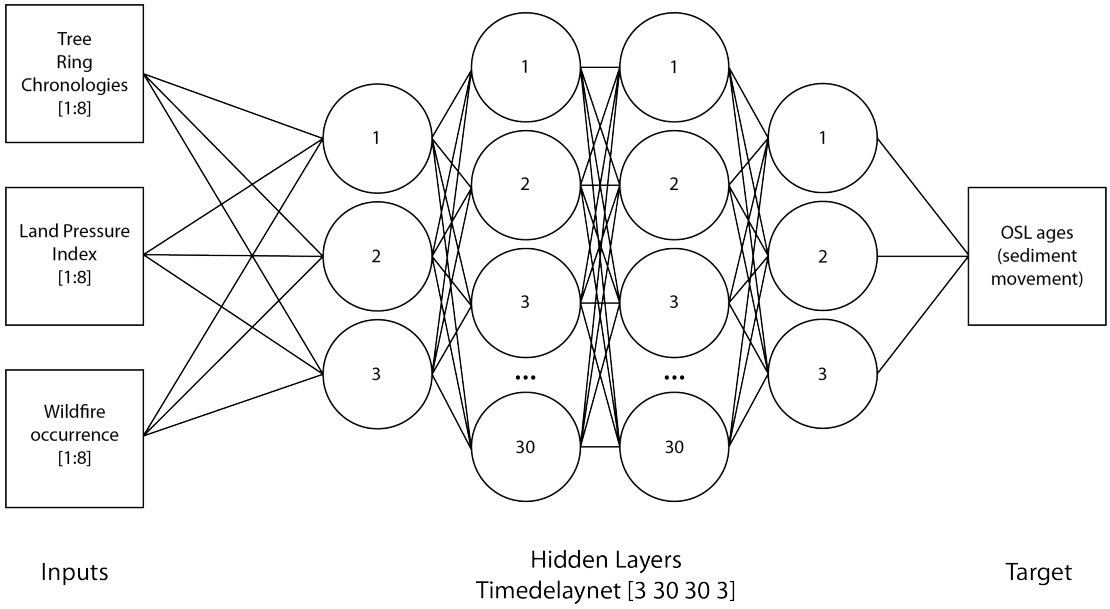


Figure 8.7 Schematic diagram demonstrating the model architecture of the final models used in ANN1. Training model was based on input-target dataset from 1590 – 1997 AD, with scenario datasets based on measured climatic data from 1998 – 2014 and simulated tree ring growth indices from 2015 – 2098.

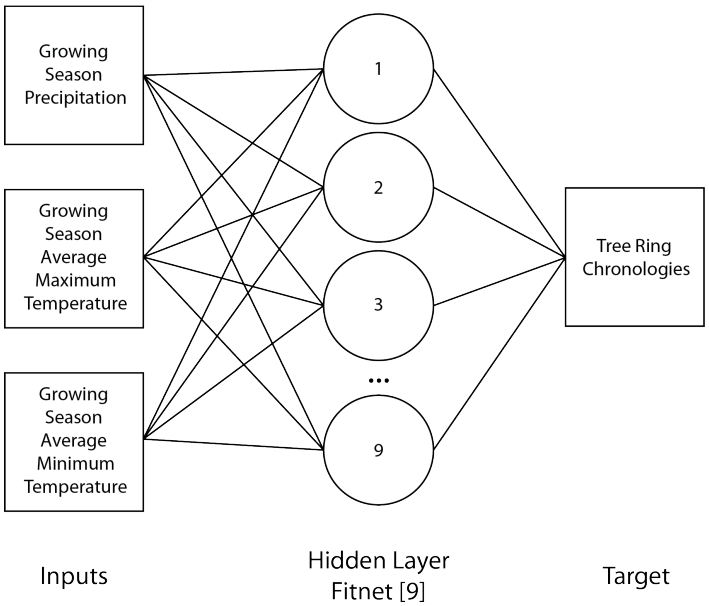


Figure 8.8 Schematic diagram demonstrating the model architecture of the final models used in ANN2. Training model was based on input-target dataset from 1908 – 1997 AD, with scenario datasets based on measured data from 1998 – 2014 and simulated data from 2015 – 2098.

8.6.3 Future scenario forecasting

Future scenario data refers to the 100 years post-1998 with the period from 1998-2014 using measured instrumental data, followed by 84 years of future 'scenario' data based on a range of climatic conditions, grazing pressure and wildfire frequency.

Scenario Forecasting (part 1): Tree Ring Growth Index

Trained ANN2 was used to model the predicted tree ring growth indices associated with two hypothetical climate scenarios and used as the new inputs alongside combinations of grazing pressure and wildfire occurrence in ANN1. Future climate data (2015 – 2100 AD) was produced using an autoregressive model to identify the normal levels of 'noise' identified in the measured historical precipitation and temperature datasets, before being added to two different future trends (Table 8.1) (see Appendix L: Note 4).

Using the training dataset (1908 – 1997 AD) to define ANN2, the model was run for 8,000 repeats with the simulated outputs associated with each network repeat stored by the model. Multiple cycles of the network ensured that the simulated target dataset was not driven by random extreme values. Repeats that produced more than seven tree ring indices >5,000 (i.e. extreme values) were excluded from the final dataset. The mean and standard error for each year was calculated for the two climatic scenarios and used as the new tree ring growth index for simulating future sediment deposition events in ANN1.

Table 8.1 Description of two different climate scenarios used to generate forecasted tree ring growth indices. Two combinations of future growing season precipitation, average maximum temperatures and average minimum temperatures have been used to produce different climatic conditions. Scenarios used do not demonstrate predicted future conditions but are used as proof on concept to demonstrate the capacity of the model under a range of forcing combinations. Climate 2 temperature settings are based on projections of the Central Great Plains region under a low emissions scenario (Bathke *et al.*, 2014). Regional climate summaries were based on IPCC models and the findings of the NCA Report (2014).

	Growing season precipitation total	**Growing season average maximum & minimum observed temperatures (°C)**
1	Growing season precipitation based on long-term average (last 100 years) ± noise generated from auto-regressive model of long-term precipitation trends.	Growing season average maximum and minimum temperatures based on long-term average (last 100 years) ± noise generated from auto-regressive model of long-term temperature trends.
2	Growing season precipitation based on long-term average (last 100 years) ± noise generated from auto-regressive model of long-term precipitation trends.	Growing season average maximum and minimum temperatures based on long-term average (last 100 years) plus low emission projections of a 2.5°C increase in temperatures by the end of the century ± noise generated from auto-regressive model of long-term temperature trends.

Scenario Forecasting (part 2): Future likelihood of sediment deposition events

Simulated tree ring indices were modelled against three levels of grazing pressure: low, moderate and heavy. Further analysis to sensitivity test the role of wildfires and additional periods of grazing pressure when applied against a background level were completed to produce six different combinations of future disturbance conditions (Table 8.2).

Table 8.2 Description of six combinations of future climatic, land use and wildfire conditions that have been used in this study to simulate alternate sediment movement likelihood predictions across the six sites studied.

	Tree ring (climate) scenario	Land use pressure	Wildfire frequency
1	Climate 1 (Long-term averages)	Current land pressure index values used for all sites.	No wildfires.
2	Climate 1 (Long-term averages)	Current land pressure used, except increase by factor of 1 for 10-year period from year 2059	No wildfires.
3	Climate 1 (Long-term averages)	Current land pressure index values used for all sites.	Wildfire in years with average maximum temperature > 26.7°C.
4	Climate 2 (Low emission)	Current land pressure index values used for all sites.	No wildfires.
5	Climate 2 (Low emission)	Current land pressure used, except increase by factor of 1 for 10-year period from year 2059	No wildfires.
6	Climate 2 (Low emission)	Current land pressure index values used for all sites.	Wildfire in years with average maximum temperature > 26.7°C.

Using the known datasets (1590-1997 AD) to define ANN1, 5,000 repeats were completed using the six training sites. The training dataset was partitioned with a relatively low training portion (50%) and high validation and testing partition (5% + 45%) (based on a short time series) to prevent over-fitting and improve the robustness of the future scenario outputs. With each repeat, the model simulated the predicted future likelihood of identifying depositional episodes in the sediment, classified as a deposition event score, according to the six future disturbance scenarios.

Model validation and selection

Repeats were assessed according to the model's ability to correctly reproduce the peaks found in the known historical deposition dataset (ANN1 training target). ANN1 training target is characterised by a continuous curve with peaks of varying magnitude, but the nature of the response is binary (i.e. sediment moves, or it does not). The size and magnitude of the model-derived peaks are therefore not significant, with the location of the peaks relative to the known dataset (Figure 8.9) a good indication of overall model performance and 'fit'. Given this, the mean squared error (MSE) of the model is not an appropriate method for determining overall model performance. In this study, we assessed the performance of the model based on the variation in location between the known and modelled peaks, with the best model identified as having the closest alignment of peaks across the six study sites. To identify the optimum models, we sum the differences between training and predicted peak positions for each model repeat across the six sites and select the models of best fit. The model identified a predicted peak which fell within a defined time window of the target peak and calculated the difference in location between the two peaks. If a target peak was not reproduced in the predicted dataset (i.e. a predicted peak does not occur within the peak window), a model penalty value (e.g. 1e6 used in this study) was assigned. Total peak location differences and penalties were summed across the identified peaks in each site, and across the six sites for each neural network repeat run. A moderate number of iterations (300) per repeat was used to prevent the model from attempting to improve the network to the optimum MSE, which is not necessarily the best peak-location-performing

model. Maximum peak window size was defined as half the distance between the two closest known peaks in the target dataset (i.e. 13 in this study).

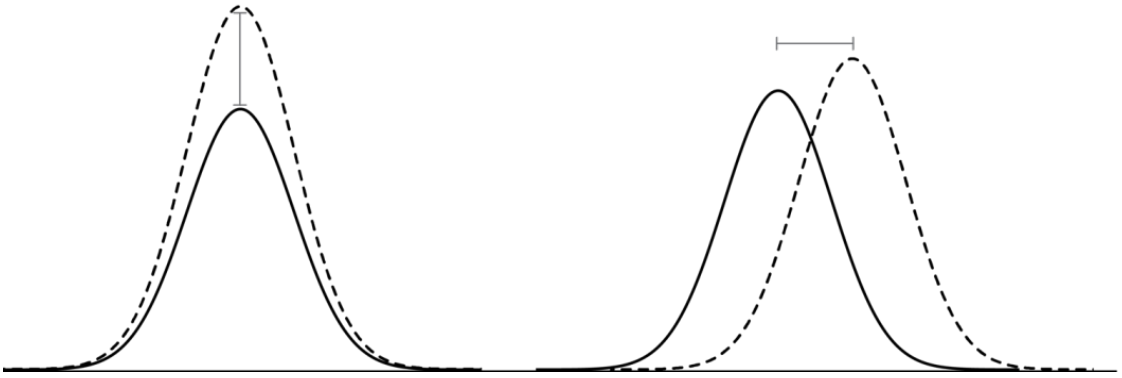


Figure 8.9 Schematic diagram demonstrating that MSE caused by variation in magnitude of peaks between training and predicted datasets (*left*) is not useful because the event occurred at the same point in time. The difference in the location of the peak (*right*) in time is a more appropriate measure of model performance.

Following 5,000 repeats, the mean and standard error associated with the repeats from the top 10% of models was calculated (model repeats for each timepoint were normally distributed). Increasing the percentage of models used to calculate the mean and standard error confidence intervals would reduce the overall uncertainty on the profile, but potentially includes the output from models that are poorly trained against the known datasets and are therefore more precise but less accurate (see Appendix L: Note 5).

SECTION FOUR

CONCLUSIONS

Chapter 9

Discussion

The research presented in this thesis has sought to explore the relationship between surface reactivation and external disturbances in the semi-arid Nebraska Sandhills. In doing so, this research has focused on three primary research questions:

- Can land surface responses to recent environmental change be identified chronologically in the sedimentary record?
- Can we associate environmental conditions with depositional episodes?
- Given our knowledge of the past, can we identify a suitable method to predict future surface reactivations leading to deposition?

This discussion chapter takes the findings of the four papers to directly address each of the research questions, consider limitations of the methodology, and comment on potential future avenues for research. The nature of the cross-disciplinary multi-method (field, laboratory and modelling) approach lends itself to some interesting discussion points that have not necessarily been addressed in the earlier papers, but are explored in this chapter.

9.1 RQ 1: Can land surface responses to recent environmental change be identified chronologically in the sedimentary record?

OSL techniques can be used to date the period that has elapsed since the measured sediment crystals were last exposed to sunlight. As such, OSL dates represent the cessation of sediment movement, capturing periods when sediment was moved and redeposited. This principle has been put to extensive use, first with the application of thermoluminescence (TL) (Singhvi *et al.*, 1982) and then through the use of more sensitive OSL (Huntley *et al.*, 1985) in investigations of Quaternary scale (i.e.10^3-10^5 years) environmental changes in dryland and coastal aeolian systems. At shorter (10^1-10^2 years) timescales, there has been limited application of the technique due to issues of partial bleaching and dim signals affecting the suitability of the luminescence signal to reliably capture recent deposition events. Bailey *et al.* (2001), Ballarini *et al.* (2003), Reimann *et al.* (2012) and Stokes *et al.* (2004), however, demonstrated that with appropriate methodological applications, OSL could be used to identify historical timescale dune activity. In this project this potential has been taken further, by developing an appropriate methodology to date shallow recently accumulated dune sediments in and around the NVP.

Prior to dating the sediments using full-preparation luminescence methods, it was important to determine the optimum locations within the sediment cores to deploy our dating efforts. Dating a whole sequence at high-resolution would be futile if the entire section proved to be of a single statistically indistinguishable depositional age. The application of changepoint analysis to coarse luminescence

measurements provided a suitable means for a rapid assessment of the OSL profile with depth for each of the individual sediment cores. The results from the changepoint analysis (shown in Paper 2) identified separate pulses of aeolian activity in the sedimentary record based on distinct changes in the luminescence profile with depth. The lack of variability in environmental dose rate amongst the sediments (Appendix F) meant that the changes in OSL with depth could be used as a proxy for age.

Not only was this application useful from the perspective of subsequently focusing luminescence dating efforts at each site, but also in highlighting the potential for dating young aeolian sediments. Near-surface, young, dim sediments have typically been rejected in favour of the older and deeper sedimentary records which naturally yield larger luminescence signals (Hesse, 2014). As deposited sediments undergo a progressive filtering with time (Bailey and Thomas, 2014), younger sediments can potentially provide greater levels of information in regards palaeoenvironmental conditions as they have not yet been as heavily eroded from the record. Combined with statistical methods of analysis we can produce high-resolution depositional profiles capturing geochronological change despite an absence of lithological change.

9.1.1 High-resolution SAR OSL dating

Using a refined SAR protocol to measure the luminescence signal in young aeolian sediments, we successfully compiled chronologies of recent land surface movement across a variety of features at NVP. As detailed in Chapters 4 and 5 (Paper 1 and 2), the application of a moderate preheat temperature, coupled with

a convex quartz lens and elevated photomultiplier tube voltage provided the most suitable measurement conditions for dating the young dim quartz samples. Once measured, processing the equivalent doses using the un-logged central age model (Arnold *et al.*, 2009; Galbraith and Roberts, 2012; Roberts *et al.*, 1999) and applying a revised rejection criteria (Chapter 4) improved the age estimation accuracy for young sediments.

Despite the noisy nature of the OSL signal, relative to older sediments, depositional ages were identified as recently as the late 1990s, with age uncertainties typically higher (c.15%) than the often reported 5-10% in the luminescence literature. These higher age uncertainties are a factor of the dim luminescence signals and higher levels of background noise. Notwithstanding the age uncertainties, only one age reversal was found (NVP16/4/2/26) within 1σ uncertainty, and no age reversals were found within 2σ of uncertainty, demonstrating the success of this high-resolution OSL technique in identifying surface deposition events in the sedimentary record. These results detail the capacity for OSL methods to extend to the far end of the luminescence dating age bracket when optimum sedimentary conditions are combined with suitable measurement procedures.

9.1.2 Capturing a more complete record

As well as proving the physical capacity to identify events in the sedimentary record with a refined luminescence protocol, an enhanced (both spatially across the landscape and with depth) sampling strategy ensured we captured a more complete geochronological record of historical events. Aeolian systems are

characterised by spatially-inconsistent sedimentary records due to localised variability in the processes that drive accumulation and erosion of the sediments (Leighton et al., 2014b; Munyikwa, 2005; Stone and Thomas, 2008; Telfer et al., 2017, 2010; Telfer and Thomas, 2007; Thomas and Burrough, 2013). To capture a signal of palaeoenvironmental change beyond localised processes, multiple sedimentary samples are needed to identify a signal amongst a background of high levels of noise.

This study adopted a novel approach which focused on extensively sampling in the field, via multiple cores along transects, and in the laboratory by taking sub-samples at centimetre-scale intervals down each 0.5 m core. Once dated, individual OSL ages from sub-samples were stacked according to each of the six individual sites to produce a more complete chronological history of sediment reactivation for each feature (Figure 7.2).

The variability found between sediment cores taken across individual blowouts and low-lying dunes perfectly demonstrates the caution that should be taken with interpreting results from single sample studies. The chronological profiles of recorded reactivation events in each of the sediment cores at each site are different, but often with some common units found between the vertical profiles. Common units found between cores taken at the same site indicate a wider phase of deposition occurring within the feature as opposed to localised noise within the profile (Figure 9.1).

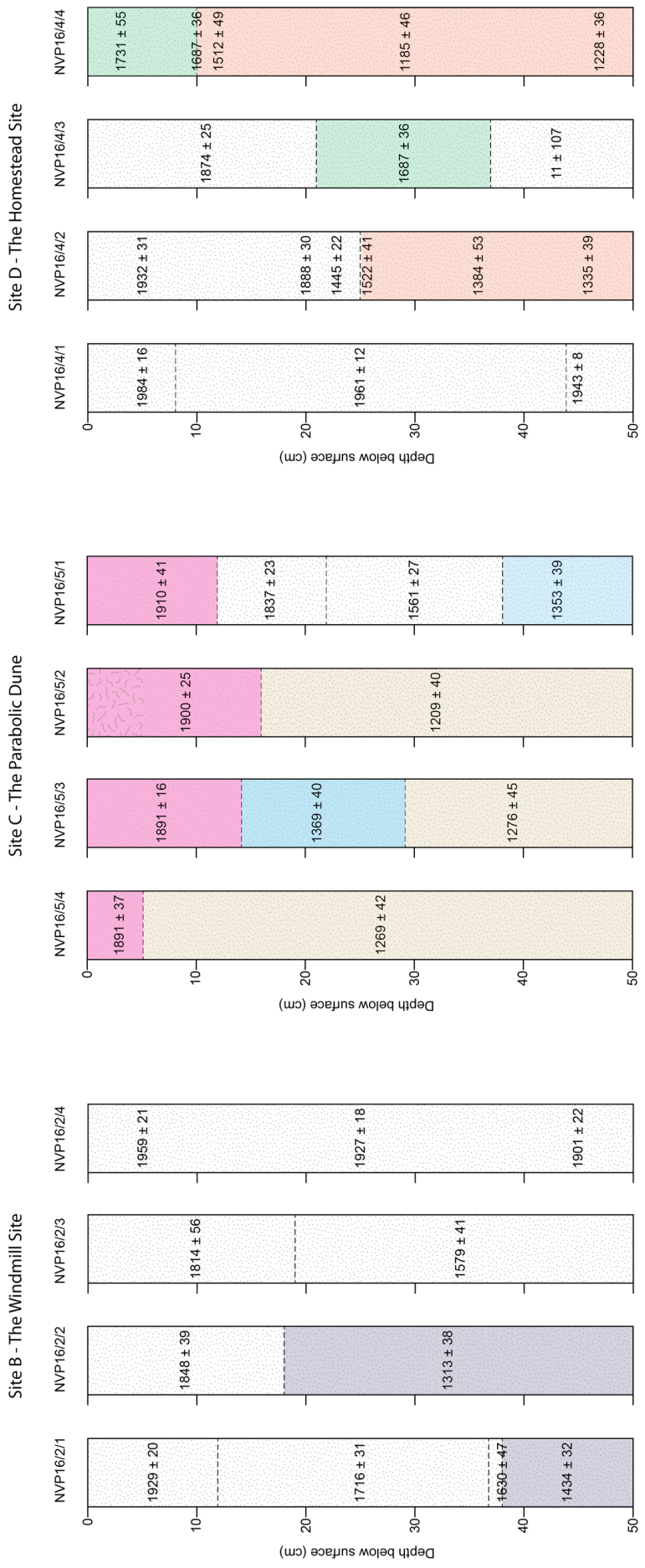


Figure 9.1. Example of common age units found between sediment cores at sites B, C and D. Units of common age (within 1σ errors) are highlighted in the same colour. Boundaries of the common units are defined from the results of the changepoint analysis. Depositional events would be lost from the geochronological reconstruction if only single cores were extracted from each of the sites.

This multi-core strategy has confirmed that single sample studies cannot be used to reconstruct a comprehensive dune accumulation history. As we have found, large age differences of reactivation between sediment samples transecting individual features, as well as between features suggest complexity in the pressures that contribute to the overall sedimentary sequence. Extracting a single sediment core and inferring climatic changes would potentially omit large sections of environmental history, which in turn affects our capacity to identify the drivers of surface reactivation.

9.1.3 Assessing the utility of the luminescence record

Despite the success of the approach in capturing a more comprehensive record, there is still a need to assess the capability of the methods to identify all of the deposition events recorded in the sedimentary profiles. Using changepoint analysis, it has been possible to focus dating efforts, and as such, define the number of deposition episodes per core that are considered statistically different from one another. With OSL methods as our chronometric technique, we are unable to resolve additional episodes that could be considered separate events within these changepoint defined periods because of the errors associated with luminescence dating.

For example, as shown in Chapter 5 (Paper 2), when sediment core NVP15/4/1 was measured twice for coarse luminescence and subsequently modelled using changepoint analysis, two separate break-point profiles were produced. The low levels of statistical difference between the individual aliquots with depth results in the break-point locations moving between repeat runs. By

comparison, repeats of a sediment core with distinct periods of aeolian activity produces comparable changepoint locations between repeat runs (Figure 5.9). Using OSL dating, we cannot achieve a suitable temporal resolution to resolve short-lived events, instead we are able to produce accurate ages associated with wider 'periods of activity'.

Based on the techniques used in this research project, the highest levels of chronometric resolution possible have been achieved. Future developments within the dating technique (e.g. single grain dating) are unlikely to refine the ages even further. Whilst single grain methods might provide accurate equivalent doses associated with individual grains, the lack of comparable accuracy with the environmental dose rate (due to sediment water content variation and spatial distribution of radionuclides) and the dim signal of the individual grain luminescence will reduce the precision of the age, producing uncertainty estimates larger than those used in this original study.

The suitability of a high-resolution OSL-based chronology as the method of choice in reconstructing recent dune reactivation history can be assessed based on several features. First, the ability to identify periods of historically-known sediment reactivation in the record suggests we can be confident that this method has produced a good reconstruction of reactivation history. For example, the knowledge that the early settlers in the late-19th century heavily degraded the land, in addition to the widely-cited 1930s Dust Bowl, provide two specific points in time when surface reactivation was known and documented. Stacked OSL chronologies across the six study sites have successfully identified clusters of sediment deposition

events during these periods, suggesting that the signal was recorded in the geomorphology and sufficiently sampled and dated in the method used.

Second, the results from the stacked OSL chronologies highlight the benefits of a multi-core strategy. Results across all sites demonstrate how the sediment is moved within a single geomorphological feature, producing different chronological profiles within each of the individual sediment cores. For example, Site A: NVP15/1/1 and NVP15/3/1, and likewise Site B and the depositional lobe (NVP16/2/4) that forms downwind of the groundwater pump. These examples display a clear zone of erosion and accumulation in the current state; 'current' because all sediment cores must have been zones of deposition to have also built any form of sedimentary profile. When stacked, NVP15/3/1 and NVP15/1/1 chronologies ensure that more of the reactivation signal is captured. The individual sediment cores from the same feature show different reactivation profiles highlighting the heterogeneous nature of aeolian records as theoretically expected, and that future work should consider this when extracting sedimentary sections.

Nevertheless, large age gaps raise the question about whether the complete environmental signal has been captured. For example, the relatively large breaks between the identified units at site C may be caused by two factors. It could suggest that the deposition of surface sands is infrequent in this feature and thus large periods elapse between new deposits. Alternatively, high levels of reactivation may remove underlying sedimentary units during movement, leaving an incomplete record. As discussed in Bailey and Thomas (2014), the likelihood of an incomplete record is almost inevitable in these dynamic environments and therefore it would be erroneous to assume there had not been any aeolian activity in the periods

between the OSL ages. However, using this intensive sampling strategy across the local sites captures a greater proportion of reactivation events on the basis that a stacked history combining all sediment cores is more indicative of the reactivation history.

Nonetheless, there are examples where the OSL results have not identified activity suggested in the aerial photography. If we are unable to recreate the dates of reactivation shown in the aerial photography, it suggests that the multi-core method has not managed to capture all the variability and activity in the environment because either: a) more cores are needed, or b) in this dynamic environment, erosion of parts of the record is inevitable, despite younger sediments being better preserved (Bailey and Thomas, 2014). For example, the shallowest sediment age in sample NVP16/5/4, 1891 ± 37 AD is of interest. This is a particularly old age despite aerial photography showing a lobe of sediment deposited over the parabolic dune arm in 2013 following the extensive wildfire in 2012 on the Preserve. This suggests that either the core was not taken exactly from the presumed location on the aerial photograph, or that whilst the broader shape of the arm may be stable, the surface sediments are highly dynamic and modern sands are constantly overturned in the upper sections.

This being said, a static aerial imagery does not capture 'movement', it captures a moment in time that demonstrates a bare surface, and the assumption is that this creates the conditions likely for sediment movement. It does not consider the role of belowground biomass (Arterburn *et al.*, 2018), crusting (Goossens, 2004; Viles, 2008), or surface moisture, all of which have been shown to be important in determining the surface erodibility potential. Contrastingly, OSL ages represent a

date of deposition and are thus directly linked to a measure of surface reactivation. Identifying periods of bare sand in the imagery that are not represented in the OSL chronology could suggest: a) stripping of the surface vegetation cover alone does not instigate surface reactivation, implying a threshold of these conditions for a sustained period is needed prior to sediment movement; or b) that sediment was moving, but due to high levels of activity, the OSL ages date the 'end' of activity, and these earlier stages of activity are not captured in the sedimentary record. The sedimentary record has undergone a series of filtering and layered on top of the natural filtering is a sampling strategy, that despite having been refined, is still a selection of the chronology and does not capture the entire geochronological record.

9.1.4 Summary

Through combining changepoint analysis, a refined OSL protocol, and extensive sampling of the sedimentary record, this project has successfully reconstructed six chronologies of deposition following reactivation across NVP and surrounding ranches from a series of geomorphological features. The OSL results, as detailed in Chapter 7, show that in the upper 50 cm of sediment, we have captured deposition events from the last 2000 years with a dominance of events noted during the 19th and early 20th centuries. Having successfully identified land surface response to environmental change chronologically in the sedimentary record, the second research question assesses whether these noted events can be ascribed to specific environmental conditions.

9.2 RQ 2: Can we associate environmental conditions with depositional episodes?

Using a combination of traditional descriptive and statistical inference analyses, Chapters 7 and 8 (Papers 3 and 4) explored the potential for integrating deposition and driver profiles to deduce whether individual depositional episodes can be associated with a set of specific forcing conditions.

Whilst on Quaternary timescales dune stratigraphies could potentially be used to reconstruct palaeoclimatic histories, on shorter more recent timescales, dune stratigraphies represent a sediment response to a range of environmental conditions including: climate-induced drought, wildfire and grazing pressure. Recent theoretical studies have identified the importance of considering these disturbance factors together when determining the sensitivity of the vegetation cover and thus sediment remobilisation to future changes. In this project, this approach has been taken further and empirically tests the theoretical model with datasets of environmental response (deposition events) and measurements of disturbance forces across climatic and anthropogenic parameters.

Is there sufficient evidence to suggest that an individual reactivation event, as identified through an OSL age of sediment deposition, was caused by a specific drought, wildfire, or overgrazing period? This section discusses the second research question under a series of focused topics: i) can specific episodes be associated with a set of driving conditions? and related, ii) can the *nature* of events driving environmental change in the region be identified? We also comment on the implications of these research findings for our wider understanding of dune

dynamics and what they represent with regards to the palaeoenvironmental history of dryland systems.

9.2.1 Can we associate specific depositional episodes to specific or combined driving conditions?

Results in Chapter 7 (Paper 3) present the selected disturbance profiles alongside the individual site and total OSL chronologies (Figure 7.3). Peaks in the overall stacked PDF (Figure 7.3j) occur in the late-19th century and 1940s, with dates associated with these two events found across all study sites assessed. As Chapter 7 concludes, the reactivation found in the late-19th century occurs alongside an increase in wildfire frequency that is indicated in the tree scar record and the period of intense European expansion in the region. Severe blizzards during the winter of 1885-86 and the worst blizzard in Nebraskan recorded history of January 1888 also featured during this period alongside extreme droughts in the early 1890s. Combined, we can identify many potential causal factors that contributed to increasing the likelihood for vegetation disturbance and subsequent sediment reactivation. Anecdotal accounts from this period (Doug Kuhre – Grazing Manager NVP – Appendix J) confirmed that by the end of the 1880s, the sediment in the region had heavily blown out, which local residents associated with over-farming on the small 160-acre plots.

Meanwhile, the peak in reactivation ages spanning the 1940s follows the widely-cited US Dust Bowl period. This period succeeded the prolonged drought of the 1930s and peak population pressure in the Sandhills as Kinkaiders flooded the region following the Kinkaid Act. The implementation of the Kinkaid Act in

1904, which permitted the purchase of 640 acres of land, opened up the Sandhills to wider settlement. Prior to that, the 1862 Homestead Act only permitted the purchase of 160 acres and farming in such limited spaces on the Sandhills was not a successful strategy. Prior to 1904, farms were located around the edges of the sand dune regions where conditions were more amenable to small-scale farming. According to original land patent records, settlement on the study sites expanded rapidly post-1904 (Figure 9.2 and Appendix H). Following the Great Depression, unsuccessful in their farming efforts, and unable to weather the drought of the 1930s, Kinkaiders left the region and ranchers expanded into the remaining territory. Since then, the NVP and surrounding areas have been continuously used for ranching purposes.

Whilst unable to ascertain the importance of each of these individual parameters to the overall likelihood for inducing near-surface remobilisation, it can be noted that evidence for reactivation, as inferred through chronologies of deposition, followed a period of extreme climate and rapid land use change. Identifying the specific role of each driving parameter is difficult for three main reasons: i) OSL age uncertainty, ii) lagged-response in the system, iii) synergies between climatic and anthropogenic parameters.

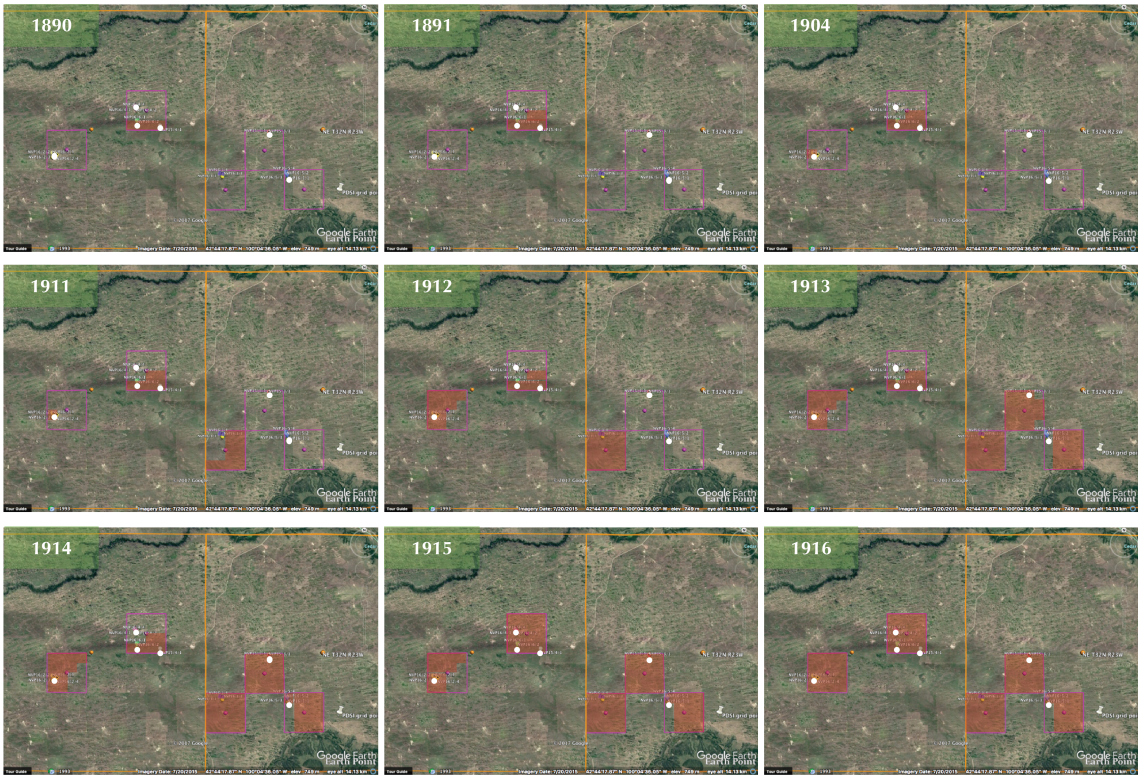


Figure 9.2 Using the exact dates from the land patent records for the original homesteading of the land sections in northern Brown County (see Appendix H), Figure 9.2 demonstrates the progressive purchasing of land during the late-19th and early-20th century. Sample sites are marked by the white dots and red patches highlight the sections of interest that have been bought by local land owners. Satellite imagery courtesy of © 2018 Google Earth Pro.

OSL age uncertainty

Whilst Chapter 7 discusses the evidence for the role of individual drivers by comparing the timing of identified periods of deposition in the OSL chronologies with measured environmental conditions and land use changes, the errors associated with OSL ages do not allow individual disturbance events to be linked to specific forcing factors. The individual OSL ages presented in this study have a 1σ uncertainty (average c.30 years across all samples), meaning that each estimated age potentially encompasses a 60-year period during which deposition occurred.

With climatic data presented annually, and land use changes measured across a range of temporal scales, ascribing an individual environmental forcing to a deposition event that could have occurred inside such a large window is increasingly difficult.

Lagged response

In addition to OSL age uncertainty, it is likely that there is a lag time between the disturbance event (e.g. drought) and the period of sediment reactivation (Barchyn and Hugenholtz, 2013a; Mangan *et al.*, 2004; Peters *et al.*, 2006). Chapter 7 explores how we might be able to identify a relationship between a disturbance event and the next subsequent luminescence age. All six sites showed evidence for sediment movement within a 5-year lag of droughts, but a notable response to land use pressure was noted at sites A, D and E (Figure 7.4). These sites yielded the youngest OSL ages and either showed evidence of bare sands during sampling (sites A & D) or were anecdotally known to have reactivated in recent decades (site E). For example, site A was overgrazed in the immediate period prior to purchase by TNC and change to NVP territory. Coupled with the relative topographic high of this particular dune in the surrounding landscape (Stubbendieck *et al.*, 1989), overgrazing has also been found to exacerbate growth of blowouts (Blanco *et al.*, 2008; Fox *et al.*, 2012). Historical aerial imagery, in combination with the presence of thin vegetation cover in the field, suggests that whilst this blowout was likely very active in previous decades, it is now beginning to recover, and stabilising vegetation species are colonising the active sands (Figure 9.3). Likewise, the homesteading and fencing off of the plots associated with site D, and the fence line associated with

site E, all point to identifiable land use interactions that could be instrumental in explaining the localised blowout and accumulation features. Nevertheless, the OSL age uncertainties restrict the capacity to draw any certain associations between 'events' and lagged responses.



Figure 9.3 Picture taken at site A of the colonising vegetation species that are typically found in blowouts across the Sandhills. Blowout grass, sandhills muhly and blowout penstemon (Weaver, 1965) are just some of the key species that grow in the active sands characterised by blowout conditions. Whilst blowout penstemon was once a common species in the Sandhills during the early 1900's (Stubbendieck *et al.*, 1989), the species is now endangered following habitat reduction with the severe drought of the 1930s (Stubbendieck, 1986; Weaver, 1954) and improved range management and wildfire control (Stubbendieck *et al.*, 1982).

Whilst simple visual methods restrict the analysis of these datasets, the application of statistical inference techniques (Chapter 8) to this particular research problem allows the accommodation of lags in a system response. Equally, whereas the OSL age uncertainties cannot be disentangled visually, using ANNs, we can identify common conditions between reactivation events that are not possible to extract through visual analysis. For example, results presented in the scenario analysis (Figure 8.5) demonstrate a lagged system response to increased grazing and wildfire occurrence that was not produced when climatic pressure alone was simulated.

Synergies between parameters

Finally, similar to complexities associated with identifying a lagged response to environmental disturbance, the likelihood that the sediment has been reactivated by a combination of parameters as opposed to a single forcing factor, is much greater. Figures 7.3h and 7.4 combine the idea of lagged response and synergies between periods of drought and land use change in Chapter 7, however, this is unable to dynamically model the myriad of potential synergies that could exist between the parameters.

Nonetheless, Chapter 8 ANNs provide a suitable tool for exploring the synergies between forcing factors. Whilst the black box statistical technique is unable to provide us with an overall quantification of the relationship between the parameters, individual weightings are ascribed to each disturbance factor based on the relationship that the model has *learnt* from the available datasets.

9.2.2 Can we identify the nature of events driving environmental change in the region?

As noted in Chapter 7 and section 9.2.1, the peaks in aeolian reactivation identified in the 1890s and 1940s are arguably a combination of extreme climatic events and rapidly changing land use and intensity pressures in the region. Despite difficulties in associating individual historic events with a suite of forcing factors, variability in the OSL chronologies and the application of statistical inference techniques across the study sites provides potential insights into the *nature* and *scale* of events driving the environmental response.

In this study, inter-site variability in OSL chronologies might have two possible explanations. There could be a heterogeneous response across a localised landscape to the same forcings, leading to differences in the resultant sedimentary record due to endogenous cycles of deposition, erosion and the heterogeneity of aeolian records in the environment (Bailey and Thomas, 2014; Leighton et al., 2014b; Stone and Thomas, 2008; Telfer et al., 2017, 2010; Telfer and Thomas, 2007; Thomas and Burrough, 2013). Unpublished work being completed as part of the Grassland Destabilisation Experiment (Professor David Wedin and colleagues at the University of Nebraska-Lincoln) is currently being used to identify spatial variability at localised scales (Figure 9.4). Localised spatial variability in net aeolian accumulation from a deflated basin at the Barta Brothers Ranch (visited as part of 2015 field season), supports the suggestion that the differences in the OSL chronologies may not be caused by the forcing, but by heterogeneous net accumulation.

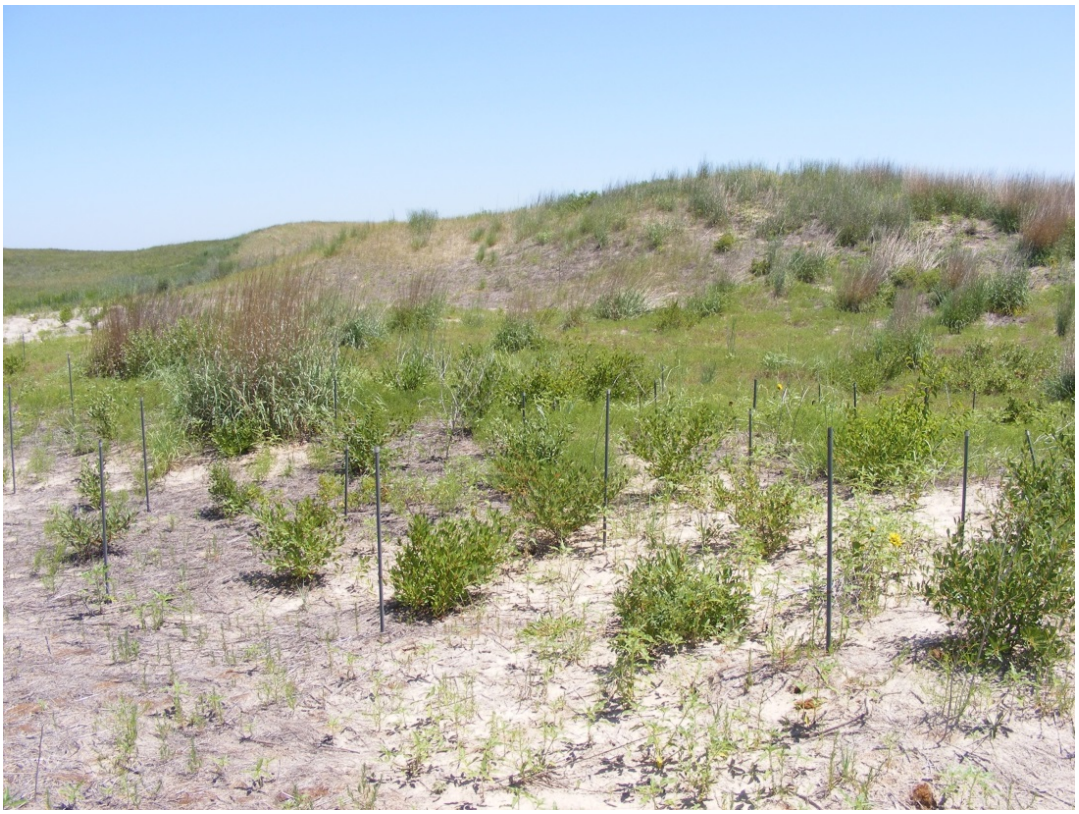


Figure 9.4 Erosion pins on the edge of a cleared deflation basin at the Barta Brothers Ranch, part of GDEX. Patches of vegetation were cleared and experiments conducted around the edges of the sections, monitoring the dynamics in aeolian transportation and net accumulation.

Alternatively, it might suggest that localised forcings (e.g. land use / grazing pressure) are important at driving frequent short-lived near-surface reactivation events. For example, the surface vegetation and underlying sediments across the six sites at NVP have responded differently over time, with dissimilar susceptibilities to the collection of forcings, as well as different grazing histories. This is supported by the ideas of Mason *et al.* (2004) who comment on the presence of blowouts in an otherwise stable dunefield, caused by disturbance to vegetation from cattle. The grouping of cattle in the lee of individual dunes (e.g. site A) or around sources of water (e.g. site B) provides the conditions for localised sand transport, even when

climatic conditions are relatively humid. For example, at site B we can see bare surface sediment across multiple aerial images, including during wet years (Appendix B). The common units found between cores taken from the same features (Figure 9.1) suggest that the whole feature was responding to an 'event' as opposed to highly localised post-depositional erosion (e.g. bioturbation, cattle trampling). The suggestion that localised forcing might be important at driving disturbance-scale features, such as blowouts is explored in the ANN sensitivity testing with different applications of wildfire and grazing pressure to two separate climatic futures (Figure 8.5)

A climate-dominated response

Results from ANN sensitivity testing suggested that the future likelihood of identifying OSL ages (representing disturbance events) in the deposited sedimentary profile was dominated by climatic pressures. Vegetation growth, inferred through a simulated tree ring growth index (ANN2), is broadly anticorrelated with the simulated OSL output when tree ring growth and varying levels of grazing pressure are applied (Appendix L: Figure L.8). Under historical average climatic conditions (climate 1), a noisy OSL output signal is produced, but a relationship can be seen between periods of declining tree ring growth and an increased likelihood of identifying a future period of sediment deposition. Under moderate grazing and heavy grazing conditions, regardless of any additional grazing pressure added to the system, the results of ANN1 remain climate-signal dominated and suggest that the record broadly reflects periods of notable climatic stress (i.e. drought in these semi-arid dryland environments).

The role of localised disturbances

Nevertheless, whilst climatic pressure explains the majority of the variability under moderately and heavily grazed systems; the low grazing model outputs show greater sensitivity to localised disturbances such as fire and grazing pressure. Although recent studies have suggested that grasslands have successfully recovered from wildfires without resulting in sediment disturbance (Arterburn *et al.*, 2018), the scenario modelling in this project found that fire had the potential to increase the likelihood (referred to as the 'Deposition Event Score'[7] in Paper 4) or extend the period associated with a deposited age (e.g. Figure 8.5b and 8.5d). The influence of fire on the overall ANN1 output profile varies between climatic scenario and grazing regime suggesting the relationship between fire and depositional profile is not linearly related or exclusively connected. It has not been possible to quantify the role of wildfire; however combined with existing knowledge of grassland-wildfire dynamics, these results agree with studies (e.g. Mangan *et al.* (2004); Whicker *et al.* (2006)) that suggest it might be synergies between wildfires and other forcing factors that are important in driving or exacerbating landscape disturbance.

The inclusion of wildfires in this study is not used to represent an entirely natural or anthropogenic environmental driver. The relationship between climate, wildfire, and human occupation is complex and does not remain the same throughout the study period. Whilst human activities in the region have previously been associated with increasing the likelihood for wildfire occurrence (e.g.

[7] Referred to as 'Deposition Event Score' in Paper 4 as the ANN1 output is not a probability metric. The changing profiles within the sensitivity analysis show an increased deposition event response when grazing and wildfire are added, but this does not translate into an identifiable percentage probability metric.

introduction of the rail road (Marlon *et al.*, 2012)), numerous wildfires also occur in the region due to frequent lightning strikes (e.g. the wildfire of 2012 on the Preserve was caused by a lightning strike on Doug Kuhre's ranch). Management techniques in recent decades mean that wildfire likelihood is now reduced due to human occupation (Forman *et al.*, 2001). This is especially the case at the NVP where regular prescribed burns are used to reduce the wildfire risk and simulate controlled levels of natural disturbance (Helzer, 2010).

Arterburn *et al.*'s (2018) study of fire effects on disturbance at NVP, suggest that fire does not cause destabilisation, with the grasslands typically recovering following a fire event (Morrison *et al.*, 1986; Pfeiffer and Steuter, 1994; Volesky and Connot, 2000). By contrast broad-scale destabilization is linked to megadroughts and the removal of belowground fine root biomass (Miao *et al.*, 2007). Based on the findings from the historical and scenario modelling of this research project, this study agrees that infrequent fire occurrence is unlikely to be the key driver associated with broad-scale reactivation (peaks broadly anti-correlate with drought-induced vegetation growth reduction), but on a smaller localised scale, fire might be important in explaining the heterogeneity we find in the NVP OSL chronologies. Identifying synergies between fire and drought will be key to determining the impact of future fires that might increase in line with anticipated climatic changes (Breshears *et al.*, 2016).

In this study we have been unable to dynamically model the occurrence of a wildfire relative to potential drivers (e.g. lightning, human fire) since historical fires have been caused by a range of both human and natural processes. Lightning strikes, for example, are almost completely unpredictable in terms of their temporal

frequency and spatial positioning. Equally, the relationship between climate and fire is complex (Guyette *et al.*, 2015). Specifically in relation to this field site, Guyette *et al.* (2015) comment on the role of maximum temperature and annual precipitation affecting fire frequency. They explore the dynamic role of precipitation as both a requirement for fuel (high precipitation), but also in terms of creating the arid conditions necessary for wildfires to begin (low precipitation). Their results suggest that a threshold exists within the Great Plains whereby the role of precipitation in relation to wildfire shifts from being too little rain to support fuel required for fire, to too much rain to support the conditions needed for a fire to start. Guyette *et al.* (2015) place this longitudinal threshold through the Niobrara Valley Preserve, highlighting the added complexity in attempting to identify the drivers and relationship associated between historical climate and wildfire occurrence. For the purposes of simplicity and to demonstrate the sensitivity analysis of individual parameters, wildfires were included when average maximum temperatures exceeded 26.7°C, however future models could integrate the drivers of fire occurrence into the simulations to produce realistic futures.

Similar to the role of fire, results from ANN analysis highlighted that the system is sensitive to changes in grazing pressure. Whilst traditional methods of analysis in Chapter 7 were unable to identify a distinct grazing component due to many potential causal factors occurring simultaneously, the scenario analysis allowed us to explore the sensitivity of the system when various disturbances were added. Additional peaks in OSL age identification (Deposition event score) were found when increased grazing pressure was added to the system under previously low-pressure grazing conditions (Figure 8.5a), with a notable peak found when

additional grazing was coupled with climate 1 (i.e. long-term averages). In comparison, when combined with progressively warming climatic conditions (climate 2), an increase in grazing pressure does not appear to exert any additional impact on the deposition event profile (Figure 8.5c). These results suggest that there is a threshold in the system above which additional grazing pressure is no longer significant as the climatic stresses are driving the prevailing conditions. For example, we can imagine a situation where persistently more arid conditions have reduced the vegetation cover to such a level that a maximum level of grazing can only be sustained before the sediment reactivates regardless of overgrazing levels. As mentioned in Chapter 8 and above, whilst drought appears to be the key determining factor in driving disturbance and influencing the periods of reactivation and thus dated deposition events, localised grazing pressures likely contribute to the heterogeneity in deposition that we have found across the near-surface sediments. As management practices, grazing strategies, and ranching pressures in the region evolve, so too will the relationship with vegetation cover and landscape stability.

9.2.3 Implications for wider dune studies

In addition to improving our understanding of recent dune dynamics in the northern Nebraska Sandhills, this research has significant implications for our understanding of dryland dune dynamics. Our results suggest that aeolian stratigraphic profiles represent a complex response to a range of both climatic and localised disturbance forces (e.g. grazing pressure and wildfire occurrence). In light of this, whilst on Quaternary timescales, aeolian stratigraphies may be considered

a direct response to climatic change (Mason *et al.*, 2004), greater coverage of sampling is needed to ascertain the response to both localised and regional forces. Whilst on Quaternary timescales human-influenced overgrazing and agricultural practices are only linked to the late Holocene, biogenic influences should still be considered when interpreting sediment burial ages as climate proxies. For example, buried bison tracks found in blowouts across the Nebraska Sandhills (Loope and Swinehart, 2000; Schmeisser *et al.*, 2009b) and bison bone evidence in sedimentary sequences across the Duchess dunefields (Wolfe *et al.*, 2002), have been linked to localised destabilisation in the surface vegetation cover and used to explain evidence of historical aeolian activity over the past 4.5 ka.

9.2.4 Summary

In sum, it is not possible to associate individual wildfires, climatic anomalies, or grazing seasons as being responsible for specific reactivation and deposition events, but equally it is unlikely that any individual event caused a response. Drylands are highly non-linear in disturbance responses (Gillson and Hoffman, 2007; Leighton *et al.*, 2014a; Lohmann *et al.*, 2012; Yizhaq *et al.*, 2009) and a threshold value of sensitivity has to be reached in order to cause a shift in the system. The variability in the OSL ages from this study suggests that localised forcing in synergy with climatic stresses likely drove reactivation in the form of blowouts (i.e. localised pockets of erosional disturbance).

Results from ANNs suggest that localised parameters (i.e. grazing and fire) do have a role in increasing sediment reactivation likelihood, although climatic extremes (i.e. drought) explain the majority of the signal with localised forcings

increasing the likelihood for reactivation when conditions allow. Aerial photographs from 1939, 1954 and 1968 (Appendix B) support this suggestion that localised pockets of the dunefield can reactivate and respond quickly whilst the remaining dunefield remains stable and vegetated.

Findings from this study have wider implications for our understanding of dune chronological histories, affirming the role of climate as key in driving sustained vegetation death that permits the reactivation of dryland surfaces whilst acknowledging grazing pressure disturbance, and wildfire to a lesser degree, in contributing towards local-scale heterogeneity in the field.

9.3 RQ 3: Can a suitable method be identified to predict future surface reactivations leading to deposition?

Using ANN techniques, this research project has developed a methodology that allows us to dynamically model the relationship between environmental response, as represented by the stacked OSL chronologies of deposition events, and disturbance drivers (i.e. climate, land use pressure and wildfire occurrence). By applying ANNs, we are able to train and test the model on known datasets prior to using the trained model for future scenario testing. The capacity of the models to reproduce the known OSL profiles when half of the dataset is used for training, or when the individual site is excluded from the model training suggests that the model is robust and theoretically can be used to predict future likelihoods of an OSL age being identified in the record under different future conditions. Unlike traditional descriptive analysis, supervised machine learning (SML) has allowed us to

incorporate non-linear dynamics, lag times and the synergies between individual drivers into the relationship.

9.3.1 Model highlights

Results from Chapter 8 have shown successful cross-validation outputs when sites are excluded from the training dataset. Both ANN1 and ANN2 have been able to train known inputs to fit the historical datasets (i.e. OSL PDFs and tree ring growth index) when the dataset is partitioned and used for training and testing purposes. To avoid over-fitting of the trained model and a reduction in prediction capabilities, ANN1 is trained on only half of the known historical dataset, with the remaining half used for validation and testing. As expected, when particular combinations are not 'seen' in the training dataset, the model is unable to recreate these conditions when tested. For example, site B is characterised by higher levels of grazing pressure than the remaining five sites; thus, the OSL profile at site B cannot be accurately reproduced when this profile is excluded from the training set (Figure 8.1). This example demonstrates the need for high volumes of sediment sampling and data entry when using such statistical inference techniques. Nonetheless, across the five remaining study sites, the cross-validated testing showed broad agreement with the known geochronological profiles suggesting that the key parameters that account for the episodes of deposition in the sedimentary records have been included in the model and that the architecture has been suitably selected. For example, the lag period of up to 8 years was selected following a series of sensitivity tests; too long a lag period reduces the overall model performance (e.g. asking the model to relate a deposition event with a drought 20

years ago). Similarly, ANN2 performs very well when only 70% of the dataset is used to train the model (Figure 8.2), suggesting the key elements explaining variability in tree ring growth have been accounted for.

9.3.2 Future scenario predicting

The capacity to accurately predict future environmental response under a range of climatic and anthropogenic disturbance scenarios is largely controlled by two factors: 1) the size and range of the training dataset, 2) model architecture. Firstly, as noted in 9.3.1 the breadth of conditions and events captured in the training dataset determines the combinations that the model can 'learn' and therefore predict under future inputs. In this study, to increase our training dataset, as opposed to training the model on one "master" OSL PDF, it was more appropriate to train the model on the six individual sites in tandem. Training the model on one stacked overall OSL PDF would lose the resolution of the individual site grazing pressures and be hindered by the overlapping and "continuous" OSL age errors. By comparison, training the model on the OSL-derived responses from the individual sites allowed for distinct events to be identified at each site and the localised pressures to be considered alongside the common parameters (e.g. climate). With a robust training model built (ANN1), ANN2 was able to construct a range of future tree ring growth indices based on two separate climatic futures (Table 8.1). When combined with different grazing pressure and wildfire conditions, a total of six scenarios (Table 8.2) were modelled to sensitivity test the role of individual parameters (see earlier Discussion). Nevertheless, despite the

broad success in this study demonstrating proof-of-concept in the future potential application of these methods, there are potential limitations that should be noted.

9.3.3 ANN model limitations

Whilst the ANN models have demonstrated high levels of agreement with the known datasets, there are limitations to the current model set-up that demonstrate the limits and capacity of the method based on these datasets:

Resolution of the target dataset

For example, the uncertainty associated with the OSL ages prevents the target dataset from reflecting the same annual resolution as the disturbance dataset. As a result, conditions in the input datasets, which are not necessarily causing a disturbance to the landscape, are wrongfully associated with a peak in the target dataset that extends across a large period (e.g. across 20 years) (Figure 8.6).

Size of the training dataset

Moreover, as discussed earlier, the capacity of a model to predict certain futures is dependent on the training dataset. If the model has not been able to "learn" a particular combination of events, it will not be able to recreate that scenario under future datasets. With this in mind, the relatively short length of the dataset used in this study (c.400 timesteps) limits the number of combinations that the model has successfully learnt. This is especially important if future climates are to become more extreme, drier and beyond any analogue that we have in the existing record. This would restrict the ability of the model to predict future

environmental change. Further to this, as human actions in the environment evolve, the model is unable to predict future landscape response based on human decision-making and changes in management strategy. The current model is based on the interactions between grazing pressure, vegetation growth and wildfire as defined by the relationship during the last four centuries, not future land use practices. Likewise, the relationship with fire is complex. As noted earlier, the risk posed by wildfires has decreased in recent decades due to human intervention (Forman *et al.*, 2001) in preventing (Helzer, 2010) and restricting the spread of fire. The model has been trained on the historical relationships with fire over the last four centuries, but it is not able to learn that the risk from fire varies as a factor of changing human agency.

Training on 'events' not stability

The training dataset of the model is further limited by solely focusing on the drivers of disturbance events that induce deposition and not those conducive of stability. Since we are only able to luminescence date the sediment that has been preserved in the environment, and not the sediment that has been eroded in subsequent reactivation events; a period without a luminescence age is only indicative of an absence of evidence as opposed to evidence of absence. As such, all periods in the model where the target dataset was reduced to 0 likelihood, were omitted from the training dataset and the model was only trained on periods when we confidently know that the sediment was deposition. However, if we were able to equally be confident in the years that were 'stable' (i.e. no surface reactivation),

we could include these in the training dataset and future research could expand the range of scenarios for the network to learn from.

Quantifying the role of drivers

Finally, given the black box nature of the SML tools, we do not know the exact relative importance of different drivers to the likelihood for an OSL age to be identified. The role of each individual driver is connected to each individual node included in the hidden layers, creating a complex multi-tiered non-linear relationship that is not independent from the other model inputs. However, sensitivity testing the role of individual parameters by gradually incorporating different levels of grazing, fire and climatic stress has begun to demonstrate ways in which we can semi-quantify and qualify the impact of each parameter (Figure 8.5).

9.3.4 Summary

Overall, the application of ANN techniques, as part of the wider SML suite of tools, has demonstrated the capability of these statistical inference methods to answer questions about landscape dynamics in a field of research dominated by traditional methods, without knowledge of the underlying process-based mechanistic model. Agreement between the known and simulated OSL profile outputs during model validation exercises proves the robustness of the model and suggests it to be a suitable tool for exploring future scenarios despite the 'small' dataset used relative to existing ANN applications. As with all SML tools, the main limitation is the ability to robustly predict future scenarios that are non-analogous

to historical conditions. For example, in this study the network was unable to predict the target dataset given a set of inputs if it had not 'seen' that specific combination in the training stages. For that reason, this technique is best applied to research questions with large volumes of data that span multiple 'events', giving the model the largest possible number of combinations to train from. Likewise, if future climates are to be hotter and precipitation variability more extreme relative to historical conditions, the model will be unable to extrapolate the learning from the training dataset onto future model predictions.

9.4 Overall conclusions

The topic of drivers and sediment reactivation potential in dryland regions is of paramount importance. This thesis aimed to explore the associations between external forcing factors and environmental response in semi-arid grasslands. Whilst existing research has acknowledged that both natural and anthropogenic forcings affect the likelihood of vegetation disturbance and subsequent land degradation, an integrated research project that assesses this relationship with the support of empirical data was lacking from the literature. With this in mind, this research project utilised a range of data sources including empirical field measurements, instrumental climate datasets and qualitative archival records to produce an integrated assessment of the evidence for historical near-surface reactivations and the associated forcing factors.

Using a refined OSL protocol and a new tool for sub-sampling in aeolian environments, this project has demonstrated the potential for OSL dating of young

sediments and the capacity to geochronologically identify distinct periods of deposition in seemingly lithologically homogeneous profiles. When deployed on sediments extracted from the Nebraska Sandhills, the application of a multi-core sampling strategy has highlighted the localised variability in episodes of deposition both between and within geomorphological features; successfully capturing a more complete history of sediment mobilisation across the landscape.

Once dated, episodes of peak sediment deposition in the near-surface dune record were noted in the late-19th century and 1940s with overlapping OSL ages spanning the last 900 years. In the late-19th century, periods of deposition occur alongside peaks in the wildfire record, the period of intense European expansion into the region and homesteading, and historically noted extreme weather conditions. Meanwhile, the peak in the 1940s follows the widely-cited US Dust Bowl, with the extreme drought of the 1930s coupled with peak Sandhills population levels.

Variability found in the OSL profiles between sampling sites suggests that no single factor is solely responsible for the deposition history of the near-surface sediments at the NVP. This is in agreement with existing studies (Barchyn and Hugenholtz, 2013a; Lee and Gill, 2015; Mangan *et al.*, 2004; Stubbendieck, 2008), and was supported by the results from ANN analysis. The novel application of statistical inference techniques to explore the driver-response relationships in aeolian systems is a first for dryland research. Results from ANN analyses have highlighted the importance of climatic conditions in driving the likelihood of identifying future episodes of deposition in the sediment record under a range of disturbance settings. Yet, despite this climatic dominance, sensitivity-testing

suggested that other disturbance factors, such as increased grazing pressure and periods of wildfire, increase the likelihood of identifying an episode of deposition when other pressures (e.g. climatic aridity) are less severe. This impacts our wider understanding about what the recent geochronological record of dunes and other aeolian features, such as blowouts, represent in dryland aeolian settings.

9.5 Future research

A widening of the original research focus, and the development of new techniques and methodological advances, provide opportunities for future research to expand upon this study. This final section of the thesis discusses some of the ways in which this study could be extended and suggests the application of this research to alternative study sites globally.

9.5.1 Additional external parameters

This study has focused on assessing the relationships between some of the main environmental conditions (climate, grazing / land use pressure and wildfire occurrence), but there are other external forcings that also contribute to the likelihood for sediment reactivation and could be included in future research.

Whilst wind speed was initially not considered a limiting factor in this study (section 6.2.6), evidence from the field suggests that wind speed may have an impact on the localised spacing of near-surface reactivation. In this particular study region, average daily wind velocities are available from the 1980s onwards but are not considered a limiting factor due to persistently high wind velocities. However,

an understanding of wind speed, topography and aspect for each study site might be useful in explaining some of the localised heterogeneity in the OSL record, in particular the evolution of blowouts which tend to develop in upland sites (Farrar, 2008). For example, when conducting pilot fieldwork at GSL, blowouts were typically found on the south facing or north west facing dune faces (i.e. facing into the direction of dominant winds). At the NVP and surrounding ranches, this spatial specificity of the blowouts was less pronounced, likely due to the more varied land uses at the study site and lower-lying dunes.

If we are able to harness a longer time series of wind velocity datasets in the future, covering a high-spatial resolution, they could also be used as another model input to look at spatial heterogeneity of the reactivation signal in the environment. In the absence of long-term measurements, an alternative approach could use paleoclimate models to reconstruct the direction and strength of historical wind velocities, although these models would compromise on spatial resolution.

9.5.2 Additional geomorphic features

As well as increasing the level of information in regards the number of disturbance mechanisms assessed, future extensions of this research could increase the number of response features analysed. First, since this project has demonstrated proof-of-concept of the method and application of ANNs to answering questions of the driver-environmental response relationship in dynamic environments, this approach could equally be extended to incorporate fluvial, colluvial and alluvial features. As discussed in section 3.2, this study prioritised aeolian geomorphic features following the abundance of blowouts and available sediment in the

Nebraska Sandhills. However, extending this project to include alternate features such as dry river beds, alluvial fans, and gully deposits could provide further information about the influence of historical hydrological disturbances in the region.

Second, increasing the number of aeolian sampling sites would expand the respective datasets associated with specific features. In order to have a dataset large enough to identify a relationship between geomorphic response and the disturbance datasets, all six study sites were modelled alongside each other in the ANN. However, increasing the number of sampling sites across blowouts, or parabolic dunes, or fenceline dunes (for example), would mean that relationships specific to individual features could be determined. For example, how have parabolic dunes versus blowouts in the NVP vicinity responded over the recent historical past? To produce a dataset large enough for modelling we were forced to 'coarse grain' the research and combine the individual sampling sites, yet extensions in the number of sites sampled could yield interesting results about the variability between and within different aeolian features across the local landscape.

9.5.3 Improving the neural network

As with all SML techniques, the derived models are always improved when the training datasets are large. The more scenarios the model is able to 'learn' from, the better the model fit when used to predict new scenarios with unseen datasets. In this research project, we were restricted to the last 100 years, with meteorological station records only available from the early-20th century. We were able to extend the training dataset to cover the period since 1600 AD by building a second neural

network that modelled the relationship between growing season climatic parameters (average temperature and precipitation totals) and tree ring growth. However, to improve the model further, datasets that capture more combinations of disturbances during deposition events are needed.

Longer chronologies

The precision of OSL dating improves with signal size, thus extending the chronology using OSL techniques beyond the time period studied in this project is not a problem but identifying a suitable secondary dataset to assess alongside is limited with instrumental records only captured during the last 100 years. Similar to the use of tree ring growth records in this study, future work could look to explore the potential of combining multiple proxies as opposed to direct parameter measurement. Whilst the use of proxies to infer climatic conditions is circular, when combined in a multiproxy study could yield interesting results which could complement and expand upon current Quaternary investigations.

Alternative semi-arid environments

Applying this technique to an alternative location that experiences more frequent near-surface reactivations will also increase the number of 'events' for the neural network to train from. We used the stacked OSL PDFs as the target dataset to train the relationship between environmental forcing factors and the likelihood for identifying a near-surface response in ANN1. The identification of an age in the sedimentary record is evidence of a reactivation event, however, the opposite is not also true. For example, the absence of a luminescence age is not evidence of

stability since post-depositional erosion-accumulation cycles erode the sedimentary record and leave us with a partially-complete reactivation history, even when multiple cores are stacked across individual features. As such, since we can only be certain on the relationship between a known event and the external parameters, during the pre-processing stage of ANN1, all 'non-events' were removed from the target dataset. This avoids falsely training the model to identify a set of environmental parameters as conducive to periods of stability.

Having established proof-of-concept in this research project, this suite of techniques can now be deployed in alternative locations to similarly model the historical relationship. A study location that experiences more frequent cycles of reactivation (and thus deposition) would provide more 'events' to train the neural network on and improve the overall capacity of the model to accurately predict future outcomes based on unseen datasets. For example, sediment samples from GSL (a more upland setting), or grasslands in southern Africa might provide more historical deposition events than the record at NVP.

Satellite datasets

Finally, satellite datasets and earth observation tools can provide incredibly high-resolution spatial and temporal datasets that measure numerous characteristics of the earth's (and sea) surface. Whilst not extending back over the time periods studied in this research project, the daily resolution of satellite data would provide the researcher with many more data points than the annual-scale of this current research project. Combined with meteorological station measurements, not only could earth observation data be used to provide inputs for the neural network model

(e.g. NDVI, above land temperatures), but also satellite imagery could be used as the target dataset. For example, our growing knowledge on vegetation patterning (e.g. Mayaud *et al.*, 2017a, 2017b) could be used to train a model to identify the relationship between climatic data and bare surface patterns / reactivation features, determining the set of environmental factors that are contributing to this process.

9.5.4 Summary

Whilst this project contributes to the luminescence, aeolian research and dryland literature, future extensions could fulfil the potential benefits of SML techniques when applied to environmental questions in data-rich topics. Expanding the datasets to capture more disturbance forces, longer chronologies of events and environments with more frequent episodes of deposition would all increase the size of the training dataset and allow for more sophisticated and accurate models to be built. Alternatively, future extensions could move away from a luminescence approach which is restricted by large age uncertainties. Combining this method with an alternative measure of landscape dynamics, such as the use of satellite imagery, could open new opportunities for identifying the relationships between climatic and anthropogenic drivers and environmental response across all ecosystems.

REFERENCES

Adamiec, G., Aitken, M., 1998. Dose-rate conversion factor: update. *Ancient TL*.

Adamson, G.C.D., Nash, D.J., 2014. Documentary reconstruction of monsoon rainfall variability over western India, 1781–1860. *Climate Dynamics* 42, 749–769. https://doi.org/10.1007/s00382-013-1825-6

Ahangar, R.G., Yahyazadehfar, M., Pournaghshband, H., 2010. The Comparison of Methods Artificial Neural Network with Linear Regression Using Specific Variables for Prediction Stock Price in Tehran Stock Exchange. *International Journal of Computer Science and Information Security* 7, 038–046.

Ahlbrandt, T.S., Fryberger, S.G., 1980. *Eolian deposits in the Nebraska Sand Hills*, Geologic and Paleoecologic Studies of the Nebraska Sand Hills. United States Government Printing Office, Washington.

Aitken, M.J., 1998. *An Introduction to Optical Dating*. Oxford University Press, NY.

Aitken, M.J., 1985. *Thermoluminescence Dating*. London, Academic Press Inc.

Aitken, M.J., Smith, B.W., 1988. Optical dating: recuperation after bleaching. *Quaternary Science Reviews* 7, 387–393.

Arnold, L.J., Roberts, R.G., Galbraith, R.F., DeLong, S.B., 2009. A revised burial dose estimation procedure for optical dating of youngand modern-age sediments. *Quaternary Geochronology* 4, 306–325. https://doi.org/10.1016/j.quageo.2009.02.017

Arterburn, J.R., Twidwell, D., Schacht, W.H., Wonkka, C.L., Wedin, D.A., 2018. Resilience of Sandhills Grassland to Wildfire During Drought. *Rangeland Ecology & Management* 71, 53–57. https://doi.org/10.1016/j.rama.2017.07.010

Ash, J.E., Wasson, R.J., 1983. Vegetation and sand mobility in the Australian desert dunefield. *Zeitschrift fur Geomorphologie Supplementband* 45, 7–25.

Atkinson, O.A.C., Thomas, D.S.G., Goudie, A.S., Bailey, R.M., 2011. Late Quaternary chronology of major dune ridge development in the northeast Rub' al-Khali, United Arab Emirates. *Quaternary Research* 76, 93–105. https://doi.org/10.1016/j.yqres.2011.04.003

Auclair, M., Lamothe, M., Huot, S., 2003. Measurement of anomalous fading for feldspar IRSL using SAR. *Radiation Measurements* 37, 487–492. https://doi.org/10.1016/S1350-4487(03)00018-0

Bailey, R.M., 2010. Direct measurement of the fast component of quartz optically stimulated luminescence and implications for the accuracy of optical dating. *Quaternary Geochronology* 5, 559–568. https://doi.org/10.1016/j.quageo.2009.10.003

Bailey, R.M., 2003. Paper II: The interpretation of measurement-time-dependent single-aliquot equivalent-dose estimates using predictions from a simple empirical model. *Radiation Measurements* 37, 685–691. https://doi.org/10.1016/S1350-4487(03)00079-9

Bailey, R.M., 1998. The form of the optically stimulated luminescence signal of quartz: implications for dating. PhD thesis, University of London.

Bailey, R.M., Arnold, L.J., 2006. Statistical modelling of single grain quartz De distributions and an assessment of procedures for estimating burial dose. *Quaternary Science Reviews* 25, 2475–2502. https://doi.org/10.1016/j.quascirev.2005.09.012

Bailey, R.M., Singarayer, J.S., Ward, S., Stokes, S., 2003. Identification of partial resetting using De as a function of illumination time. *Radiation Measurements* 37, 511–518. https://doi.org/10.1016/S1350-4487(03)00063-5

Bailey, R.M., Smith, B.W., Rhodes, E.J., 1997. Partial bleaching and the decay form characteristics of quartz OSL. *Radiation Measurements* 27, 123–136.

Bailey, R.M., Thomas, D.S.G., 2014. A quantitative approach to understanding dated dune stratigraphies. *Earth Surface Processes and Landforms* 39, 614–631. https://doi.org/10.1002/esp.3471

Bailey, S.D., Wintle, A.G., Duller, G.A.T., Bristow, C.S., 2001. Sand deposition during the last millennium at Aberffraw, Anglesey, North Wales as determined by OSL dating of quartz. *Quaternary Science Reviews* 20, 701–704. https://doi.org/10.1016/S0277-3791(00)00053-6

Ballarini, M., Wallinga, J., Murray, A.S., Van Heteren, S., Oost, A.P., Bos, A.J.J., Van Eijk, C.W.E., 2003. Optical dating of young coastal dunes on a decadal time scale. *Quaternary Science Reviews* 22, 1011–1017. https://doi.org/10.1016/S0277-3791(03)00043-X

Ballarini, M., Wallinga, J., Wintle, A.G., Bos, A.J.J., 2007. A modified SAR protocol for optical dating of individual grains from young quartz samples. *Radiation Measurements* 42, 360–369. https://doi.org/10.1016/j.radmeas.2006.12.016

Baltensperger, B.H., 1985. *Nebraska: A Geography*. Westview Press, Inc., Boulder, Colorado.

Banerjee, D., Murray, A.S., Foster, I.D.L., 2001. Scilly Isles, UK: Optical dating of a possible tsunami deposit from the 1755 Lisbon earthquake. *Quaternary Science Reviews* 20, 715–718. https://doi.org/10.1016/S0277-3791(00)00042-1

Barchyn, T.E., Hugenholtz, C.H., 2013a. Reactivation of supply-limited dune fields from blowouts: A conceptual framework for state characterization. *Geomorphology* 201, 172–182. https://doi.org/10.1016/j.geomorph.2013.06.019

Barchyn, T.E., Hugenholtz, C.H., 2013b. Dune field reactivation from blowouts: Sevier Desert, UT, USA. *Aeolian Research* 11, 75–84. https://doi.org/10.1016/j.aeolia.2013.08.003

Bateman, M.D., Boulter, C.H., Carr, A.S., Frederick, C.D., Peter, D., Wilder, M., 2007. Detecting post-depositional sediment disturbance in sandy deposits using optical luminescence. *Quaternary Geochronology* 2, 57–64. https://doi.org/10.1016/j.quageo.2006.05.004

Bateman, M.D., Rushby, G., Stein, S., Ashurst, R.A., Stevenson, D., Jones, J.M., Gehrels, W.R., 2017. Can sand dunes be used to study historic storm events? *Earth Surface Processes and Landforms* 2. https://doi.org/10.1002/esp.4255

Bateman, M.D., Stein, S., Ashurst, R.A., Selby, K., 2015. Instant luminescence chronologies? High resolution luminescence profiles using a portable luminescence reader. *Quaternary Geochronology* 30, 141–146. https://doi.org/10.1016/j.quageo.2014.12.007

Bathke, D.J., Oglesby, R.J., Rowe, C.M., Wilhite, D.A., 2014. *Understanding and Assessing Climate Change: Implications for Nebraska*. University of Nebraska-Lincoln

Bell, W.T., 1979. Thermoluminescence Dating: Radiation dose-rate data. *Archaeometry* 21, 243–245.

Belsky, A.J., 1992. Effects of grazing, competition, disturbance and fire on speices composition and diversity in grassland communities. *Journal of Vegetation Science* 3, 187–200.

Biondini, M.E., Patton, B.D., Nyren, P.E., 1998a. Grazing intensity and ecosystem processes in northern-mixed grass prarie, USA. *Ecological Applications* 8, 469–479. https://doi.org/10.1890/1051-0761(1998)008[0469:GIAEPI]2.0.CO;2

Biondini, M.E., Patton, B.D., Nyren, P.E., 1998b. Grazing intensity and ecosystem processes in northern-mixed grass prairie, USA. *Ecological Applications* 8, 469–479. https://doi.org/10.1890/1051-0761(1998)008[0469:GIAEPI]2.0.CO;2

Biondini, M.E., Steuter, A.A., Hamilton, R.G., 1999. Bison Use of Fire-Managed Remnant Prairies. *Journal of Range Management* 52, 454. https://doi.org/10.2307/4003772

Blanco, P.D., Rostagno, C.M., del Valle, H.F., Beeskow, A.M., Wiegand, T., 2008. Grazing Impacts in Vegeated Dune Fields: Predictions From Spatial Pattern Analysis. *Rangeland Ecology & Management* 61, 194–203.

Bleed, A.S., 1998. Introduction, in: Bleed, A.S., Flowerday, C.A. (Eds.), *An Atlas of the Sand Hills*. pp. 1–16.

Blockley, S.P.E., Lane, C.S., Hardiman, M., Rasmussen, S.O., Seierstad, I.K., Steffensen, J.P., Svensson, A., Lotter, A.F., Turney, C.S.M., Bronk Ramsey, C., 2012. Synchronisation of palaeoenvironmental records over the last 60,000 years, and an extended INTIMATE1event stratigraphy to 48,000 b2k. *Quaternary Science Reviews* 36, 2–10. https://doi.org/10.1016/j.quascirev.2011.09.017

Blott, S.J., Pye, K., 2001. Gradistat: A Grain Size Distribution and Statistics Package for the Analysis of Unconcolidated Sediments. *Earth Surface Processes and Landforms* 26, 1237–1248. https://doi.org/10.1002/esp.261

Bogle, R., Redsteer, M.H., Vogel, J., 2015. Geomorphology Field measurement and analysis of climatic factors affecting dune mobility near Grand Falls on the Navajo Nation , southwestern United States. *Geomorphology* 228, 41–51. https://doi.org/10.1016/j.geomorph.2014.08.023

Bøtter-Jensen, L., Bulur, E., Duller, G.A.T., Murray, A.S., 2000. Advances in luminescence measurement systems. *Radiation Measurements* 32, 523–528.

Bowman, D.M.J.S., Balch, J., Artaxo, P., Bond, W.J., Cochrane, M.A., D'Antonio, C.M., Defries, R., Johnston, F.H., Keeley, J.E., Krawchuk, M.A., Kull, C.A., Mack, M., Moritz, M.A., Pyne, S., Roos, C.I., Scott, A.C., Sodhi, N.S., Swetnam, T.W., 2011. The human dimension of fire regimes on Earth. *Journal of Biogeography* 38, 2223–2236. https://doi.org/10.1111/j.1365-2699.2011.02595.x

Boyd, M., 2002. Identification of anthropogenic burning in the paleoecological record of the Northern Prairies: A new approach. *Annals of the Association of American Geographers* 92, 471–487. https://doi.org/10.1111/1467-8306.00300

Bragg, T.B., 1995. Climate, soils and fire: the physical environment of North American grasslands, in: Joern, A. (Ed.), *The Changing Prairie*. Oxford University Press, NY.

Breshears, D.D., Knapp, A.K., Law, D.J., Smith, M.D., Twidwell, D., Wonkka, C.L., 2016. Rangeland Responses to Predicted Increased in Drought Extremity. *Rangelands* 38, 191–196.

Bronk Ramsey, C., 2009. Bayesian Analysis of Radiocarbon Dates. *Radiocarbon* 51, 337–360. https://doi.org/10.2458/azu_js_rc.v51i1.3494

Brown, P.M., Woodhouse, C.A., Bragg, T., n.d. Niobrara Valley Preserve - PIPO - Tree Ring Index - ITRDB NE004.

Buckland, C.E., Bailey, R.M., Thomas, D.S.G., 2018. Identifying chronostratigraphic breaks in aeolian sediment profiles using near-surface luminescence dating and changepoint analysis. *Quaternary Geochronology* 46, 45–58. https://doi.org/10.1016/j.quageo.2018.03.011

Bullard, J.E., Thomas, D.S.G., Livingstone, I., Wiggs, G.F.S., 1997. Dunefield Activity and Interactions With Climatic Variability in the Southwest Kalahari Desert. *Earth Surface Processes and Landforms* 22, 165–174.

Bullard, J.E., Thomas, D.S.G., Livingstone, I., Wiggs, G.F.S., 1996. Wind energy variations in the Southwestern Kalahari desert and implications for linear dunefield activity. *Earth Surface Processes and Landforms* 21, 263–278. https://doi.org/10.1002/(SICI)1096-9837(199603)21:3<263::AID-ESP627>3.0.CO;2-I

Burrough, S.L., Thomas, D.S.G., 2013. Central southern Africa at the time of the African Humid Period: A new analysis of Holocene palaeoenvironmental and palaeoclimate data. *Quaternary Science Reviews* 80, 29–46. https://doi.org/10.1016/j.quascirev.2013.08.001

Burzlaff, D.F., 1962. A soil and vegetation inventory and analysis of three Nebraska Sandhills range sites. *Research Bulletin: Bulletin of the Agricultural Experiment Station of Nebraska No. 206*.

Buylaert, J.-P., Jain, M., Murray, A.S., Thomsen, K.J., Thiel, C., Sohbati, R., 2012. A robust feldspar luminescence dating method for Middle and Late Pleistocene

sediments. *Boreas* 41, 435–451. https://doi.org/10.1111/j.1502-3885.2012.00248.x

Buylaert, J.P., Murray, A.S., Thomsen, K.J., Jain, M., 2009. Testing the potential of an elevated temperature IRSL signal from K-feldspar. *Radiation Measurements* 44, 560–565. https://doi.org/10.1016/j.radmeas.2009.02.007

Chase, B., 2009. Evaluating the use of dune sediments as a proxy for palaeo-aridity: A southern African case study. *Earth-Science Reviews* 93, 31–45. https://doi.org/10.1016/j.earscirev.2008.12.004

Christensen, J.H., Hewitson, B., Busuioc, A., Chen, A., Gao, X., Held, I., Jones, R., Koli, R.K., Kwon, W.-T., Laprise, R., Rueda, V.M., Mearns, L., Menendez, C.G., Räisänen, J., Rinke, A., Sarr, A., Whetton, P., 2007. Regional Climate Projections, in: Solomon, S., Qin, D., Manning, M., Chen, Z., Maquis, M., Averyt, K.B., Tignor, M., Miller, H.L. (Eds.), *The Physical Science Basis. Contribution of Working Group I to the Fourth Assessment Report of the Intergovernmental Panel on Climate Change*. Cambridge University, Cambridge, UK, pp. 847–940. https://doi.org/10.1080/07341510601092191

Colarossi, D., Duller, G.A.T., Roberts, H.M., Tooth, S., Lyons, R., 2015. Comparison of paired quartz OSL and feldspar post-IR IRSL dose distributions in poorly bleached fluvial sediments from South Africa. *Quaternary Geochronology* 30, 233–238. https://doi.org/10.1016/j.quageo.2015.02.015

Colarossi, D., Duller, G.A.T.A.T., Roberts, H.M.M., 2018. Exploring the behaviour of luminescence signals from feldspars: Implications for the single aliquot regenerative dose protocol. *Radiation Measurements* 109, 35–44. https://doi.org/10.1016/j.radmeas.2017.07.005

Cook, B.I., Miller, R.L., Seager, R., 2009. Amplification of the North American "Dust Bowl" drought through human-induced land degradation. *Proceedings of the National Academy of Sciences of the United States of America* 106, 4997–5001. https://doi.org/10.1073/pnas.0810200106

Cook, E.R., Krusic, P.J., 2004. *The North American Drought Atlas*. Lamont-DOherty Earth Observatory and the National Science Foundation

Cook, E.R., Woodhouse, C.A., Eakin, C.M., Meko, D.M., Stahle, D.W., 2004. Long-term aridity changes in the western United States. *Science (New York, N.Y.)* 306, 1015–1018. https://doi.org/10.1126/science.1102586

Cordova, C., 2005. Great Plains Research : A Journal of Natural Preliminary Assessment of Sand Dune Stability Along a Bioclimatic Gradient , North Central and Northwestern Oklahoma. *Great Plains Research* 15, 227–249.

Cunfer, G., Waiser, B., 2016. *Bison and People on the North American Great Plains: A Deep Environmental History*. College Station: Texas A&M University Press.

Cunningham, A., Evans, M., Knight, J., 2015a. Quantifying bleaching for zero-age fluvial sediment: A Bayesian approach. *Radiation Measurements* 81, 55–61.

Cunningham, A., Wallinga, J., Hobo, N., Versendaal, A.., Makaske, B., Middelkoop, H., 2015b. Re-evaluating luminescence burial doses and bleaching of fluvial deposits using Bayesian computational statistics. *Earth Surface Dynamics* 3, 55–65.

Cunningham, A.C., Wallinga, J., 2012. Quaternary Geochronology Realizing the potential of fl uvial archives using robust OSL chronologies. *Quaternary Geochronology* 12, 1–9. https://doi.org/10.1016/j.quageo.2012.05.007

Cunningham, A.C., Wallinga, J., 2010. Selection of integration time intervals for quartz OSL decay curves. *Quaternary Geochronology* 5, 657–666. https://doi.org/10.1016/j.quageo.2010.08.004

Cunningham, A.C., Wallinga, J., 2009. Optically stimulated luminescence dating of young quartz using the fast component. *Radiation Measurements* 44, 423–428. https://doi.org/10.1016/j.radmeas.2009.02.014

Damberg, L., AghaKouchak, A., 2014. Global trends and patterns of drought from space. *Theoretical and Applied Climatology* 117, 441–448. https://doi.org/10.1007/s00704-013-1019-5

Duller, G.A.T., 2015. The Analyst software package for luminescence data : overview and recent improvements. *Ancient TL* 33, 1–8.

Duller, G.A.T., 2008. Luminescence Dating: guidelines on using luminescence dating in archaeology. Swindon. English Heritage.

Duller, G.A.T., 2003. Distinguishing quartz and feldspar in single grain luminescence measurements. *Radiation Measurements* 37, 161–165. https://doi.org/10.1016/S1350-4487(02)00170-1

Duller, G.A.T., 1996. Recent developments in luminescence dating of Quaternary sediments. *Progress in Physical Geography* 20, 127–145. https://doi.org/10.1177/030913339602000201

Duller, G.A.T., Bøtter-Jensen, L., Murray, A.S., 2003. Combining infrared- and green-laser stimulation sources in single-grain luminescence measurements of feldspar and quartz. *Radiation Measurements* 37, 543–550. https://doi.org/10.1016/S1350-4487(03)00050-7

Duller, G.A.T., Bøtter-Jensen, L., Murray, A.S., 2000. Optical dating of single sand-sized grains of quartz: Sources of variability. *Radiation Measurements* 32, 453–457. https://doi.org/10.1016/S1350-4487(00)00055-X

Duller, G.A.T., Murray, A.S., 2000. Luminescence dating of sediments using individual mineral grains. *Geologos* 5, 87–106.

Durcan, J.A., King, G.E., Duller, G.A.T., 2015. DRAC: Dose Rate and Age Calculator for trapped charge dating. *Quaternary Geochronology* 28, 54–61. https://doi.org/10.1016/j.quageo.2015.03.012

Durcan, J.A., Roberts, H.M., Duller, G.A.T., Alizai, A.H., 2010. Testing the use of range-finder OSL dating to inform field sampling and laboratory processing

strategies. *Quaternary Geochronology* 5, 86–90. https://doi.org/10.1016/j.quageo.2009.02.014

Esteves, T.C.J., Kirkby, M.J., Shakesby, R.A., Ferreira, A.J.D., Soares, J.A.A., Irvine, B.J., Ferreira, C.S.S., Coelho, C.O.A., Bento, C.P.M., Carreiras, M.A., 2012. Mitigating land degradation caused by wildfire: Application of the PESERA model to fire-affected sites in central Portugal. *Geoderma* 191, 40–50. https://doi.org/10.1016/j.geoderma.2012.01.001

Evans, J., Geerken, R., 2004. Discrimination between climate and human-induced dryland degradation. *Journal of Arid Environments* 57, 535–554. https://doi.org/10.1016/S0140-1963(03)00121-6

Fang, K.Y., Gou, X.H., Chen, F.H., Zhang, F., Li, Y.J., Peng, J.F., 2000. Comparisons of drought variability between central High Asia and monsoonal Asia: Inferred from tree rings. *Frontiers of Earth Science* 4, 277–288.

Farrar, J., 2008. Blowouts. *Nebraskaland* 10–19.

Feng, S., Hu, Q., Huang, W., Ho, C.H., Li, R., Tang, Z., 2014. Projected climate regime shift under future global warming from multi-model, multi-scenario CMIP5 simulations. *Global and Planetary Change* 112, 41–52. https://doi.org/10.1016/j.gloplacha.2013.11.002

Fitzsimmons, K.E., Rhodes, E.J., Magee, J.W., Barrows, T.T., 2007. The timing of linear dune activity in the Strzelecki and Tirari Deserts, Australia. *Quaternary Science Reviews* 26, 2598–2616. https://doi.org/10.1016/j.quascirev.2007.06.010

Fitzsimmons, K.E., Telfer, M.W., 2008. Sedimentary History and the Interpretation of Late Quaternary Dune Records: Examples from the Tirari Desert, Australia and the Kalahari, South Africa. *Chungara: Revista De Antropologia Chilena* 40, 295–308. https://doi.org/10.4067/S0717-73562008000300006

Forman, S.L., Marín, L., Gomez, J., Pierson, J., 2008. Late Quaternary eolian sand depositional record for southwestern Kansas: Landscape sensitivity to droughts. *Palaeogeography, Palaeoclimatology, Palaeoecology* 265, 107–120. https://doi.org/10.1016/j.palaeo.2008.04.028

Forman, S.L., Marín, L., Pierson, J., Gómez, J., Miller, G.H., Webb, R.S., 2005. Aeolian sand depositional records from western Nebraska: landscape response to droughts in the past 1500 years. *The Holocene* 15, 973–981. https://doi.org/10.1191/0959683605hl871ra

Forman, S.L., Oglesby, R., Webb, R.S., 2001. Temporal and spatial patterns of Holocene dune activity on the Great Plains of North America: Megadroughts and climate links. *Global and Planetary Change* 29, 1–29. https://doi.org/10.1016/S0921-8181(00)00092-8

Fox, T.A., Hugenholtz, C.H., Bender, D., Gates, C.C., 2012. Can bison play a role in conserving habitat for endangered sandhills species in Canada? *Biodiversity and Conservation* 21, 1441–1455. https://doi.org/10.1007/s10531-012-0255-9

Frolik, A.L., Sheperd, W.O., 1940. Vegetative composition and grazing capacity

of a typical area of Nebraska Sandhill range land. *Research Bulletin: Bulletin of the Agricultural Experiment Station of Nebraska No. 117*.

Fryberger, S.G., 1979. Dune forms and wind regime, in: McKee, E.D. (Ed.), *A Study of Global Sand Seas (US Geological Survery Professional Paper 1052)*. Reston, VA: US Geological Survey, pp. 137–169.

Galbraith, R.F., Roberts, R.G., 2012. Statistical aspects of equivalent dose and error calculation and display in OSL dating: An overview and some recommendations. *Quaternary Geochronology* 11, 1–27. https://doi.org/10.1016/j.quageo.2012.04.020

Galbraith, R.F., Roberts, R.G., Laslett, G.M., Yoshida, H., Olley, J.M., 1999. Optical dating of single and multiple grains of quartz from jinmium rock sheltern, northern Australia: Part I, experimental design and statistical models. *Archaeometry* 41, 339–364. https://doi.org/10.1111/j.1475-4754.1999.tb00987.x

Geist, H.J., Lambin, E.F., 2004. Dynamic Causal Patterns of Desertification. *BioScience* 54, 817. https://doi.org/10.1641/0006-3568(2004)054[0817:DCPOD]2.0.CO;2

Gillson, L., Hoffman, M.T., 2007. Rangeland Ecology in a Changing World. *Science* 315, 53–54.

Goble, R.J., Mason, J.A., Loope, D.B., Swinehart, J.B., 2004. Optical and radiocarbon ages of stacked paleosols and dune sands in the Nebraska Sand Hills, USA. *Quaternary Science Reviews* 23, 1173–1182. https://doi.org/10.1016/j.quascirev.2003.09.009

Goossens, D., 2004. Effect of soil crusting on the emission and transport of wind-eroded sediment: field measurements on loamy sandy soil. *Geomorphology* 58, 145–160.

Goossens, D., 2003. On-site and off-site effects of wind erosion, in: Warren, A. (Ed.), *Wind Erosion on Agricultural Land in Europe*. Luxembourg: European Commission, pp. 29–38.

Grab, S.W., Nash, D.J., 2010. Documentary evidence of climate variability during cold seasons in Lesotho, Southern Africa, 1833-1900. *Climate Dynamics* 34, 473–499. https://doi.org/10.1007/s00382-009-0598-4

Grassini, P., You, J., Hubbard, K.G., Cassman, K.G., 2010. Soil water recharge in a semi-arid temperate climate of the Central U.S. Great Plains. *Agricultural Water Management* 97, 1063–1069. https://doi.org/10.1016/j.agwat.2010.02.019

Guérin, G., 2013. Luminescence Dating, Dose Rates, in: Rink, W.J., Thompson, J. (Eds.), *Encyclopedia of Scientific Dating Methods*. Springer Netherlands, Dordrecht, pp. 1–6. https://doi.org/10.1007/978-94-007-6326-5_33-1

Guérin, G., Mercier, N., Adamiec, G., 2011. Dose-rate conversion factors : update. *Ancient TL* 29, 5–8.

Guérin, G., Mercier, N., Nathan, R., Adamiec, G., Lefrais, Y., 2012. On the use of

the infinite matrix assumption and associated concepts: A critical review. *Radiation Measurements* 47, 778–785. https://doi.org/10.1016/j.radmeas.2012.04.004

Guyette, R.P., Stambaugh, M.C., Marschall, J., Abadir, E., 2015. An analytic approach to climate dynamics and fire frequency in the great plains. *Great Plains Research* 25, 139–150. https://doi.org/10.1353/gpr.2015.0031

Guyette, R.P., Stambaugh, M.C., Marschall, J.M., 2011. A quantitative analysis of fire history at national parks in the Great Plains. A report prepared for the Great Plains Cooperative Ecosystem Studies Unit and National Part Service 78pp.

Halfen, A.F., Johnson, W.C., 2013. A review of Great Plains dune field chronologies. *Aeolian Research* 10, 135–160. https://doi.org/10.1016/j.aeolia.2013.03.001

Halfen, A.F., Johnson, W.C., Hanson, P.R., Woodburn, T.L., Young, A.R., Ludvigson, G.A., 2012. Activation history of the Hutchinson dunes in east-central Kansas, USA during the past 2200years. *Aeolian Research* 5, 9–20. https://doi.org/10.1016/j.aeolia.2012.02.001

Hanson, P.R., Joeckel, R.M., Young, A.R., Horn, J., 2009. Late Holocene dune activity in the Eastern Platte River Valley, Nebraska. *Geomorphology* 103, 555–561. https://doi.org/10.1016/j.geomorph.2008.07.018

Hedges, H., Elliott, F.F., 1930. Types of Farming in Nebraska. University of Nebraska, College of Agriculture Experimental Station Bulletin 244.

Helzer, C., 2010. *The Ecology and Management of Prairies in the Central United States*. University of Iowa Press.

Herrmann, S.M., Anyamba, A., Tucker, C.J., 2005. Recent trends in vegetation dynamics in the African Sahel and their relationship to climate. *Global Environmental Change* 15, 394–404. https://doi.org/10.1016/j.gloenvcha.2005.08.004

Hesp, P.A., 2002. Foredunes and blowouts: initiation, gemorphology and dynamics. *Geomorphology* 48, 245–268.

Hesse, P.P., 2014. How do longitudinal dunes respond to climate forcing? Insights from 25 years of luminescence dating of the Australian desert dunefields. *Quaternary International* 1–19. https://doi.org/10.1016/j.quaint.2014.02.020

Hesse, P.P., Magee, J.W., Van Der Kaars, S., 2004. Late Quaternary climates of the Australian arid zone: a review. *Quaternary International* 118–119, 87–102.

Holliday, V.T., 2001. Stratigraphy and geochronology of upper Quaternary eolian sand on the Southern High Plains of Texas and New Mexico, United States. *GSA Bulletin* 113, 88–108.

Houser, C., Bishop, M.P., Barrineau, P., 2015. Characterizing instability of aeolian environments using analytical reasoning. *Earth Surface Processes and Landforms* 40, 696–705. https://doi.org/10.1002/esp.3679

Hugenholtz, C.H., Bender, D., Wolfe, S.A., 2010. Declining sand dune activity in the southern Canadian prairies: Historical context, controls and ecosystem implications. *Aeolian Research* 2, 71–82. https://doi.org/10.1016/j.aeolia.2010.05.002

Hugenholtz, C.H., Wolfe, S.A., 2006. Morphodynamics and climate controls of two aeolian blowouts on the northern Great Plains, Canada. *Earth Surface Processes and Landforms* 31, 1540–1557.

Hugenholtz, C.H., Wolfe, S.A., 2005a. Biogeomorphic model of dunefield activation and stabilization on the northern Great Plains. *Geomorphology* 70, 53–70. https://doi.org/10.1016/j.geomorph.2005.03.011

Hugenholtz, C.H., Wolfe, S.A., 2005b. Recent stabilization of active sand dunes on the Canadian prairies and relation to recent climate variations. *Geomorphology* 68, 131–147. https://doi.org/10.1016/j.geomorph.2004.04.009

Hughes, P.D., 2010. Geomorphology and Quaternary stratigraphy: The roles of morpho-, litho-, and allostratigraphy. *Geomorphology* 123, 189–199. https://doi.org/10.1016/j.geomorph.2010.07.025

Huntley, D.J., Godfrey-Smith, D.I., Thewalt, M.L.W., 1985. Optical dating of sediments. *Nature* 313, 105–107.

Huntley, D.J., Lamothe, M., 2001. Ubiquity of anomalous fading in K-feldspars and the measurement and correction for it in optical dating. *Canadian Journal of Earth Sciences* 38, 1093–1106. https://doi.org/10.1139/e01-013

Jacobs, Z., Duller, G.A.T., Wintle, A.G., 2006. Interpretation of single grain Dedistributions and calculation of De. *Radiation Measurements* 41, 264–277. https://doi.org/10.1016/j.radmeas.2005.07.027

Jacobs, Z., Hayes, E.H., Roberts, R.G., Galbraith, R.F., Henshilwood, C.S., 2013. An improved OSL chronology for the Still Bay layers at Blombos Cave, South Africa: Further tests of single-grain dating procedures and a re-evaluation of the timing of the Still Bay industry across southern Africa. *Journal of Archaeological Science* 40, 579–594. https://doi.org/10.1016/j.jas.2012.06.037

Jain, M., Buylaert, J.P., Thomsen, K.J., Murray, A.S., 2015. Further investigations on "non-fading" in K-Feldspar. *Quaternary International* 362, 3–7. https://doi.org/10.1016/j.quaint.2014.11.018

Jain, M., Murray, A.S., Bøtter-Jensen, L., 2003. Characterisation of blue-light stimulated luminescence components in different quartz samples: Implications for dose measurement. *Radiation Measurements* 37, 441–449. https://doi.org/10.1016/S1350-4487(03)00052-0

Jamali, A.A., Zarekia, S., Randhir, T.O., 2018. Risk assessment of sand dune disaster in relation to geomorphic properties and vulnerability in the Saduq-Yazd Erg. *Applied Ecology and Environmental Research* 16, 579–590.

Kay, J., Anthone, D., Kay, R., Hugly, C., 1989. Nebraska Historic Buidlings Survey Reconnaissance Survey Final Report of Brown County, Nebraska.

Keyantash, J., Dracup, J. A., 2002. The quantification of drought: An evaluation of drought indices. *Bulletin of the American Meteorological Society* 83, 1167–1180. https://doi.org/10.-0477

Killick, R., Eckley, I.A., 2014. changepoint: An R Package for changepoint analysis. *Journal of Statistical Software* 58, 1–15. https://doi.org/10.1359/JBMR.0301229

Killick, R., Fearnhead, P., Eckley, I.A., 2012. Optimal detection of changepoints with a linear computational cost. *Journal of the American Statistical Association* 107, 1590–1598. https://doi.org/10.1080/01621459.2012.737745

King, G.E., Robinson, R.A.J., Finch, A.A., 2013. Apparent OSL ages of modern deposits from Fåbergstølsdalen, Norway: implications for sampling glacial sediments. *Journal of Quaternary Science* 28, 673–682. https://doi.org/10.1002/jqs.2666

Knorr, W., Kaminski, T., Arneth, A., Weber, U., 2014. Impact of human population density on fire frequency at the global scale. *Biogeosciences* 11, 1085–1102. https://doi.org/10.5194/bg-11-1085-2014

Kocurek, G., Lancaster, N., 1999. Aeolian system sediment state: Theory and Mojave Desert Kelso dune field example. *Sedimentology* 46, 505–515. https://doi.org/10.1046/j.1365-3091.1999.00227.x

Kreutzer, S., 2017. fit_CWCurve(): Nonlinear Least Squares Fit for CQ-OSL curves [beta version]. In: Kreutzer, S., Dietze, M., Burow, C., fuchs, M.C., Schmidt, C., Fischer, M., Friedrich, J. Luminescence: Comprehensive Luminescence Dating Data Analysis. R package version 0.7.

Kreutzer, S., Burow, C., 2017. analyse_FadingMeasurement(): Analyse fading measurements and returns the fading rate per decade (g-value). Function version 0.1.5. In: Kreutzer, S., Dietze, M., Burow, C., Fuchs, M.C., Schmidt, C., Fischer, M., Friedrich, J. (2017). Luminescence: Comprehe.

Lancaster, N., 1988. Development of linear dunes in the southwestern Kalahari, Southern Africa. *Journal of Arid Environments* 14, 233–244.

Lancaster, N., Helm, P., 2000. A tets of climatic index of dune mobility using measurements from the southwestern United States. *Earth Surface Processes and Landforms* 25, 197–207.

Lark, T.J., Meghan Salmon, J., Gibbs, H.K., 2015. Cropland expansion outpaces agricultural and biofuel policies in the United States. *Environmental Research Letters* 10, 044003. https://doi.org/10.1088/1748-9326/10/4/044003

Lary, D.J., Alavi, A.H., Gandomi, A.H., Walker, A.L., 2016. Machine learning in geosciences and remote sensing. *Geoscience Frontiers* 7, 3–10. https://doi.org/10.1016/j.gsf.2015.07.003

Lary, D.J., Zewdie, G.K., Liu, X., Wu, D., Levetin, E., Allee, R.J., Malakar, N., Walker, A., Mussa, H., Mannino, A., Aurin, D., 2018. Machine Learning Applications for Earth Observation, in: Mathieu, P.-P., Aubrecht, C. (Eds.), *Earth*

Observation Open Science and Innovation. Springer International Publishing, Cham, pp. 165–218. https://doi.org/10.1007/978-3-319-65633-5_8

Lee, J.A., Gill, T.E., 2015. Multiple causes of wind erosion in the Dust Bowl. *Aeolian Research* 19, 15–36. https://doi.org/10.1016/j.aeolia.2015.09.002

Leighton, C.L., Bailey, R.M., 2015. Investigating the potential of HCl-only treated samples using range-finder OSL dating. *Quaternary Geochronology* 25, 1–9. https://doi.org/10.1016/j.quageo.2014.08.002

Leighton, C.L., Bailey, R.M., Thomas, D.S.G., 2014a. Interpreting and modelling late Quaternary dune accumulation in the southern Arabian Peninsula. *Quaternary Science Reviews* 102, 1–13. https://doi.org/10.1016/j.quascirev.2014.08.002

Leighton, C.L., Thomas, D.S.G., Bailey, R.M., 2014b. Reproducibility and utility of dune luminescence chronologies. *Earth-Science Reviews* 129, 24–39. https://doi.org/10.1016/j.earscirev.2013.11.007

Leighton, C.L., Thomas, D.S.G., Bailey, R.M., 2013. Allostratigraphy and Quaternary dune sediments: Not all bounding surfaces are the same. *Aeolian Research* 11, 55–60. https://doi.org/10.1016/j.aeolia.2013.09.001

Levin, N., Levental, S., Morag, H., 2012. The effect of wildfires on vegetation cover and dune activity in Australia's desert dunes: A multisensor analysis. *International Journal of Wildland Fire* 21, 459–475. https://doi.org/10.1071/WF10150

Liu, J., Diamond, J., 2005. China's environment in a globalizing world. *Nature* 435, 1179–1186. https://doi.org/10.1038/4351179a

Livingstone, D., 2009. *Artificial Neural Networks: Methods and Applications*. Totowa, NJ: Humana Press.

Livingstone, I., Wiggs, G.F.S., Weaver, C.M., 2007. Geomorphology of desert sand dunes: A review of recent progress. *Earth-Science Reviews* 80, 239–257. https://doi.org/10.1016/j.earscirev.2006.09.004

Lohmann, D., Tietjen, B., Blaum, N., Joubert, D.F., Jeltsch, F., 2012. Shifting thresholds and changing degradation patterns: Climate change effects on the simulated long-term response of a semi-arid savanna to grazing. *Journal of Applied Ecology* 49, 814–823. https://doi.org/10.1111/j.1365-2664.2012.02157.x

Lomax, J., Hilgers, A., Radtke, U., 2011. Palaeoenvironmental change recorded in the palaeodunefields of the western Murray Basin, South Australia - New data from single grain OSL-dating. *Quaternary Science Reviews* 30, 723–736. https://doi.org/10.1016/j.quascirev.2010.12.015

Loope, D.B., Swinehart, J.B., 2000. Thinking Like a Dune Field: Geologic History in the Nebraska Sand Hills. *Great Plains Research* 10, 5–35.

Lu, X., Kelsey, K.C., Yan, Y., Sun, J., Wang, X., Cheng, G., Neff, J.C., 2017. Effects of grazing on ecosystem structure and function of alpine grasslands in Qinghai-

Tibetan Plateau: A synthesis. *Ecosphere* 8. https://doi.org/10.1002/ecs2.1656

Madsen, A.T., Buylaert, J.-P., Murray, A.S., 2011. Luminescence dating of young coastal deposits from New Zealand using feldspar. *Geochronometria* 38, 379–390. https://doi.org/10.2478/s13386-011-0042-5

Madsen, A.T., Murray, A.S., Andersen, T.J., Pejrup, M., 2007. Optical dating of young tidal sediments in the Danish Wadden Sea. *Quaternary Geochronology* 2, 89–94. https://doi.org/10.1016/j.quageo.2006.05.008

Mangan, J.M., Overpeck, J.T., Webb, R.S., Wessman, C., Goetz, A.F.H., 2004. Response of Nebraska Sand Hills natural vegetation to drought, fire, grazing, and plant functional type shifts as simulated by the Century model. *Climatic Change* 63, 49–90. https://doi.org/10.1023/B:CLIM.0000018516.53419.90

Marlon, J.R., Bartlein, P.J., Gavin, D.G., Long, C.J., Anderson, R.S., Briles, C.E., Brown, K.J., Colombaroli, D., Hallett, D.J., Power, M.J., Scharf, E.A., Walsh, M.K., 2012. Long-term perspective on wildfires in the western USA. *Proceedings of the National Academy of Sciences* 109, E535–E543. https://doi.org/10.1073/pnas.1112839109

Mason, J.A., Swinehart, J.B., Goble, R.J., Loope, D.B., 2004. Late-Holocene dune activity linked to hydrological drought, Nebraska Sand Hills, USA. *The Holocene* 14, 209–217. https://doi.org/10.1191/0959683604hl677rp

Mason, J.A., Swinehart, J.B., Hanson, P.R., Loope, D.B., Goble, R.J., Miao, X., Schmeisser, R.L., 2011. Late Pleistocene dune activity in the central Great Plains, USA. *Quaternary Science Reviews* 30, 3858–3870. https://doi.org/10.1016/j.quascirev.2011.10.005

Mayaud, J.R., Bailey, R.M., Wiggs, G.F.S., 2017a. Modelled responses of the Kalahari Desert to 21st century climate and land use change. *Scientific Reports* 7, 3887. https://doi.org/10.1038/s41598-017-04341-0

Mayaud, J.R., Bailey, R.M., Wiggs, G.F.S., 2017b. A coupled vegetation/sediment transport model for dryland environments. *Journal of Geophysical Research: Earth Surface* 122, 875–900. https://doi.org/10.1002/2016JF004096

McKee, T.B., Doesken, N.J., Kleist, J., 1993. Drought monitoring with multiple timescales, in: *Eight Conference on Applied Climatology*. *American Meteorological Society*. Anaheim, CA, pp. 179–184.

Mejdahl, V., 1979. Thermoluminescence Dating: Beta-dose attenuation in quartz grains. *Archaeometry* 21, 61–72.

Miao, X., Mason, J.A., Swinehart, J.B., Loope, D.B., Hanson, P.R., Goble, R.J., Liu, X., 2007. A 10,000 year record of dune activity, dust storms, and severe drought in the central Great Plains. *Geology* 35, 119–122. https://doi.org/10.1130/G23133A.1

Middleton, N., 2016. Rangeland management and climate hazards in drylands: dust storms, desertification and the overgrazing debate. *Natural Hazards* 1–14. https://doi.org/10.1007/s11069-016-2592-6

Middleton, N., 2011. The human impact, in: Thomas, D.S.G. (Ed.), *Arid Zone Geomorphology: Process, Form and Change in Drylands*. Wiley, pp. 571–579.

Middleton, N., Stringer, L., Goudie, A., Thomas, D.S.G., 2011. *The Forgotten Billion: MDG achievement in the drylands*. UNDP-UNCCD, New York (64pp).

Middleton, N.J., Sternberg, T., 2013. Climate hazards in drylands: A review. *Earth-Science Reviews* 126, 48–57. https://doi.org/10.1016/j.earscirev.2013.07.008

Milchunas, D.G., Lauenroth, W.K., Chapman, P.L., Mohammad, K.K., 1989. Effects of Grazing, Topography, and Precipitation on the Structure of a Semiarid Grassland Author(s): Daniel G. Milchunas, William K. Lauenroth, Philip L. Chapman and Mohammad K. Kazempour Source: *Vegetatio* 80, 11–23.

Miller, M.E., Bowker, M.A., Reynolds, R.L., Goldstein, H.L., 2012. Post-fire land treatments and wind erosion - Lessons from the Milford Flat Fire, UT, USA. *Aeolian Research* 7, 29–44. https://doi.org/10.1016/j.aeolia.2012.04.001

Miller, S.M., 1998. Land Development and Use, in: Bleed, A.S., Flowerday, C.A. (Eds.), *An Atlas of the Sand Hills*. Lincoln: Conservation and Survey Division, University of Nebraska-Lincoln, pp. 219–238.

Morrison, L.C., DuBois, J.D., Kapustka, L.A., 1986. The vegetational response of a Nebraska Sandhills grassland to a naturally occurring fall burn. *The Prairie Naturalist* 18, 179–184.

Muhs, D.R., 2004. Mineralogical maturity in dunefields of North America, Africa and Australia. *Geomorphology* 59, 247–269. https://doi.org/10.1016/j.geomorph.2003.07.020

Muhs, D.R., Holliday, V.T., 1995. Evidence of active dune sand on the great plains in the 19th entury from accounts of early explorers. *Quaternary Research* 43, 198–208.

Muhs, D.R., Maat, P.B., 1993. The potential response of eolian sands to greenhouse warming and precipitation reduction on the Great Plains of the U.S.A. *Journal of Arid Environments* 25, 351–361.

Muhs, D.R., Reynolds, R.L., Been, J., Skipp, G., 2003. Eolian sand transport pathways in the southwestern United States: importance of the Colorado River and local sources. *Quaternary International* 104, 3–18.

Muhs, D.R., Wolfe, S.A., 1999. Sand dunes of the Northern Great Plains of Canada and the United States, in: Lemmen, D.S., Vance, R.E. (Eds.), *Holocene Climate and Environmental Change in the Palliser Triangle; a Geoscientific Context for Evaluation of the Impacts of Climate Change on the Southern Canadian Prairies*. Ottawa: Geological Survey of Canada Bulletin 534, pp. 183–197.

Munyikwa, K., 2005. The role of dune morphogenetic history in the interpretation of linear dune luminescence chronologies: a review of linear dune dynamics. *Progress in Physical Geography* 29, 317–336. https://doi.org/10.1191/0309133305pp451ra

Munyikwa, K., Brown, S., 2014. Rapid equivalent dose estimation for eolian dune sands using a portable OSL reader and polymineralic standardised luminescence growth curves: Expedited sample screening for OSL dating. *Quaternary Geochronology* 22, 116–125. https://doi.org/10.1016/j.quageo.2014.04.002

Murray, A.S., Olley, J.M., 2002. Precision and accuracy in the optically stimulated luminescence dating of sedimentary quartz: A status review. *Geochronometria* 21, 1–16.

Murray, A.S., Wintle, A.G., 2003. The single aliquot regenerative dose protocol: potential for improvements in reliability. *Radiation Measurements* 37, 377–381.

Murray, A.S., Wintle, A.G., 2000. Luminescence dating of quartz using an improved single-aliquot regenerative-dose protocol. *Radiation Measurements* 32, 57–73. https://doi.org/10.1016/S1350-4487(99)00253-X

Nash, D.J., Pribyl, K., Klein, J., Neukom, R., Endfield, G.H., Adamson, G.C.D., Kniveton, D.R., 2016. Seasonal rainfall variability in southeast Africa during the nineteenth century reconstructed from documentary sources. *Climatic Change* 134, 605–619. https://doi.org/10.1007/s10584-015-1550-8

Nelson, M.S., Rittenour, T.M., 2015. Using grain-size characteristics to model soil water content: Application to dose-rate calculation for luminescence dating. *Radiation Measurements* 81, 142–149. https://doi.org/10.1016/j.radmeas.2015.02.016

Nicholson, S.E., 2001a. A semi-quantitative, regional precipitation data set for studying African climates of the nineteenth century, part I. Overview of the data set. *Climatic Change* 50, 317–353. https://doi.org/10.1023/A:1010674724320

Nicholson, S.E., 2001b. Climatic and environmental change in Africa during the last two centuries. *Climate Research* 17, 123–144. https://doi.org/10.3354/cr017123

Nicholson, S.E., Dezfuli, A.K., Klotter, D., 2012a. A two-century precipitation dataset for the continent of Africa. *Bulletin of the American Meteorological Society* 93, 1219–1231. https://doi.org/10.1175/BAMS-D-11-00212.1

Nicholson, S.E., Klotter, D., Dezfuli, A.K., 2012b. Spatial reconstruction of semi-quantitative precipitation fields over Africa during the nineteenth century from documentary evidence and gauge data. *Quaternary Research (United States)* 78, 13–23. https://doi.org/10.1016/j.yqres.2012.03.

Nickling, W.G., Wolfe, S.A., 1994. The morphology and origins of Nebkhas, region of Mopti, Mali, West Africa. *J. Arid Environments* 0, 13–30.

Olley, J.M., Caitcheon, G.G., Roberts, R.G., 1999. Origin of dose distributions in fluvial sediments, and the prospect of dating single grains from fluvial deposits using optically stimulated luminescence. *Radiation Measurements* 30, 207–217. https://doi.org/10.1016/S1350-4487(99)00040-2

Osborn, B., 1996. Overgrazing: Is A Solution Available? *Nebraska Anthropologist* 99, 17–22.

Palmer, W.C., 1965. Meteorological Drought. *Research Paper 45, U.S. Dept. of Commerce* 58.

Paudel, K.P., Andersen, P., 2010. Assessing rangeland degradation using multi temporal satellite images and grazing pressure surface model in Upper Mustang, Trans Himalaya, Nepal. *Remote Sensing of Environment* 114, 1845–1855. https://doi.org/10.1016/j.rse.2010.03.011

Perry, L.J., Stubbendieck, J., 1976. Nebraska handbook of range management. *Nebraska Extension Circular* 76–131, 43.

Peters, D.P.C., Bestelmeyer, B.T., Herrick, J.E., Fredrickson, E.L., Monger, H.C., Havstad, K.M., 2006. Disentangling Complex Landscapes: New Insights into Arid and Semiarid System Dynamics. *BioScience* 56, 491. https://doi.org/10.1641/0006-3568(2006)56[491:DCLNII]2.0.CO;2

Pfeiffer, K.E., Steuter, A.A, 1994. Preliminary response of Sandhills prairie to fire and bison grazing. *Journal of Range Management* 47, 395–397. https://doi.org/10.2307/4002337

Pham, B.T., Prakash, I., Tien Bui, D., 2018. Spatial prediction of landslides using a hybrid machine learning approach based on Random Subspace and Classification and Regression Trees. *Geomorphology* 303, 256–270. https://doi.org/10.1016/j.geomorph.2017.12.008

Pool, R.J., 1914. A study of the vegetation of the Sandhills of Nebraska. *Minnesota Botanical Studies* 4, 189–312.

Prescott, J.R., Hutton, J.T., 1994. Cosmic ray contributions to dose rates for luminescence and ESR dating: Large depths and long-term time variations. *Radiation Measurements* 23, 497–500. https://doi.org/10.1016/1350-4487(94)90086-8

Preusser, F., Dergering, D., Fuchs, M., Hilgers, A., Kadereit, A., Klasen, N., Krbetschek, M., Richter, D., G, S.J.Q., 2008. Luminescence dating: basics, methods and applications. *Eiszeitalter und Gegenwart Quaternary Science Journal* 57, 95–149.

Propastin, P.A., Kappas, M., 2008. Reducing Uncertainty in Modeling the NDVI-Precipitation Relationship: A Comparative Study Using Global and Local Regression Techniques. *GIScience & Remote Sensing* 45, 47–67. https://doi.org/10.2747/1548-1603.45.1.47

Provoost, S., Jones, M.L.M., Edmondson, S.E., 2011. Changes in landscape and vegetation of coastal dunes in northwest Europe: A review. *Journal of Coastal Conservation* 15, 207–226. https://doi.org/10.1007/s11852-009-0068-5

Rahmati, O., Tahmasebipour, N., Haghizadeh, A., Pourghasemi, H.R., Feizizadeh, B., 2017. Evaluation of different machine learning models for predicting and mapping the susceptibility of gully erosion. *Geomorphology* 298, 118–137. https://doi.org/10.1016/j.geomorph.2017.09.006

Ravi, S., D'Odorico, P., Wang, L., White, C.S., Okin, G.S., Macko, S.A., Collins,

S.L., 2009. Post-fire resource redistribution in desert grasslands: A possible negative feedback on land degradation. *Ecosystems* 12, 434–444. https://doi.org/10.1007/s10021-009-9233-9

Reimann, T., Thomsen, K.J., Jain, M., Murray, A.S., Frechen, M., 2012. Single-grain dating of young sediment using the pIRIR signal from feldspar. *Quaternary Geochronology* 11, 28–41.

Reimann, T., Tsukamoto, S., 2012. Dating the recent past (<500 years) by post-IR IRSL feldspar - Examples from the North Sea and Baltic Sea coast. *Quaternary Geochronology* 10, 180–187. https://doi.org/10.1016/j.quageo.2012.04.011

Reimann, T., Tsukamoto, S., Naumann, M., Frechen, M., 2011. The potential of using K-rich feldspars for optical dating of young coastal sediments - a test case from Darss-Zingst peninsula (southern Baltic Sea coast). *Quaternary Geochronology* 6, 207–222.

Reynolds, J.F., Maestre, F.T., Kemp, P.R., Stafford-Smith, M., Lambin, E., 2007a. Natural and Human Dimensions of Land Degradation in Drylands: Causes and Consequences, in: Canadell, J.G., Pataki, D.E., Pitelka, L.F. (Eds.), *Terrestrial Ecosystems in a Changing World*. Springer, pp. 247–257.

Reynolds, J.F., Smith, D.M.S., Lambin, E.F., Ii, B.L.T., Mortimore, M., Batterbury, S.P.J., Downing, T.E., Dowlatabadi, H., Fernández, R.J., Herrick, J.E., Huber-Sannwald, E., Jiang, H., Leemans, R., Lynam, T., Maestre, F.T., Ayarza, M., Walker, B., Turner, B.L., Mortimore, M., Batterbury, S.P.J., Downing, T.E., Dowlatabadi, H., Fernández, R.J., Herrick, J.E., Huber-Sannwald, E., Jiang, H., Leemans, R., Lynam, T., Maestre, F.T., Ayarza, M., Walker, B., 2007b. Global desertification: building a science for dryland development. *Science (New York, N.Y.)* 316, 847–851. https://doi.org/10.1126/science.1131634

Rhodes, E.J., 2011. Optically Stimulated Luminescence Dating of Sediments over the Past 200,000 Years. *Annual Review of Earth and Planetary Sciences* 39, 461–488. https://doi.org/10.1146/annurev-earth-040610-133425

Rich, J., 2013. A 250,000-year record of lunette dune accumulation on the Southern High Plains, USA and implications for past climates. *Quaternary Science Reviews* 62, 1–20. https://doi.org/10.1016/j.quascirev.2012.11.015

Roberts, H.M., 2012. Testing Post-IR IRSL protocols for minimising fading in feldspars, using Alaskan loess with independent chronological control. *Radiation Measurements* 47, 716–724. https://doi.org/10.1016/j.radmeas.2012.03.022

Roberts, H.M., Duller, G.A.T., 2004. Standardised growth curves for optical dating of sediment using multiple-grain aliquots. *Radiation Measurements* 38, 241–252. https://doi.org/10.1016/j.radmeas.2003.10.001

Roberts, H.M., Durcan, J.A., Duller, G.A.T., 2009. Exploring procedures for the rapid assessment of optically stimulated luminescence range-finder ages. *Radiation Measurements* 44, 582–587. https://doi.org/10.1016/j.radmeas.2009.02.006

Roberts, R.G., Galbraith, R.F., Olley, J.M., Yoshida, H., Laslett, G.M., 1999. Optical dating of single and multiple grains of quartz from Jinmium Rock Shelter, northern Australia: Part II, results and implications. *Archaeometry* 41, 365–395.

Salkind, N., 2007. Encyclopedia of Measurement and Statistics. https://doi.org/10.4135/9781412952644

Sanderson, D.C.W., Murphy, S., 2010. Quaternary Geochronology Using simple portable OSL measurements and laboratory characterisation to help understand complex and heterogeneous sediment sequences for luminescence dating. *Quaternary Geochronology* 5, 299–305. https://doi.org/10.1016/j.quageo.2009.02.001

Santín, C., Doerr, S.H., 2016. Fire effects on soils: The human dimension. *Philosophical Transactions of the Royal Society B: Biological Sciences* 371, 28–34. https://doi.org/10.1098/rstb.2015.0171

Saqqa, W.A., Saqqa, A.W., 2007. A computer program (WDTSRP) designed for computation of sand drif potential (DP) and plotting sand roses. *Earth Surface Processes and Landforms* 32, 832–840.

Schmeisser McKean, R.L., Goble, R.J., Mason, J.B., Swinehart, J.B., Loope, D.B., 2014. Temporal and spatial variability in dune reactivation across the Nebraska Sand Hills, USA. *The Holocene* 25, 523–535. https://doi.org/10.1177/0959683614561889

Schmeisser, R.L., Loope, D.B., Mason, J.A., 2010. Modern and late Holocene wind regimes over the Great Plains (central U.S.A.). *Quaternary Science Reviews* 29, 554–566. https://doi.org/10.1016/j.quascirev.2009.11.003

Schmeisser, R.L., Loope, D.B., Wedin, D.A., 2009a. Clues To the Medieval Destabilization of the Nebraska Sand Hills, Usa, From Ancient Pocket Gopher Burrows. *Palaios* 24, 809–817. https://doi.org/10.2110/palo.2009.p09-037r

Schmeisser, R.L., Loope, D.B., Wedin, D.A., 2009b. Clues to the medieval destabilisation of the Nebraska Sandhills, USA, from ancient pocket gopher burrows. *Palaios* 24, 809–817. https://doi.org/10.2110/palo.2009.p09-037r

Schmieder, J., Fritz, S.C., Grimm, E.C., Jacobs, K.C., Brown, K.J., Swinehart, J.B., Porter, S.C., 2012. Holocene variability in hydrology, vegetation, fire, and eolian activity in the Nebraska Sand Hills, USA. *The Holocene* 23, 515–527. https://doi.org/10.1177/0959683612463100

Schmieder, J., Fritz, S.C., Swinehart, J.B., Shinneman, A.L.C., Wolfe, A.P., Daniels, N., Jacobs, K.C., Grimm, E.C., 2011. A regional-scale climate reconstruction of the last 4000 years from lakes in the Nebraska Sand Hills, USA. *Quaternary Science Reviews* 30, 1797–1812. https://doi.org/10.1016/j.quascirev.2011.04.011

Schubert, S.D., Suarez, M.J., Pegion, P.J., Koster, R.D., Bacmeister, T., 2004. On the Cause of the 1930s Dust Bowl Published by : American Association for the Advancement of Science Stable URL : http://www.jstor.org/stable/3836515 .

Science 303, 1855–1859.

Shanmugam, S., Lucas, N., Phipps, P., Richards, A., Barnsley, M., 2016. Assessment of Remote Sensing Techniques for Habitat Mapping in Coastal Dune Ecosystems. *Journal of Coastal Research* 19, 64–75.

Shaw, P.A., Thomas, D.S.G., 2002. Late Quaternary environmental change in central southern Africa: new data, synthesis, issues and prospects. *Quaternary Science Reviews* 21, 783–797.

Simunek, J., Senja, M., van Genutchen, M.T., 2008. Code for simulating the one-dimensional movement of water, heat, and multiple solutes in variably saturated porous media: Hydrus-1D, Version 4.16.0090. USDA-ARS, California.

Singarayer, J.S., Bailey, R.M., 2003. Further investigations of the quartz optically stimulated luminescence components using linear modulation. *Radiation Measurements* 37, 451–458. https://doi.org/10.1016/S1350-4487(03)00062-3

Singhvi, A.K., Porat, N., 2008. Impact of luminescence dating on geomorphological and palaeoclimate research in drylands. *Boreas* 37, 536–558. https://doi.org/10.1111/j.1502-3885.2008.00058.x

Singhvi, A.K., Sharma, Y.P., Agrawal, D.P., 1982. Thermoluminescence dating of sand dunes in Rajasthan, India. *Nature* 295, 313–315.

Smedley, R.K., Duller, G.A.T., Roberts, H.M., 2015. Bleaching of the post-IR IRSL signal from individual grains of K-feldspar: Implications for single-grain dating. *Radiation Measurements* 79, 33–42. https://doi.org/10.1016/j.radmeas.2015.06.003

Smith, B.W., Rhodes, E.J., Stokes, S., Spooner, N.A., Aitken, M.J., 1990. Optical dating of sediments: Initial quartz results from Oxford. *Archaeometry* 32, 19–31.

Sridhar, V., Loope, D.B., Swinehart, J.B., Mason, J.A., Oglesby, R.J., Rowe, C.A., 2006. Large wind shift on the Great Plains during the Medieval Warm Period. *Science* 313, 345–347.

Stambaugh, M.C., Guyette, R.P., McMurry, E.R., Marschall, J.M., Willson, G., 2008. Six centuries of fire history at Devils Tower National Monument with comments on regionwide temperature influence. *Great Plains Research* 18, 177–187.

Stevens, T., Armitage, S.J., Lu, H., Thomas, D.S.G., 2006. Sedimentation and diagenesis of Chinese loess: Implications for the preservation of continuous, high-resolution climate records. *Geology* 34, 849–852. https://doi.org/10.1130/G22472.1

Stokes, S., Bailey, R.M., Fedoroff, N., O'Marah, K.E., 2004. Optical dating of aeolian dynamism on the West African Sahelian margin. *Geomorphology* 59, 281–291. https://doi.org/10.1016/j.geomorph.2003.07.021

Stokes, S., Swinehart, J.B., 1997. Middle- and late-Holocene dune reactivation in the Nebraska Sand Hills, USA. *The Holocene* 7, 263–272.

Stokes, S., Thomas, D.S.G., Shaw, P.A., 1997a. New chronological evidence for the nature and timing of linear dune development in the southwest Kalahari Desert. *Geomorphology* 20, 81–93.

Stokes, S., Thomas, D.S.G., Washington, R., 1997b. Multiple episodes of aridity in southern Africa since the last interglacial period. *Nature* 388, 154–158.

Stone, A.E.C., Bateman, M.D., Thomas, D.S.G., 2015. Rapid age assessment in the Namib Sand Sea using a portable luminescence reader. *Quaternary Geochronology* 30, 134–140. https://doi.org/10.1016/j.quageo.2015.02.002

Stone, A.E.C., Thomas, D.S.G., 2008. Linear dune accumulation chronologies from the southwest Kalahari, Namibia: challenges of reconstructing late Quaternary palaeoenvironments from aeolian landforms. *Quaternary Science Reviews* 27, 1667–1681. https://doi.org/10.1016/j.quascirev.2008.06.008

Stubbendieck, J., 2008. Seventy-eight years of vegetation dynamics in a sandhills grassland. *Natural Areas Journal* 28, 58–65.

Stubbendieck, J., 1998. Range Management, in: Bleed, A.S., Flowerday, C.A. (Eds.), *An Atlas of the Sand Hills*. Lincoln: Conservation and Survey Division, University of Nebraska-Lincoln, pp. 239–246.

Stubbendieck, J., 1986. Blowout penstemon: The Sandhills rare jewel. *Nebraska Quaterly* 32.

Stubbendieck, J., Engel, R.K., Schacht, W., Traeger, J., Weedon, R.R., 1982. Germination characteristics of Penstemon haydenii. *Proceedings of the Nebraska Academy of Sciences* 92.

Stubbendieck, J., Flessner, T.R., Weedon, R.R., 1989. Blowouts in the Nebraska Sandhills: the habitat of Penstemon haydenii. *Proceedings of the Eleventh North American Prairie Conference* 223–225.

Swain, S., Wardlow, B.D., Narumalani, S., Tadesse, T., Callahan, K., 2011. Assessment of Vegetation Response to Drought in Nebraska Using Terra-MODIS Land Surface Temperature and Normalized Difference Vegetation Index. *GIScience & Remote Sensing* 48, 432–455. https://doi.org/10.2747/1548-1603.48.3.432

Swinehart, J.B., 1998. Wind-blown deposits, in: Bleed, A.S., Flowerday, C. (Eds.), *An Atlas of the Sand Hills*. Lincoln: Conservation and Survey Division, University of Nebraska-Lincoln, pp. 43–56.

Telfer, M.W., 2011. Growth by extension, and reworking, of a south-western Kalahari linear dune. *Earth Surface Processes and Landforms* 36, 1125–1135. https://doi.org/10.1002/esp.2140

Telfer, M.W., Bailey, R.M., Burrough, S.L., Stone, A.E.S., Thomas, D.S.G., Wiggs, G.F.S., 2010. Understanding linear dune chronologies: Insights from a simple accumulation model. *Geomorphology* 120, 195–208. https://doi.org/10.1016/j.geomorph.2010.03.030

Telfer, M.W., Bateman, M.D., Carr, A.S., Chase, B.M., 2008. Testing the applicability of a standardized growth curve (SGC) for quartz OSL dating: Kalahari dunes, South African coastal dunes and Florida dune cordons. *Quaternary Geochronology* 3, 137–142. https://doi.org/10.1016/j.quageo.2007.08.001

Telfer, M.W., Hesse, P.P., Perez-Fernandez, M., Bailey, R.M., Bajkan, S., Lancaster, N., 2017. Morphodynamics, boundary conditions and pattern evolution within a vegetated linear dunefield. *Geomorphology* 290, 85–100. https://doi.org/10.1016/j.geomorph.2017.03.024

Telfer, M.W., Thomas, D.S.G., 2007. Late Quaternary linear dune accumulation and chronostratigraphy of the southwestern Kalahari: implications for aeolian palaeoclimatic reconstructions and predictions of future dynamics. *Quaternary Science Reviews* 26, 2617–2630. https://doi.org/10.1016/j.quascirev.2007.07.006

Thiel, C., Buylaert, J.-P., Murray, A., Terhorst, B., Hofer, I., Tsukamoto, S., Frechen, M., 2011. Luminescence dating of the Stratzing loess profile (Austria) - Testing the potential of an elevated temperature post-IR IRSL protocol. *Quaternary International* 234, 23–31. https://doi.org/10.1016/j.quaint.2010.05.018

Thomas, D.S.G., 2013. Reconstructing paleoenvironments and palaeoclimates in drylands: What can landform analysis contribute? *Earth Surface Processes and Landforms* 38, 3–16. https://doi.org/10.1002/esp.3190

Thomas, D.S.G., 1988. The geomorphological role of vegetation in the dune systems of the Kalahari, in: Dardis, G., Moon, B.P. (Eds.), *Geomorphological Studies in Southern Africa*. Balkema, Rotterdam, pp. 145–158.

Thomas, D.S.G., Bailey, R.M., 2017. Is there evidence for global-scale forcing of southern hemisphere Quaternary desert dune accumulation? A quantitative method for testing hypotheses of dune system development. *Earth Surface Processes and Landforms*. https://doi.org/10.1002/esp.4183

Thomas, D.S.G., Bailey, R.M., Shaw, P.A., Durcan, J.A., Singarayer, J., 2009. Late Quaternary highstands at Lake Chilwa, Malawi: Frequency, timing and possible forcing mechanisms in the last 44 ka. *Quaternary Science Reviews* 28, 526–539. https://doi.org/10.1016/j.quascirev.2008.10.023

Thomas, D.S.G., Burrough, S.L., 2013. Luminescence-based dune chronologies in southern Africa: Analysis and interpretation of dune database records across the subcontinent. *Quaternary International*. https://doi.org/10.1016/j.quaint.2013.09.008

Thomas, D.S.G., Burrough, S.L., 2012. Interpreting geoproxies of late Quaternary climate change in African drylands: Implications for understanding environmental change and early human behaviour. *Quaternary International* 253, 5–17. https://doi.org/10.1016/j.quaint.2010.11.001

Thomas, D.S.G., Knight, M., Wiggs, G.F.S., 2005. Remobilization of southern African desert dune systems by twenty-first century global warming. *Nature* 435, 1218–1221. https://doi.org/10.1038/nature03717

Thomas, D.S.G., Leason, H.C., 2005. Dunefield activity response to climate variability in the southwest Kalahari. *Geomorphology* 64, 117–132.

Thomas, D.S.G., Wiggs, G.F.S., 2008. Aeolian system responses to global change: challenges of scale, process and temporal integration. *Earth Surface Processes and Landforms* 33, 1396–1418.

Thomsen, K.J., Murray, A.S., Jain, M., Bøtter-Jensen, L., 2008. Laboratory fading rates of various luminescence signals from feldspar-rich sediment extracts. *Radiation Measurements* 43, 1474–1486. https://doi.org/10.1016/j.radmeas.2008.06.002

Tiwari, R.K., Maiti, S., 2011. Bayesian neural network modeling of tree-ring temperature variability record from the Western Himalayas. *Nonlinear Processes in Geophysics* 18, 515–528. https://doi.org/10.5194/npg-18-515-2011

Tsoar, H., 2005. Sand dunes mobility and stability in relation to climate. *Physica A: Statistical Mechanics and its Applications* 357, 50–56.

Tsukamoto, S., Rink, W.J., Watanuki, T., 2003. OSL of tephric loess and volcanic quartz in Japan and an alternative procedure for estimating De from a fast OSL component. *Radiation Measurements* 37, 459–465. https://doi.org/10.1016/S1350-4487(03)00054-4

Twidwell, D., Fuhlendorf, S.D., Taylor, C.A., Rogers, W.E., 2013. Refining thresholds in coupled fire-vegetation models to improve management of encroaching woody plants in grasslands. *Journal of Applied Ecology* 50, 603–613. https://doi.org/10.1111/1365-2664.12063

United Nations, 2008. Desertification [WWW Document]. URL www.un.org/esa/sustdev/publications/trends2008/desertification.pdf (accessed 8.27.18).

van Genutchen, M.T., 1980. A closed-form equation for predicting the hydraulic conductivity of unsaturated soils. *Soil Science Society of America Journal* 44, 892–898.

Vaz, D.A., Silvestro, S., 2014. Mapping and characterization of small-scale aeolian structures on Mars: An example from the MSL landing site in Gale Crater. *Icarus* 230, 151–161. https://doi.org/10.1016/j.icarus.2013.08.007

Viglizzo, E.F., Frank, F.C., 2006. Ecological interactions, feedbacks, thresholds and collapses in the Argentine Pampas in response to climate and farming during the last century. *Quaternary International* 158, 122–126.

Viles, H.A., 2008. Understanding Dryland Landscape Dynamics: Do Biological Crusts Hold the Key? *Geography Compass* 23, 899–919. https://doi.org/10.1111/j.1749-8198.2008.00099.x

Volesky, J.D., Connot, S.B., 2000. Vegetation response to late growing-season wildfire on Nebraska Sandhills rangeland. *Journal of Range Management* 53, 421–426.

Wallinga, J., 2002. Optically stimulated luminescence dating of uvial deposits : a review 31, 303–322.

Wallinga, J., Murray, A.S., Wintle, A.G., 2000. Single-aliquot regnereative-dose (SAR) protocol applied to coarse-grain feldspar. *Radiation Measurements* 32, 529–533.

Wang, L., D'Odorico, P., Evans, J.P., Eldridge, D.J., McCabe, M.F., Caylor, K.K., King, E.G., 2012. Dryland ecohydrology and climate change: critical issues and technical advances. *Hydrology and Earth System Sciences* 16, 2585–2603. https://doi.org/10.5194/hess-16-2585-2012

Wang, X., Yang, Y., Dong, Z., Zhang, C., 2009. Responses of dune activity and desertification in China to global warming in the twenty-first century. *Global and Planetary Change* 67, 167–185. https://doi.org/10.1016/j.gloplacha.2009.02.004

Wasson, R.J., Nanninga, P.M., 1986. Estimating wind transport of sand on vegetated surfaces. *Earth Surface Processes and Landforms* 11, 505–514. https://doi.org/10.1002/esp.3290110505

Weaver, J.E., 1965. *Native Vegetation of Nebraska*, Agronomy and Horticulture - Faculty Publications. University of Nebraska Press, Lincoln. https://doi.org/10.2307/2257649

Weaver, J.E., 1954. *North American prairie*. Johnsen Publising Company, Lincoln, Nebraska.

Wessels, K.J., Prince, S.D., Malherbe, J., Small, J., Frost, P.E., VanZyl, D., 2007. Can human-induced land degradation be distinguished from the effects of rainfall variability? A case study in South Africa. *Journal of Arid Environments* 68, 271–297. https://doi.org/10.1016/j.jaridenv.2006.05.015

Whicker, J.J., Breshears, D.D., Wasiolek, P.T., Kirchner, T.B., Tavani, R. a, Schoep, D. a, Rodgers, J.C., 1999. Temporal and spatial variation of episodic wind erosion in unburned and burned semiarid shrubland. *Journal of environmental quality* 31, 599–612. https://doi.org/10.2134/jeq2002.0599

Whicker, J.J., Pinder, J.E., Breshears, D.D., 2006. Increased Wind Erosion from Forest Wildfire: Implications for Contaminant-Related Risks. *Journal of Environmental Quality* 35, 468–478. https://doi.org/10.2134/jeq2005.0112

White, P., Webber, D.J., Helvin, A., 2010. Testing for a structural change of gradient in regression modelling. *Empirical Economics Letters* 9, 819–826.

Wiggs, G.F.S., 2011a. Geomorphological hazards in drylands, in: Thomas, D.S.G. (Ed.), *Arid Zone Geomorphology: Process, Form and Change in Drylands*. Wiley, pp. 583–598.

Wiggs, G.F.S., 2011b. Sediment mobilisation by the wind, in: Thomas, D.S.G. (Ed.), *Arid Zone Geomorphology: Process, Form and Change in Drylands*. Wiley, pp. 455–486.

Wiggs, G.F.S., Livingstone, I., Thomas, D.S.G., Bullard, J.E., 1994. Effect of

vegetation removal on airflow patterns and dune dynamics in the southwest Kalahari desert. *Land Degradation & Development* 5, 13–24. https://doi.org/10.1002/ldr.3400050103

Wilhite, D.A., Hubbard, K.G., 1998. Climate, in: Bleed, A.S., Flowerday, C.A. (Eds.), *An Atlas of the Sand Hills*. Lincoln: Conservation and Survey Division, University of Nebraska-Lincoln, pp. 17–28.

Wintle, A.G., 1973. Anomalous Fading of Thermoluminescence in Mineral Samples. *Nature* 245, 143–144. https://doi.org/10.1038/245143a0

Wintle, A.G., Murray, A.S., 2006. A review of quartz optically stimulated luminescence characteristics and their relevance in single-aliquot regeneration dating protocols. *Radiation Measurements* 41, 369–391. https://doi.org/10.1016/j.radmeas.2005.11.001

Wolfe, S.A., Hugenholtz, C.H., Evans, C.P., Huntley, D.J., Ollerhead, J., 2007. Potential Aboriginal-Occupation-Induced Dune Activity , Elbow Sand Hills , Northern Great Plains , Canada.

Wolfe, S.A., Nickling, W.G., 1997. Sensitivity of eolian process to climate change in Canada. *Geological Survey of Canada Bulletin* 421.

Wolfe, S.A., Nickling, W.G., 1993. The protective role of sparse vegetation in wind erosion. *Progress in Physical Geography* 17, 50–68. https://doi.org/10.1177/030913339301700104

Wolfe, S.A., Ollerhead, J., Huntley, D.J., Campbell, C., 2002. Late Holocene Dune Activity in the Duchess Dune Field, Alberta. *Geological Survey of Canada Bulletin*.

Woodhouse, C.A., 1999. Artificial neural networks and dendroclimatic reconstructions: An example from the Front Range, Colorado, USA. *Holocene* 9, 521–529. https://doi.org/10.1191/095968399667128516

Woodhouse, C.A., Brown, P.M., 2001. Tree-ring evidence for Great Plains drought. *Tree-ring Research* 57, 89–103.

Worster, D., 1979. *Dust Bowl*. Oxford University Press, NY.

Yan, L., Zhou, G., Zhang, F., 2013. Effects of different Grazing intensities on grassland production in China: A meta-analysis. *PLoS ONE* 8. https://doi.org/10.1371/journal.pone.0081466

Yan, N., Baas, A.C.W., 2015. Parabolic dunes and their transformations under environmental and climatic changes: Towards a conceptual framework for understanding and prediction. *Global and Planetary Change* 124, 123–148. https://doi.org/10.1016/j.gloplacha.2014.11.010

Yang, L., Lai, Z., Long, H., Zhang, J., 2011. Construction of a quartz OSL standardised growth curve (SGC) for aeolian samples from the horqin dunefield in Northeastern China. *Geochronometria* 38, 391–396. https://doi.org/10.2478/s13386-011-0045-2

Yizhaq, H., Ashkenazy, Y., Tsoar, H., 2009. Sand dune dynamics and climate change: A modeling approach. *Journal of Geophysical Research: Earth Surface* 114, 1–11. https://doi.org/10.1029/2008JF001138

Yizhaq, H., Ashkenazy, Y., Tsoar, H., 2007. Why do active and stabilised dunes coexist under the same climatic conditions? *Physical Review Letters* 98.

Zhang, Q.B., Hebda, R.J., Zhang, Q.J., Alfaro, R.I., 2000. Modeling tree-ring growth responses to climatic variables using artificial neural networks. *Forest Science* 46, 229–239.

Zhang, W., Li, J., Li, Z.-B., Li, Z., 2018. Predicting postoperative facial swelling following impacted mandibular third molars extraction by using artificial neural networks evaluation. *Scientific Reports* 8, 12281. https://doi.org/10.1038/s41598-018-29934-1

Zhang, Y., Liang, X., Wang, Z., Xu, L., 2015. A novel approach combining self-organizing map and parallel factor analysis for monitoring water quality of watersheds under non-point source pollution. *Scientific Reports* 5, 1–12. https://doi.org/10.1038/srep16079

Zou, J., Han, Y., So, S.., 2009. Overview of Artifical Neural Networks, in: Livingstone, D. (Ed.), *Artificial Neural Networks: Methods and Applications*. Totowa, NJ: Humana Press, pp. 15–24.

APPENDICES

Appendix A – Author contribution

The vast majority of work completed in this thesis is my own (CB), however, a small proportion has been contributed by the co-authors (supervisors) of the four submitted papers. Field sampling on both field seasons (2015 and 2016) was conducted by myself (CB) and Prof Dave Thomas (DT) following discussion of sampling strategy and approach with RB. Cutting of sediment tubes, sub-sampling, sample preparation, laboratory work, dating was conducted by CB. After discussion with Dr Richard Bailey (RB) and DT, all papers were drafted and finalised by CB. Individual author contributions for the papers are detailed below:

Paper 1 (Chapter 4)

CB conducted all of the laboratory work, sediment dating, analysis and writing for this paper. RB contributed to planning appropriate experiments to compare luminescence qualities, discussion of results, commenting on a draft version of the paper prior to submission and revisions in light of reviewers' comments. DT assisted with sample collection in the field. All figures and tables were produced by CB.

Paper 2 (Chapter 5)

CB conducted all of the laboratory work associated with measuring coarse luminescence signals and completing particle size analysis. RB gave useful advice on the data analysis methods that should be explored. Script for all Changepoint modelling was written and performed by CB. Data analysis and writing for this paper was completed by CB after discussion of results with RB and DT. RB and DT

provided comments on a draft version of this paper prior to submission. All figures, tables and appendices were produced by CB.

Paper 3 (Chapter 7)

CB conducted all of the laboratory work associated with dating sediments using luminescence techniques and preparing samples for ICP-MS measurement. RB gave useful advice on the methods that should be explored, including lagged-analysis, and discussion of the luminescence results. All luminescence ages, data analysis and writing for this paper was completed by CB. DT provided comments on two draft versions of this paper prior to submission. All figures, tables and appendices were produced by CB.

Paper 4 (Chapter 8)

Script for ANN analysis was co-written by CB and RB. RB wrote the script for the autoregressive model used to generate noise associated with hypothetical climate datasets (Appendix L). RB gave useful advice on the specific analysis methods that should be explored. Scenario datasets, model repeats, analysis and writing for this paper was completed by CB. DT and RB provided comments on draft versions of this paper prior to submission. All figures, tables and appendices were produced by CB.

Appendix B – Aerial site imagery and site descriptions

This appendix displays the aerial imagery used in this study to help inform the choice of sampling location at NVP and identify expected past landscape dynamics. Archived aerial imagery, accessed from the USDA FSA collection held at the University of Nebraska-Lincoln, captured pictures from 1939, 1954 and 1968. In addition, Google Earth imagery from 1993 – present provides a higher resolution of recent changes in vegetation cover dynamics across the six field sites that were used in the main dating and analysis of this project. A brief description of the initial interpretations about each site based on field understandings and analysis of the aerial imagery prior to dating is provided in the details below.

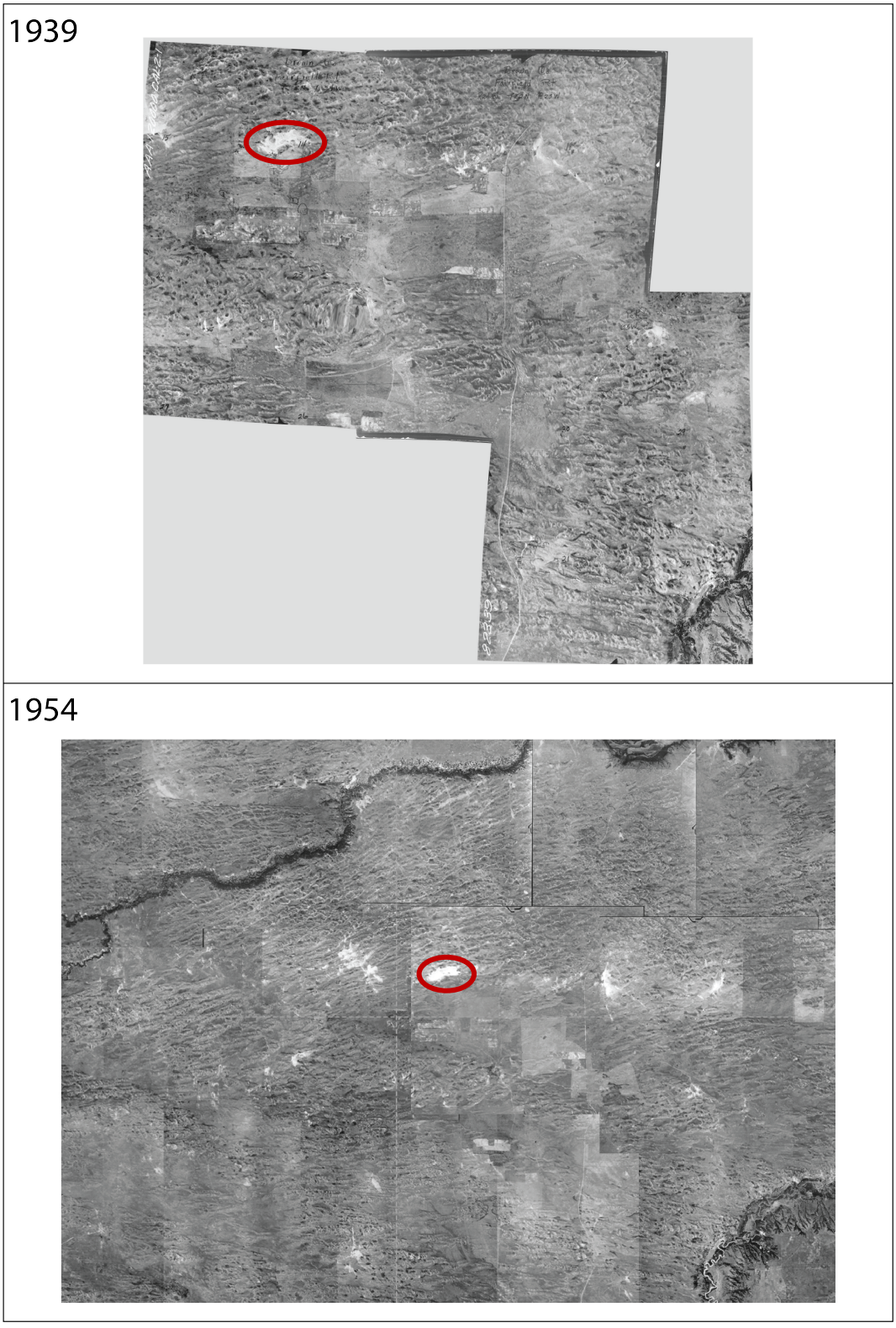


Figure B.1 Archived aerial photographs of the United States Department of Agriculture (USDA) Farm Service Agency (FSA) held at the University of Nebraska-Lincoln from 1939, 1954 and 1968 taken over the study area in Brown County, Nebraska. Site D has been circled in all three images as an aide to viewing and interpreting the photos.

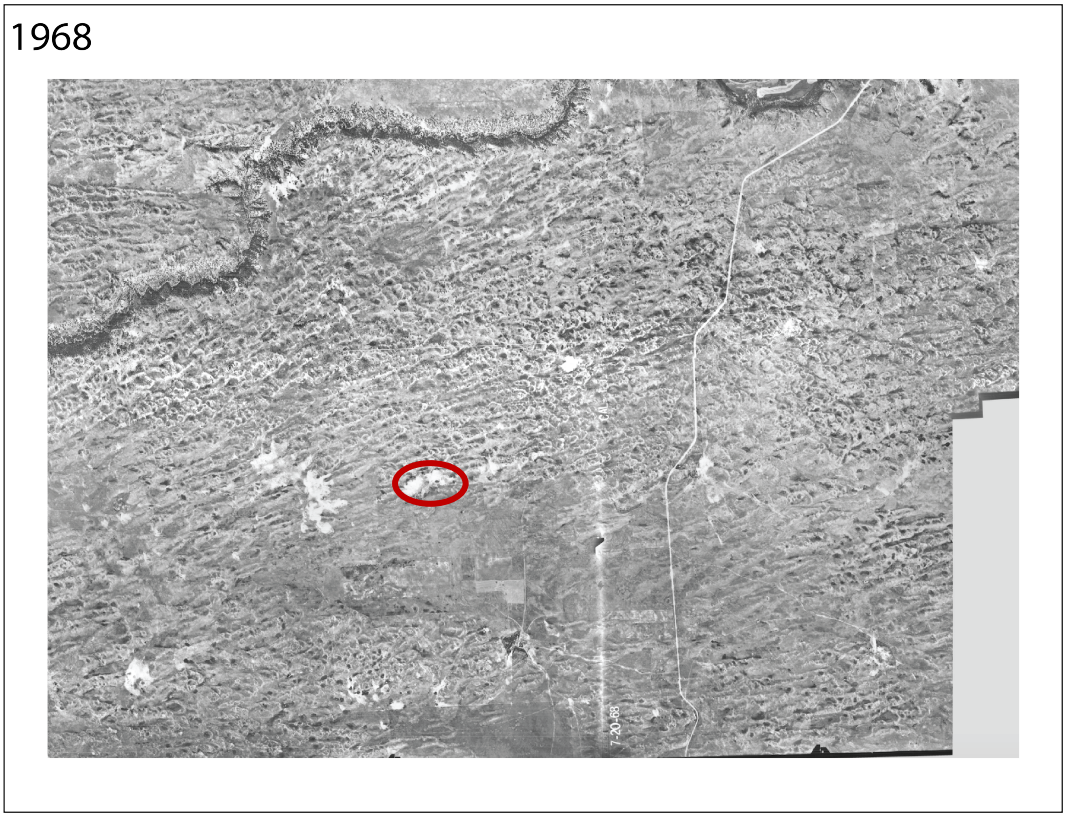
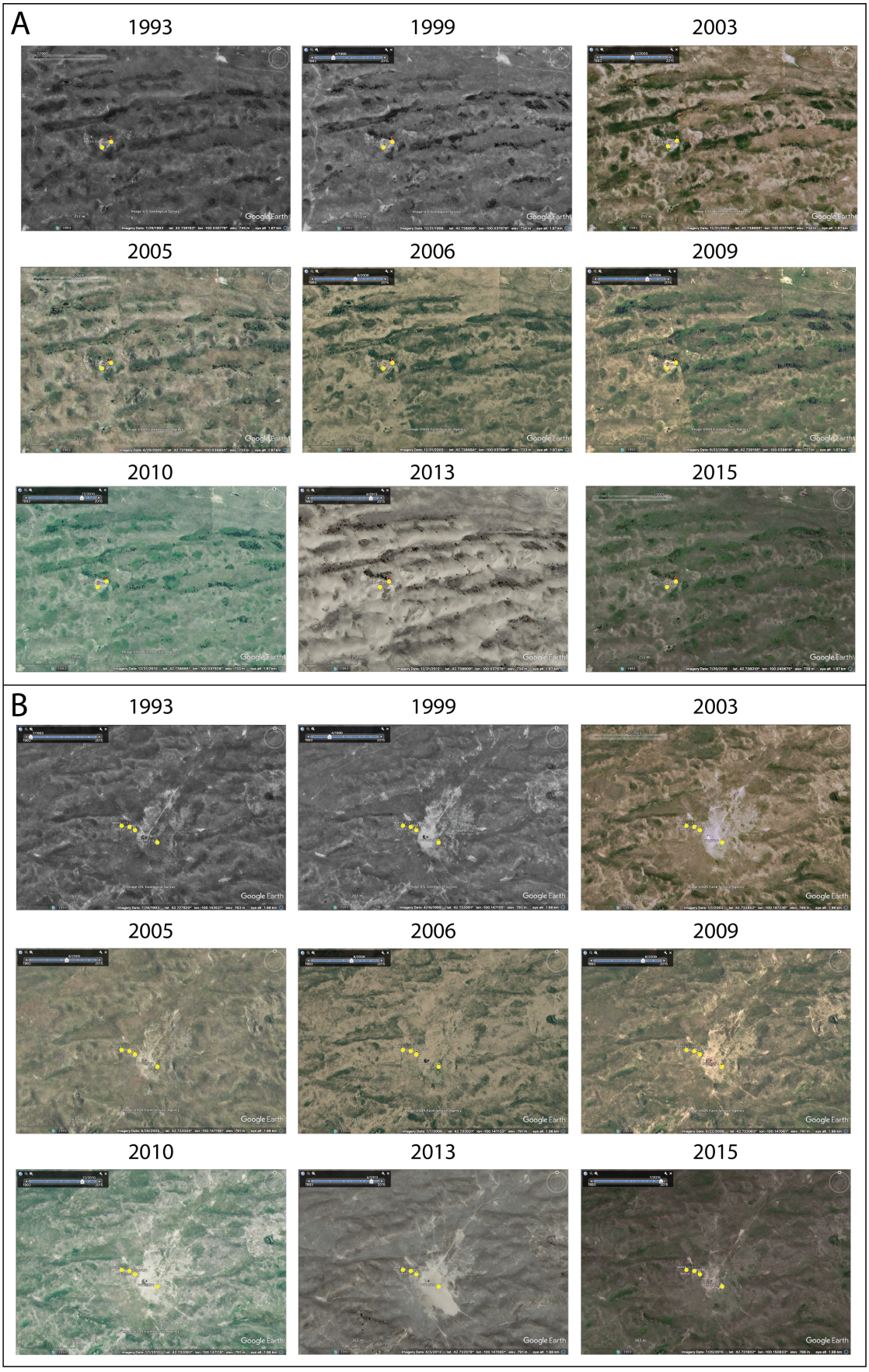


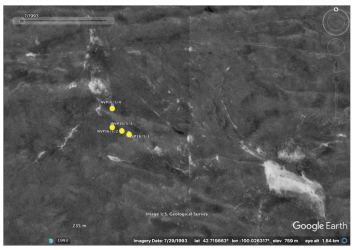
Figure B.1 *(continued from previous page).*

Figure B.2 *(opposite) – see figure caption overleaf*

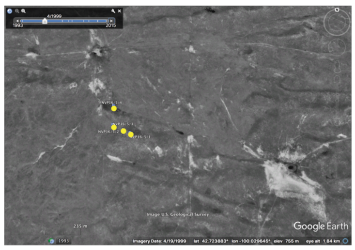

A
1993
1999
2003
2005
2006
2009
2010
2013
2015
B
1993
1999
2003
2005
2006
2009
2010
2013
2015

C

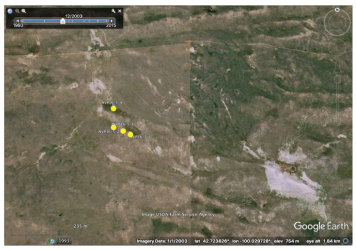
1993



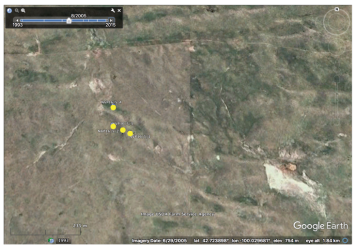
1999



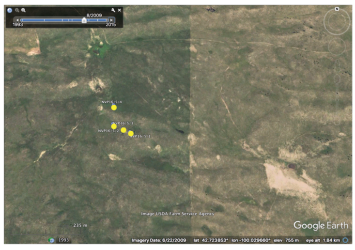
2003



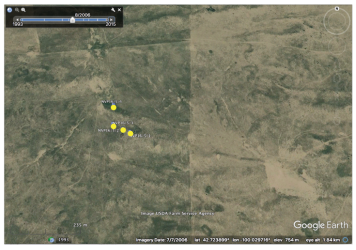
2005



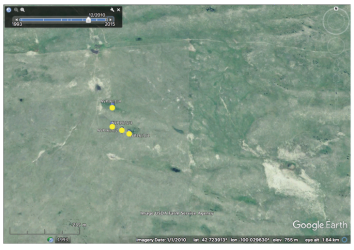
2006



2009



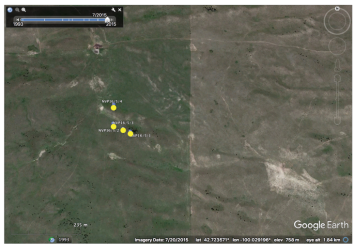
2010



2013

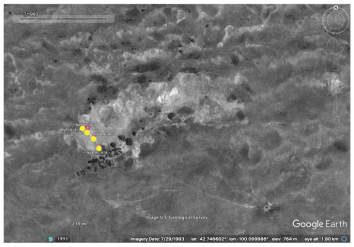


2015

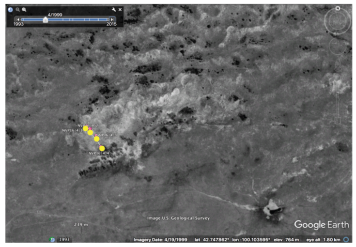


D

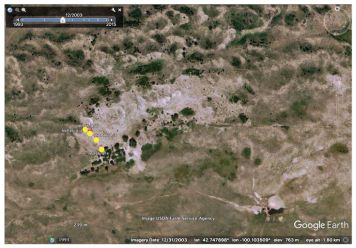
1993



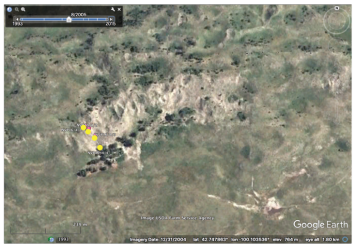
1999



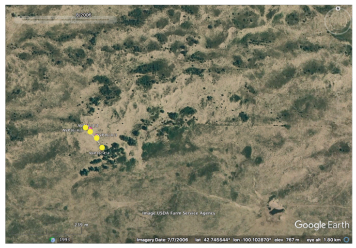
2003



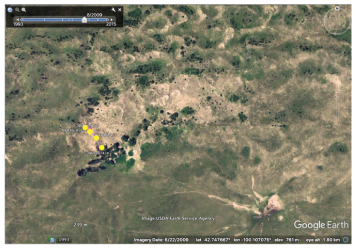
2005



2006



2009



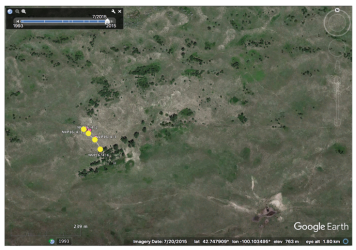
2010



2013



2015



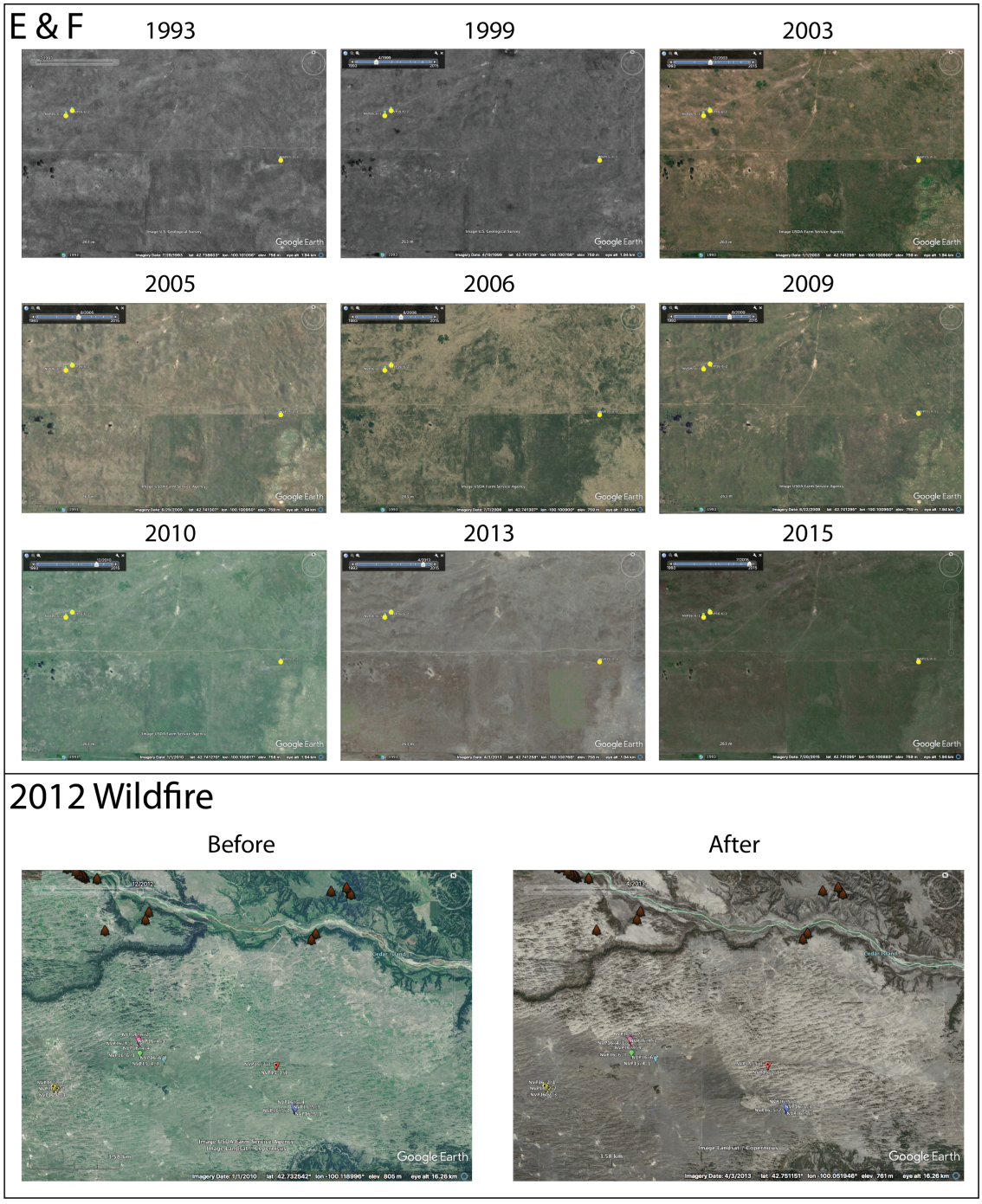


Figure B.2 Google Earth images taken of the six study sites from 1993 – 2015. Yellow circles mark the points where sediment cores referred to in this study were extracted. Images show the transitions in vegetation cover over a 22-year period. Final two images show the region affected by the 2012 wildfire before and after the event. Satellite imagery courtesy of © 2017 Google Earth Pro, Landsat / Copernicus.

Based on a combination of field interpretations and analysis of the aerial imagery, initial descriptions of the six study sites are detailed below:

Site A: Blowout feature

Site A is a blowout on a relatively high point in the local landscape (Figure B.3). Field observations and aerial photographs suggest that sediment is scoured from the base of the blowout by winds coming from the westerly direction and deposited on the top of the ridge (NVP15/1/1). Based on this hypothesis we would expect to find older OSL ages in the base of the blowout (NVP15/3/1) as sediment is continuously eroded away, whilst new material is accumulating on the flanks of the blowout headwall (i.e. NVP15/1/1, or on the lower ridge NVP15/2/1). 2/1 was not included in the final dating analysis.

Aerial photographs suggest that the blowout was active with bare sand in 1954 and the cores were taken from one of the most active blowouts in the local vicinity (Figure B.1). Overall there is bare sand across the location where the sediment cores were extracted and there is a thin layer of patchy vegetation within the basin of the blowout. By 1968, the blowout appears to have increased in activity since the image from 1954, and the local area is very active with only patches of vegetation found in the interdune areas.

Google Earth images (Figure B.2) suggest that whilst the blowout appeared to be active in 1993, the three cores were largely extracted from locations with patchy vegetation with NVP15/3/1 taken from the edge of patchy vegetation and bare sand. In 1999, both NVP15/1/1 and NVP15/3/1 were located on areas of bare sand and the surface of the blowout appears to have been active. By 2003, the

blowout was very active with no vegetation in the basin and all three cores were taken from areas of bare sand. However, by 2005 the blowout had started to recover and NVP15/1/1 was covered with a thin vegetation cover, whilst NVP15/2/1 had patchy vegetation cover. 2006 was a very arid year and both the blowout and the surrounding area appear active. In 2009 and 2010, the local area had begun to recover from the bare sand in 2006, yet, both NVP15/3/1 and NVP15/2/1 were largely still positioned on areas of bare sand and NVP15/1/1 was on the edge pf a patchy vegetated area. The 2013 image shows that the area was stripped of vegetation during the 2012 wildfire; bare sand can be seen in the wider area which would likely blow into and around the blowout. Some small grasses are beginning to colonize the slopes of the blowout. The blowout and surrounding area continued to recover by 2015, however all cores are still taken from areas devoid of vegetation.



Figure B.3 Site A (Blowout feature). Photograph taken from the location where NVP15/1/1 was extracted looking westwards in the direction where NVP15/3/1 was sampled from.

Site B: Windmill site

This site represents a choppy dune area with a windmill-powered groundwater pump and evidence of heavy cattle trampling. Blowouts form on the SE side of the dune from winds from the NW. Winds blow down the dune slope and have scoured out a series of ridges and basins on the SE side of the dune (Figure B.4). The biggest basin is located at the base of the dune where the pumping station is located. No samples were taken from the basin where heavy trampling from cattle would lead to constant over-turning of the sediment. Core NVP16/2/4 is taken from a depositional lobe downwind of the pumping station. We suggest that sediment is eroded from the topographic highs, whilst NVP16/2/4 represents an accumulation feature and will show a general growth in luminescence ages over time.

Aerial photographs show that the water pump was present in the region during 1954 and the area of active sand around the pump does extend to include NVP16/2/4 whilst there was patchy vegetation in NVP16/2/1, NVP16/2/2 and NVP16/2/3 (B.1). By 1968 the area of active sands had expanded and in particular a large depositional dune can be seen downwind of the water pump extending in a SE direction beyond NVP16/2/4.

Google Earth images show that in 1993 all four sites where sediment cores were taken were relatively stable and the area of activity and bare sand was restricted and localised around the water pump (Figure B.2). However, by 1999 the area of activity had expanded and whilst it does not overlap with any of the four cores, it is likely that sand blew from the pump region and can be found in the depositional lobe core at NVP16/2/4. By 2003, all four cores were partially vegetated with large patches of bare sand present. It seems that activity was

occurring at all four sites, with the hypothesis being that NVP16/2/1, NVP16/2/2 and NVP16/2/3 are erosional settings – or perhaps rolling and transferring sediment from one to another, whilst NVP16/2/4 is a depositional setting slowly accruing sand over time. By 2005 the system had begun to recover, and the area of bare sand is localised along cattle tracks and around the water pump. Vegetation cover remains patchy on the depositional lobe, most likely as sand from around the pump continues to be blown into the region, depositing on the lobe. 2006, much like the rest of the region, represents an incredibly active and dry year. The entire area was dry with bare sand likely exposed to aeolian reactivation. Very small patches of occasional grass can be found on the depositional lobe, but NVP16/2/1, NVP16/2/2 and NVP16/2/3 appear very active. By 2009, the system had begun to recover and only NVP16/2/4 is partially vegetated, the other three cores show a greater level of stability. In 2010 the area of bare sand had expanded to encompass the core sites again and by 2013, the depositional lobe downwind of the water pump has expanded (now reaching over 100 m in length from the water pump) and is completely bare. Site B lies outside of the wildfire limits from 2012. In 2013 there was extensive evidence of cattle tracks to the region and therefore the upper sediments are likely to have been disturbed. By 2015, there is thin patchy vegetation across all four sites, but still relatively under-established.

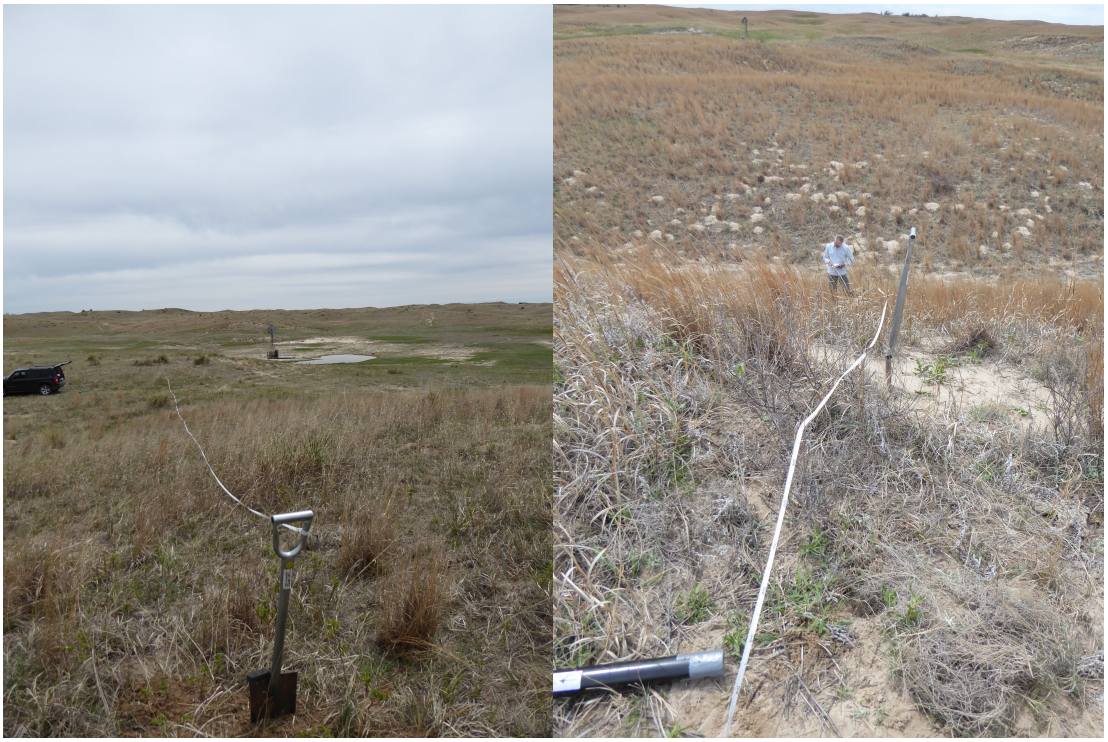


Figure B.4 Site B (Windmill site). *Left*: Point where core NVP16/2/4 was extracted looking in a NW direction up the transect. *Right*: Point where core NVP16/2/2 was extracted, looking in SE direction at where NVP16/2/3 and NVP16/2/4 were sampled.

Site C: Parabolic dune

This site is a parabolic dune facing in a SE direction with arms pointing upwind in a westerly direction. Samples taken from NVP16/5/1 on the crest of the dune should be relatively young as the dune is accumulating and rolling forwards. Samples taken from NVP16/5/3 should theoretically be older, with modern sediments overlying older sediments - this deflation basin is not accumulating and the older sediments are being exposed. Sample NVP16/5/4 taken from the arm of the dune should yield some of the oldest ages from the actual dune. We expect luminescnece dates to be young near the surface, but increase in age continuously

with depth. It is likely that the dune grew gradually producing an identifiable parabolic dune shape.

Aerial photography from 1954 shows that the arms and crest of the dune had thinner vegetation cover whilst NVP16/5/3 and NVP16/5/2 had relatively thicker vegetation cover (Figure B.1). Google Earth images (Figure B.2) show that all four cores were taken from vegetated areas in 1993, with the greatest cover found at NVP16/5/3. The situation was similar in 1999, however the vegetation was even thicker on the arm of the dune where sample NVP16/5/4 was taken. By 2003, thick vegetaiton at sites NVP16/5/3 and NVP16/5/4 remained, however, the vegetation was much patchier at NVP16/5/2 where the sand is most likely being eroded and potentially deposited at site NVP16/5/1. 2006 represented an arid and active phase in the area, however, this sampling site had slightly more vegetation than the surrounding dunes. Google Earth images showed good vegetation cover until 2013 when a new dune (lobe) blew onto the northern arm of the parabolic dune following the 2012 wildfire. This additional lobe of sand was still present on the parabolic arm during sampling in 2016, but was now vegetated. Site C was outside of the extent of the 2012 wildfire.

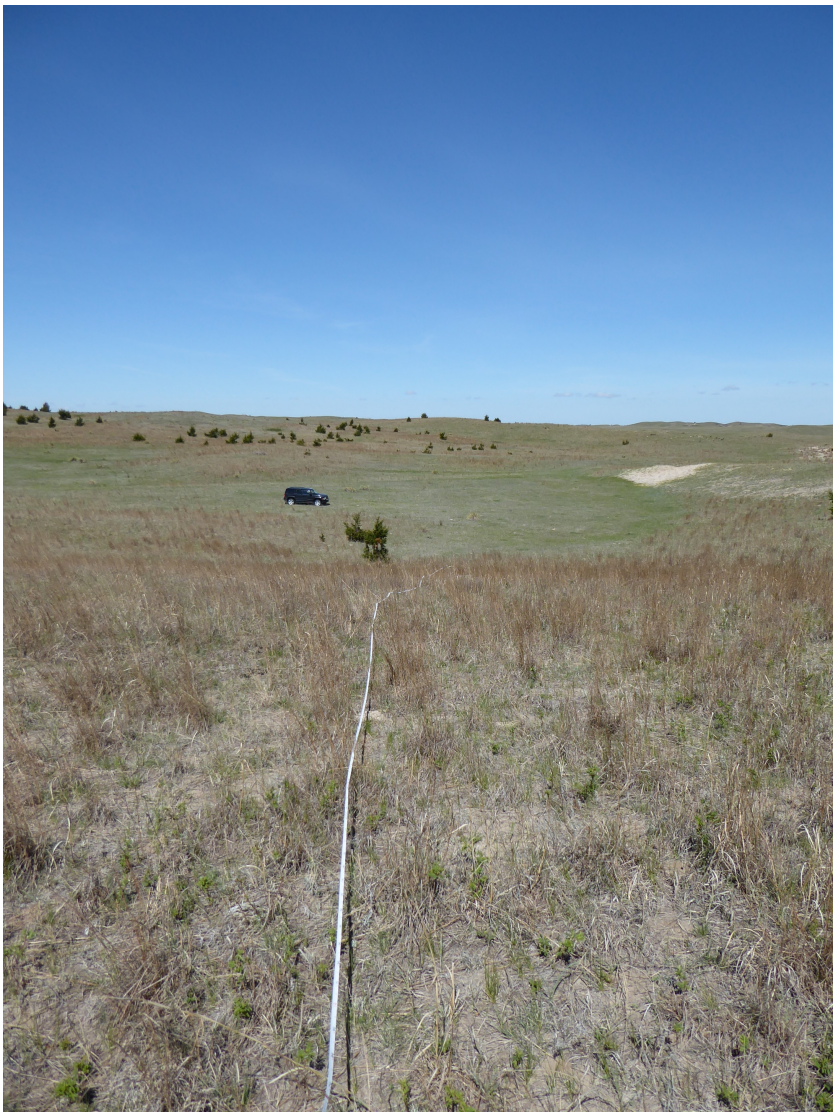


Figure B.5 Site C (Parabolic dune) at point where NVP16/5/1 was extracted on the nose of the dune looking westwards in the direction where NVP16/5/2, 5/3 and 5/4 were sampled from. Note the lobe of sand that has been deposited over the northern parabolic arm. Whilst most of this is now vegetated, aerial imagery suggests this lobe of bare sand was deposited post-2012 wild fire.

Site D: Homestead site

Site D is characterised by relatively larger choppier dunes and basin features banked up against a historical fenceline (Figure B.6), homestead and planted wind break. The large basin feature displays bare surface sand in all of the archived images (Figure B.1) and continues to show evidence of active surace conditions

during fieldwork. Sampling was completed from the NW crest across the basin in the direction of the NW winds. Initial field interpretations suggest that this dune-basin feature has formed as a result of land use change / human disturbance to the area and has accumulated against the fence line where the homestead was built. Trees have been planted along the south side of the dune in an attempt to stabilize the large blowout. Based on the direction of the prevailing winds and the shape of the blowout, I suspect that sediment is scoured in a SE direction from the NW winds and redeposited on the dune flank (i.e. NVP16/4/4 location).

Aerial photographs show that throughout 1939, 54 and 68 the large blowout, surrounding slopes and crests were all active. Whether there were any periods of stability between these three photos is unknown, but also unlikely. Only in 1968 is core NVP16/4/1 taken from a semi-vegetated area, but the other sites are always taken from bare sands. The image from 1939 suggests that the fence line extends underneath the dune, suggesting that the dune post-dates the fence and has been produced in response to the fencing off of the plot. There is a change in the number of trees planted to try and stabilise the landscape and reduce wind velocity. In 1939 there were only 2-3 trees planted downwind of the dune but by 1954, more trees had been planted downwind of the dune, likely in an attempt to reduce the susceptibility to aeolian erosion in the landscape.

Google Earth images from 1993 show that sample NVP16/4/1 was semi-vegetated whilst NVP16/4/2, NVP16/4/3 and NVP16/4/4 were taken from areas of active sand. Only by 2009 was sample NVP16/4/4 positioned within an area with patchy grass and vegetation, whilst NVP16/4/2 and NVP16/4/3 were still from bare sand with very little areas of grass. In 2013, the area had a very thin layer of

vegetation and this sampling site was bare with very little vegetation. The sampling site is located just outside the limits of the 2012 wildfire. By 2015, the area had begun to recover and a thin smattering of vegetation can be seen across the dune. However, the growth of the vegetation has also highlighted the spatial patterning and presence of the cattle tracks and trampling – suggesting another disturbance to the area that perhaps we could not identify in earlier imagery due to the bare nature of the sand (Figure B.2).



Figure B.6 Site D (Homestead site). *Left*: taken from NVP16/4/1 looking across the large eroded basic down transect to where sediment cores NVP16/4/2, 4/3 and 4/4 were extracted. Trees in distance are those seen in *right* image from opposing direction. *Right*: taken from south of sampling transect looking north at the original homestead. Note the tree species are not native to Nebraska and have been planted, likely at the time of the original homestead settlement when settlers attempted to plant windbreaks from the strong winds across the plains. The location of the windbreak and fence lines crossing through the blowout basin feature suggest these human interactions have been critical in the development of the eroded basin.

Site E: 1930s dune

Al Steuter (ranch owner of sample site E) notes that the dune this sample (NVP15/4/1) was extracted from was active and blowing in the 1930s. Al comments that this dune was accumulating along a fenceline during the 1930s and we would therefore perhaps expect to see sediment of this age present in the sequence, unless it has been subsequently eroded away. Alternatively, it may have been too active in the 1930s for any of the sediment to accumulate on the dune since it represents a relative topographic high in the local area. The dune appears to have grown along an E-W transect, perhaps representing a transverse dune built in response to winds from the south or a dune banked against a fence line in response to the winds from the south. Upwind of the dune (in a southerly direction) there is a prairie dog town which sits at a lower elevation (Figure B.7).

Aerial photographs suggest that the site was vegetated in 1939, but the pasture it is located in had many fence divisions and was probably farmed (Figure B.1). 1954 shows a similar environment to 1939, however, there were some bare patches on the surrounding fence lines. Finally, 1968 imagery shows that vegetation cover was slightly thinner than in the earlier images, but still not characterised by exposed bare sane. This area represents a subtle ridge within a pasture environment as opposed to the larger choppier dunes in the surrounding sections.

Google Earth images show that NVP15/4/1 has been located on a very subdued ridge that runs from E-W and has been continuously vegetated since photos begin in 1993 (Figure B.2). 2006 was the only year which showed pockets of exposed sand on a broadly vegetated ridge.



Figure B.7 Site E (1930s dune) location where NVP15/4/1 was extracted looking southwards in the direction of the prairie dog town (brown shading in the distance).

Site F: Old rolling dunes

Organics found in the top of NVP16/6/2 core coupled with the rolling dune topography found at this sampling site suggests that these dunes are more stabilised than the surrounding blowout features and have not reactivated in recent years by external disturbances. The presence of a soil in the top of NVP16/6/2 at the base of the dune confirms that the immediate landscape has been stable for a period long enough to allow for the formation of a thick (c.10 cm) organic layer (Figure B.8). Likewise, sandy organics found in the top of core NVP16/6/1 suggests that this area has also been relatively more stable than samples NVP15/4/1 and NVP16/4 which

were taken directly due south and north from site F but do not display any evidence of organic material. Based on land use information and history from the region these soils may have formed in the late 1890s following the drought from 1890-1895, or they may have formed in the 1940s in the rains that came following The Great Depression. The age of the underlying sediment therefore, may be of a much older depositional period.

Aerial photographs from 1939 suggest that these two cores have been taken from within a fenced area, perhaps farmed given the period (Figure B.1). The rolling topography is less obvious in the aerial photographs, where the choppier dunes in the region are more easily identified with bare crests and notably vegetated interdunes. By 1968, general vegetation cover appeared thinner than the previous two aerial photographs. Vegetation was suggestively thicker in NVP16/6/2 (darker patch on the aerial photograph). Google Earth images for the site since 1993 show that the area has been persistently vegetated apart from in 2003, when the crest core (NVP16/6/1) was partially bare (Figure B.2). Also note there is visible cattle track marks which trend north of the two core sites; expect regular turnover of surface sediments due to trampling.



Figure B.8 Site F (Old rolling dunes). *Left*: taken from the location where NVP16/6/1 was extracted looking northwards across the low-lying rolling topography in the direction of Site D the Homestead site. *Right*: photograph showing the organics found at the top of sediment core NVP16/6/2 with underlying sandy sediments.

Appendix C – Additional sediment cores

Appendix C presents the details of the sediment cores that were collected as part of the pilot and final fieldwork seasons but were not used in the final dating and analyses of this project (Table C.1). Figure 5.2 (Paper 2) is a map of all the sites where vertical cores were extracted during the 2016 field season.

Based on a lack of historical aerial imagery at the time of sampling, sampling sites at GSL were selected systematically with a total of 41 cores extracted across ten sites. Samples at GSL were taken from transects across blowout features found across the top of two linear dune ridges. By comparison, aerial imagery from 1939, 1954 and 1968 was used to guide sampling strategy at NVP, allowing us to identify and focus on features of localised disturbance that had varying degrees of activity over the study period. Prioritisation and rationale for focusing on the final sediment cores from NVP is detailed in Chapter 3.

Some sediment samples taken from BBR and GSL during the pilot field season were used in Papers 1 and 2 when conducting initial experimental studies to identify the optimum measurement and analysis conditions for processing young aeolian sediments.

Table C.1 Table of sediment cores extracted as part of the field work for this research project, but not dated in the final reconstruction of historical sediment reactivations. Some sediment cores taken from GSL and BBR are referred to in Papers 1 and 2 for experimental purposes.

Site	Core reference	Vertical / horizontal sample	Latitude (°)	Longitude (°)	Elevation (m a.s.l)
Pilot field season (2015)					
Gudmundsen Sandhills Laboratory	GSL15/1/1 (Yao's Blowout)	V	42.08627	-101.36721	1077
	GSL15/1/2 (Yao's Blowout)	H	42.08627	-101.36721	1077
	GSL15/1/3 (Yao's Blowout)	H	42.08627	-101.36721	1077
	GSL15/2/1	V	42.07573	-101.38669	1109
	GSL15/2/2	V	42.07565	-101.38675	1109
	GSL15/2/3	V	42.07568	-101.38685	1109
	GSL15/2/4	V	42.07575	-101.38680	1109
	GSL15/2/5	V	42.07569	-101.38677	1109
	GSL15/3/1	V	42.07586	-101.38704	1108
	GSL15/3/2	H	42.07586	-101.38704	1107
	GSL15/3/3	H	42.07586	-101.38704	1105
	GSL15/4/1	V	42.07587	-101.38709	1101
	GSL15/5/1	V	42.07587	-101.38731	1103
Niobrara Valley Preserve	NVP15/2/1	V	42.73498	-100.03757	762
	NVP15/5/1	V	42.73107	-100.07153	761
	NVP15/6/1	V	42.73175	-100.07125	764
Barta Brothers Ranch	BBR15/1/1	V	42.24580	-99.65433	796
	BBR15/2/1	V	42.24387	-99.65503	785
Field season 2016					
Gudmundsen Sandhills Laboratory	GSL16/1/1	V	42.06363	-101.42465	1135
	GSL16/1/2	V	42.06339	-101.42475	1122
	GSL16/1/3	V	42.06317	-101.42488	1113
	GSL16/1/4	V	42.06285	-101.42528	1114
	GSL16/2/1	V	42.06318	-101.40527	1095
	GSL16/2/2	V	42.06295	-101.40523	1090
	GSL16/2/3	V	42.06261	-101.40501	1075
	GSL16/2/4	V	42.06240	-101.40483	1079
	GSL16/3/1	V	42.06569	-101.38418	1078
	GSL16/3/2	V	42.06588	-101.38376	1074
	GSL16/3/3	V	42.06598	-10138351	1077
	GSL16/3/4	V	42.06610	-101.38329	1080

Site	Core reference	Vertical / horizontal sample	Latitude (°)	Longitude (°)	Elevation (m a.s.l)
	GSL16/4/1	V	42.06684	-101.36461	1072
	GSL16/4/2	V	42.06698	-101.36456	1069
	GSL16/4/3	V	42.06719	-101.36451	1066
	GSL16/4/4	V	42.06784	-101.36432	1063
	GSL16/5/1	V	42.07550	-101.40309	1099
	GSL16/5/2	V	42.07544	-101.40283	1096
	GSL16/5/3	V	42.07536	-101.40255	1093
	GSL16/5/4	V	42.07515	-101.40218	1085
	GSL16/6/1	V	42.07339	-101.42828	1083
	GSL16/6/2	V	42.07333	-101.42838	1078
	GSL16/6/3	V	42.07330	-101.42859	1077
	GSL16/6/4	V	42.07331	-101.42865	1078
	GSL16/7/1	V	42.06775	-101.45338	1140
	GSL16/7/2	V	42.06771	-101.45361	1136
	GSL16/7/3	V	42.06761	-101.45385	1132
	GSL16/7/4	V	42.06735	-101.45373	1136
	GSL16/8/1	V	42.08619	-101.45838	1124
	GSL16/8/2	V	42.08635	-101.45823	1118
	GSL16/8/3	V	42.08650	-101.45805	1113
	GSL16/8/4	V	42.08652	-101.45805	1114
Niobrara Valley Preserve	NVP16/1/1	V	42.72022	-100.06112	797
	NVP16/1/2	V	42.72032	-100.06214	794
	NVP16/1/3	V	42.72035	-100.06310	783
	NVP16/1/4	V	42.72068	-100.06302	790
	NVP16/3/1	V	42.74388	-100.11596	759
	NVP16/3/2	V	42.74386	-100.11605	757
	NVP16/3/3	V	42.74382	-100.11617	752
	NVP16/3/4	V	42.74380	-100.11634	756

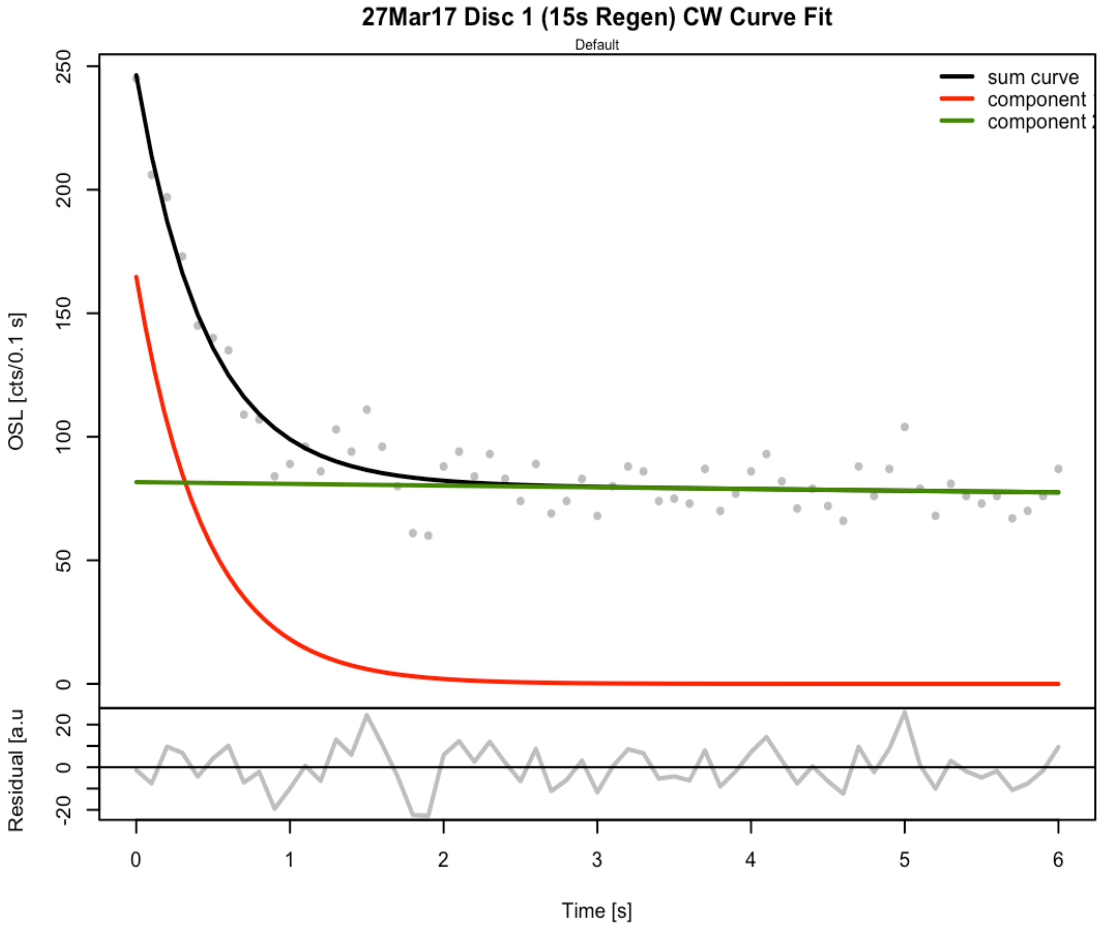
Appendix D – Integration interval analysis

Multiple steps were taken during integration interval analysis based on the discussion in Cunningham and Wallinga (2010). The below steps detail the processing of the data that led to the final integration interval selection used in the luminescence dating stages of this research project. Analysis was completed using script written by CB and the 'Luminescence' package in R.Studio.

Step 1: Identify individual components in the luminescence signal

'fit_CWCurve' (Kreutzer, 2017) in R.Studio (version 3.4.1) was used to identify the multiple signal components within OSL decay curve. The decay curve from a regenerative dose point was used in analysis since the natural luminescence signal was too weak to identify the individual components. Equations and split of the individual component curves are presented in Figure D.1.

Figure D.1 *(opposite)* Example of the component fitting code output based on the luminescence signal measured for a single regeneration point. fit_CWCurve has identified two components within the overall signal, c1 refers to the fast component of the signal. Plot shows the relative decay of the individual and combined components with time over a 6 second period.




```
Fitting was finally done using a 2-component function (max=5):
--------------------------------------------------------------------------------
y ~ I0.1 * lambda.1 * exp(-lambda.1 * x) + I0.2 * lambda.2 * exp(-lambda.2 * x)

           I0 I0.error    lambda lambda.error          cs cs.rel
c1   77.38067       NA 2.1319292           NA 2.502932e-17 1.0000
c2 7066.59275       NA 0.0113565           NA 1.333278e-19 0.0053
--------------------------------------------------------------------------------
pseudo-R^2 = 0.8439
```

Step 2: Calculate individual components

Using the equation and constants identified during component fitting, the individual component portions of the total signal for each channel were calculated.

NVP16/4/4/47										
27Mar17b01	Disc 1	15s Regen								
Component	I0	I0 Error	Lambda	Lambda Error						
C1	77.38067	10.13408	2.1319292	0.32467						
C2	7066.59275	21.29.87375	0.0113565	0.00376						
Time (x) in second	OSL total (y)	C1 (y)	I0 * lambda	-lambda * x	Exp(-lambda	C2 (y)	I0 * lambda	-lambda * x	Exp(-lambda	C1 / Total
0	245.2218705	164.9701099	164.97011	0	1	80.2517606	80.2517606	0	1	67%
0.1	213.4565632	133.2958888	164.97011	-0.2131929	0.80800024	80.1606744	80.2517606	-0.0011357	0.99886499	62%
0.2	187.7728021	107.7031105	164.97011	-0.4263858	0.65286439	80.0696916	80.2517606	-0.0022713	0.99773128	57%
0.3	167.0029515	87.02413947	164.97011	-0.6395788	0.52751459	79.9788121	80.2517606	-0.003407	0.99659885	52%
0.4	150.2035615	70.31552582	164.97011	-0.8527717	0.42623191	79.8880357	80.2517606	-0.0045426	0.9954677	47%
0.5	136.6123243	56.81496193	164.97011	-1.0659646	0.34439549	79.7973623	80.2517606	-0.0056783	0.99433784	42%
0.6	125.6132949	45.90650303	164.97011	-1.2791575	0.27827164	79.7067919	80.2517606	-0.0068139	0.99320926	37%
0.7	116.7087898	37.0924656	164.97011	-1.4923504	0.22484355	79.6163242	80.2517606	-0.0079496	0.99208196	32%
0.8	109.4966805	29.97072121	164.97011	-1.7055434	0.18167365	79.5259593	80.2517606	-0.0090852	0.99095595	27%
0.9	103.6520469	24.21635001	164.97011	-1.9187363	0.14679235	79.4356969	80.2517606	-0.0102209	0.98983121	23%
1	98.91235364	19.56681669	164.97011	-2.1319292	0.11860825	79.345537	80.2517606	-0.0113565	0.98870774	20%
1.1	95.06547197	15.80999263	164.97011	-2.3451221	0.0958355	79.2554793	80.2517606	-0.0124922	0.98758555	17%
1.2	91.94000183	12.77447789	164.97011	-2.558315	0.07743511	79.1655239	80.2517606	-0.0136278	0.98646464	14%
1.3	89.39745188	10.32178123	164.97011	-2.771508	0.06256758	79.0756706	80.2517606	-0.0147635	0.985345	12%
1.4	87.32592107	8.340001742	164.97011	-2.9847009	0.05055462	78.9859193	80.2517606	-0.0158991	0.98422662	10%

$$OSL\ counts\ (Y) for\ C1 = I0_1 \times \lambda_1 \times exp(-\lambda_1 \times X)$$

$$Where\ 'X' = Time\ in\ seconds$$

Figure D.2 Example calculation of the individual component levels and proportions of the signal for each 0.1 second channel of the measurement time. Equation details the method used to calculate the signal for each component at each point in time (given in seconds).

Step 3: Calculate percentage of net signal from fast component

By varying the length of signal and background intervals, we calculated the percentage of net signal from the fast component (Figure D.3).

Y0 for 0-0.6	1100.270073	=SUM of OSL total from 0 - 0.5s (inclusive)
Y0 % C1	620.1237365	=SUM of C1 from 0 - 0.5s (inclusive)
Y0 % C2	480.1463366	=SUM of C2 from 0 - 0.5s (inclusive)
Y hat for 0.6-2.1	560.8932859	=(SUM of OSL total from 0.6 - 2.1s (inclusive)) / (number of background channels/number of signal channels)
Y hat % C1	86.70217114	=(SUM of C1 from 0.6 - 2.1s (inclusive)) / (number of background channels/number of signal channels)
Y hat % C2	474.1913098	=(SUM of C2 from 0.6 - 2.1s (inclusive)) / (number of background channels/number of signal channels)
Net OSL signal	539.3767872	=Y0 - Y hat
Net OSL signal fro	99%	=(C1 signal - C1 background) / Net OSL signal

Figure D.3 Example of calculating the net OSL signal from the fast component based on a signal window of 0-0.5 seconds (Y_0) and background interval from 0.6-2.1 seconds ($\bar{Y}$).

Step 4: Calculate relative standard error (RSE) and percentage of net signal from fast component

For different combinations of signal and background interval lengths, we calculated the RSE versus signal internal length and RSE versus % fast component (Figure D.4).

NVP16/4/4/47					27Mar17b01		15s Regen							
	Integration length	Signal	Background	n	m	k	Y_0	$\bar{Y}$	$\hat{u}_s$	$\bar{Y}/k$	SQRT(Y0+($\bar{Y}$/k))	rse ($\hat{u}_s$)	rse ($\hat{u}_s$)	% net signal from fast componen
Disc 1	0.6	0-0.6	0.6-2.1	6	16	2.666667	1100.27	560.8933	539.3768	210.335	36.2022797	0.067119	6.71%	99%
Disc 1	0.5	0-0.5	0.6-2.1	5	16	3.2	963.6577	467.411	496.2468	146.0659	33.31251525	0.067129	6.71%	99%
Disc 1	0.4	0-0.4	0.6-2.1	4	16	4	813.4542	373.9288	439.5254	93.48219	30.11538441	0.068518	6.85%	99%
Disc 1	0.3	0-0.3	0.6-2.1	3	16	5.333333	646.4512	280.4466	366.0047	52.58373	26.43926943	0.072238	7.22%	99%
Disc 1	0.2	0-0.2	0.6-2.1	2	16	8	458.6784	186.9644	271.7141	23.37055	21.95561389	0.080804	8.08%	99%
Disc 1	0.1	0-0.1	0.6-2.1	1	16	16	245.2219	93.48219	151.7397	5.842637	15.84501522	0.104422	10.44%	99%
Disc 1	0.3	0-0.3	0.3-1.2	3	10	3.333333	646.4512	358.5622	287.889	107.5687	27.45942295	0.095382	9.54%	99%
Disc 1	0.2	0-0.2	0.2-0.9	2	8	4	458.6784	274.2656	184.4128	68.5664	22.96181258	0.124513	12.45%	100%
Disc 1	0.1	0-0.1	0.1-0.4	1	4	4	245.2219	179.609	65.6129	44.90224	17.03303005	0.259599	25.96%	100%
Disc 1	1.2	0-1.2	1.2-3.5	12	24	2	1749.719	970.7566	778.9621	485.3783	47.27681243	0.060692	6.07%	98%
Disc 1	2	0-2	2-8.9	20	70	3.5	2434.979	1512.557	922.4217	432.1593	53.54566612	0.058049	5.80%	91%
Disc 1	2.4	0-2.4	2.4-10.3	24	80	3.333333	2755.179	1794.2	960.979	538.2599	57.38848993	0.059719	5.97%	89%
Disc 1	0.2	0-0.2	0.2-0.6	2	5	2.5	458.6784	306.882	151.7965	122.7528	24.112885	0.15885	15.89%	100%
Disc 1	0.4	0-0.4	0.4-1.3	4	10	2.5	813.4542	447.0408	366.4134	178.8163	31.50032545	0.085969	8.60%	99%
Disc 1	0.6	0-0.6	0.6-2	6	15	2.5	1100.27	566.1917	534.0783	226.4767	36.42453527	0.068201	6.82%	99%
Disc 1	0.8	0-0.8	0.8-2.7	8	20	2.5	1342.592	690.9549	651.6372	276.382	40.23647754	0.061747	6.17%	98%
Disc 1	1	0-1	1-3.4	10	25	2.5	1555.741	823.3087	732.4322	329.3235	43.41732777	0.059278	5.93%	98%

$$net\ signal\ (\hat{\mu}_s) = Y_0 - \bar{Y}$$

$$\%\ net\ signal\ from\ fast\ component\ (C1) = \frac{Y_{o\,C1} - \bar{Y}_{C1}}{\hat{\mu}_s}$$

$$rse(\hat{\mu}_s) = \frac{\sqrt{Y_0 + \bar{Y}/_k}}{Y_0 - \bar{Y}}$$

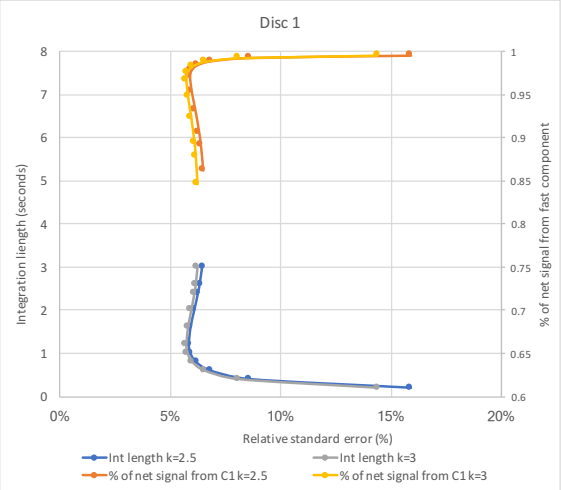


Figure D.4 Example of calculating RSE and fast component proportions based on a range of signal and background interval lengths. Integration length: length in seconds of signal window. Signal: the window defining initial signal portion. Background: the window defining background signal portion. 'n' = length of signal window (channels), 'm' = length of background window (channels), 'k' = m/n. Equations show methods used to calculate the % net signal from the fast component, the net overall signal, and the RSE of the signal. Plot shows results for keeping k-value constant at either 2.5 or 3. For young samples, results show little benefit in RSE with increase in percentage of fast component, the benefit is negligible. Optimum results are those which reduce RSE to lower values (due to maximising signal size – wide signal interval) followed by immediate background (k=3).

Step 5: Calculate the RSE based on same background window (0.6-2.1 s) versus varying signal window (0-0.1 to 0-0.5 s) (Figure D.5)

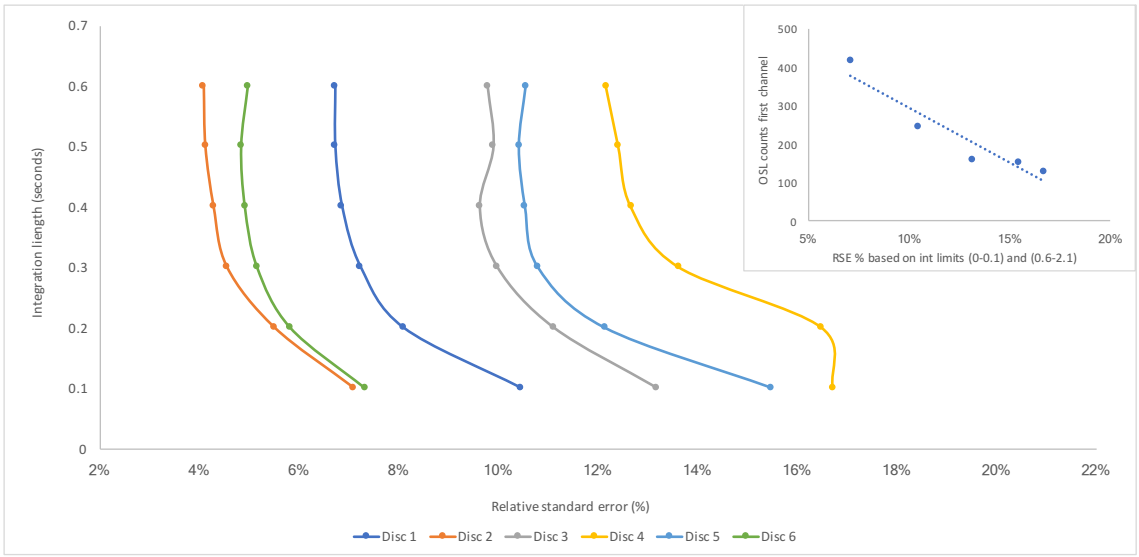


Figure D.5 Plot demonstrating how varying the signal window whilst keeping the background integration interval constant changes the RSE of the net calculated signal (for six different discs). As signal window increases, RSE decreases. *Inset*: RSE versus OSL total counts from the first channel. Results indicate the minimum luminescence signal size needed for specific RSE thresholds to be achieved. As expected, RSE decreases as OSL counts in the first channel increase.

Step 6: Compare impact on RSE and percentage of fast component between Early and Late background subtraction.

Results show that early background subtraction (placing the background signal window adjacent to the signal window) improves the percentage of net signal from the fast component, whilst increasing the interval length improves the RSE. Optimum settings are therefore those with a wide signal window and early background subtraction (Figure D.6)

	Signal intervals (inclusive)	Backgroun d intervals	n	m	k	Y0	Y0 C1	Y0 C2	Ŷ	Ŷ C1	Ŷ C2	Net OSL signal	% Net OSL signal from fast	Ŷ/k	SQRT(Y0 +(Ŷ/k))	rse (û,)
Early	0-0.5	0.6-2.0	6	15	2.5	1100.27	620.1237	480.1463	566.1917	91.732006	474.4597	534.0783	98.94%	226.4767	36.42454	6.82%
Late	0-0.5	58.6-60.0	6	15	2.5	1100.27	620.1237	480.1463	245.5498	1.825E-52	245.5498	854.7203	72.55%	98.21992	34.61921	4.05%
Early	0-0.1	0.2-0.6	2	5	2.5	458.6784	298.266	160.4124	306.882	147.1057	159.7763	151.7965	99.58%	122.7528	24.11289	15.89%
Late	0-0.1	58.2-58.6	2	5	2.5	458.6784	298.266	160.4124	82.68991	2.926E-52	82.68991	375.9885	79.33%	33.07596	22.17554	5.90%
Early	0-1.9	2-6.9	20	50	2.5	2434.979	847.133	1587.846	1530.978	4.8348634	1526.143	904.0014	93.17%	612.3911	55.20299	6.11%
Late	0-1.9	55-59.9	20	50	2.5	2434.979	847.133	1587.846	835.9797	4.097E-49	835.9797	1598.999	52.98%	334.3919	52.62481	3.29%

Figure D.6 Example data which shows the % net OSL signal from fast component and RSE of the net signal when different combinations of signal and background window are used. Results show the variability that can be found when window lengths are kept constant and background window is moved from an early subtraction to a late background subtraction.

Having established that the optimum settings are those with a wide signal window and early background subtraction, we then needed to calculate what size 'k' should be. If 'k' is too big, the percentage of net OSL signal from the fast component decreases, reducing accuracy in the age estimation. If 'k' is too small, there is increased susceptibility to peaks and troughs in the noisy signal, again reducing accuracy in the age estimate (Figure D.7).

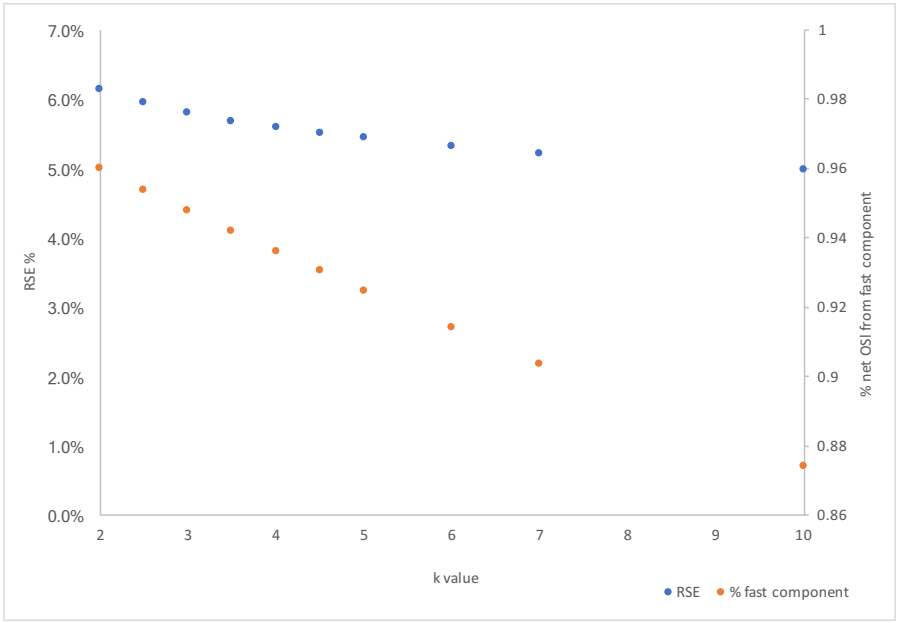


Figure D.7 Plot shows that as 'k' increases, the both the percentage of net OSL signal from fast component and the RSE decrease.

Step 7: Identifying the optimum value of 'k' based on the RSE of L_x/T_x

By including the test dose decay curve, calculations were completed to identify how the RSE on the sensitivity-corrected net luminescence signal (L_x/T_x) was affected by changing values of 'k' (Equation D.1).

$$net\ OSL\ signal\colon\ \hat{\mu}_s = Y_0 - \bar{Y}$$

$$sensitivity\ corrected\ net\ OSL\ signal\colon\ \frac{L_x}{T_x} = \frac{Y_{0\,L} - \bar{Y}_L}{Y_{0\,T} - \bar{Y}_T}$$

$$RSE\ of\ \frac{L_x}{T_x}\colon \partial\frac{L_x}{T_x} = \frac{L_x}{T_x} \times \sqrt{\left[\frac{Y_{0\,L} + \bar{Y}_L}{(Y_{0\,L} - \bar{Y}_L)^2}\right] + \left[\frac{Y_{0\,T} + \bar{Y}_T}{(Y_{0\,T} - \bar{Y}_T)^2}\right] + \left(\frac{\frac{I.E}{100}}{1}\right)^2}$$

Equation D.1 Three equations used in the calculation of the RSE of the sensitivity-corrected net luminescence signal. Using these equations, RSE of L_x/T_x was calculated based on a range of 'k' values. I.E refers to instrumental error (2.5% used).

The sensitivity-corrected luminescence signal was then converted into an equivalent dose (D_e) measurement using an example of a linear luminescence growth curve and plotted the relationship between D_e error and 'k' (Figure D.8). Results show that D_e error percentage decreases with increase in 'k'. However, we also know that increased 'k' leads to a decrease in the percentage of net OSL signal from the fast component: *increased 'k' improves precision but reduces accuracy*. A low/moderate 'k' value and an early background interval are optimal. For all final equivalent doses produced in this study, the integration intervals 0.1-1.5 seconds

for initial signal, and 1.6-6 seconds for background signal with a k-value 3 were used.

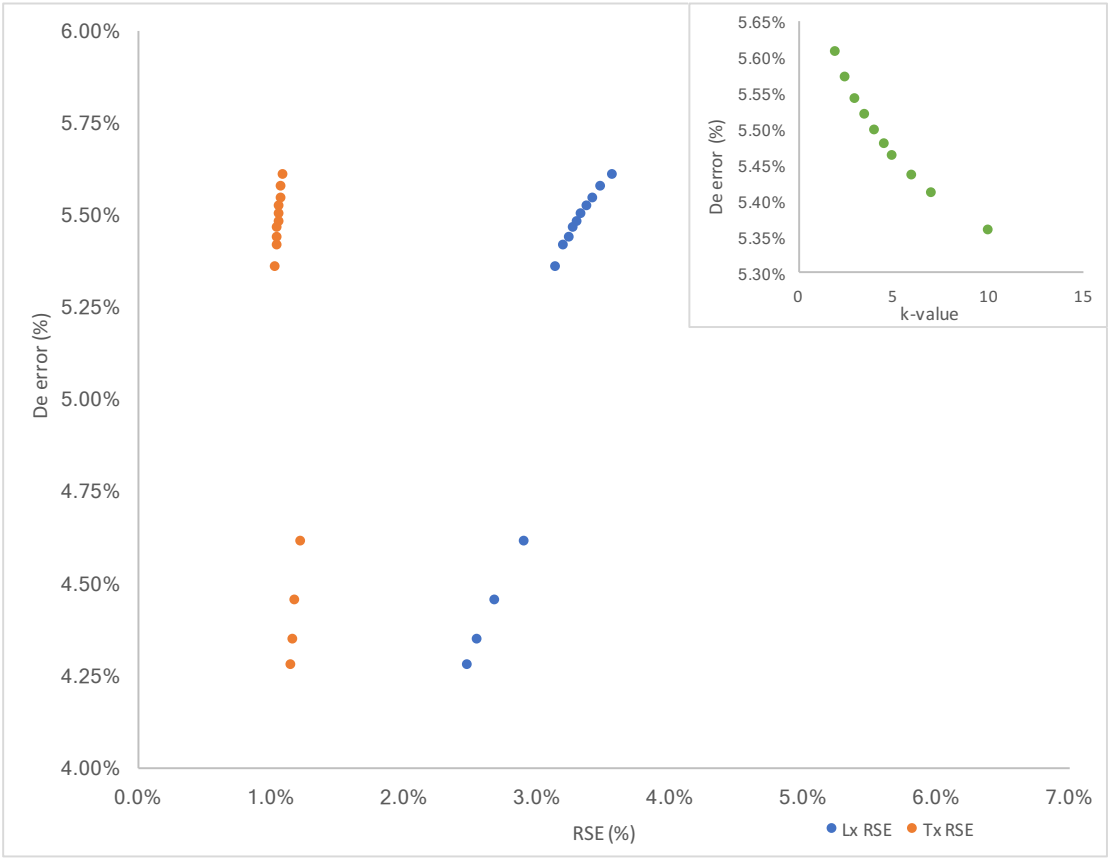


Figure D.8 Figure shows the comparison between the sensitivity-corrected natural / regenerative signal and the sensitivity-corrected test dose for both a regenerative dose point and the natural signal for different values of 'k'. The plot shows that the variability in the D_e error is not related to the RSE of T_x, the signal size is significantly greater than the natural or regenerative dose points. Inset: Plot of D_e error against k-value.

Appendix E – Environmental dose rates

As detailed in Section 3.4.8, where no stratigraphic change was noted, and radionuclide concentrations were normally distributed between sub-samples of the same sediment core, a weighted average of radionuclide concentrations was used for multiple sub-samples within the respective sediment cores. Table E.1 shows the final radionuclide concentrations used for each sample / sediment core.

Table E.1 Details of uranium, thorium and potassium contents used for environmental dose rate calculation for sub-samples used in OSL dating. For sediment cores NVP15/1/1, NVP15/3/1, NVP15/4/1, NVP16/2, NVP16/4 and NVP16/5/4, there was not any lithological variation present within the core and individual ICP-MS measurements taken from multiple depths within the core showed that the radionuclide measurements are normally distributed.

Sediment core	Sub-sample	Uranium (ppm)	Thorium (ppm)	Potassium (%)
NVP15/1/1	All sub-samples	0.80 ± 0.00	3.50 ± 0.00	1.57 ± 0.02
NVP15/3/1	All sub-samples	0.60 ± 0.00	2.44 ± 0.09	1.27 ± 0.01
NVP15/4/1	All sub-samples	1.17 ± 0.00	4.91 ± 0.03	1.86 ± 0.00
NVP16/2/1-4	All sub-samples	0.83 ± 0.00	4.72 ± 0.02	1.69 ± 0.00
NVP16/4/1-4	All sub-samples	0.87 ± 0.00	4.94 ± 0.02	1.65 ± 0.00
NVP16/5/1	All sub-samples	0.94 ± 0.00	4.75 ± 0.01	1.84 ± 0.00
NVP16/5/2	NVP16/5/2/9	0.94 ± 0.01	5.04 ± 0.07	1.66 ± 0.00
	NVP16/5/2/32	0.86 ± 0.07	5.03 ± 0.05	1.47 ± 0.02
NVP16/5/3	NVP16/5/3/7	1.11 ± 0.02	4.57 ± 0.05	1.84 ± 0.01
	NVP16/5/3/21	1.56 ± 0.03	6.52 ± 0.13	2.00 ± 0.00
	NVP16/5/3/39	1.11 ± 0.03	4.69 ± 0.09	1.88 ± 0.01
NVP16/5/4	All sub-samples	0.95 ± 0.00	4.96 ± 0.01	1.85 ± 0.00
NVP16/6/1	NVP16/6/1/4	1.00 ± 0.01	5.09 ± 0.06	1.77 ± 0.01
	NVP16/6/1/12	1.06 ± 0.01	5.56 ± 0.04	1.88 ± 0.00
	NVP16/6/1/25	1.07 ± 0.01	5.45 ± 0.05	1.87 ± 0.01
	NVP16/6/1/41	0.98 ± 0.01	5.63 ± 0.04	1.84 ± 0.01
NVP16/6/2	NVP16/6/2/7	1.20 ± 0.01	6.22 ± 0.05	1.80 ± 0.01
	NVP16/6/2/15	1.23 ± 0.01	5.40 ± 0.04	1.88 ± 0.00
	NVP16/6/2/34	1.20 ± 0.01	5.51 ± 0.05	1.82 ± 0.02

Final environmental dose rates for sub-samples were calculated using DRAC using the methods and conversion factors detailed in section 3.4.8 (Table E.2).

Table E.2 Table of individual dose rate contributions for each sample calculated using DRAC. Water attenuated beta and gamma dose rates are presented alongside the cosmic contribution and total environmental dose rate for each sub-sample.

Sub-sample	Beta dose rate ($Gy.ka^{-1}$)	Gamma dose rate ($Gy.ka^{-1}$)	Cosmic dose rate ($Gy.ka^{-1}$)	Total env. dose rate ($Gy.ka^{-1}$)
NVP15/1/1/1	1.28 ± 0.04	0.37 ± 0.01	0.33 ± 0.03	1.98 ± 0.05
NVP15/1/1/10	1.28 ± 0.04	0.54 ± 0.01	0.30 ± 0.03	2.13 ± 0.05
NVP15/1/1/20	1.28 ± 0.04	0.60 ± 0.02	0.28 ± 0.03	2.15 ± 0.05
NVP15/1/1/25	1.28 ± 0.04	0.60 ± 0.02	0.27 ± 0.03	2.15 ± 0.05
NVP15/1/1/30	1.28 ± 0.04	0.61 ± 0.02	0.26 ± 0.03	2.15 ± 0.05
NVP15/1/1/40	1.28 ± 0.04	0.62 ± 0.02	0.25 ± 0.03	2.15 ± 0.05
NVP15/1/1/50	1.28 ± 0.0	0.62 ± 0.02	0.24 ± 0.02	2.14 ± 0.05
NVP15/3/1/1	1.03 ± 0.03	0.28 ± 0.01	0.33 ± 0.03	1.65 ± 0.05
NVP15/3/1/10	1.03 ± 0.03	0.42 ± 0.01	0.30 ± 0.03	1.75 ± 0.04
NVP15/3/1/20	1.03 ± 0.03	0.46 ± 0.01	0.28 ± 0.03	1.76 ± 0.04
NVP15/3/1/25	1.03 ± 0.03	0.47 ± 0.01	0.27 ± 0.03	1.76 ± 0.04
NVP15/3/1/30	1.03 ± 0.03	0.47 ± 0.01	0.26 ± 0.03	1.76 ± 0.04
NVP15/3/1/40	1.03 ± 0.03	0.48 ± 0.01	0.25 ± 0.03	1.75 ± 0.04
NVP15/3/1/50	1.03 ± 0.03	0.48 ± 0.01	0.24 ± 0.02	1.74 ± 0.04
NVP15/4/1/5	1.57 ± 0.04	0.63 ± 0.02	0.32 ± 0.03	2.51 ± 0.06
NVP15/4/1/10	1.57 ± 0.04	0.70 ± 0.02	0.30 ± 0.03	2.57 ± 0.06
NVP15/4/1/15	1.57 ± 0.04	0.74 ± 0.02	0.29 ± 0.03	2.60 ± 0.05
NVP15/4/1/20	1.57 ± 0.04	0.76 ± 0.02	0.28 ± 0.03	2.61 ± 0.05
NVP15/4/1/25	1.57 ± 0.04	0.78 ± 0.02	0.27 ± 0.03	2.61 ± 0.05
NVP15/4/1/30	1.57 ± 0.04	0.78 ± 0.02	0.26 ± 0.03	2.61 ± 0.05
NVP15/4/1/35	1.57 ± 0.04	0.79 ± 0.02	0.25 ± 0.03	2.61 ± 0.05
NVP15/4/1/40	1.57 ± 0.04	0.79 ± 0.02	0.25 ± 0.03	2.61 ± 0.05
NVP15/4/1/45	1.57 ± 0.04	0.79 ± 0.02	0.24 ± 0.02	2.60 ± 0.05
NVP16/2/1/6	1.40 ± 0.04	0.57 ± 0.01	0.32 ± 0.03	2.29 ± 0.05
NVP16/2/1/25	1.40 ± 0.04	0.69 ± 0.02	0.27 ± 0.03	2.36 ± 0.05
NVP16/2/1/38	1.40 ± 0.04	0.70 ± 0.02	0.25 ± 0.03	2.36 ± 0.05
NVP16/2/1/44	1.40 ± 0.04	0.71 ± 0.02	0.25 ± 0.03	2.35 ± 0.05
NVP16/2/2/9	1.40 ± 0.04	0.61 ± 0.02	0.31 ± 0.03	2.32 ± 0.05
NVP16/2/2/33	1.40 ± 0.04	0.70 ± 0.02	0.26 ± 0.03	2.36 ± 0.05
NVP16/2/3/10	1.40 ± 0.04	0.62 ± 0.02	0.20 ± 0.03	2.33 ± 0.05

Sub-sample	Beta dose rate ($Gy.ka^{-1}$)	Gamma dose rate ($Gy.ka^{-1}$)	Cosmic dose rate ($Gy.ka^{-1}$)	Total env. dose rate ($Gy.ka^{-1}$)
NVP16/2/3/34	1.40 ± 0.04	0.70 ± 0.02	0.26 ± 0.03	2.36 ± 0.05
NVP16/2/4/5	1.40 ± 0.04	0.56 ± 0.01	0.32 ± 0.03	2.28 ± 0.05
NVP16/2/4/25	1.40 ± 0.04	0.69 ± 0.02	0.27 ± 0.03	2.36 ± 0.05
NVP16/2/4/45	1.40 ± 0.04	0.71 ± 0.02	0.24 ± 0.02	2.35 ± 0.05
NVP16/4/1/5	1.38 ± 0.04	0.56 ± 0.01	0.32 ± 0.03	2.26 ± 0.05
NVP16/4/1/25	1.38 ± 0.04	0.70 ± 0.02	0.27 ± 0.03	2.35 ± 0.05
NVP16/4/1/45	1.38 ± 0.04	0.71 ± 0.02	0.24 ± 0.02	2.34 ± 0.05
NVP16/4/2/5	1.38 ± 0.04	0.56 ± 0.01	0.32 ± 0.03	2.26 ± 0.05
NVP16/4/2/20	1.38 ± 0.04	0.69 ± 0.02	0.28 ± 0.03	2.34 ± 0.05
NVP16/4/2/23	1.38 ± 0.04	0.69 ± 0.02	0.27 ± 0.03	2.35 ± 0.05
NVP16/4/2/26	1.38 ± 0.04	0.70 ± 0.02	0.27 ± 0.03	2.35 ± 0.05
NVP16/4/2/36	1.38 ± 0.04	0.71 ± 0.02	0.25 ± 0.03	2.34 ± 0.05
NVP16/4/2/46	1.38 ± 0.04	0.71 ± 0.02	0.24 ± 0.02	2.34 ± 0.05
NVP16/4/3/11	1.38 ± 0.04	0.64 ± 0.02	0.30 ± 0.03	2.32 ± 0.05
NVP16/4/3/29	1.38 ± 0.04	0.70 ± 0.02	0.26 ± 0.03	2.35 ± 0.05
NVP16/4/3/43	1.38 ± 0.04	0.71 ± 0.02	0.25 ± 0.03	2.34 ± 0.05
NVP16/4/4/4	1.38 ± 0.04	0.50 ± 0.01	0.32 ± 0.03	2.21 ± 0.05
NVP16/4/4/10	1.38 ± 0.04	0.63 ± 0.02	0.30 ± 0.03	2.31 ± 0.05
NVP16/4/4/12	1.38 ± 0.04	0.64 ± 0.02	0.30 ± 0.03	2.32 ± 0.05
NVP16/4/4/29	1.38 ± 0.04	0.70 ± 0.02	0.26 ± 0.03	2.35 ± 0.05
NVP16/4/4/47	1.38 ± 0.04	0.71 ± 0.02	0.24 ± 0.02	2.34 ± 0.05
NVP16/5/1/7	1.52 ± 0.04	0.63 ± 0.02	0.31 ± 0.03	2.46 ± 0.05
NVP16/5/1/17	1.52 ± 0.04	0.72 ± 0.02	0.28 ± 0.03	2.52 ± 0.05
NVP16/5/1/30	1.52 ± 0.04	0.75 ± 0.02	0.26 ± 0.03	2.53 ± 0.05
NVP16/5/1/43	1.52 ± 0.04	0.75 ± 0.02	0.25 ± 0.03	2.52 ± 0.05
NVP16/5/2/9	1.40 ± 0.04	0.63 ± 0.02	0.30 ± 0.03	2.33 ± 0.05
NVP16/5/2/32	1.26 ± 0.04	0.67 ± 0.02	0.26 ± 0.03	2.18 ± 0.05
NVP16/5/3/7	1.54 ± 0.04	0.64 ± 0.02	0.31 ± 0.03	2.48 ± 0.06
NVP16/5/3/21	1.74 ± 0.05	0.91 ± 0.02	0.27 ± 0.03	2.92 ± 0.06
NVP16/5/3/39	1.57 ± 0.04	0.78 ± 0.02	0.25 ± 0.03	2.59 ± 0.05
NVP16/5/4/3	1.54 ± 0.04	0.54 ± 0.01	0.33 ± 0.03	2.40 ± 0.06
NVP16/5/4/27	1.54 ± 0.04	0.76 ± 0.02	0.26 ± 0.03	2.56 ± 0.05
NVP16/6/1/4	1.48 ± 0.04	0.56 ± 0.01	0.32 ± 0.03	2.37 ± 0.05
NVP16/6/1/12	1.58 ± 0.04	0.74 ± 0.02	0.30 ± 0.03	2.61 ± 0.06
NVP16/6/1/25	1.57 ± 0.04	0.79 ± 0.02	0.27 ± 0.03	2.63 ± 0.06
NVP16/6/1/41	1.54 ± 0.04	0.80 ± 0.02	0.25 ± 0.03	2.59 ± 0.05
NVP16/6/2/7	1.55 ± 0.04	0.70 ± 0.02	0.31 ± 0.03	2.57 ± 0.06
NVP16/6/2/15	1.59 ± 0.04	0.77 ± 0.02	0.29 ± 0.03	2.65 ± 0.06
NVP16/6/2/34	1.56 ± 0.04	0.81 ± 0.02	0.26 ± 0.03	2.62 ± 0.06

Appendix F – Supplementary Information from Paper 2 (Chapter 5)

Grain size data

Grain size data was measured at 2 cm intervals along selected sediment 50 cm cores to determine the homogeneity of sediments within a 50 cm vertical profile for two reasons. First, grain size data was measured to determine if samples that visually appeared homogenous were equally comparable in grain size properties along the length of the 50 cm core. Second, particle size analysis for a selection of cores was used to determine if any significant changes in particle size down core correspond with the depths of break points identified in the changepoint analysis of the L_x/T_x data. Particle size was measured using a Malvern Mastersizer 3000 and analysed using GRADISTAT software version 8.0 (Blott and Pye, 2001). Six sediment cores across the two locations (Niobrara Valley Preserve and Gudmundsen Sandhills Laboratory) were selected for particle size analysis providing a range of cores that showed different levels of visual homogeneity during sub-sampling. Sub-samples at every 2 cm were measured for particle size distributions, with three repeat measurements made per depth. Results are shown in Table F.1.

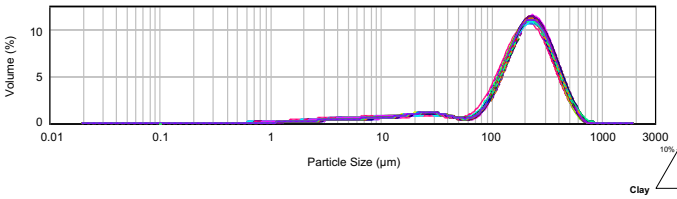
Table F.1 Grain size distribution results for six sediment cores used in this study. For each sediment core, results show particle size by volume measurements for each 2 cm depth measured, mean grain size and standard deviation, and description of predominant grain size.

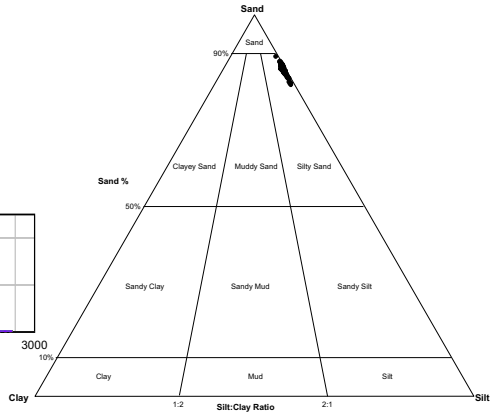
NVP16/2/3

Mean grain size: 248 µm

Standard deviation: 10 µm

Coarse silty medium – fine sand throughout core



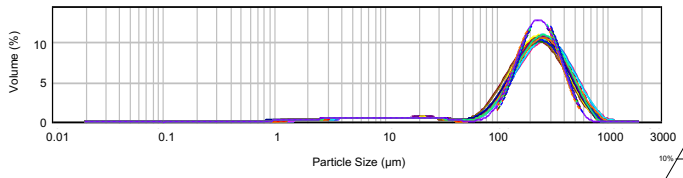


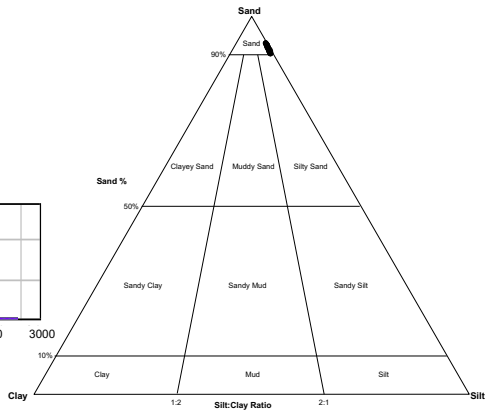
NVP16/4/3

Mean grain size: 261 µm

Standard deviation: 15 µm

Poorly sorted medium – fine sands throughout core



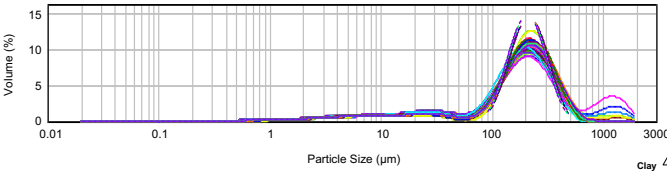


NVP16/5/2

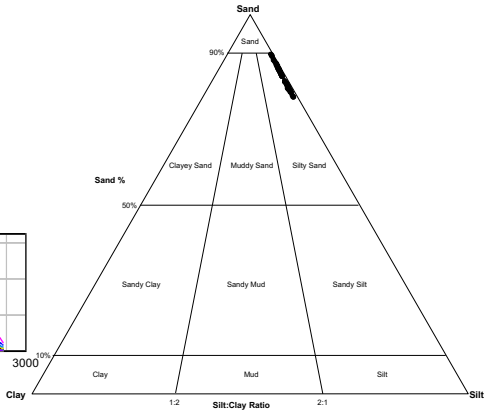
Mean grain size: 247 µm

Standard deviation: 37 µm

Very coarse silty sand found in the upper 4 cm following by coarse silty medium sand until 44 cm with poorly sorted medium sands in the lower 4-5



cm

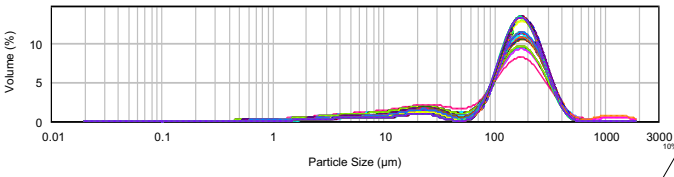


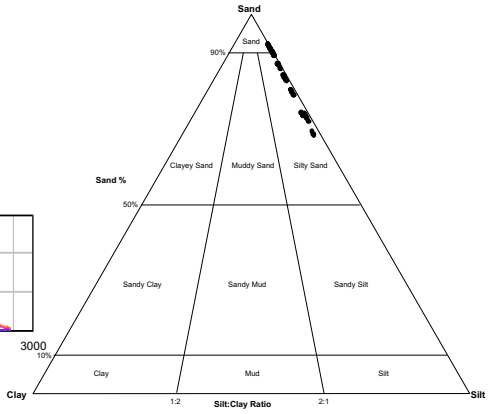
GSL16/3/2

Mean grain size: 200 µm

Standard deviation: 26 µm

Transitions from coarse silty find sand in the upper half to moderately sorted fine sands at c.32 cm depth



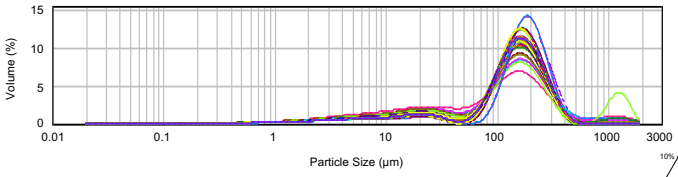


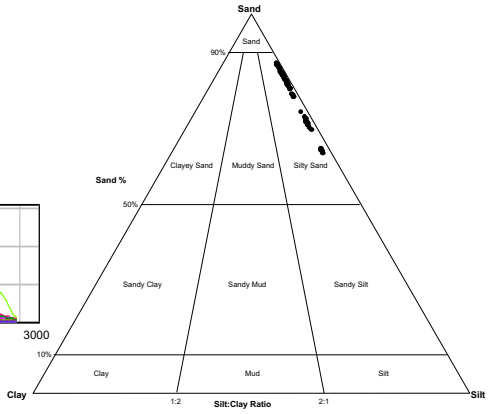
GSL16/4/3

Mean grain size: 184 µm

Standard deviation: 24 µm

Coarse silty fine sand throughout core



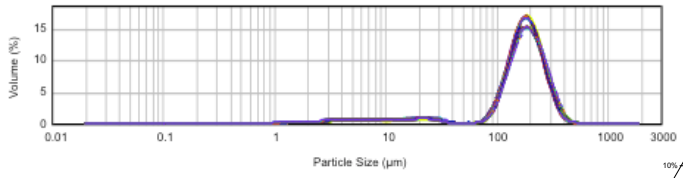


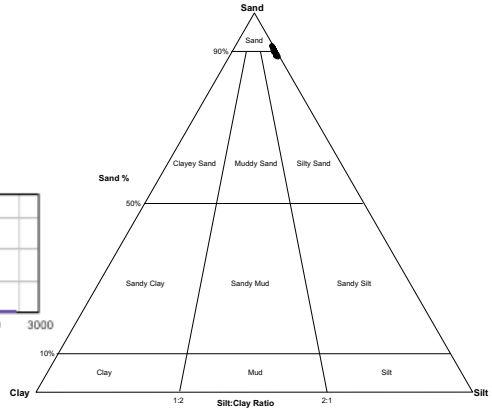
GSL16/5/1

Mean grain size: 207 µm

Standard deviation: 4 µm

Moderately sorted fine sands throughout core





Defining measurement conditions

Preheat plateau tests were completed to identify the most suitable measurement conditions for completing L_x/T_x measurements and fully-prepped SAR equivalent dose calculations. Small aliquots of fully-prepped quartz (125-180 μm) were used in the preheat plateau experiments, testing preheats in the range 160 – 260°C. A typical example of the preheat test results produced in this study are shown in Figure F.1 for sample NVP16/5/1/30. Whilst the preheat plateau test does not show any noticeable change in D_e with preheat temperature, analysis of the levels of recuperation found at both the beginning and end of the SAR cycle show that much higher levels of recuperation are found when temperatures >200°C are used. With 200°C selected as a suitable preheat temperature, dose recovery results for a series of samples are shown in Table F.2. Results from the dose recovery tests demonstrate the suitability of these preheat conditions for measuring the sediment samples used in this study.

Table F.2 Dose recovery results from six samples following the measurement conditions noted in Chapter 7. A preheat temperature of 200°C for 10 seconds was used following the results of the preheat plateau test detailed above, and OSL measurements were made at 130°C. Table details sample name, number of accepted aliquots, normalised $D_e \pm 1\sigma$, and overdispersion (%).

Sample	***n***	**Normalised $D_e \pm \sigma$**	**Overdispersion**
NVP15/1/1/25	15	1.01 ± 0.06	5.8 %
NVP15/4/1/25	20	1.01 ± 0.03	0 %
NVP16/2/1/25	11	0.99 ± 0.04	0 %
NVP16/4/4/12	12	1.03 ± 0.03	6.3 %
NVP16/5/3/21	15	1.0 ± 0.03	6.9 %
NVP16/5/4/3	11	0.95 ± 0.03	0 %

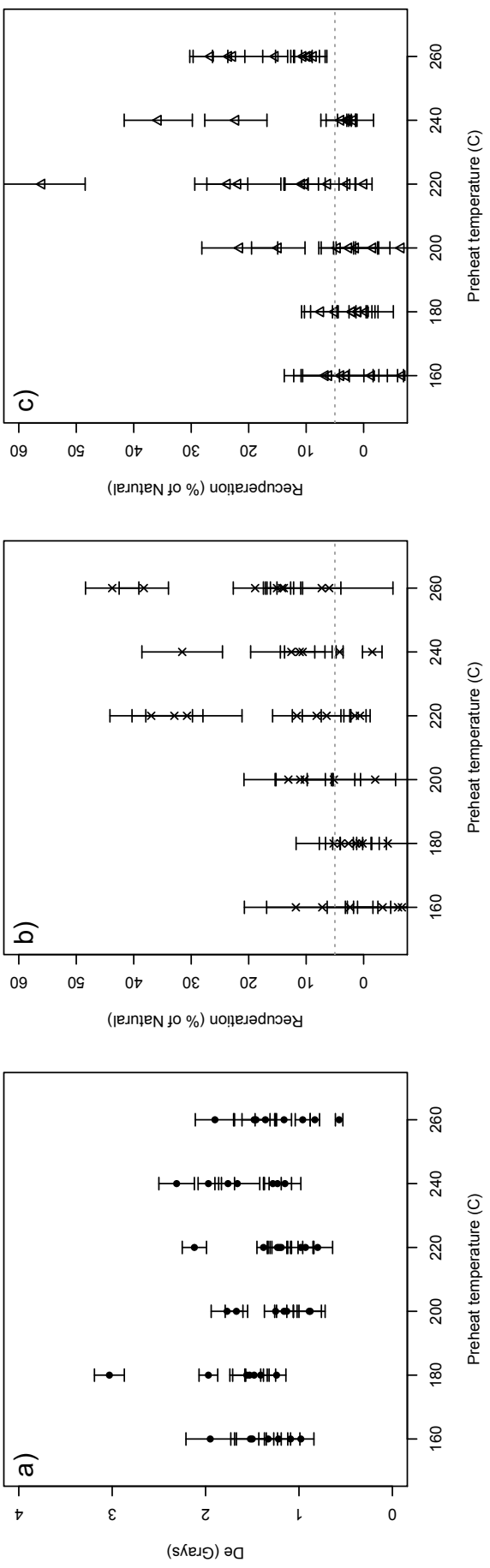


Figure F.1 Preheat test results for sample NVP16/5/1/30. a) Preheat versus natural D_e measurements. b) Preheat versus recuperation (found at beginning of the SAR cycle) as % of natural D_e. c) Preheat versus recuperation (found at the end of the SAR cycle) as % of natural D_e. Grey dashed line delimits 5% recuperation level in plots b) and c).

Shallow sample dose rate data

Using DRAC (Durcan *et al.*, 2015) individual components of the environmental dose rate were calculated using individual sub-sample depths and ICP-MS radionuclide measurements (Table F.3).

Table F.3 Table of dose rate component measurements for multiple depths within sediment cores NVP15/1/1, NVP15/3/1 and NVP15/4/1. Proportions of components contributing to the total dose rate, mean and standard deviation measurements are also presented for each sediment core.

Depth below surface	Water-corrected dose rate components			Environmental dose rate	Component proportions of total dose rate (%)		
	Beta	Gamma	Cosmic		Beta	Gamma	Cosmic
Sediment core: NVP15/1/1 (Site A at NVP)							
1 cm	1.27 ± 0.04	0.37 ± 0.01	0.33 ± 0.03	1.97 ± 0.05	64%	19%	17%
10 cm	1.27 ± 0.04	0.54 ± 0.02	0.30 ± 0.03	2.12 ± 0.05	60%	26%	14%
20 cm	1.39 ± 0.04	0.58 ± 0.02	0.28 ± 0.03	2.25 ± 0.05	62%	26%	12%
25 cm	1.39 ± 0.04	0.59 ± 0.02	0.27 ± 0.03	2.25 ± 0.05	62%	26%	12%
30 cm	1.39 ± 0.04	0.60 ± 0.02	0.26 ± 0.03	2.25 ± 0.05	62%	27%	12%
40 cm	1.30 ± 0.04	0.63 ± 0.02	0.25 ± 0.03	2.18 ± 0.05	60%	29%	11%
50 cm	1.30 ± 0.04	0.63 ± 0.02	0.24 ± 0.02	2.17 ± 0.05	60%	29%	11%
Mean				2.17			
Standard Deviation				0.10			
Sediment core: NVP15/3/1 (Site A at NVP)							
1 cm	1.01 ± 0.03	0.28 ± 0.01	0.33 ± 0.03	1.62 ± 0.05	62%	17%	21%
10 cm	1.01 ± 0.03	0.41 ± 0.01	0.30 ± 0.03	1.72 ± 0.05	59%	24%	18%
20 cm	1.23 ± 0.03	0.55 ± 0.01	0.28 ± 0.03	2.06 ± 0.05	60%	27%	13%
25 cm	1.23 ± 0.03	0.56 ± 0.01	0.27 ± 0.03	2.06 ± 0.05	60%	27%	13%
30 cm	1.23 ± 0.03	0.57 ± 0.01	0.26 ± 0.03	2.06 ± 0.05	60%	27%	13%
40 cm	1.04 ± 0.03	0.49 ± 0.01	0.25 ± 0.03	1.78 ± 0.04	59%	27%	14%
50 cm	1.04 ± 0.03	0.49 ± 0.01	0.24 ± 0.02	1.77 ± 0.04	59%	28%	13%
Mean				1.87			
Standard Deviation				0.19			
Sediment core: NVP15/4/1 (Site B at NVP)							
5 cm	1.50 ± 0.05	0.61 ± 0.02	0.32 ± 0.03	2.43 ± 0.06	62%	25%	13%
10 cm	1.80 ± 0.05	0.79 ± 0.02	0.30 ± 0.03	2.89 ± 0.06	62%	27%	10%
15 cm	1.68 ± 0.05	0.78 ± 0.02	0.29 ± 0.03	2.75 ± 0.06	61%	28%	10%
20 cm	1.56 ± 0.05	0.76 ± 0.02	0.28 ± 0.03	2.60 ± 0.06	60%	29%	11%
25 cm	1.68 ± 0.05	0.80 ± 0.02	0.27 ± 0.03	2.74 ± 0.06	61%	29%	10%
30 cm	1.64 ± 0.05	0.78 ± 0.02	0.26 ± 0.03	2.68 ± 0.06	61%	29%	10%
35 cm	1.61 ± 0.05	0.79 ± 0.02	0.25 ± 0.03	2.65 ± 0.06	61%	30%	10%
40 cm	1.48 ± 0.04	0.74 ± 0.02	0.25 ± 0.03	2.46 ± 0.05	60%	30%	10%
45 cm	1.46 ± 0.05	0.74 ± 0.02	0.24 ± 0.02	2.45 ± 0.06	60%	30%	10%
Mean				2.63			
Standard Deviation				0.16			

Results from sediment cores NVP15/1/1, NVP15/3/1 and NVP15/4/1 show that the combined contribution of cosmic and gamma dose rate remain relatively constant down core as the cosmic dose rate component decreases with depth, whilst the gamma dose rate component increases with a greater volume of surrounding sediment to contribute to the dose rate. There is little variability in the overall environmental dose rate found between sub-samples of the same sediment core, resulting in low standard deviations. Given the lack of variability in dose rate with depth, these results further support the use of L_x/T_x data points as a method for providing a coarse view of luminescence (and therefore relative age) variability with depth.

Appendix G – Wildfire tree scar records

The historical wildfire record was taken from Guyette *et al.* (2011) and listed in Table G.1. The original fire scar record was collected by Professor T. Bragg and others (1985) and unpublished. Professor T. Bragg was contacted for this research project and has provided the GPS details for the trees that were used in the original research project (Figure G.1).

Table G.1 Wildfire occurrence alongside the number of tree scar records each fire was recorded in.

Fire scar date (years AD)	Number of trees fire scar recorded in	Number of trees covering time period	% of trees fire recorded in
1736	1	3	33%
1750	1	3	33%
1789	1	6	17%
1814	1	8	13%
1824	1	11	9%
1826	1	16	6%
1832	1	19	5%
1839	2	23	9%
1841	1	24	4%
1848	6	27	22%
1850	1	28	4%
1856	8	29	28%
1862	8	31	29%
1866	2	32	6%
1872	10	32	31%
1874	2	32	6%
1876	3	32	9%
1879	3	32	9%
1885	6	33	18%
1887	12	34	35%
1889	2	34	6%
1893	1	34	3%
1895	5	35	14%
1899	6	36	17%
1901	1	36	3%

Fire scar date (years AD)	Number of trees fire scar recorded in	Number of trees covering time period	% of trees fire recorded in
1909	13	37	35%
1926	27	38	71%
1934	4	38	11%
1941	5	38	13%
1971	2	38	5%

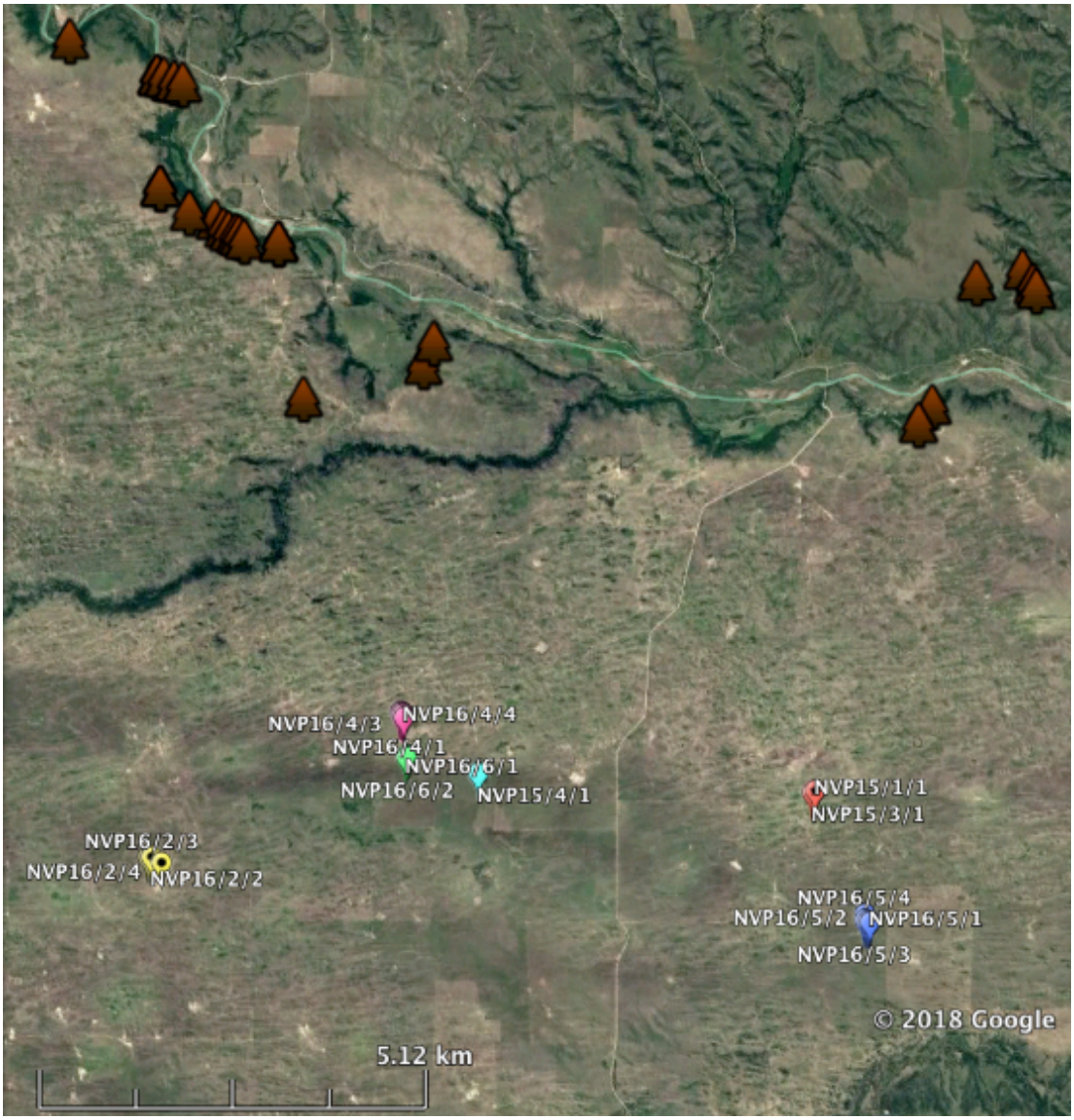


Figure G.1 Approximate GPS location of the trees that were used in the Bragg *et al.* (1985) fire scar collection analysis. Scar records were extracted from trees lining the banks of the Niobrara River, just north of the region where dune sediment samples were collected from. Satellite imagery courtesy of © 2018 Google Earth Pro.

Appendix H – Homesteading Deeds

Original land patents from when the Homestead Act came into place in 1863 AD were sourced from the General Land Office Records (https://glorecords.blm.gov/) and used to identify the dates when each of the sampling sites changed ownership history.

Table H.1 Table presents the date that each of the sections containing the sample sites used in this research project were first bought as part of the homestead act and the transition from 'unorganised' to 'organised' territory. Table details the specific owner and date that each plot was first acquired.

Sample site	Sediment cores	Township, Range & Section	Aliquot(s) of sediment cores	Name	Date
Site A	NVP15/1/1 NVP15/3/1	Township 32N Range 23W Section 20	NW ¼ of NE ¼	Arthur B White	10th February 1913
Site B	NVP16/2/1 NVP16/2/2 NVP16/2/3 NVP16/2/4	Township 32N Range 24W Section 21	NW ¼ of SW ¼	Harry Sherman	8th September 1904
Site C	NVP16/5/1 NVP16/5/2 NCP16/5/3 NVP16/5/4	Township 32N Range 23W Section 28	NW ¼ of NW ¼	Nicholas W Plummer	9th March 1914
Site D	NVP16/4/1 NVP16/4/2 NVP16/4/3 NVP16/4/4	Township 32N Range 24W Section 14	SW ¼ of NW ¼ NW ¼ of SW ¼ NE ¼ of SW ¼	James F Shepard	8th October 1915
Site E	NVP15/4/1	Township 32N Range 24W Section 14	SW ¼ of SW ¼	William Halsted	6th November 1890
Site F	NVP16/6/1 NVP16/6/2	Township 32N Range 24W Section 14	S ½ of SW ¼	John M Halsted	6th November 1890

Appendix I – Genealogy website data

Key extracts of information from a range of historical and genealogy websites that were used to help inform our general understanding of the social, economic and environmental history of the region for the land use / grazing pressure index are detailed below:

USGENNET: http://www.usgennet.org/usa/ne/county/brown/

- Cattle ranches were the first settlements. Stocked with Texas longhorn cattle that were driven over the old Chisholm Trail and turned out to fend for themselves. The cattle men were attracted by the rich, abundant prairie grasses which offered excellent range for their herds.
- Fort Niobrara was established April 22,1880, near present time Valentine.
- The cattlemen were followed by farmers, with a few doctors, lawyers, preachers, and merchants, all seeking the free land which could be obtained under the homestead law. The head of a family, or anyone 21 years old, could obtain 160 acres of land (Homestead Act – 1863) by living on it for five years and making a few improvements such as building a small house and ploughing a few acres of prairie.
- Passage of the "Kinkaid Law" in 1904 stimulated many families to move to northwest Nebraska. The law granted 640 acres to anyone who lived on the land for five years and added improvements worth $800.00. Persons who had already homesteaded 160 acres or less, could file again and bring their holdings to a full section or 640 acres. The Kinkaid Act opened up the Sand Hills that had proved unsuitable for small farms. The population increased and so did the value of grain, livestock and personal property.
- In late summer of 1882 the railroad was completed across the present boundaries of the county. A station was established on the homestead of John Berry, for whom Johnstown is thought to have been named.
- Although no records were kept the early settlers in this area said that the rains were plentiful and that harvests were abundant, especially wheat which was of excellent quality. Garden products grew with almost no cultivation and were of excellent quality also, during 1884 and as late as 1888.
- By 1890 crops were starting to fail and many families failed to raise enough to feed their stock and families. They applied to the county for relief. The county, in turn, appealed to the state. Small amounts of money received afforded some relief for the needy, but there was need for very rigid economy everywhere.
- The dry seasons continued and each year more families were obliged to ask for relief. Farms were deserted, stock sold at low prices, given away or turned loose. Banks failed and some businesses were forced to close. By 1895 the population had dwindled to about one half of what it had been before the dry years.

Access Genealogy and Memorial Library online resources:

https://www.accessgenealogy.com/nebraska/days-of-yore-early-history-of-brown-county-nebraska.htm

http://www.memoriallibrary.com/NE/Brown/1937/history.htm

- In the last 1870's the cattlemen came ahead of the railroad. They were attracted by the rich, abundant grasses of the prairies which offered excellent range for their herds, with water, shelter and firewood to be found in the canyons.

- 1880-1881 hard winter in Brown County, Nebraska - one of the most severe that was ever known. The prairies were covered with snow so deep that the cattle could not graze on the buffalo grass on which the ranchers relied for their winter feed. Of the 3,000 head on the Cook ranch only 800 were left in the spring. Other ranchers had similar losses and were obliged to close out, thus leaving the fertile prairies open to settlement by the farmers who came a few years later.

- 1890 Drought of Brown County Nebraska

- 1893-1895 Drought Years in Brown County, Nebraska:
  - About one-half of each homestead was broken up by 1893.
  - In the spring of 1894 it was very damp. The drought hit in May and June the wheat died before it headed out. Crops failed.
  - In 1895 crops were a little better, producing just enough so the people managed to get through. People left Brown County by wagon loads.

- In 1904 the Kinkaid Law was passed permitting a homestead of 640 acres to be acquired by five years residence thereon and placing improvements upon it to the value of $800.
  - This law proved of great value to all of northwest Nebraska and its passage resulted in the settling of the sand hills in a very few years. Again new settlers came into the county, and a most prosperous period followed their coming. The population was greatly increased, livestock, grain and other personal property was almost doubled in a very short time. Small but prosperous cattle ranches with a few acres in grain and other produce soon covered the sand hills sections.
  - Several new precincts were formed, schools and post offices established, roads laid out and a few bridges built.

Summary of key events in the Brown County / NVP vicinity

- 1841: The Preemption Act gave title to 160 acres to the head of a family over 21 years of age
- 1862: Homesteader's Act brought in – up to 160 acres per family – didn't really affect the Sandhills – more the surrounding farmland area
- 1860s-1880s: Cattle ranchers from Texas travel north and arrive and settle in Brown County. The Sawyer Trail was established as a main route in 1865. Ranchers generally settled along water or in canyons where they had access to water, shelter and firewood. They were attracted to the rich abundant prairie grasses which offered excellent range for their herds
- 1872: Homesteading first started in Brown County – but again, this was mainly not on the Sandhills land but further north and east in the county
- 1880: Fort Niobrara established in the area – idea to protect settlers from the Indians and outlaws
- 1880-81: Very hard winter in Brown County – many animals did not survive and the ranching population largely left the area
- 1881-82: Railroad reached Brown County and then was completed by 1882
- 1883: Brown County officially organised from unorganised territory
- 1883-1890: Early settlers begin to arrive in Brown County and the population increases. Early settlers noted that the rains were plentiful, harvests were abundant, and even the wheat was excellent
- 1888: Worst blizzard in Nebraska history recorded 12th January 1888 – not sure of the impact on individual counties – this is a state-wide statistic
- 1890-1895: Crops started to fail and the dry season continued through into 1895. Farms were deserted and given away or turned loose. The population of Brown County halved by 1895
- 1904: Kinkaid Act brought in – up to 640 acres per family – led to the mass settling on the Sandhills and the boom in population across the region up until The Great Depression
- 1904-1920s: Numerous small ranches sprung up in the area containing not only grazing cattle, but also wheat and dairy cattle
- 1930s: The Great Depression – population fell as many Kinkaiders left the area during The Great Depression
- 1980: The Nature Conservancy purchased The Niobrara Valley Preserve
- 1985: The Nature Conservancy re-introduced bison to the preserve after their absence for more than 100 years in the local area

Appendix J – Conversations with grassland ecologists & local ranchers

Please find below bullet point comments and key pieces of information extracted from conversations in the field and subsequently with local ranchers and grassland ecologists.

Conversations with Al Steuter (ranch owner for study site E & ex-preserve manager at Niobrara Valley Preserve)

Dr Al Steuter is a grassland ecologist and current ranch owner of the Sandhill and Sun Ranch where sample NVP15/4/1 was extracted. Al Steuter has a long history in the region since he was also the ex-preserve manager at the Niobrara Valley Preserve and continues to consult on ranch management and ecosystem health. Al was instrumental in the field with gaining access to field sites both on his ranch and the neighbouring ranch of Larry O'Keif. Comments from conversations with Al include:

- Sediment core NVP15/4/1 was taken from the top of a ridge hypothetically formed along a fence line during the 1930s. New fence was built bordering the ridge in the 1980s. Prairie dog town south of ridge. Al suggests that sediment was blown up from the southern field (in the southerly summer winds) and deposited north in E-W ridge. Al also noted potential activity in the 1950s which may have contributed to the dune structure
- 2012 wildfire: Ponderosa pine died out in the wildfire, normally this species is relatively resistant to wildfire, ***but*** extensive juniper growth in the understory led to a much hotter fire which wiped out the pines

- NVP East – An old centre pivot system from the 1970s can be seen on aerial photography. Some bare features in the centre pivot system can still be identified – this section is outside of the final study site area
- Big Hill pasture (waypoint 257, N 42.73120°, W 100.03062°) located in the middle of all the rolling dunes. Preferential zones of higher parabolics which are younger than the surrounding lower dunes. With the smaller, higher parabolics forming due to blow outs – caused by a localised disturbance
- Some gullies and rills form during high rainfall events

Dr Al Steuter was also consulted on the grazing / land use pressure index referred to in Chapter 7 (Paper 3). Dr Al Steuter confirmed that the timing brackets, relative indices and commentary was reflective of the history in the local region. Additional comments that Al provided which were included in the index include:

- Prior to 1870, bison grazing intensities on all sites was probably in the '2-3' range due to the value of the Niobrara River and its tributaries as a reliable source of water throughout the year. There were year-long bison herds roaming and grazing in the near Niobrara River area making full use of available forage.
- Rate grazing intensity on sites B, D, E & F as a '2' in the 1980 onwards period. These sites are on commercial cattle operations and moderate grazing is the norm.

Conversations with Doug Kuhre (cattle manager at Niobrara Valley Preserve)

As well as being the current cattle manager at the Niobrara Valley Preserve, Doug Kuhre was able to provide us with unique first-hand accounts of environmental and social change in the region. Doug Kuhre's ancestors were some of the original homesteaders in Brown County and settled on the site in 1891 (data based on the land patent records of William F Kuhre). A history of key reactivation episodes has been passed on from generation-to-generation with Doug able to provide us with a

site-specific history for the region. Key points from conversations with Doug in the field include:

- There is typically preferential grazing on new growth that grows in the place of burned areas
- Patch-burn grazing – movement of cattle between areas by burning areas
- On NVP-owned land: cattle are rotated every 6 weeks, grazing them hard in each area – in the east and in the west pasture: 210 cows over 2,500 acres – end of next grazing season is spring, and they will then be moved to the next pasture, each pasture has a full year's rest
- EAST: Bison pasture all burnt down and now trying to build 10,000 acres back up. 150 mature cows currently, and can take a capacity of up to 300
- WEST: 14,000 acres with 160 cows and 75 yearlings growing back to levels pretty fast
- 1880s: Blown out initially as everyone was only given 160 acres – people tried to farm but people starved to death. People massively tried to over farm their plots and this led to massive degradation and blow out of the landscape
- Pigs were farmed up until the 1960s
- Railroad built through Thedford in the 1870s/1880s
- There aren't so many hay valleys in the northern Sandhills near NVP, unlike GSL and BBR, this is because the water table is too low
- Doug said that from 1971-1980 (up until when the NVP was established) – the area was overgrazed and probably blew out
- NVP established in 1980 and bison re-introduced to the area for the first time in 100 years in 1985
- A move to more conservative grazing strategies in the region only occurred since the 1980s. History of more extensive blowouts can be identified by the presence of *Little Bluestem* (grass species) as this species occurs in locations which were previously overgrazed (*little bluestem* noted as the last grass species that livestock would like to consume)
- 2012 wildfire was initiated by a lightning strike on Doug Kuhre's land

Telephone conversation with Larry O'Keif (ranch owner for study sites B, D & F)

Larry O'Keif is the rancher and owner of the plots where sample sites NVP16/2, NVP16/3, NVP16/4 and NVP16/6 were taken. Larry granted us access to his private ranch for sampling whilst we were in the field but was not available to meet. A separate telephone call was made following fieldwork to gather any additional information he could provide us in regards his ranch. Key comments from the telephone conversation with Larry include:

- Cattle tracks found around the windmill (NVP16/2) come from the North
- Larry operates a 21 or 30-day rotation on his land – however, he will rotate the cattle more frequently during the dry years and wean the cattle early in a dry year
- 40 years ago, Larry comments it was really blowy and windy
- Larry's father was born in 1895 and bought the land sometime between 1945-1950 - the site has always been grazed since it has been in the family
- Summer grazing takes place from 5th May – November / December (depending on the weather)
- In reference to the Homestead Site (NVP16/4), this piece of land was bought by the family in 1981
- As well as the droughts of the 1930s, plagues of grasshoppers and locusts ate all the grass
- Specifically comments that the 2012 drought year was a bad year for vegetation and grazing

Appendix K – Supplementary Information from Paper 3 (Chapter 7)

Part 1: OSL characteristics

OSL decay curves from aliquots of samples NVP16/4/2/26 and NVP16/6/2/7 are shown below in Figure K.1 to demonstrate the typical OSL characteristics of the samples OSL dated in this study. NVP16/6/2/7 and NVP16/4/2/26 are examples of both young and relatively older sediments measured in this luminescence study. Due to the young nature of the sediments, dose response curves were fitted with a linear function using Analyst V4.31 (Duller, 2015)

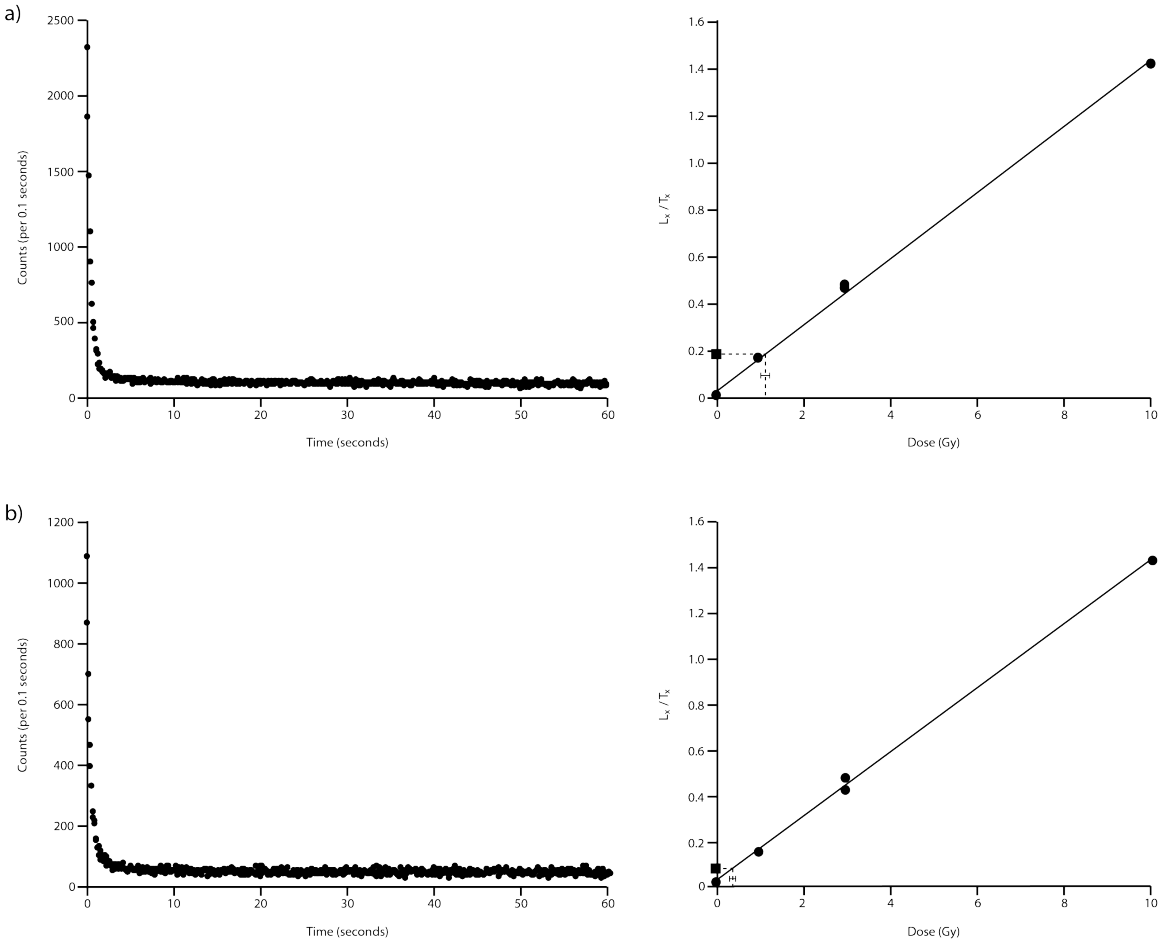


Figure K.1 Typical OSL decay curves and dose response curves for samples (a) NVP16/4/2/26 and (b) NVP16/6/2/7.

Part 2: Bayesian age-depth profiles

Sediment cores with overlapping OSL ages between sub-samples were Bayesian modelled (Bronk Ramsey, 2009) using OxCal 4.3 to reduce uncertainty estimates and improve chronological resolution. See age-depth profiles of sediment cores NVP15/1/1, NVP15/3/1 and NVP15/4/1 below (Figures K.2 & 3).

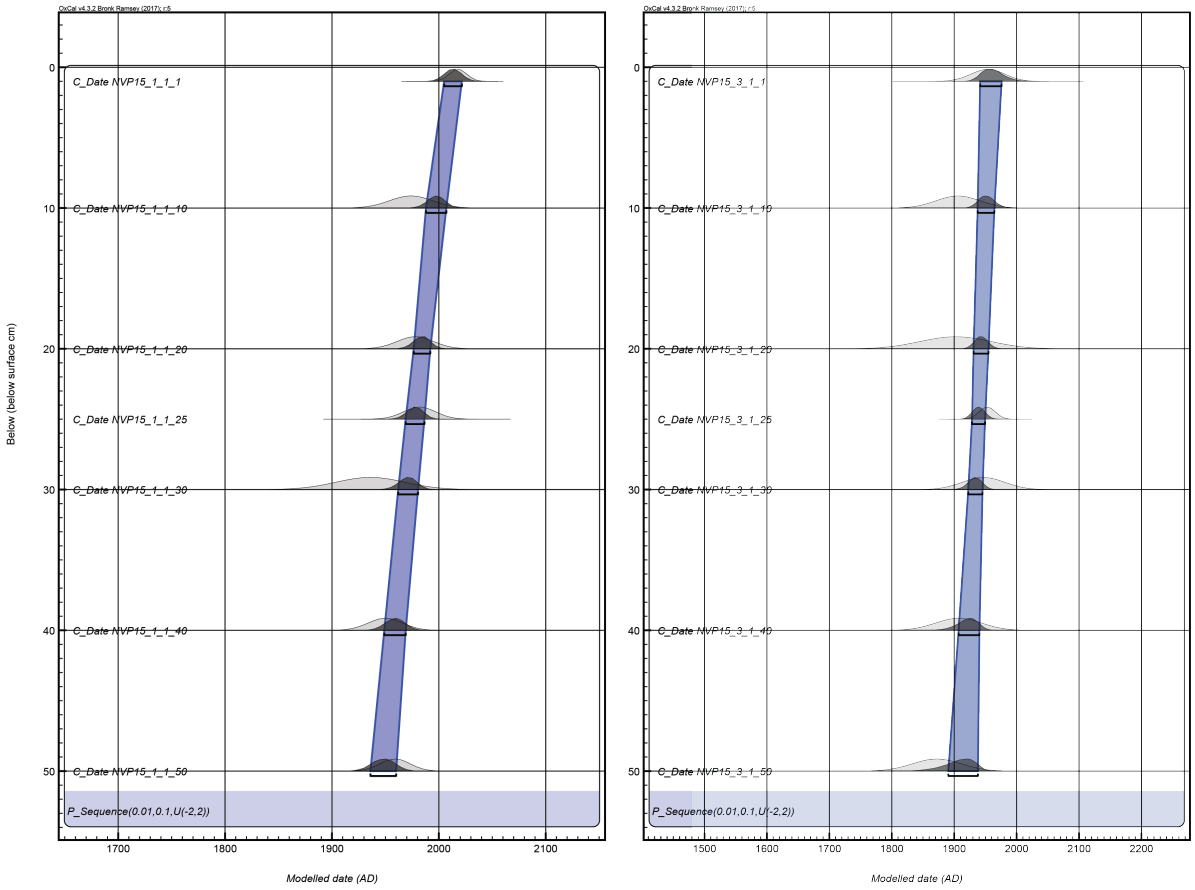


Figure K.2 Bayesian modelled age-depth plot for sediment cores NVP15/1/1 and NVP15/3/1 taken from Site A.

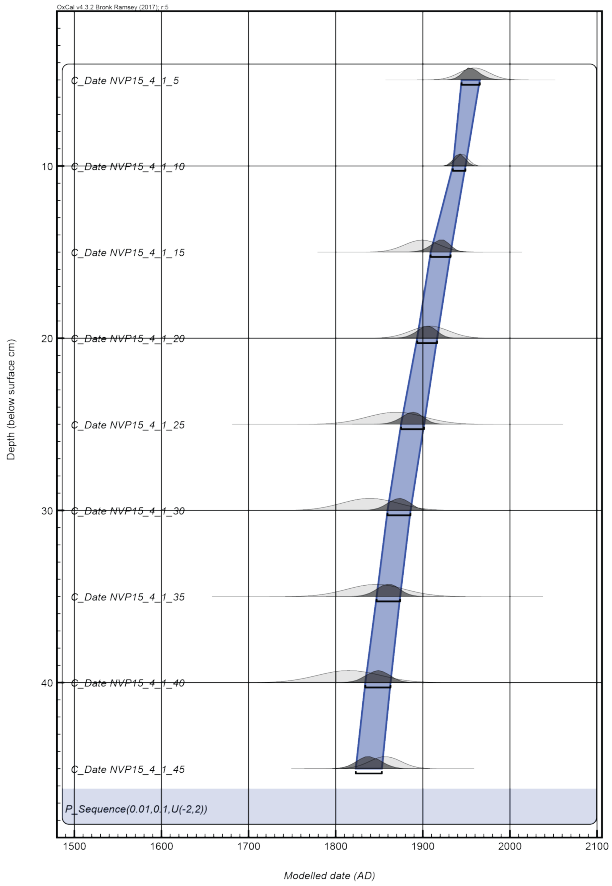


Figure K.3 Bayesian modelled age-depth plot for sediment core NVP15/4/1 taken from Site E.

Part 3: Historical aerial imagery

Archived United States Department of Agriculture (USDA) Farm Service Agency (FSA) historical aerial photography for the study region from 1939, 1954 and 1968 was gathered from the University of Nebraska-Lincoln historical imagery stores and used to guide sampling strategy and highlight visible changes in the vegetation cover across the sampling sites over time. Please see below examples of the images used (Figure K.4).



Figure K.4 Historical aerial images of western section of study area in Brown County, Nebraska. Circled blowout shows location of sample site D in 1939 (left), 1954 (centre) and 1968 (right).

Appendix L – Supplementary Information from Paper 4 (Chapter 8)

1. Study sites

Study sites used are part of a wider project investigating the drivers of near-surface reactivation in the northern Nebraska Sandhills, US. Six sites in the vicinity of the Niobrara Valley Preserve (NVP) and surrounding ranches were sampled for near-surface dune sediments and periods of surface deposition were dated using luminescence (optically stimulated luminescence – OSL) methods (see Paper 3) (Figure L.1). OSL ages date the period that has elapsed since the sediment was last exposed to sunlight, as such providing a date of deposition in the landscape.

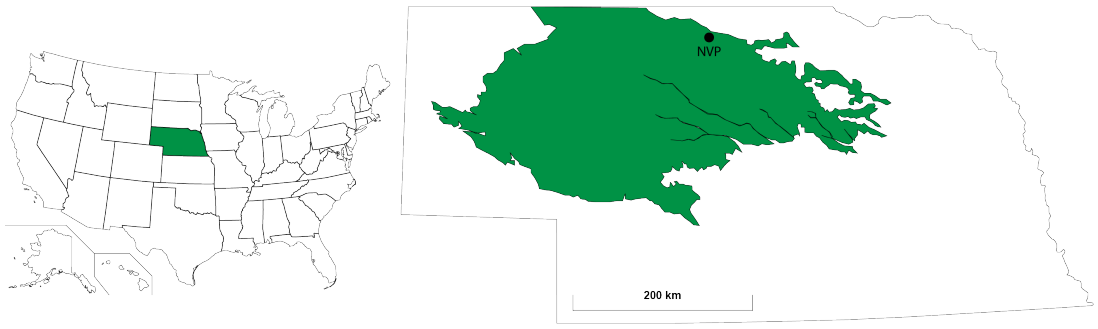


Figure L.1 Location map of NVP within the Nebraska Sandhills (green inset) and US. Six study sites were measured for depositional history in the NVP and surrounding ranches. Please see Buckland *et al.* submitted – 16/08/2018 for further details on the geomorphic setting of individual study sites.

2. ANN1 Inputs

Tree ring index (also used as ANN2 target) from 1590-1997: A local tree ring growth index (Brown *et al.*, n.d.) produced using samples of *Pinus ponderosa* was used as a proxy for historical climatic conditions for the last 400 years (Figure L.2).

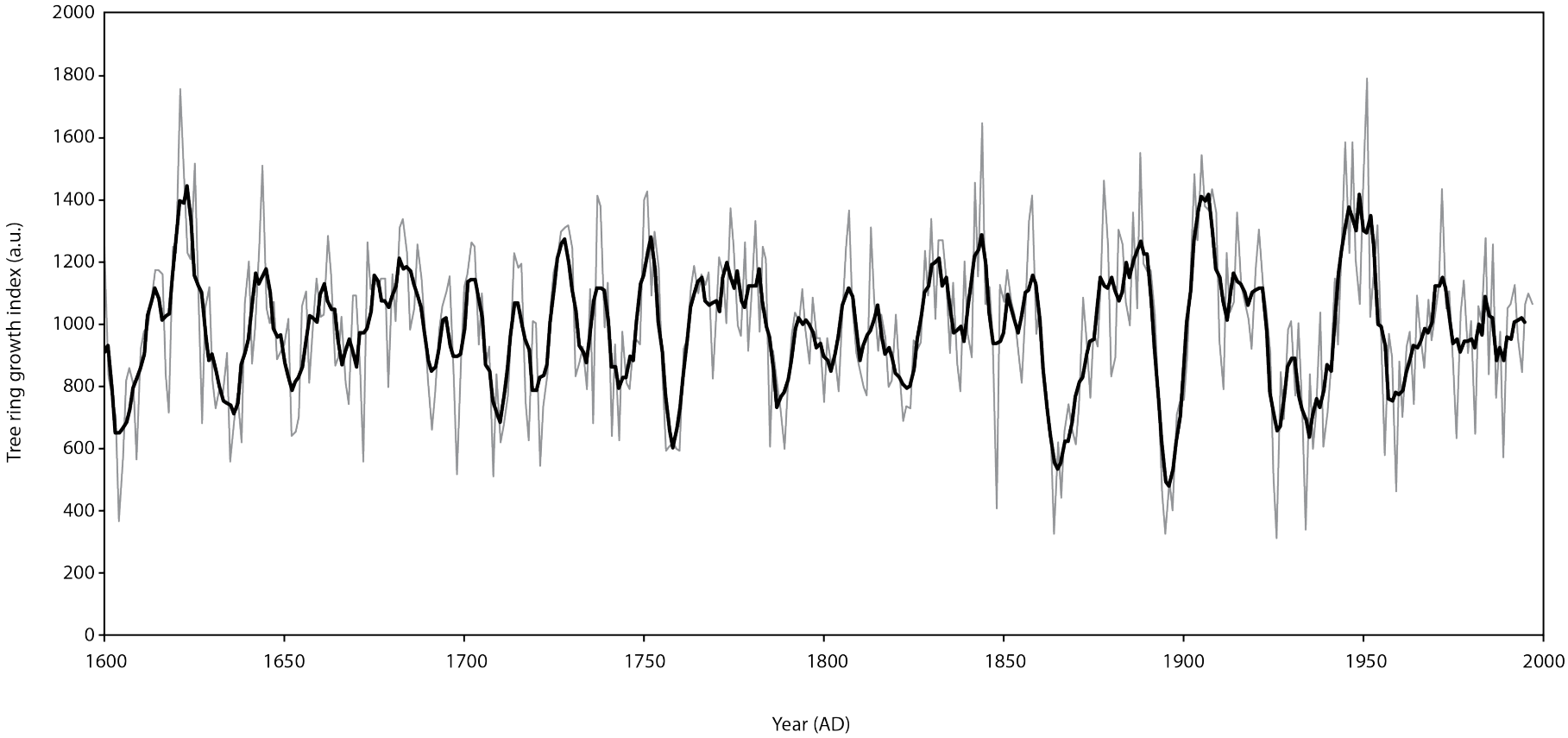


Figure L.2 Tree ring growth index compiled using multiple ring widths from Ponderosa pines in the vicinity of the NVP. Grey line depicts annual tree ring growth index values, whilst the black line shows a 5-year rolling average (illustrated here to demonstrate natural peaks and troughs in the record and the association with climatic episodes – e.g. note the troughs associated with the widely reported droughts of the 1890s, 1930s and 1950s).

Grazing pressure: Annual grazing (or land use) relative pressure on the landscape was defined by a three-point scale reflecting the changes in relative grazing pressure on the local sampling sites over the past 400 years (Table L.1). Without access to historical stocking rates and animal movements over this period, a three-point scale of relative pressure was used to depict broad-scale changes in the levels of pressure exerted on the land at each of the six sites over time. Refer to Paper 3 for further details on the construction of this index.

Wildfire record: A history of wildfire occurrence in the local area was extracted from a local tree scar record (collected by Professor T Bragg – University of Nebraska-Omaha) (Guyette *et al.*, 2011). A binary input was used to reference years when a wildfire did ('1') and did not ('0') occur with no pre-processing of the dataset required.

Table L.1 Summary table of the grazing pressure exerted on each of the six sites over the last 400 years. A three-point scale of relative pressure was used to capture the combination of population dynamics, grazing and agricultural practices, land ownership chronologies and wild grazing versus commercial ranching. Time brackets and intensity scores have been discussed and ratified with local grassland ecologist Dr Al Steuter. Classification scores reflect: 1 – low pressure, 2 – moderate grazing pressure, 3 – high grazing pressure.

Period	Site and Intensity score
Pre-1870s	All sites: 2
1870-1880	All sites: 1
1880-1890	All sites: 1
1890-1904	Sites A, B, C & D: 2 Sites E & F: 3
1904-1930	All sites: 3
1930-1940	Sites A, C, D, E & F: 2 Site B: 3
1940-1970	Sites A, C, D, E & F: 2 Site B: 3
1970-1980	Sites A, B & C: 3 Sites D, E & F: 2
1980s onwards	Sites A & C: 1 Site B: 3 Sites D, E & F: 2

3. ANN1 Target: OSL PDF datasets

The target dataset used in ANN1 is a stacked chronology of the identified periods of sediment deposition at six sites within the Niobrara Valley Preserve and surrounding ranches. At each of the six dune sites, a series of OSL dates were calculated to reconstruct a history of episodes of sediment deposition that had occurred in the recent history across the different sampling sites (Paper3). The target dataset used in this study represents a likelihood of identifying a luminescence age (referring to a period of deposition) in the sampled sediment, it does not necessarily capture every sediment deposition event that has occurred, but only those that have not been eroded from the sequence (Bailey and Thomas, 2014).

The final luminescence ages (Table L.4) associated were stacked in a probability density function (Figure L.3) for each of the six sites to produce the target dataset used in ANN1.

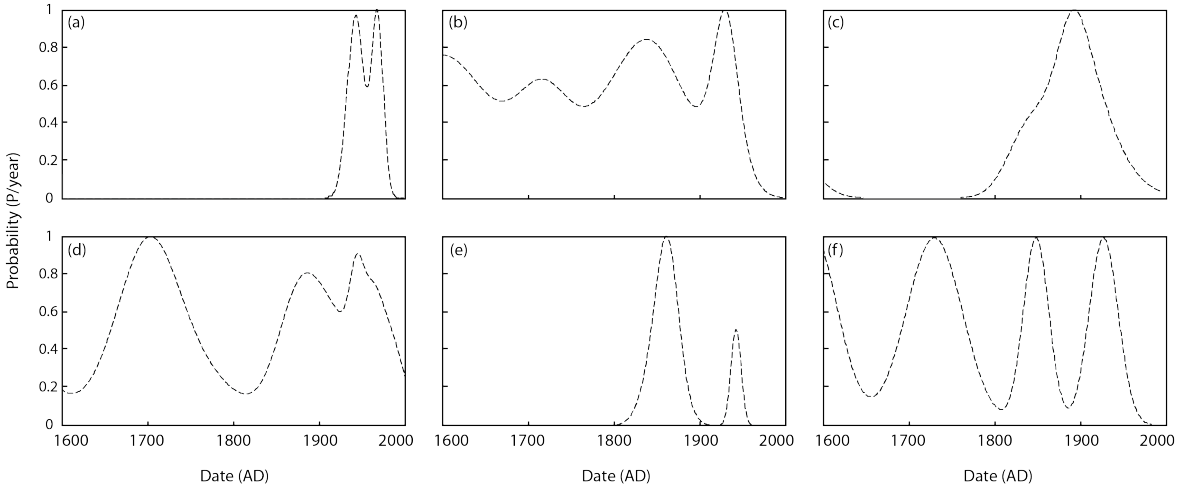


Figure L.3 PDF of stacked OSL ages taken from six sites (a-f) across the Niobrara Valley Preserve and surrounding ranches, northern Nebraska Sandhills. OSL PDFs have been standardised and 'non-events' have been removed from the dataset as part of the pre-processing methods.

Table L.4 Final OSL dates of deposition were calculated using the un-logged CAM of all ages from one defined changepoint section (i.e. sites A & E ages modelled to produce one date per section).

Site	Sample	Age ± 1σ (ka)	Date ± 1σ (AD)*
Site A	NVP15/1/1/1	-0.003 ± 0.008	
	NVP15/1/1/10	0.041 ± 0.02	
	NVP15/1/1/20	0.037 ± 0.017	
	NVP15/1/1/25	0.033 ± 0.015	1966 ± 7
	NVP15/1/1/30	0.079 ± 0.032	
	NVP15/1/1/40	0.065 ± 0.016	
	NVP15/1/1/50	0.056 ± 0.014	
	NVP15/3/1/1	0.061 ± 0.027	
	NVP15/3/1/10	0.109 ± 0.035	
	NVP15/3/1/20	0.113 ± 0.057	
	NVP15/3/1/25	0.062 ± 0.013	1940 ± 10
	NVP15/3/1/30	0.068 ± 0.034	
	NVP15/3/1/40	0.108 ± 0.037	
	NVP15/3/1/50	0.143 ± 0.039	
Site B	NVP16/2/1/6	0.087 ± 0.02	1929 ± 20
	NVP16/2/1/25	0.3 ± 0.031	1716 ± 31
	NVP16/2/1/38	0.386 ± 0.047	1630 ± 47
	NVP16/2/1/44	0.582 ± 0.032	1434 ± 32
	NVP16/2/2/9	0.168 ± 0.039	1848 ± 39
	NVP16/2/2/33	0.703 ± 0.038	1313 ± 38
	NVP16/2/3/10	0.202 ± 0.056	1814 ± 56
	NVP16/2/3/34	0.437 ± 0.041	1579 ± 41
	NVP16/2/4/5	0.057 ± 0.021	1959 ± 21
	NVP16/2/4/25	0.089 ± 0.018	1927 ± 18
	NVP16/2/4/45	0.115 ± 0.022	1901 ± 22
Site C	NVP16/5/1/7	0.106 ± 0.041	1910 ± 41
	NVP16/5/1/17	0.179 ± 0;023	1837 ± 23
	NVP16/5/1/30	0.455 ± 0.027	1561 ± 27
	NVP16/5/1/43	0.663 ± 0.039	1353 ± 39
	NVP16/5/2/9	0.116 ± 0.025	1900 ± 25
	NVP16/5/2/32	0.807 ± 0.04	1209 ± 40
	NVP16/5/3/7	0.125 ± 0.016	1891 ± 16
	NVP16/5/3/21	0.647 ± 0.04	1369 ± 40
	NVP16/5/3/39	0.74 ± 0.045	1276 ± 45
	NVP16/5/4/3	0.125 ± 0.037	1891 ± 37
	NVP16/5/4/27	0.747 ± 0.042	1269 ± 42
Site D	NVP16/4/1/5	0.032 ± 0.016	1984 ± 16
	NVP16/4/1/25	0.055 ± 0.012	1961 ± 12
	NVP16/4/1/45	0.073 ± 0.008	1943 ± 8
	NVP16/4/2/5	0.084 ± 0.031	1932 ± 31
	NVP16/4/2/20	0.128 ± 0.03	1888 ± 30
	NVP16/4/2/23	0.571 ± 0.022	1445 ± 22
	NVP16/4/2/26	0.494 ± 0.041	1522 ± 41
	NVP16/4/2/36	0.632 ± 0.053	1384 ± 53
	NVP16/4/2/46	0.681 ± 0.039	1335 ± 39
	NVP16/4/3/11	0.142 ± 0.025	1874 ± 25
	NVP16/4/3/29	0.311 ± 0.031	1705 ± 31
	NVP16/4/3/43	2.01 ± 0.107	11 ± 107
	NVP16/4/4/3	0.285 ± 0.055	1731 ± 55
	NVP16/4/4/10	0.329 ± 0.036	1687 ± 36
	NVP16/4/4/12	0.504 ± 0.049	1512 ± 49
	NVP16/4/4/29	0.831 ± 0.046	1185 ± 46
	NVP16/4/4/47	0.788 ± 0.036	1228 ± 36
Site E	NVP15/4/1/5	0.056 0.017	
	NVP15/4/1/10	0.07 0.007	1943 ± 6
	NVP15/4/1/15	0.116 0.02	
	NVP15/4/1/20	0.107 0.022	
	NVP15/4/1/25	0.146 0.033	
	NVP15/4/1/30	0.176 0.032	1863 ± 12
	NVP15/4/1/35	0.169 0.033	
	NVP15/4/1/40	0.2 0.036	
	NVP15/4/1/45	0.158 ± 0.018	
Site F	NVP16/6/1/4	0.089 ± 0.017	1927 ± 17
	NVP16/6/1/12	0.287 ± 0.033	1729 ± 33
	NVP16/6/1/25	0.567 ± 0.055	1449 ± 55
	NVP16/6/1/41	0.722 ± 0.041	1294 ± 41
	NVP16/6/2/7	0.168 ± 0.015	1848 ± 15
	NVP16/6/2/15	0.43 ± 0.03	1586 ± 30
	NVP16/6/2/34	0.695 ± 0.037	1321 ± 37

4. ANN2 Inputs

Historical growing season precipitation and growing season average maximum and minimum temperatures are taken from weather station records kept at Ainsworth Meteorological station, Nebraska (42.58° N, -100.05° W, <10 miles from the study sites) sourced from the National Centres of Environmental Information (https://www.ncdc.noaa.gov/ - accessed on 04/01/2018) from 1908-2014 AD (Figure L.4).

Future climate projections

A new set of generated annual growing seasons precipitation totals and average maximum and minimum growing seasons temperatures based on noise levels extracted from historical records and three different climate trends.

An autoregressive model was used to identify the historical trends, and thus level of noise found in the growing season precipitation and temperature profiles from 1908 – 1997 AD (Figure L.5). Synthetic noise was calculated based on the residual profile of the historical noise relative to the trend from the instrumental climate data. The synthetic noise profile was then added to two combinations of precipitation and temperature data to produce the different climate futures.

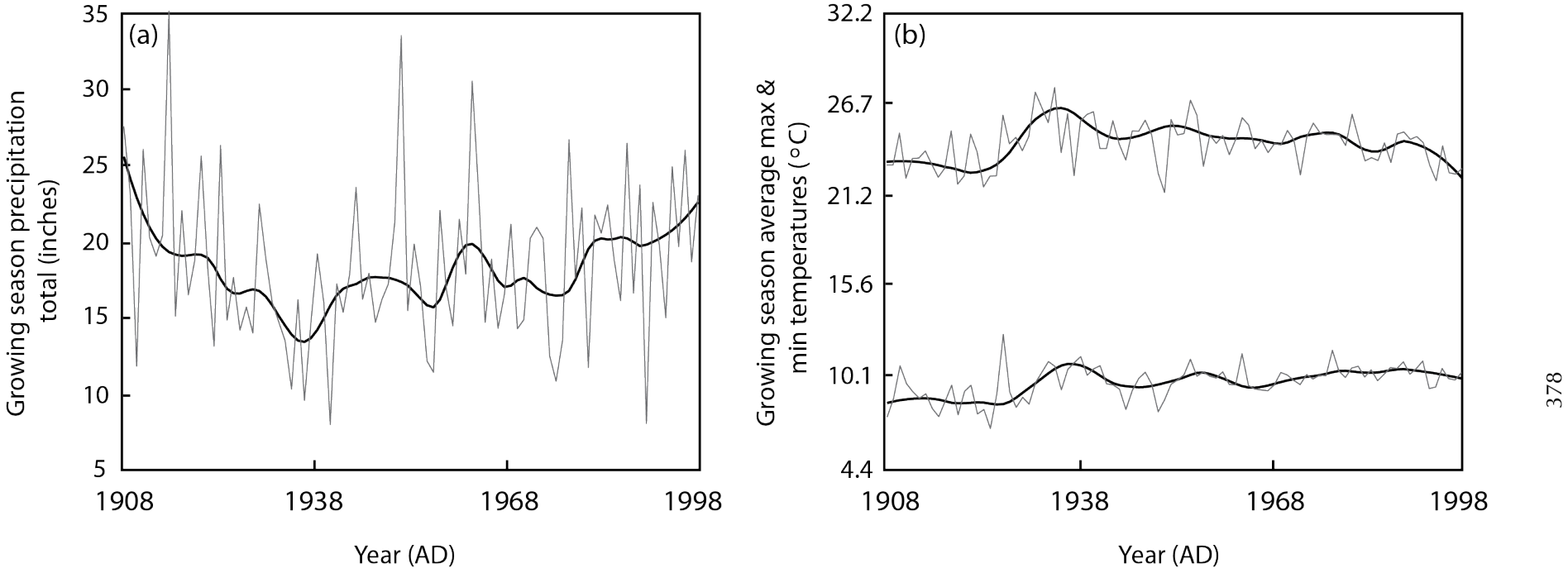


Figure L.4 Historical annual growing season weather data 1908 – 1998 AD: (a) Precipitation totals (inches). Grey line refers to pre-processed growing season annual totals; black line is the post-processed smoothed values that were used by the neural network. (b) Average max and min daily temperatures (°C). Grey line refers to pre-processed annual values; black line is the post-processed smoothed values that were used by the neural network.

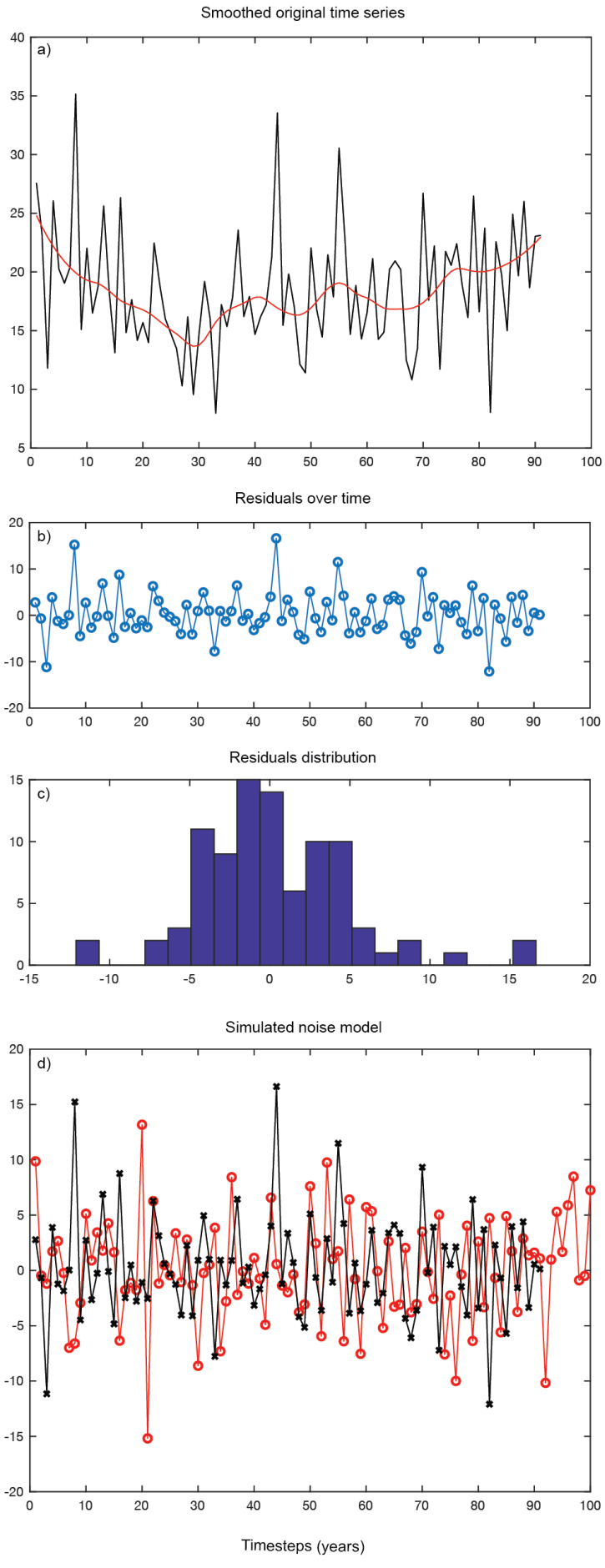


Figure L.5 Example outputs from autoregressive model to identify the level of noise associated with the growing season precipitation dataset and simulate new 'noise' for future climates. a) Empirical growing season precipitation measurements with smoothed trend. b) Calculation of annual residuals based on smoothed trend from a). c) Residuals are normally-distributed. d) New simulated noise profile based on the residuals and lags identified in the autoregressive model.

The two climate future trends simulated are detailed in Methods and broadly reflect: Climate 1 – historical long-term averages, and Climate 2 – a gradual increase in temperatures (2.5°C by end of century) to reflect low emissions scenario (Bathke *et al.*, 2014). The climatic scenarios do not demonstrate predicted future conditions but are used as proof on concept to demonstrate the capacity of the model under a range of forcing combinations (Figure L.6).

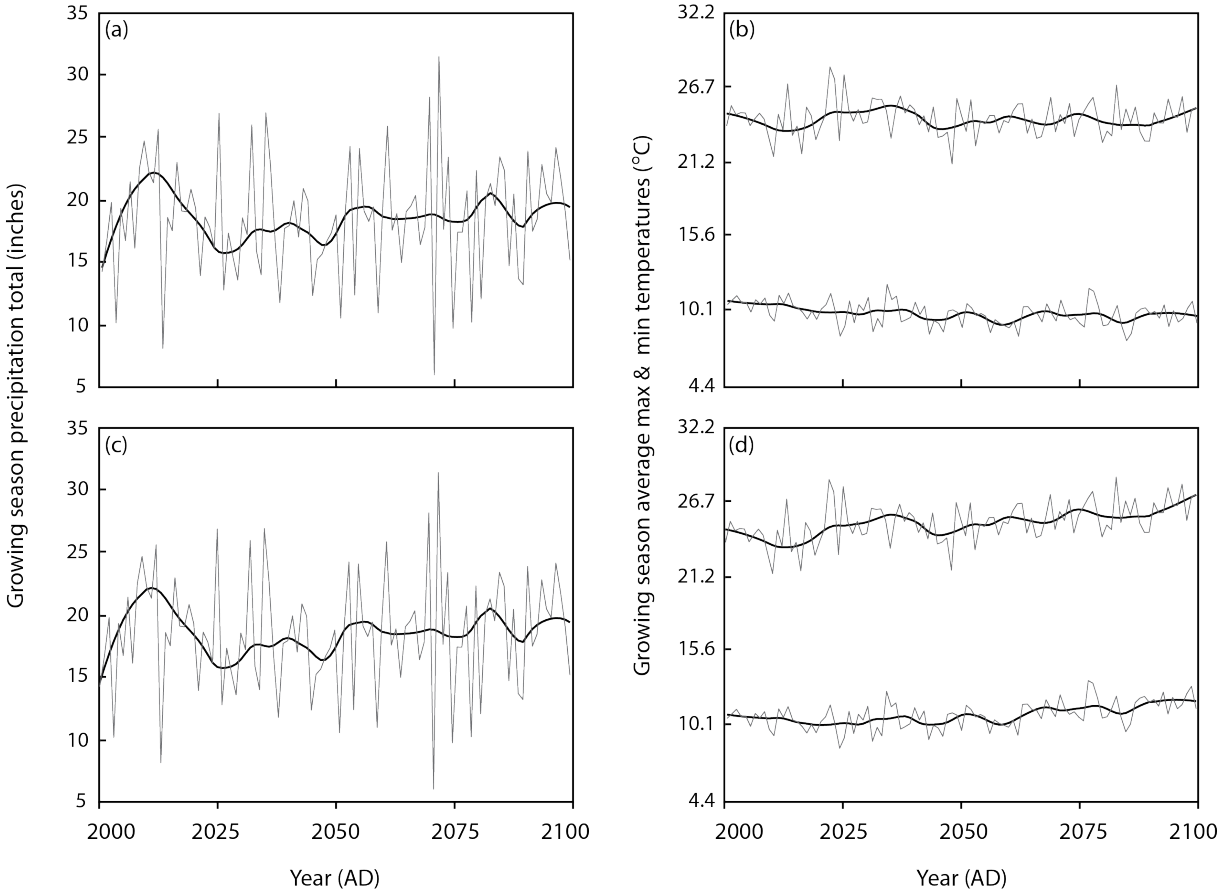


Figure L.6 Growing season precipitation totals and average maximum and minimum growing season daily temperatures associated with the two simulated climate scenarios: Climate 1 (a-b), Climate 2 (c-d).

5. Processing future scenario outputs

Final mean and associated standard errors for the predicted output profiles was based on selecting a percentage of the best performing models and their associated output datasets. Reducing the % of accepted models in the dataset improves the accuracy of the final output profile, with only the best performing models used to simulate the predicted likelihood of identifying episodes of deposition. Meanwhile, increasing the number of repeats used in the final mean calculation reduced the overall standard error, increasing the precision of the profile. To improve the standard error, therefore, 5,000 repeats were completed to increase the size of the dataset from which we could subsequently select the top % of model repeats. Figure L.7 demonstrates how increasing the number of repeats drastically reduces the standard error associated with the profile, whilst reducing the number of datasets based on model performance improves the resolution of the signal within the dataset; features are not 'averaged out'. Using an example dataset (Figure L.7), results from repeat sensitivity analysis suggested that selecting the top 10% of models from 5,000 repeats provided us with a profile with minimal errors yet was not overly sensitive to noise (e.g. top 5%) (Figure L.7). Two distinct identifiable peaks can be seen in all of the 5,000 repeat profiles, suggesting these peaks are a true feature and have not been produced through selective model refinement, with the peaks becoming more pronounced as the model selection becomes more stringent.

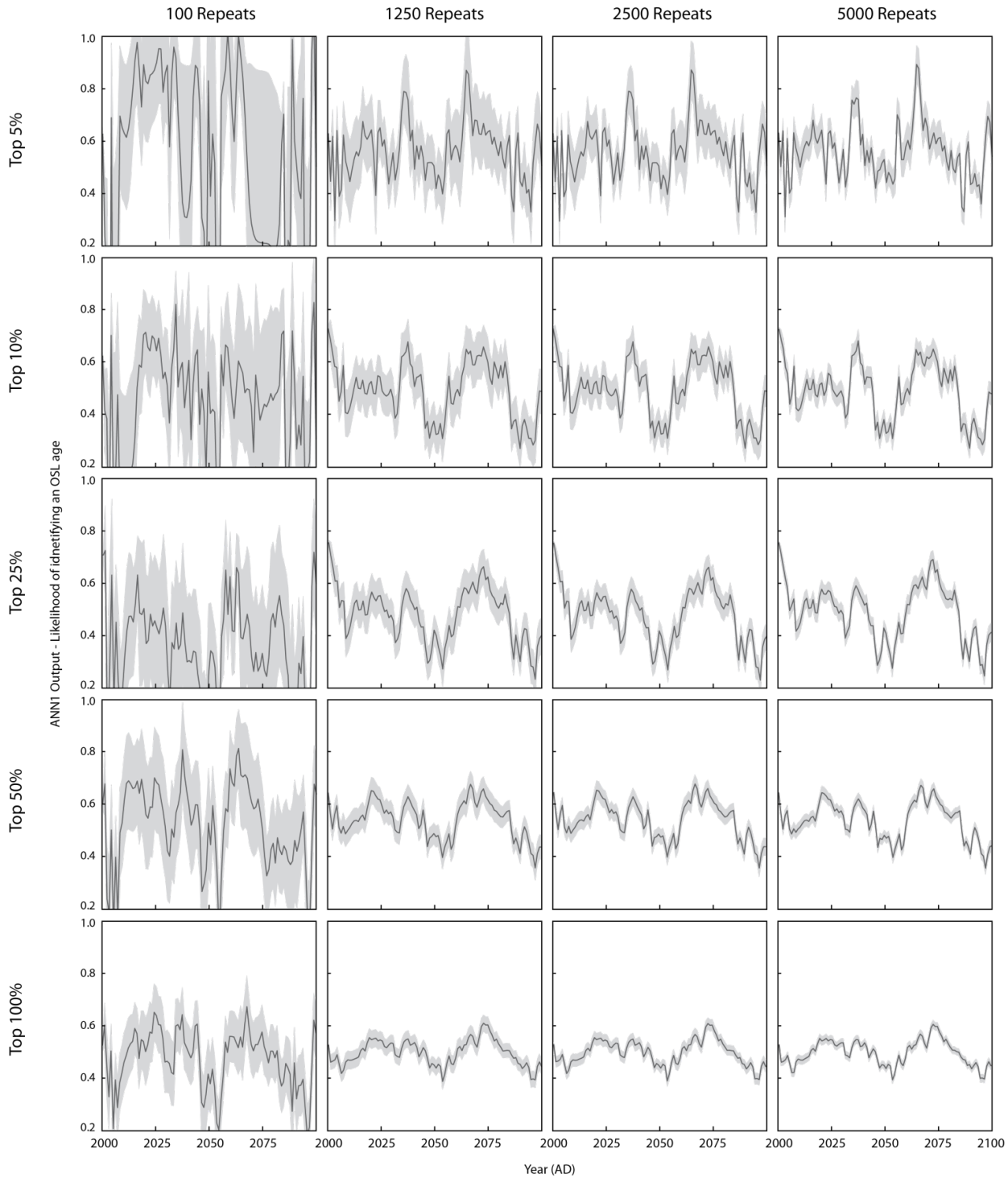


Figure L.7 Example of change in mean and standard error output profile when different numbers of repeats and % of best peak performing models were used in final calculation. Example is based on a hypothetical climate future not used in the main text analysis.

6. Dominance of climatic signal

Results from the scenario forecasting suggest that the majority of the variability found in the likelihood for identifying deposition event output is explained by the trends shown in the simulated tree ring growth index Include. When the two parameters are plotted against one another, we find a weak anticorrelation associated with vegetation growth (ANN2 output) and the likelihood for periods of sediment deposition (ANN1 output) (Figure L.8).

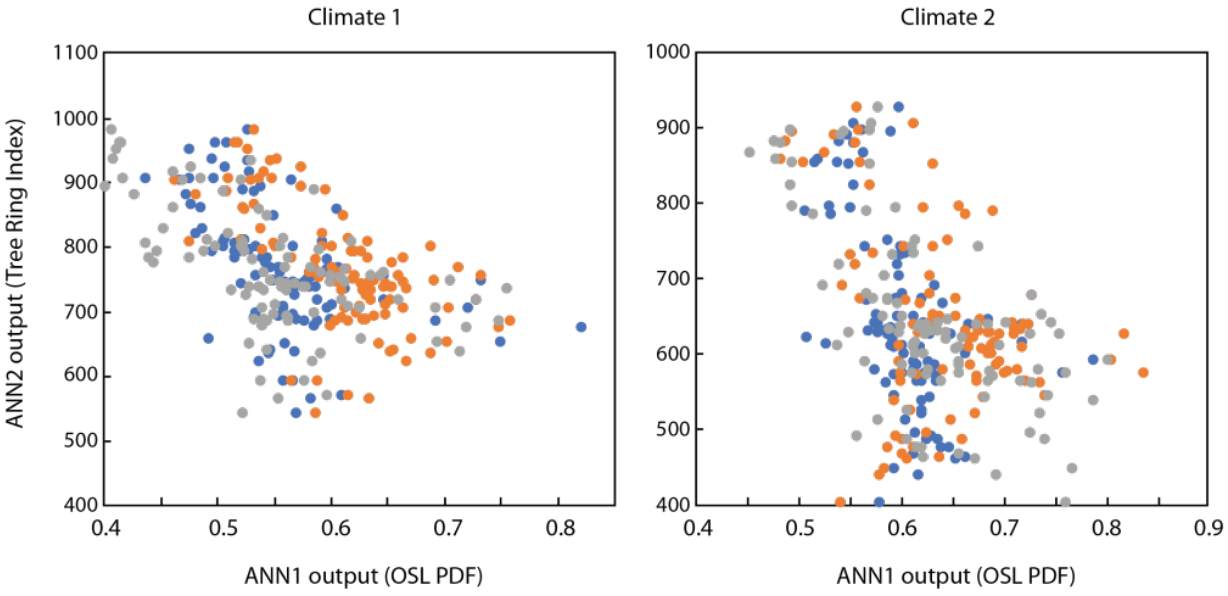


Figure L.8 Plots demonstrating the weak anticorrelation associating tree ring growth with the likelihood for episodes of sediment deposition across the two climate profiles simulated. Grey dots: low grazing pressure, orange dots: moderate grazing pressure, blue dots: heavy grazing pressure.